Dust and Gas in the Early Universe - An Observational Perspective on Galaxy Formation and Evolution

THOMAS RODRIGUEZ GREVE

Institute for Astronomy
School of Physics

A thesis submitted to the University of Edinburgh
for the degree of Doctor of Philosophy

August 2004

Declaration

I hereby declare that this thesis is not substantially the same as any that I have submitted for a degree or diploma or other qualification at any other University. I further state that no part of my thesis has already been or is being concurrently submitted for any such degree, diploma or other qualification.

This thesis is the outcome of my own work except except for in chapter 3 where I have been responsible for only part of the work presented. This includes:

- Contribution to the initial reduction of the radio data.
- Reduction and photometric calibration of the V-band image of ELAIS N2 and the I-band image of the Lockman Hole.
- Creation of true colour postamps in the Lockman Hole.
- Estimation of photometric redshifts and overall redshift distribution of the SCUBA population (Table 6, Figure 8 and 9).
- Writing section 3.4.5.
- Figure 10 and significant contribution to the writing of section 3.5.1.
- Figure 14 and writing section 3.5.5.
- Overall comments and suggestions to the paper.

Thomas R. Greve
Edinburgh,
August 2004.

Acknowledgements

The guidance, comments and support by my various co-authors and other collaborators have been of invaluable importance, and is acknowledged in the footnotes or acknowledgements of the appropriate chapters. However, I'd like to take this opportunity to thank my 'mentors', Rob J. Ivison and Padelli P. Papadopoulos, for their insight, enthusiasm and friendship from which I have benefitted tremendously.

I'd like to once again acknowledge the generous support I have received from the Danish Research Council and from the European Union RTN network, which has allowed be to attend a considerable number of conferences, summer schools and observing runs over the past few years. I'm also grateful to the Perren Studentship which supported me during the first year of my PhD at University College London. Special thanks goes to the A25 society.

f, m, d, m - this is for you.

Contents

Abstract

This thesis deals with the formation and evolution of galaxies from an observational point of view. In the work presented here observations of dust-enshrouded galaxies at high redshifts have been carried out at a range of different wavelengths - spanning from radio and (sub-)millimetre wavelengths to the optical regime. Single dish continuum observations as well interferometric heterodyne observations which probe the dust and gas in the interstellar medium of galaxies have been performed.

The first part of the thesis presents the results from unbiased surveys at millimetre (1200 μm) and radio (1.4 GHz) wavelengths of the ELAIS N2 and Lockman Hole East fields both of which have previously been mapped at 850 μm. From the first survey the most accurate number counts at 1200 μm to date are derived and are found to match simple parametric models of galaxy evolution remarkably well. Exploiting the well-matched data in all three wavebands we address the issue of the reliability of low signal-to-noise (sub)mm surveys and extract an extremely robust sample of sources detected in the radio and both of the (sub)mm bands. Constraints are also imposed on the redshift distribution of submm sources using spectral templates representative of local starburst galaxies. The radio data is used in conjunction with optical/near-infrared imaging to obtain robust radio counterparts and thereby pinpoint the location of the optical/near-infrared host galaxies for an unprecedented large sample of submm sources. The optical/near-infrared colours and morphologies are summarised revealing that about 60 per cent of the host galaxies display highly structured or complex morphology, suggestive of merging or interacting systems.

In the second part of the thesis the potential of the molecule carbonmonoxide (CO) to trace gas and the properties of the interstellar medium of galaxies at high redshifts is explored. A simple numerical code which simulates the non-LTE excitation conditions of CO in a spherical molecular cloud of H_2 is constructed and is subsequently used to constrain the density and kinetic temperature in two case-studies of high redshift galaxies. Finally, the results from a first systematic interferometric CO survey of luminous submm galaxies are presented. The bulk properties such as gas mass and CO linewidths of an unprecedented large sample of bright submm galaxies are derived and compared with local starburst galaxies as well with other galaxy populations at high redshifts. Based on the average dynamical and total baryonic masses as well as the typical gas exhaustion time of submm galaxies an evolutionary scenario is proposed which attempts to link them to massive evolved galaxies at $z \sim 1$ and old giant ellipticals at the present day. Lower limits are imposed on the co-moving number density of massive galaxies at high redshifts and a comparison with predictions from semi-analytical models of galaxy formation reveals the shortcomings of current models to explain the rapid assembly of massive galaxies in the early Universe.

Chapter 1

Introduction

The story of submillimetre (submm) astronomy is a 'classic' – one that is encountered many times in the history of observational astronomical research: technological advances lead to the development of new sensitive detectors, often in a hitherto unexplored wavelength regime, paving the way for a major break-through such as the discovery of an entirely new population of astronomical objects, say, which ultimately leads to a significant improvement in our understanding of a particular field of astronomy. In the case of (sub)millimetre astronomy the technological break-through came with the construction of large-format bolometer arrays capable of imaging substantial areas of the sky at wavelengths $450-1300\,\mu$m. The first pioneering observations were made with the Submillimetre Common-User Bolometer Array (SCUBA - Holland et al. 1999) and the Max Planck Millimetre Bolometer array (MAMBO - Kreysa et al. 1998) - still the main two bolometer arrays in use today - and had an almost instant impact on our understanding of galaxy formation and evolution (Smail, Ivison & Blain 1997; Hughes et al. 1998; Bertoldi et al. 2000).

The cosmology which sets the backdrop for any theory of galaxy formation and evolution is remarkably well determined. This is largely owing to recent successful space-born experiments, which have measured the cosmic microwave background in great detail (Spergel et al. 2003), as well as ambitious efforts on the ground to map the large scale structure of the Universe (e.g. Percival et al. 2002), and as a result the key parameters governing the dynamics of the Universe are known to great accuracy. From an optimistic viewpoint one could argue that the only missing piece in 'the puzzle' is understanding how large baryonic structures such as galaxies and clusters of galaxies formed.

Broadly speaking our current understanding of how galaxies form and evolve can be split into two families of models and has to do with how we think the baryons in the early Universe condensed into bound structures such as galaxies. In the first family of models structures form hierarchically, meaning that small entities are the first to form while larger structures such as giant ellipticals seen in the Universe at the present day, are formed gradually over time through mergers of smaller structures (White & Rees 1978; Cole et al. 1994). An alternative scenario of how structures formed is the 'monolithic collapse' model (Oggen, Lynden-Bell & Sandage 1962; Larson et al. 1974). While substantial observational effort has gone into pinpointing which scenario is the right one, the result is still inconclusive, with observational evidence favouring both models. In this context, submm observations have proven to be a powerful tool due to the large negative k-correction at these wavelengths, which enables us to detect galaxies in their formative stages with equal sensitivity throughout the redshift range $1 \lesssim z \lesssim 8$.

Ground-based submm observations are complicated by the fact that except for in a number of spectral windows the atmosphere is virtually opaque to submm emission. To makes things worse, the fluctuating submm background of the atmosphere itself typically outshines astronomical

objects by an order of magnitude. Only the invention of ingenious observing techniques (Emerson, Klein & Haslam 1979; Emerson 1995), which essentially cancels out the varying sky background, together with extremely cold detectors, has prevented a degradation of the sensitivity to a level where it would render submm observations futile. In fact, had detectors been only a factor of two less sensitive very few if any extragalactic submm sources would have been discovered.

Despite these difficulties substantial effort and telescope time has been invested in submm observations over the last 7-8 years which has resulted in the publication of a number of major extra-galactic (sub)mm surveys (e.g. Barger et al. 1998; Eales et al. 1999; Scott et al. 2002; Webb et al. 2003; Borys et al. 2003; Greve et al. 2004). The majority have been unbiased blank-field surveys of regions with existing or planned observations at a multitude of different wavelengths (e.g. Hughes et al. 1998; Barger et al. 1998; Scott et al. 2002). Others have concentrated on mapping clusters of galaxies in a clever attempt to utilise the clusters gravitational potential as a 'cosmic gravitational telescope' to probe beyond the formal sensitivity and confusion limits of SCUBA (Smail, Ivison & Blain 1997; Smail et al. 2002). In total, these surveys have imaged more than 1000 square arcminutes of sky at submm wavelengths and uncovered several hundred sources in the flux range $0.5 - 15$ mJy.

The single most important discovery to come out of extragalactic submm surveys is the existence of a significant population of luminous dust-obscured high-redshift galaxies which are responsible for a substantial fraction of the total energy output produced by galaxies over the history of the Universe. In the local Universe the abundance of far-infrared luminous galaxies is far too low to account for the observed diffuse far-infrared/submm extragalactic background which contains as much energy as the total energy density in the optical. The far-infrared/submm extragalactic background thus provides a 'fossil record' of much earlier times where far-infrared luminous galaxies were much more abundant. However, the nature of submm sources and how they fit into the overall picture of galaxy formation and evolution is only just now starting to be unraveled largely owing to a number of comprehensive and meticulous multi-wavelength follow-up observations (Smail et al. 2002; Ivison et al. 2002; Chapman et al. 2003; Alexander et al. 2003; Blain et al. 2004; Smail et al. 2004; Swinbank et al. 2004; Greve et al. 2004; Chapman et al. 2004). This development is reflected in the overall structure of this thesis which almost exclusively deals with observations of submm sources at complementary wavelengths.

In chapter 2, a large, unbiased 1200 μm MAMBO survey of the ELAIS N2 and Lockman Hole East fields is presented. The 1200 μm number counts are derived and compared to analytical models of galaxy evolution. Evidence for clustering amongst the MAMBO sources is sought for by employing two different clustering statistics. The chapter closes with a detailed comparison between the MAMBO and SCUBA source catalogues.

Chapter 3 presents the results from deep radio imaging of the ELAIS N2 and Lockman Hole East regions. The fraction of submm galaxies with robust radio counterparts is derived, and the optical/near-infrared properties of their host galaxies are studied.

In chapter 4, the attention is turned to the CO molecule and its excitation properties in clouds of molecular hydrogen. The theory behind the Large Velocity Gradient (LVG) model is discussed and a LVG-model is constructed.

In chapters 5 and 6, Very Large Array observations of CO $J = 1 - 0$ in the extremely red object ERO J164502+4626.4 and the high-redshift radio galaxy 4C 60.07 are presented. The distribution of molecular gas in these two systems is studied, and constraints are put on their

molecular and dynamical masses. The LVG model developed in chapter 4 is used to constrain the physical conditions of the molecular gas.

A systematic interferometric survey of CO emission towards submm galaxies is presented in Chapter 7. The average molecular, dynamical and baryonic masses of the bright-end of the submm population are derived and compared with that of other galaxy populations. The implications these findings have on theories of structure formation are discussed.

Chapter 8 gives a brief summary of the main results and conclusions of the thesis.

References

Alexander, D.M., Bauer, F.E., Brandt, W.N., et al. 2003, AJ, 126, 539.
Barger, A.J., Cowie, L.L., Sanders, D.B., Fulton, E., Taniguchi, Y., Sato, Y., Kawara, K., & Okuda, H. 1998, Nature, 394, 248.
Bertoldi, F., Menten, K.M., Kreysa, E., Carilli, C.L., & Owen, F. 2000, 24th meeting of the IAU, Joint Discussion 9, Manchester, England.
Blain, A.W., Chapman, S.C., Smail, I., & Ivison, R.J. 2004, ApJ, in press, (0405035).
Borys, C., Chapman, S., Halpern, M., & Scott, D. 2003, MNRAS, 344, 385.
Chapman, S.C., Blain, A.W., Ivison, R.J. & Smail. I. 2003a, Nature, 422, 695.
Chapman, S.C., Blain, A.W., Ivison, R.J., & Smail,I. 2004, ApJ, in press.
Cole, S. et al. 1994, MNRAS, 271, 781.
Eales S.A, Lilly S.J., Gear W.K., Dunne L., Bond J.R., Hammer F., Le Fèvre O., & Crampton D., 1999, ApJ, 515, 518.
Eggen, O.J., Lynden-Bell, D. & Sandage, A. 1962, ApJ, 136, 748.
Emerson, D.T., Klein, U. & Haslam, C.G.T. 1979, A&A, 76, 92.
Emerson, D.T. 1995, in ASP Conf. Ser. 75, Multi-Feed Systems for Radio Telescopes, eds. D.T. Emerson & J.M. Payne (San Francisco: ASP), 309.
Greve, T.R., Ivison, R.J., Bertoldi, F., et al. 2004, MNRAS, in press.
Holland W.S. et al., 1999, MNRAS, 303, 659.
Hughes, D.H., Serjeant, S., Dunlop, J., et al. 1998, Nature, 394, 241.
Ivison, R.J., Greve, T.R., Smail, I., et al. 2002, MNRAS, 337, 1.
Kreysa, E., Gemuend, H.-P., Gromke, J., Haslam, et al. 1998, Proc SPIE 3357, 319.
Larson, R.B. 1974, MNRAS, 166, 585.
Percival, W.J. et al. 2002, MNRAS, 337, 1068.
Scott, S.E., Fox, M.J., Dunlop, J.S., et al. 2002, MNRAS, 331, 817.
Smail, I., Ivison, R.J., & Blain, A.W. 1997, ApJ, 490, L5.
Smail, I., Ivison, R.J., Blain, A.W., & Kneib, J.-P. 2002, MNRAS, 331, 495.
Smail, I., Chapman, S.C., Blain, A.W., & Ivison, R.J. 2004, ApJ, submitted.
Spergel, D.N. et al, 2003, ApJS, 148, 175.
Swinbank, A.M., Smail, I., Chapman, S.C., Blain, A.W., Ivison, R.J., & Keel, W.C. 2004, ApJ, submitted.
Webb T.M.A., Eales S.A., Lilly S.J., Clements D.L., Dunne L., Gear W.K., Flores H., & Yun M., 2003, 587, 41.
White, S.D.M. & Rees, M.J. 1978, MNRAS, 183, 341.

Chapter 2

A 1200 μm MAMBO survey of ELAIS N2 and the Lockman Hole: I. Maps, sources and number counts

Abstract. We present a deep, new 1200 μm survey of the ELAIS N2 and Lockman Hole fields using the Max Planck Millimeter Bolometer array (MAMBO). The areas surveyed are 160 arcmin^2 in ELAIS N2 and 197 arcmin^2 in the Lockman Hole, covering the entire SCUBA '8-mJy Survey'. In total, 27 (44) sources have been detected at a significance $\geq 4.0\sigma$ ($\geq 3.5\sigma$). The primary goals of the survey were to investigate the reliability of (sub)millimetre galaxy (SMG) samples, to analyse SMGs using flux ratios sensitive to redshift at $z > 3$, and to search for 'SCUBA drop-outs', i.e. galaxies at $z >> 3$. We present the 1200 μm number counts and find tentative evidence of a fall at bright flux levels. Employing parametric models for the evolution of the local 60 μm *IRAS* luminosity function (LF), we are able to account simultaneously for the 1200 and 850 μm counts, suggesting that the MAMBO and SCUBA sources trace the same underlying population of high-redshift, dust-enshrouded galaxies. From a nearest-neighbour clustering analysis we find tentative evidence that the most significant MAMBO sources come in pairs, typically separated by $\sim 23''$. Our MAMBO observations unambiguously confirm around half of the SCUBA sources. In a robust sub-sample of 13 SMGs detected by both MAMBO and SCUBA at a significance $\geq 3.5\sigma$, only one has no radio counterpart. Furthermore, the distribution of 850/1200 μm flux density ratios for this sub-sample is consistent with the spectroscopic redshift distribution of radio-detected SMGs (Chapman et al. 2003). Finally, we have searched for evidence of a high-redshift tail of SMGs amongst the 18 MAMBO sources which are not detected by SCUBA. While we cannot rule out that some of them are SCUBA drop-outs at $z >> 3$, their overall 850-to-1200 μm flux distribution is statistically indistinguishable from that of the 13 SMGS which were robustly identified by both MAMBO and SCUBA.

2.1 Introduction

In a time of 'high-precision cosmology' one of the fundamental questions about which we remain largely ignorant is the formation and evolution of galaxies and clusters of galaxies. One of the most important breakthroughs in this field was the discovery of a significant population of far-IR-luminous, high-redshift sources in surveys at submillimetre (submm) and millimetre (mm) wavelengths using SCUBA and MAMBO (Smail, Ivison & Blain 1997; Hughes et al. 1998; Barger et al. 1999; Eales et al. 2000; Bertoldi et al. 2000), resolving at least half of the far-IR/submm background detected by the *DIRBE* and *FIRAS* experiments (e.g. Hauser et al. 1998).

It is widely believed that the large far-IR luminosities ($\gtrsim 10^{12}\,L_\odot$) of these sources is caused by intense UV light from starbursts and/or active galactic nuclei (AGN) being absorbed by dust and

Greve, T.R, Ivison, R.J., Bertoldi, F., Stevens, J.A., Dunlop, J.A., Lutz, D., & Carilli, C.L. 2004, MNRAS, in press.

re-radiated longwards of 100 μm. The negative k-correction at $\lambda \geq 400\,\mu$m allows submm/mm observations to select star-forming galaxies at $z > 1$ in an almost distance-independent manner, providing an efficient method of finding obscured, star-forming galaxies at $1 < z < 10$ (Blain & Longair 1993). The large star-formation rates ($\sim 1000\,M_{\odot}$ yr^{-1}) found for (sub)mm galaxies (hereafter SMGs) are sufficient to construct a giant elliptical ($\sim 10^{11}\,M_{\odot}$) in less than a Gyr, providing that the starburst is continuously fueled. This has led people to speculate that SMGs could be the progenitors of such galaxies (e.g. Dunlop 2001), a scenario which is further strengthened by the fact that the co-moving number density of SMGs appears to be consistent with that of today's massive ellipticals (Scott et al. 2002; Dunne, Eales & Edmunds 2003). However, the nature of SMGs, and in particular their relationship with possible present-day counterparts, is not known, just as their relation to other high-redshift populations such as Lyman-break galaxies (LBGs) and extremely red objects (EROs) is not well understood.

Progress has been hampered by the large positional uncertainties of the SMGs. The relatively large beams of (sub)mm telescopes (11–14″, FWHM) makes it impossible to reliably tie an SMG to an optical or near-IR counterpart, unless additional data at a complementary wavelength are available. Since a characteristic feature of both starburst galaxies and AGN is radio emission, deep radio imaging has proven to be a highly efficient way of accurately identifying optical/near-IR counterparts to SMGs (Ivison et al. 1998, 2000; Smail et al. 2000; see also chapter 3). Use of the radio-to-submm spectral index as an redshift indicator (Hughes et al. 1998; Carilli & Yun 1999, 2000) has shown that the SMGs lie at high redshift, with an estimated median redshift of ≥ 2 (chapter 3). Recently, Chapman et al. (2003, 2004) have obtained spectroscopic redshifts for $\sim$90 SMGs and found they span $0.8 < z < 4$, with a median of 2.4, although they cautioned that the distribution might be skewed towards lower redshifts since a requirement for getting a spectrum was that the SMGs had μJy counterparts in the radio. In a very deep radio survey of the Lockman Hole and ELAIS N2 fields, Ivison et al. (2002) found that about one third of SMGs did not have radio counterparts. One plausible explanation was that some of these radio-blank SMGs lie at very high redshifts. Such a population of SMGs — the so-called 'high-redshift tail' — would ask difficult questions of popular hierarchical models. The high-redshift SMGs would have low $S_{850\mu\mathrm{m}}/S_{1200\mu\mathrm{m}}$ flux ratios (see Eales et al. 2003) and would be readily detectable with MAMBO. Blain, Barnard & Chapman (2003), amongst others, have pointed out the limitations of photometric redshift techniques: the redshift is degenerate with the far-IR luminosity as parametrised by the dust temperature, T_{d}. In principle, however, a comparison between the 850, 1200 μm and 1.4-GHz flux densities allows us, in some cases at least, to break this degeneracy, assuming that SMGs follow the radio/far-IR correlation. For example, an SMG which has a 'warm' $S_{850\mu\mathrm{m}}/S_{1200\mu\mathrm{m}}$ ratio but has no radio counterpart is likely to be at high redshift. The $S_{850\mu\mathrm{m}}/S_{1200\mu\mathrm{m}}$ redshift estimator is particular sensitive at $z > 3$ and is currently the most effective way to assess whether there is a significant high-redshift tail of SMGs.

The primary advantage of a mapping survey, rather than pointed photometry (on–off) observations of known sources (e.g. Eales et al. 2003), is that one obtains an unbiased view of the sky. Data are not skewed by the choice of targets, by possible errors in coordinates, or by potentially spurious assumptions about how the sky is expected to appear. A key goal of our new survey was to determine unbiased flux densities for the radio-blank SCUBA sources using MAMBO, and to search for new populations of mm-bright sources, in particular a sign of a dusty, star-forming $z >> 5$ population — 'SCUBA drop-outs' — that would be expected to be below the typical SCUBA detection threshold at 850 μm but detectable by MAMBO at 1200 μm.

In this paper we present a new, unbiased 1200 μm survey, using MAMBO on the IRAM 30m telescope, of the Lockman Hole and ELAIS N2, the two regions observed by the SCUBA 8 mJy survey (Scott et al. 2002; Fox et al. 2002). A plethora of multi-wavelength observations exist for

both fields, including very deep X-ray, optical, near-IR, mid-IR and radio imaging (Hasinger et al. 2001; Manners et al. 2002; Almaini et al. 2002; chapter 3). Our observations, data reduction and maps are described in §2 and 3. The source extraction technique and the source catalogues for each field are presented in §4, as are the results of Monte Carlo simulations to assess completeness, positional accuracy, flux boosting, etc. In §5 and 6 we present our measurements of the source counts and the clustering properties of MAMBO sources. Finally, §7 describes our joint analysis of the 850 and 1200 μm samples, and implications for ongoing (sub)mm surveys and for the redshift distribution of SMGs. Throughout, we have adopted a flat cosmology, with $\Omega_m = 0.3$, $\Omega_\Lambda = 0.7$ and $H_0 = 70\,\mathrm{km\,s^{-1}\,Mpc^{-1}}$.

2.2 Observations

The survey was carried out with the 37- and 117-channel MPIfR Max Planck Millimeter Bolometer arrays (MAMBO-I and MAMBO-II; Kreysa et al. 1998) at the IRAM 30m telescope on Pico Veleta near Granada in Spain. Both MAMBO-I and MAMBO-II are He^3-cooled arrays operating at an effective frequency of 250 GHz or 1200 μm with a half-power spectral bandwidth of 80 GHz. At 1200 μm, the 30m telescope has an effective beam of 10.7″ (FWHM). The arrays are background limited and the performance of the array routinely gives noise equivalent flux densities (NEFDs) of 30 – 45 $\mathrm{mJy\,Hz^{-1/2}}$. The bolometer feedhorns are arranged in a compact hexagonal pattern each with a diameter of $2F\lambda$ which ensures an optimal coupling to the incoming radiation from a point source. MAMBO-II is amongst the largest (sub)mm bolometer arrays currently in use. In combination with the IRAM 30m dish which has a surface accuracy of 75 μm rms, it is the most powerful tool for large blank-field surveys at (sub)mm wavelengths, and will remain so until the advent of APEX/LABOCA, JCMT/SCUBA2 and LMT/Bolocam.

Scan-mapping along the azimuthal direction is the only method available at the 30m to map large areas of the sky. The signal from the sky is modulated by the secondary mirror (the wobbler) which is wobbling in the scan direction (azimuth). The wobbler frequency is 2 Hz which reflects a compromise between wanting to eliminate changes in the atmosphere on as short a timescale as possible and the challenges involved in moving a 2m secondary at this frequency and keeping it mechanically stable. We used a standard on-the-fly MAMBO scan-map, typically 300″ × 320″ in size, scanned at a velocity of $5''\,\mathrm{s^{-1}}$, and with an elevation spacing between each subscan of 8″. Hence, a map consists of 41 subscans of 60s each. This results in a fully-sampled map over a 300″ × 320″ region in ∼43 min (this includes ∼ 3s of overhead per subscan). In order to obtain uniform coverage, a regular grid with a grid-spacing of 2′ was defined across each of the two fields. Each grid position was observed once which in practice means that, in the final map, each point on the sky has been observed at least two times. In principle, this ensures that an rms of $\sim 0.8\,\mathrm{mJy\,beam^{-1}}$ is reached across most of the field. In practice, however, scans were taken in slightly different weather conditions which means that the noise is not entirely uniform. In order to eliminate any possible systematics and any residual effects from the double beam profile, wobbler throws in the range 36″ – 45″ were used. Furthermore, maps were taken with different scan-directions, just as care was taken to map each grid position once while the field was rising and once while it was setting. All this served the purpose of minimising any systematic effects from the atmosphere and/or instrument which may otherwise had arisen from observing the same grid-position in two consecutive maps using identical wobbler- and scan-configuration.

The two fields were only observed when above 30° and below 70° in elevation. The latter constraint, which avoids distorted scan-maps, was particularly troublesome for the ELAIS N2 field which reaches a maximum elevation of 85° at Pico Veleta. Since observations were pooled, they were done only under good weather conditions, i.e. when the atmospheric zenith opacity

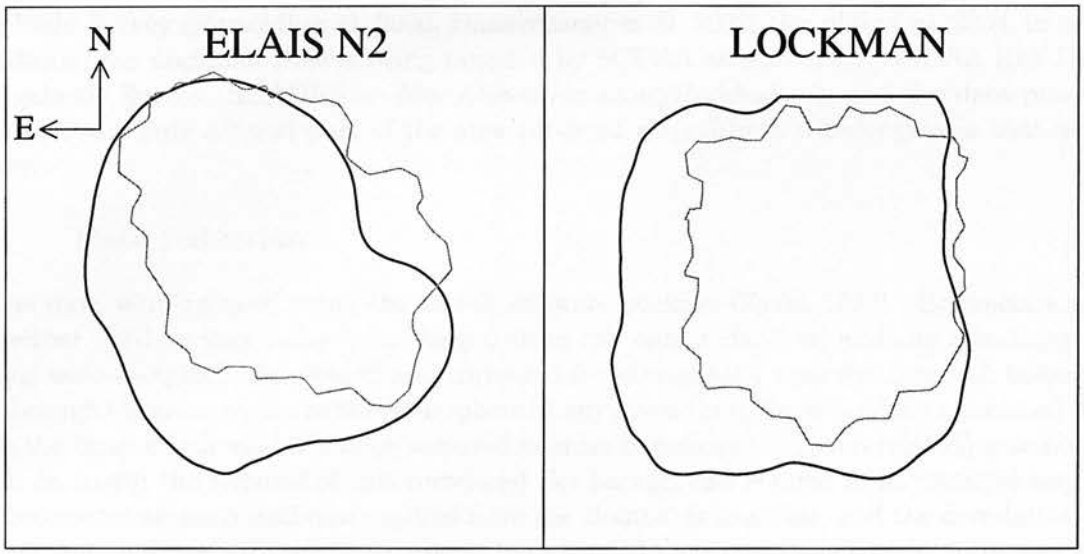

Figure 2.1: The MAMBO survey regions (outlined in black) of the ELAIS N2 and Lockman Hole fields. The mapped areas are 160 and 197 sq. arcmin in ELAIS N2 and Lockman Hole, respectively. For comparison, the coverage of the SCUBA UK 8 mJy Survey (Scott et al. 2002) is also shown (grey curve). The boxes are 21′.7 × 21′.7.

at 1200 μm was less than 0.3, with low sky-background variations. After each map, i.e. every hour, the telescope was pointed and focused. The opacity of the atmosphere was measured every other hour by doing a skydip but was also continuously monitored with a radiometer located next to the telescope. Variations in the sky-background were monitored from the pointings by on-line measurements of the correlation of the horns across the array. Also quick on-offs of the pointing sources were done throughout the night in order to check the sky noise and calibration. In order to tie down the absolute flux calibration, primary flux calibrators (including planets when available) were observed at the beginning and end of each run, and resulted in an absolute flux calibration of better than 20 per cent.

In total, 34 scan-maps, corresponding to 26 hrs, went into the final map of ELAIS N2, all of which were obtained with MAMBO-II as part of the pooled observing mode during the winter period of the 2001-2002 and 2002-2003 seasons. The bulk of the observations of the Lockman Hole were also obtained during that time using MAMBO-II, although, early observations of the Lockman Hole during the winter of 2000–01, and to some extent also 2001–02, were obtained with the 37-channel MAMBO-I array. For the Lockman Hole, 19 and 51 scan-maps taken with MAMBO-I and MAMBO-II, respectively, were used for the final map, equivalent to a total integration time of 53 hr.

The areas surveyed were 160 arcmin^2 in the ELAIS N2 field and 197 arcmin^2 in the Lockman Hole. In the case of ELAIS N2 the MAMBO observations were designed to cover the region observed at 850 μm as part of the SCUBA UK 8 mJy Survey (Scott et al. 2002). The small fraction of the SCUBA map which is not covered by our observations (Figure 2.1) is also the most noisy, and no 850 μm sources were detected in that region. However, in the Lockman Hole the overlap between MAMBO and SCUBA observations is complete, as is seen from Fig. 2.1. The Lockman Hole MAMBO data presented in this paper are part of the larger area MAMBO

Deep Field Survey (Bertoldi et al. 2000; Dannerbauer et al. 2002; Bertoldi et al. 2004, in prep.). In addition, the Lockman Hole is being targeted by SCUBA as part of the SCUBA Half Degree Extragalactic Survey (SHADES — *http://www.roe.ac.uk/ifa/shades/*), and the data presented here constitute only a small part of the area surveyed at (sub)mm wavelengths in that part of the sky.

2.3 Data reduction

The data were reduced using the MOPSI software package (Zylka 1998). Bolometers which were either dead or very noisy were flagged from the data reduction, and the remaining data streams were de-spiked, flat-fielded and corrected for atmospheric opacity. Since all bolometers look through the same region of the atmosphere at any given time, there will be a correlated signal across the array which will have to be removed in order to recover the (uncorrelated) astronomical signal. In MOPSI the removal of this correlated sky background is done in an iterative way. For each bolometer an inner and outer radius from the channel is specified, and the correlation with every bolometer lying within this annulus is computed. In our case, we chose an inner and outer radius of $1''$ and $60''$, respectively, which is suitable for compact weak sources. The correlated signals of the surrounding 6 channels with the best correlation were then chosen and the average correlated noise subtracted from the bolometer in question. This procedure is then repeated until the sky background has been removed satisfactorily across the array.

Up until this point in the data reduction, the signal from each chopping position (called the on and off phase) was processed separately, the reason being that in a single phase the bolometers correlate much better which results in a much more reliable subtraction of the background. MOPSI then calculated the phase difference, thereby effectively removing any electronic systematics between the data obtained in one wobbler position and the other. Additional de-spiking and baseline-fitting was then done on the phase differences, from which the weights for each bolometer were calculated.

Finally, the data were restored and rebinned using a shift-and-add technique which for each map produces a positive image bracketed by two negative images of half the intensity located one wobbler throw away. The rebinning was done onto a grid of 1 square arcsec pixels, with the flux in each pixel being a noise-weighted average of the bolometers hitting that position. MOPSI also outputs a weight image, W, which at pixel position (i, j) is given by $W(i,j) = \sum_k 1/\sigma_k^2$, i.e. the error on the noise-weighted average, where k denotes summing over the bolometers 'seen' by pixel (i, j). The noise maps are shown in Figure 2.2. The rms noise in the deepest parts of the maps is $\sim$0.6 mJy beam^{-1}, increasing towards the edges. The Lockman Hole received more integration time than the ELAIS N2 field and as a result it is slightly deeper and has more uniform noise properties than the latter.

2.4 Source extraction and Monte Carlo Simulations

2.4.1 Source extraction

Scan-mapping is the only option for large area mapping at the IRAM 30m telescope, and as a result the chopping direction is not fixed on the sky but varies with time which means that the chops are smeared out in the final map. Hence, unlike SCUBA jiggle maps, one cannot utilise the extra information contained in the position of the negative side-lobes for source extraction. Instead, a simple matched-filtering technique was adopted, using a Gaussian as the filter. However, as is seen from the noise images shown in Figure 2.2, the noise is not entirely uniform across the two fields and any attempt at extracting sources has to take this into account. This was done

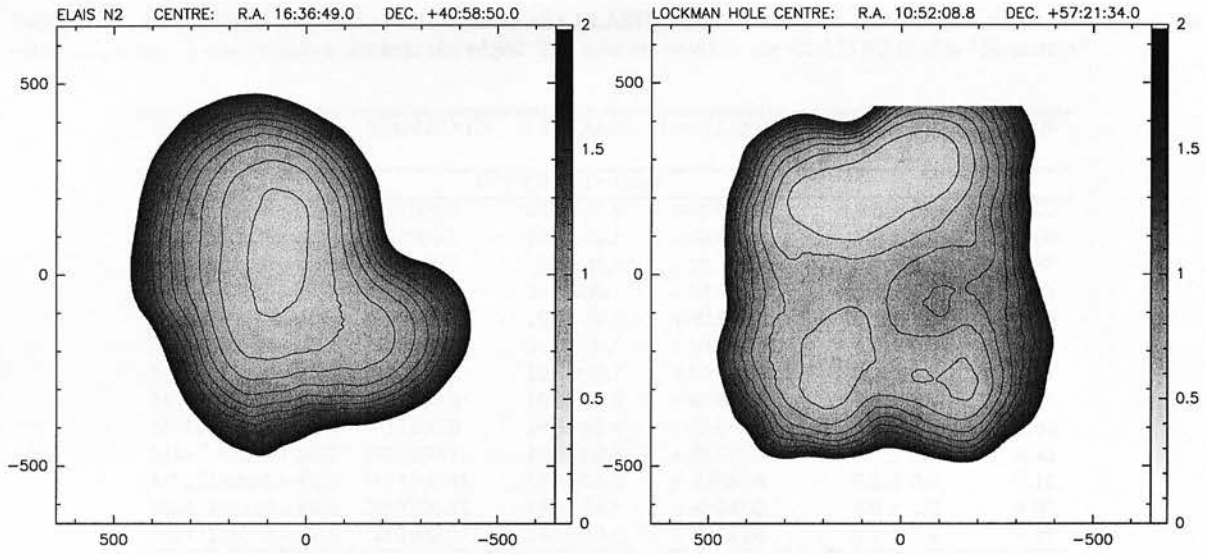

Figure 2.2: Noise maps of the ELAIS N2 and Lockman Hole East fields. Contours are at 0.7, 0.8 ... 1.5 mJy beam^{-1}. The axes denote the offset (arcsec) from the map centre, and the intensity scale is in units of mJy beam^{-1}.

by adopting a noise-weighted convolution technique similar to that of Serjeant et al. (2003). In order to account for the 10.7″ beam and the typical pointing error of 3″ rms, a Gaussian PSF, $P(x,y)$, with a FWHM of $\sqrt{10\farcs7^2 + 3\farcs0^2} = 11.1''$ was fitted to each pixel in the image $S(i,j)$ by minimising the following expression:

$$\chi^2(i,j) = \sum_{x,y} W(i-x, j-y)\,(S(i-x, j-y) - FP(x,y))^2 \tag{2.1}$$

where W is the weight image which is related to the noise by $W = 1/N^2$, and F is the best-fit flux value to pixel (i,j) and is given by:

$$F(i,j) = \frac{\sum_{x,y} S(i-x, j-y)W(i-x, j-y)P(x,y)}{\sum_{x,y} W(i-x, j-y)P(x,y)^2}. \tag{2.2}$$

The error on the flux can then be shown to be:

$$\Delta F(i,j) = \frac{1}{\sqrt{\sum_{x,y} W(i-x, y-j)P(x,y)^2}}. \tag{2.3}$$

The signal-to-noise images, $F/\Delta F$, obtained in this way are shown in Figure 2.3 and 2.4 for the ELAIS N2 field and Lockman Hole, respectively. The final source catalogues for ELAIS N2 and the Lockman Hole are listed in Tables 1 and 2. We find a total of 13 sources at significance $\geq 4.0\sigma$, and 21 sources with $\geq 3.5\sigma$ in the ELAIS N2 region while the number of sources in the Lockman Hole are 14 and 23 at $\geq 4.0\sigma$ and $\geq 3.5\sigma$, respectively.

2.4.2 Monte Carlo Simulations

Extensive Monte Carlo simulations were performed in order to determine the reliability of the source extraction technique, i.e. how large a fraction of the extracted sources are due to spurious

Table 2.1: 1200 μm MAMBO source catalogue in the ELAIS N2 field. The rms noise in the centre of the map is $\sim$0.65 mJy beam^{-1} and increases towards the edges. The area surveyed in the ELAIS N2 field is 160 arcmin^2.

ID	MAMBO ID	RA (J2000)	Dec (J2000)	$S_{1200\mu m} \pm \sigma_{1200\mu m}$ mJy	S/N
$\sigma \geq 4.0$ Detections					
MM J163647+4054	N2 1200.1	16:36:47.9	+40:54:46	4.0 ± 0.8	5.00
MM J163639+4053	N2 1200.2	16:36:39.1	+40:53:26	5.0 ± 1.0	5.00
MM J163635+4055	N2 1200.3	16:36:35.7	+40:55:59	3.9 ± 0.8	4.87
MM J163639+4056	N2 1200.4	16:36:39.1	+40:56:36	3.4 ± 0.7	4.85
MM J163632+4059	N2 1200.5	16:36:32.1	+40:59:46	5.7 ± 1.2	4.75
MM J163708+4054	N2 1200.6	16:37:08.3	+40:54:18	4.2 ± 0.9	4.66
MM J163640+4056	N2 1200.7	16:36:40.7	+40:56:46	3.2 ± 0.7	4.57
MM J163710+4055	N2 1200.8	16:37:10.5	+40:55:02	4.0 ± 0.9	4.44
MM J163705+4054	N2 1200.9	16:37:05.8	+40:54:26	4.0 ± 0.9	4.44
MM J163650+4057	N2 1200.10	16:36:50.3	+40:57:36	3.1 ± 0.7	4.42
MM J163656+4058	N2 1200.11	16:36:56.3	+40:58:14	2.5 ± 0.6	4.16
MM J163713+4054	N2 1200.12	16:37:13.8	+40:54:03	4.9 ± 1.2	4.08
MM J163619+4054	N2 1200.13	16:36:19.5	+40:54:00	5.7 ± 1.4	4.07
$4.0 > \sigma \geq 3.5$ Detections					
MM J163640+4058	N2 1200.14	16:36:40.4	+40:58:44	3.1 ± 0.8	3.87
MM J163636+4057	N2 1200.15	16:36:36.2	+40:57:19	3.1 ± 0.8	3.87
MM J163644+4102	N2 1200.16	16:36:44.8	+41:02:01	2.7 ± 0.7	3.85
MM J163706+4053	N2 1200.17	16:37:06.7	+40:53:15	4.2 ± 1.1	3.81
MM J163655+4059	N2 1200.18	16:36:55.9	+40:59:12	2.2 ± 0.6	3.66
MM J163658+4104	N2 1200.19	16:36:58.3	+41:04:37	2.9 ± 0.8	3.62
MM J163647+4055	N2 1200.20	16:36:47.9	+40:55:39	2.5 ± 0.7	3.57
MM J163715+4055	N2 1200.21	16:37:15.6	+40:55:40	3.9 ± 1.1	3.54

noise peaks, and how well does the extraction reproduce fluxes and positions as a function of signal-to-noise? Due to the slight difference in survey depth and also geometry between the ELAIS N2 and Lockman Hole maps, we decided to perform separate Monte Carlo simulations for each of the two fields.

In order to assess the contamination from spurious noise peaks to the source catalogues, we produced maps based on the real data but with the astrometry corrupted. This was done by randomising the array parameters of each scan and then producing final maps using the same MOPSI data reduction pipeline as for the real map. The advantage of this method is that the correlated noise in the raw data is preserved, and is taken out during the data reduction process in the same manner as for the real map. As a result, this method should give a realistic picture of the number of spurious noise peaks expected in our maps. We produced 100 such astrometrically corrupted maps and counted the number of positive spurious sources as a function of detection threshold. The results are shown in Figure 2.5 with empty and filled circles referring to the ELAIS N2 and Lockman Hole maps, respectively. As expected, the number of spurious detections drops off exponentially as a function of signal-to-noise threshold. From Figure 2.5 we find that a threshold of 4.0σ results in less than one spurious source expected at random, while a cut-off at 3.5σ yields less than 2-3 spurious sources per field. We adopt 3.5σ as the detection cut-off for sources in both fields since it provides a good compromise between catalogue size and source reliability.

Monte Carlo simulations were also used to test the completeness and reliability of the flux and position estimates. Sources in the flux range 1–12 mJy were added to the map in steps of 0.25 mJy, one at a time and each at a random position, with 50 sources in each flux bin. We used a scaled beam pattern as the template for the artificial sources. However, due to sky-rotation,

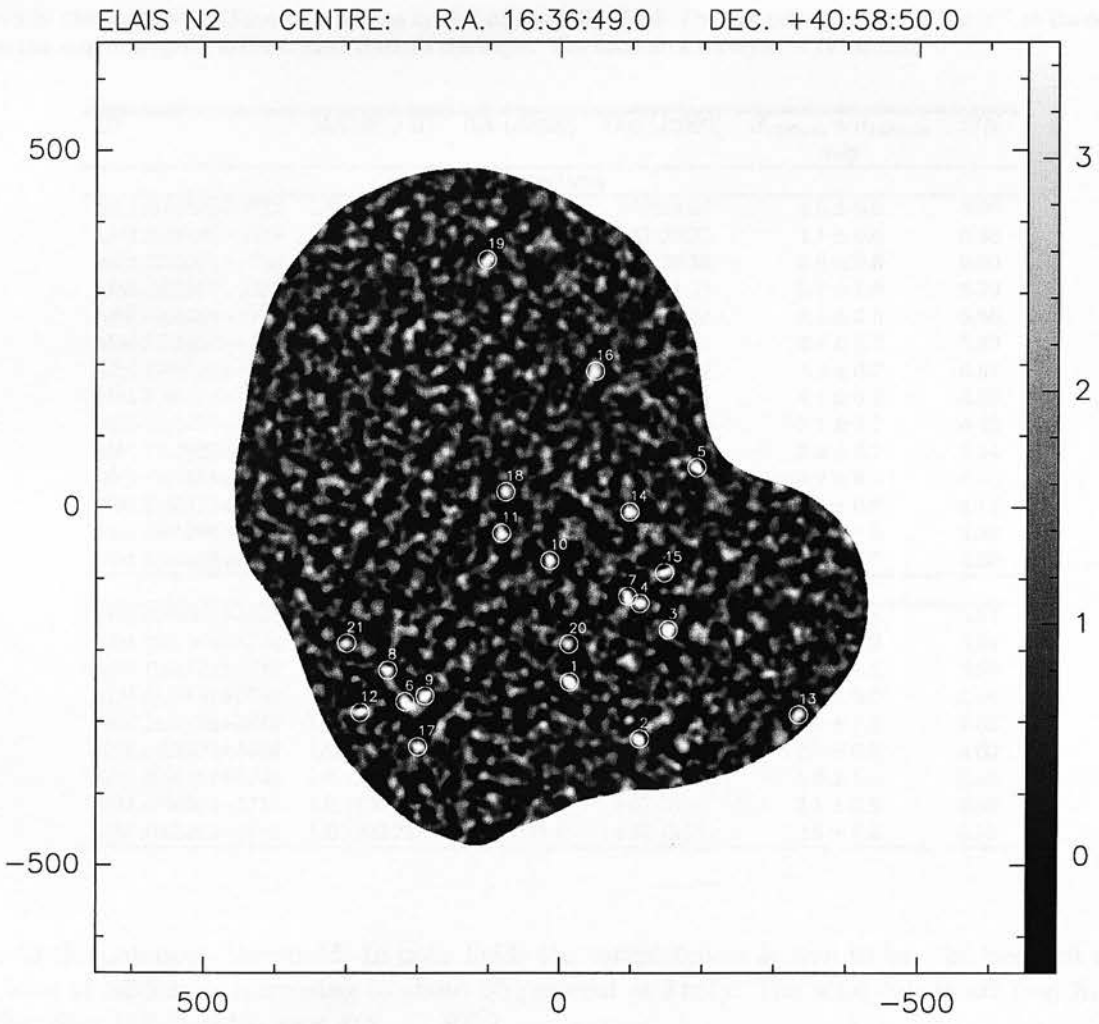

Figure 2.3: 1200 μm MAMBO signal-to-noise map of the ELAIS N2 field. Sources detected at $\geq 3.5\sigma$ are circled in white, and are numbered in order of significance. The axes denote the offset (arcsec) from the map centre.

the double-beam profile varies across the map and as a result a separate multi-beam PSF had to be constructed for each source, depending on its position in the map. To accomplish this, the source — with its correct intensity and position — was added to the data stream and then the data were reduced in the same manner as the real data. Thus, each artificial source added to the map had exactly the right multi-beam profile corresponding to its position in the map. Finally, sources were extracted using the same detection threshold as used for the real map. If a simulated source happened to fall within half a beam width of a real source in the map, it was discarded from the analysis. The results from these Monte Carlo simulations are shown in Figure 2.6, again with open and filled circles representing results based on the ELAIS N2 and Lockman Hole fields, respectively.

Figures 2.6a and b show the completeness of the survey, i.e. the percentage of recovered sources in our Monte Carlo simulations as a function of input flux density. As expected the source extraction does well in extracting all of the brighter sources, but fares less well for sources

Table 2.2: 1200 μm MAMBO source catalogue in the Lockman Hole field. The rms noise is $\sim$0.6 mJy beam^{-1} at the centre where the map is deepest, and increases towards the edges. The total area surveyed is 197 arcmin^2.

ID	MAMBO ID	RA (J2000)	Dec (J2000)	$S_{1200\mu m} \pm \sigma_{1200\mu m}$ mJy	S/N
		$\sigma \geq 4.0$ Detections			
MM J105238+5724	LE 1200.1	10:52:38.3	+57:24:37	4.8 ± 0.6	8.00
MM J105238+5723	LE 1200.2	10:52:38.8	+57:23:22	4.1 ± 0.6	6.83
MM J105204+5726	LE 1200.3	10:52:04.1	+57:26:58	3.6 ± 0.6	6.00
MM J105257+5721	LE 1200.4	10:52:57.0	+57:21:07	5.7 ± 1.0	5.70
MM J105201+5724	LE 1200.5	10:52:01.3	+57:24:48	3.4 ± 0.6	5.66
MM J105227+5725	LE 1200.6	10:52:27.5	+57:25:15	2.8 ± 0.5	5.60
MM J105204+5718	LE 1200.7	10:52:04.7	+57:18:12	3.2 ± 0.7	4.57
MM J105142+5719	LE 1200.8	10:51:42.0	+57:19:51	4.1 ± 0.9	4.55
MM J105227+5722	LE 1200.9	10:52:27.6	+57:22:20	3.1 ± 0.7	4.42
MM J105229+5722	LE 1200.10	10:52:29.9	+57:22:05	2.9 ± 0.7	4.14
MM J105158+5717	LE 1200.11	10:51:58.3	+57:17:53	2.9 ± 0.7	4.14
MM J105155+5723	LE 1200.12	10:51:55.5	+57:23:10	3.3 ± 0.8	4.12
MM J105246+5724	LE 1200.13	10:52:46.9	+57:24:47	2.4 ± 0.6	4.00
MM J105200+5724	LE 1200.14	10:52:00.0	+57:24:25	2.4 ± 0.6	4.00
		$4.0 > \sigma \geq 3.5$ Detections			
MM J105245+5716	LE 1200.15	10:52:45.1	+57:16:05	3.1 ± 0.8	3.87
MM J105244+5728	LE 1200.16	10:52:44.8	+57:28:12	5.0 ± 1.3	3.84
MM J105121+5718	LE 1200.17	10:51:21.5	+57:18:40	4.8 ± 1.3	3.69
MM J105157+5728	LE 1200.18	10:51:57.7	+57:28:00	2.2 ± 0.6	3.66
MM J105128+5719	LE 1200.19	10:51:28.4	+57:19:47	4.0 ± 1.1	3.63
MM J105224+5724	LE 1200.20	10:52:24.4	+57:24:20	1.8 ± 0.5	3.60
MM J105131+5720	LE 1200.21	10:51:31.3	+57:20:06	3.6 ± 1.0	3.60
MM J105203+5715	LE 1200.22	10:52:03.0	+57:15:46	2.8 ± 0.8	3.50
MM J105223+5715	LE 1200.23	10:52:23.4	+57:15:27	2.8 ± 0.8	3.50

close to the detection threshold. In both fields the completeness is seen to be $\sim$50 per cent at a flux level of $\simeq$2.5 mJy, increasing to about 95 per cent at 3 mJy. The solid curves are best fits of the function $f(S_{in}) = 1 - exp(A(S_{in} - B)^C)$.

In Figures 2.6c and d we have plotted the ratio between the input and output fluxes S_{out}/S_{in}, as a function of the input flux density. It is seen that fainter sources tend to have higher extracted fluxes than brighter sources. This effect — 'flux boosting' in Scott et al. (2002) — is due to the instrumental noise from the array itself and the confusion noise from faint sources below the detection threshold conspiring to scatter the retrieved fluxes upwards. As expected, flux boosting has the greatest impact at faint flux levels, where we find it can be as high as $\sim$30 per cent. However, for input fluxes $\geq$2 mJy the boosting is on average no more than $\sim$20 per cent, which is comparable to the calibration errors, see section 2.2. It is also comparable to the boosting factor reported by Eales et al. (2003) from a comparison of MAMBO fluxes obtained from a map and from photometry observations. An average flux boosting factor of $\sim$15 per cent was derived by Scott et al. (2002) from Monte Carlo simulations of their 8 mJy Survey. The solid lines in Figures 2.6c and d represent best fits to the data points of the function $f(S_{in}) = 1 + Aexp(BS_{in}^C)$.

The average positional offset between the input and output positions of the added sources is shown as a function of flux density in Figures 2.6e and f. Not surprisingly, the source extraction reproduces the true positions less well for faint sources than for brighter sources. It is seen that, in the flux range 2–5 mJy where most of our sources lie, the positional error is of the order 1.5–3.0″. This is slightly better than the 3–4″ errors typically quoted by SCUBA surveys (Webb et al. 2003; Scott et al. 2002; Borys et al. 2003) and may be due to the smaller MAMBO beam.

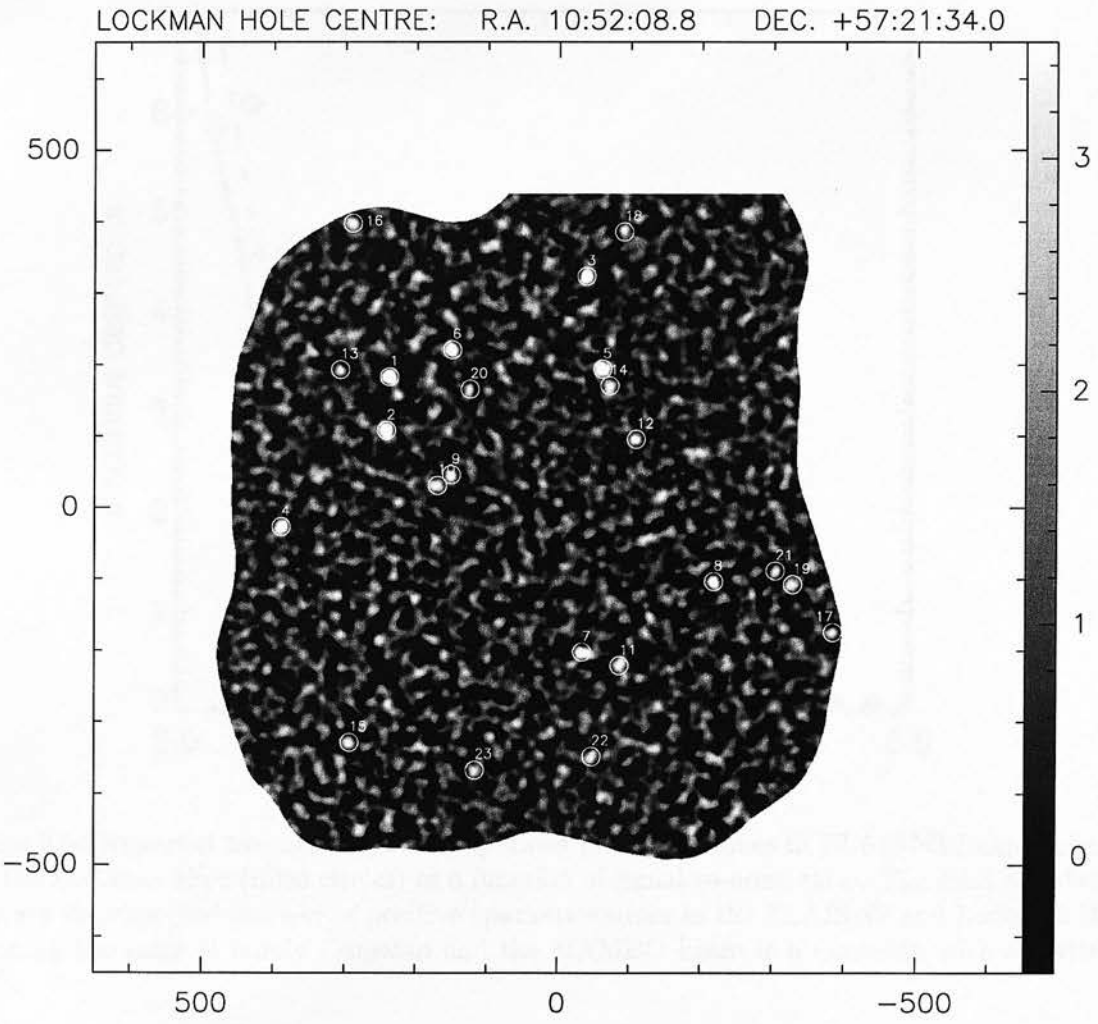

Figure 2.4: 1200 μm MAMBO signal-to-noise map of the Lockman Hole field. Sources detected at $\geq 3.5\sigma$ are circled in white, and are numbered in order of significance. The axes denote the offset (arcsec) from the map centre.

2.5 Number counts of MAMBO sources

In order to derive the 1200 μm number counts we must correct the raw number counts for the effects of flux boosting and the fact that the survey is not complete at faint flux levels. Finally, we need to assess to what degree spurious sources contaminate the number counts.

Addressing the last issue first, it is seen from Figure 2.5 that at a detection threshold of 4.0σ we expect no spurious positive sources; at a threshold of 3.5σ we expect at most two. Furthermore, the flatness of the curves at 3.5σ implies that a slight error in the noise estimate will not change the number of false sources dramatically. This would not have been the case had we used a lower threshold of 3.0σ. As a result, we have used the $\geq 3.5\sigma$ catalogues to derive the number counts. While we cannot predict which flux bins the spurious sources will fall into, it is seen from Tables 1 and 2 that the $\geq 3.5\sigma$ sources span a wide range in flux. It is therefore unlikely that the spurious sources will be restricted to a single flux bin, and as a result their

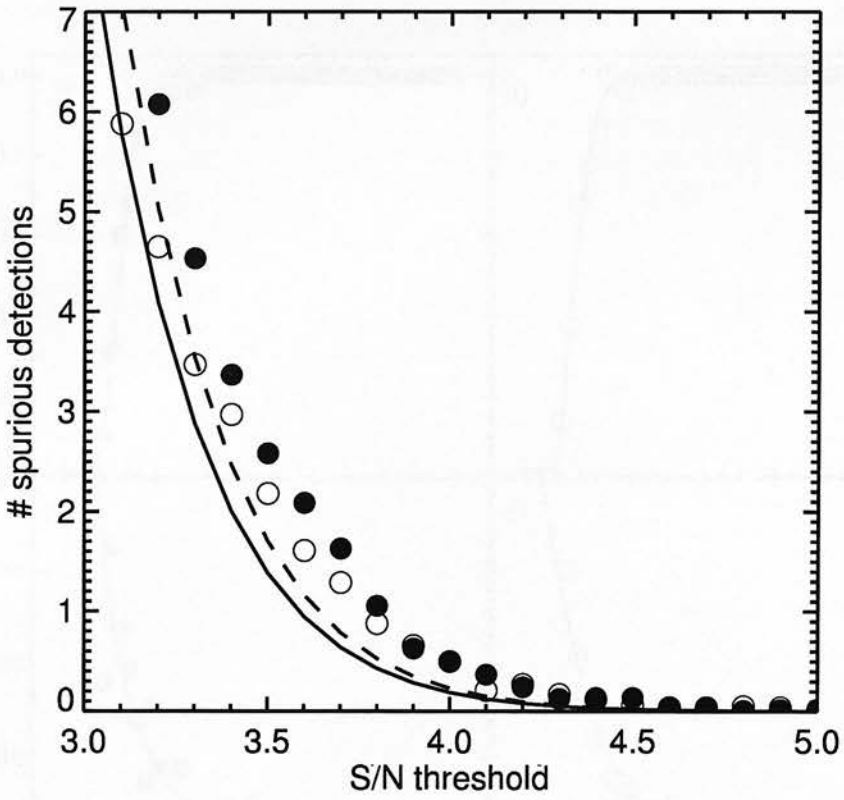

Figure 2.5: Expected average number of spurious positive sources in ELAIS N2 (empty circles) and the Lockman Hole (filled circles) as a function of signal-to-noise ratio. The solid and dashed lines are the expected number of positive spurious sources in the ELAIS N2 and Lockman Hole, assuming the noise is purely Gaussian and the MAMBO beam is a Gaussian with a FWHM of 10.7″.

effect on the number counts is expected to be negligible. Flux boosting was corrected for in a statistical way by applying the best-fit curves in Figures 2.6c and d to the raw output fluxes. The boost-corrected number counts obtained in this way were then corrected for completeness using the fitted completeness curves in Figures 2.6a and b.

The final integrated number counts in flux bins 2.75, 3.25, 3.75, 4.25, 4.75, and 5.25 mJy are given in Table 3 along with the raw number counts. The table shows the counts derived for the ELAIS N2 and Lockman Hole separately, as well as the combined number counts. The quoted errors correspond to the 95 per cent two-sided confidence level of a Poissonian distribution. The number counts derived from the two fields separately are seen to agree well within the error. In Figure 2.7 we have plotted the corrected accumulative 1200 μm number counts as derived from the MAMBO survey presented in this paper. While the surface density of SCUBA sources detected at 850 μm has been fairly well constrained over a large range in flux density thanks to a number of large submm surveys (Smail et al. 1997; Scott et al. 2002), only one other published MAMBO survey has so far attempted to constrain the 1200 μm number counts (Bertoldi et al. 2000). For comparison we have also plotted the 850 μm source counts as derived from a number of SCUBA surveys. It is seen that the 1200 μm counts are lower than those at 850 μm. This is expected if one assumes that the MAMBO and SCUBA sources trace the same population of dust-enshrouded

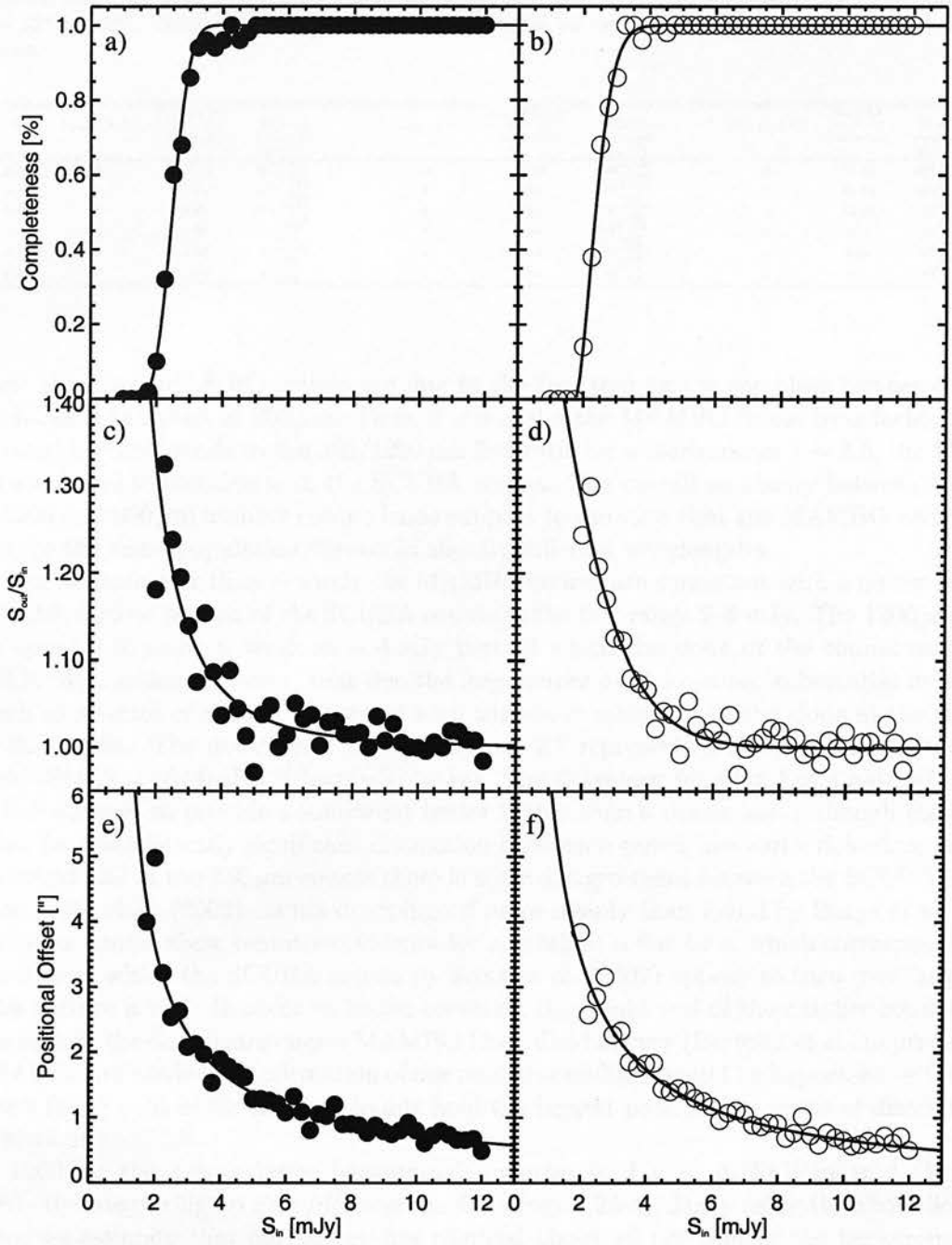

Figure 2.6: Results from Monte Carlo simulations. The solid lines in all three panels represent best fits to the points, see text for details. As in Figure 2.5, empty and filled circles refer to results from the ELAIS N2 and Lockman Hole maps. **Top:** Percentage of added sources recovered against input flux in the range 1 to 12 mJy. **Middle:** The 'boosting' factor, i.e. the factor by which the input flux is scattered upwards due to instrumental and confusion noise (Eddington bias), plotted against input flux. **Bottom:** Deviations between true (input) positions and the positions derived from the source extraction technique as a function of input flux.

Table 2.3: 1200 μm source counts as derived from the ELAIS N2 field (columns 2–4), Lockman Hole (columns 5–7), and the combined fields (columns 8–10). Only the $\geq 3.5\sigma$ catalogue is used. The area surveyed in the three cases are 160, 197, and 357 arcmin^2, respectively. The errors corresponds to 95 per cent two-sided confidence levels of a Poissonian distribution.

	ELAIS N2			LOCKMAN			TOTAL		
S [mJy]	$N_{raw}(>S)$	$N(>S)$ corrected	$N(>S)$ corrected [deg^{-2}]	$N_{raw}(>S)$	$N(>S)$ corrected	$N(>S)$ corrected [deg^{-2}]	$N_{raw}(>S)$	$N(>S)$ corrected	$N(>S)$ corrected [deg^{-2}]
2.75	16	19.99	450^{+218}_{-187}	14	17.49	320^{+178}_{-136}	30	37.48	378^{+136}_{-113}
3.25	11	11.47	258^{+185}_{-134}	9	9.39	172^{+141}_{-96}	20	20.86	210^{+101}_{-85}
3.75	9	9.05	204^{+181}_{-111}	6	6.03	110^{+128}_{-70}	15	15.08	152^{+98}_{-66}
4.25	4	4.00	90^{+140}_{-65}	4	4.00	73^{+114}_{-53}	8	8.00	81^{+78}_{-46}
4.75	4	4.00	90^{+140}_{-65}	2	2.00	37^{+96}_{-32}	6	6.00	61^{+71}_{-38}
5.25	2	2.00	45^{+117}_{-40}	1	1.00	18^{+84}_{-18}	3	3.00	30^{+68}_{-24}

galaxies: the lower MAMBO counts are due to the fact that one is sampling further down the Rayleigh-Jeans tail than at 850 μm. Thus, if one scales the MAMBO fluxes by a factor of $\sim$2.5, which roughly corresponds to the 850/1200 μm flux ratio for a starburst at $z \sim 2.5$, the MAMBO counts are found to coincide with the SCUBA counts. The overall similarity between the shape of the 1200 and 850 μm number counts lends support to the view that the MAMBO and SCUBA sources are the same population viewed at slightly different wavelengths.

At flux levels fainter than $\sim$ 4 mJy the MAMBO counts are consistent with a power-law slope of $\alpha \sim -2.3$, similar to that of the SCUBA counts in the flux range 2–9 mJy. The 1200 μm source counts appears to show a break at $\sim$ 4 mJy beyond which the slope of the counts steepens to $\alpha \sim -4.7$. We caution, however, that due the large errors on the counts, substantial uncertainty (as much as a factor of two) is associated with the above estimates of the slope at the faint and bright flux levels. The dot-dashed curve in Figure 2.7 represents a Schechter-type function of the form $dN/dS \propto (S/4\mathrm{mJy})^{-2.3}\exp(-S/4\mathrm{mJy})$. The Schechter function has a natural break at 4 mJy and appears to provide a somewhat better match than a power law, although the data do not allow for a statistically significant distinction between a power law and a Schechter function. At the bright end of the 850 μm counts there is some disagreement between the SCUBA surveys, with the Scott et al. (2002) counts dropping off more steeply than found by Borys et al. (2003). The 1200 μm counts show tentative evidence for a break at a flux level which corresponds to the 850 μm flux at which the SCUBA counts by Scott et al. (2002) appear to turn over, suggesting that this feature is real. In order to better constrain the bright end of the number counts, larger surveys such as the one square degree MAMBO Deep Field Survey (Bertoldi et al., in preparation) and SHADES are needed. Confirmation of our tentative findings would be important — the bright (and very faint) ends of the number counts hold the biggest potential in terms of discriminating between models.

At 1200 μm the extragalactic background amounts to $I_\nu \nu \sim 0.16\,\mathrm{nW\,m^2\,sr^{-1}}$ (Fixsen et al, 1998). By integrating up SdN/dS over the flux range 2.25–5.75 mJy using the above Schechter function, we estimate that our survey has resolved about 10 per cent of the background light at 1200 μm. This is comparable to the UK 8 mJy Survey which also resolved $\sim$ 10 per cent of the extragalactic background at 850 μm. If indeed MAMBO and SCUBA sources are the same, then it should be possible to construct models which can simultaneously reproduce the 850 and 1200 μm counts. In order to do so, we considered a simple parametric model which is based on the local 60 μm LF, $\Phi_o(L_{60})$, as derived from *IRAS* data (Saunders et al. 1990). The latter provides the best estimate of the far-IR LF of dusty galaxies in the local Universe to date, and is thus a useful template to try and model the number counts of dusty high-redshift galaxies. While a local 850 μm LF has been established by Dunne et al. (2000), who used SCUBA to observe a large number of galaxies from the *IRAS* Bright Galaxy Sample, the bright end of this function

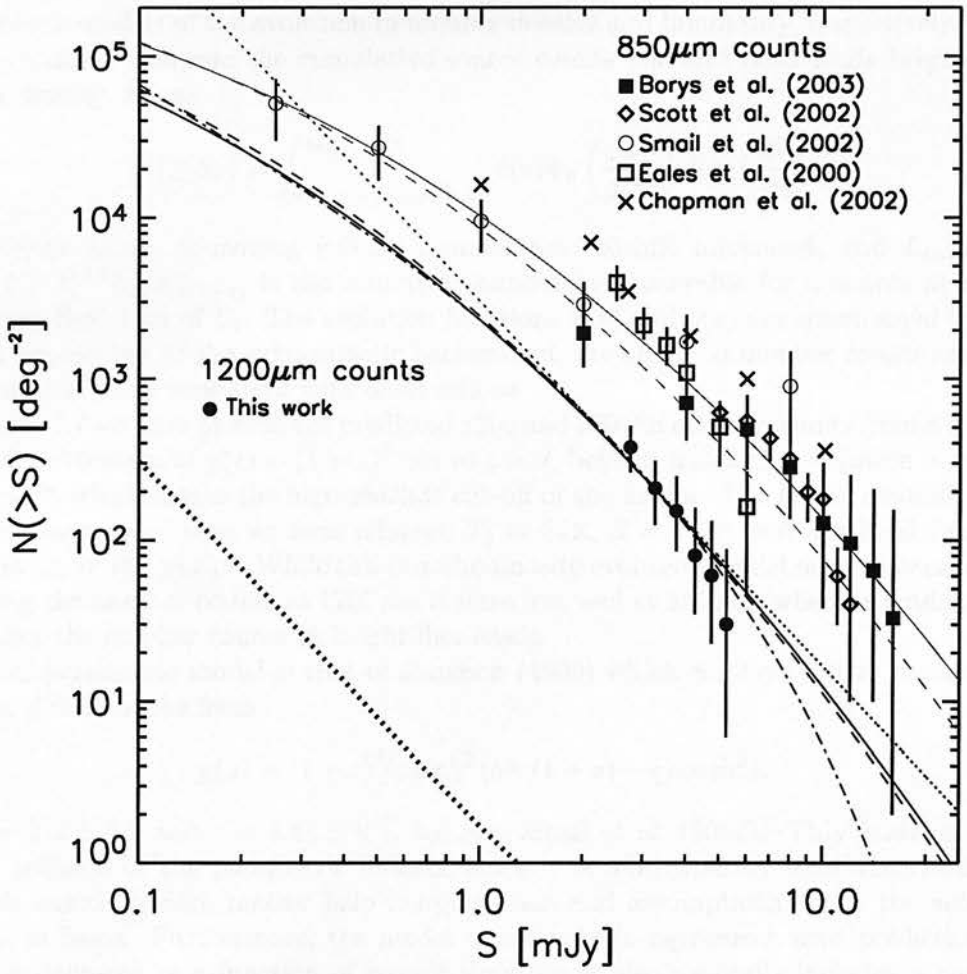

Figure 2.7: Cumulative number counts at 1200 μm (solid circles) based on the $\geq 3.5\sigma$ MAMBO source catalogue presented in this paper. The error bars represent 95 per cent two-sided confidence levels on a Poissonian distribution. Also shown are 850 μm cumulative number counts from a number of recent SCUBA surveys. The dashed black and grey lines show the number counts at 1200 and 850 μm, respectively, as predicted by a pure luminosity scenario in which $g(z) = (1+z)^3$ out to $z = 2$, beyond which no further evolution occurs. The solid black and grey curves represent predicted number counts at 1200 and 850 μm, respectively, based on the galaxy evolution model by Jameson et al. (1999), see text for details. The thin dotted line corresponds to a simple power law with slope $\alpha = -2.3$, while the dark solid curve represents the Schechter function $dN/dS \propto (S/S_o)^{-\alpha} exp(-S/S_o)$, where $\alpha = 2.3$ and $S_o = 4$ mJy. Finally, the thick dotted line represent a no-evolution scenario.

is still highly uncertain. Furthermore, if the majority of the MAMBO sources are at redshifts $z > 2$ and have similar dust temperatures to the *IRAS* galaxies (30–40 K), then the 60 μm LF will be a better approximation to the rest-frame far-IR LF of the MAMBO sources. We have therefore adopted the 60 μm LF as the reference LF at $z = 0$. In order to assess the evolution in the far-IR LF, we used a simple approach in which the LF at redshift z is given by a simple scaling and/or translation of the local LF, i.e. $\Phi(L, z) = f(z)\Phi_o(L/g(z))$, where $f(z)$ and $g(z)$

are parametric models of the evolution in number density and luminosity, respectively. It is then straightforward to compute the cumulative source counts per unit solid angle brighter than a given flux density, S_ν, as

$$N(\geq S_\nu) = \int_0^{z_{max}} \int_{L_{min}(S_\nu,z)}^{\infty} f(z)\Phi_o\left(\frac{L}{g(z)}\right) dlogL\frac{dV_c}{dz}dz, \tag{2.4}$$

where dV_C/dz is the co-moving volume element per redshift increment, and $L_{min}(S_\nu, z) = 4\pi D_L^2 S_\nu(1+z)^{-1}L_\nu/L_{\nu(1+z)}$ is the minimum luminosity observable for a source at redshift z and a survey flux limit of S_ν. The evolution functions $f(z)$ and $g(z)$ are constrained by the fact that their predictions of the extragalactic background, the observed number counts and redshift distribution has to be consistent with observations.

In Figure 2.7 we have plotted the predicted 1200 and 850 μm number counts from a model with a luminosity evolution of $g(z) = (1+z)^3$ out to $z = 2$, beyond which the evolution is unchanged out to $z = 10$, which marks the high-redshift cut-off of the model. The model assumes the same SED for all sources — here we have adopted $T_\mathrm{d} = 44\,\mathrm{K}$, $\beta = +1.2$, and a critical frequency of $\nu_c = 2\,\mathrm{THz}$ ($\lambda_c = 150\ \mu\mathrm{m}$)[1] . While this pure-luminosity evolution model does an excellent job at reproducing the number counts at 1200 μm it fares less well at 850 μm, where it tends to slightly underpredict the number counts at bright flux levels.

Another parametric model is that of Jameson (1999) which employs a pure luminosity evolution (i.e. $f = 1$) of the form

$$g(z) = (1+z)^{3/2} sech^2\left(b\ln(1+z) - c\right) cosh^2 c, \tag{2.5}$$

where $b = 2.2 \pm 0.1$ and $c = 1.84 \pm 0.1$, see also Smail et al. (2002). This model is arguably the most realistic of the parametric models, since it is motivated by semi-analytical models, i.e. models based on dark matter halo merging trees and assumptions about the astrophysics of the gas in halos. Furthermore, the model is not only in agreement with predictions of the chemical enrichment as a function of cosmic time but it also naturally includes a peak in the evolution at $z \simeq 2$ which is in agreement with the recently determined redshift distribution of radio-identified SMGs (Chapman et al. 2003). In Figure 2.7 we have plotted the predicted 1200 and 850 μm number counts for this model, under the assumption that the SEDs of all MAMBO and SCUBA sources are well matched by modified blackbody law with $T_\mathrm{d} = 37\,\mathrm{K}$, $\beta = +1.5$, and a critical frequency of $\nu_c = 2\,\mathrm{THz}$. It is seen that this physically more realistic model is able to reproduce both the MAMBO and SCUBA number counts extremely well, suggesting that the MAMBO and SCUBA sources trace the same population of high-redshift, far-IR-luminous, starburst galaxies.

While the mm number counts at faint as well as bright flux levels is still too poorly determined to warrant a detailed test of models of galaxy evolution, it is clear from the comparison with simple analytical model made above, that a scenario in which no evolution takes place at all, as illustrated by the thick dotted line in Figure 2.7, can be ruled out.

2.6 Clustering of MAMBO sources

The next big step forward in our understanding of SMGs is likely to come from determining how they are clustered. Their clustering properties may then provide a link to a present-day population of galaxies. If SMGs are the progenitors of massive elliptical galaxies, as suggested

[1] The critical frequency refers to the frequency at which the dust becomes optically thick. The rest-frame SED adopted here has the form $S_\nu \propto \frac{2h\nu^3}{c^2}\frac{1}{exp[h\nu/kT_d]-1}\left(1-e^{-(\nu/\nu_c)^\beta}\right)$.

by their star-formation rates, molecular/dynamical masses and co-moving space densities, then they are expected to be strongly clustered. This follows from the way peaks in the density field in the early Universe are biased in mass (e.g. Benson et al. 2001). Giant ellipticals, being the most luminous objects in the local Universe, are often found residing in the centres of galaxy clusters; as such they pin-point the most overdense and therefore mass-biased regions in the Universe.

Submm surveys of various depths and sizes have searched for clustering among SMGs and have all failed to detect a significant signal (Scott et al. 2002; Webb et al. 2003; Borys et al. 2003). This has been due largely to the limited size of the survey regions, though efforts are further hampered by the fact the (sub)mm population spans a broad range in redshift — the quartile range is $z = 1.9$–2.8 (Chapman et al. 2003, 2004) with a possible high-redshift tail extending to $z \gtrsim 4$ — and any clustering signal will thus, when projected onto the sky, become heavily diluted. Any detection of angular clustering will therefore be a lower limit on the real 3D clustering. One lesson learned from these surveys was that very large ($\sim$1 square degree) areas containing several hundred sources with strong redshift constraints are required in order to determine the clustering properties of SMGs. Here, we present the results for the the MAMBO population using two independent clustering statistics.

The first test calculates the angular two-point correlation function, $w(\theta)$, which quantifies the excess probability of finding a source within an angle, θ, of a randomly selected source, over that of a random distribution, i.e.

$$\delta P(\theta) = N^2(1 + w(\theta))\delta\Omega_1\delta\Omega_2, \tag{2.6}$$

where $\delta P(\theta)$ is the probability of finding a source within a solid angle $\delta\Omega_1$, and another source in another solid angle $\delta\Omega_2$ within a angular distance θ of each other (see e.g. Coles & Lucchin 2002). N is the mean surface density of objects on the sky. Several estimators of $w(\theta)$ have been suggested in the literature, and here we shall use the one first proposed by Landy & Szalay (1993):

$$w(\theta) = \frac{\langle DD\rangle - 2\langle DR\rangle + \langle RR\rangle}{\langle RR\rangle}, \tag{2.7}$$

where $\langle DD\rangle$ is the number of real source pairs which fall within a bin of width $\delta\theta$ in the map. $\langle RR\rangle$ is the number of random–random pairs extracted from simulated maps in which the sources are randomly distributed. Similarly, $\langle DR\rangle$ is the number of data–random pairs. In order to generate the random catalogues we created simulated maps by drawing sources from a source count model and placing them randomly throughout the field. We used the best fit to the observed number counts as provided by the Schechter function in section 2.5. Noise was added using one of the pure noise maps obtained by randomising the array parameters (section 2.4.2) thereby ensuring that the noise mimicked the properties of the real map as closely as possible. Mock source catalogues were then generated by applying our source extraction technique to the simulated maps. This exercise was repeated 500 times. By taking the ensemble average, the catalogues $\langle RR\rangle$ and $\langle DR\rangle$ were obtained. Furthermore, the $\langle RR\rangle$ and $\langle DR\rangle$ catalogues were normalised to have the same number of objects as $\langle DD\rangle$. The clustering analysis described here is similar to that of Borys et al. (2003) in the sense that our analysis takes the negative off-beams properly into account when estimating the clustering: our simulated maps have the same global chop-pattern as the real map. However, this effect is expected to be very small for MAMBO maps, where the off beams are smeared out due to sky rotation.

The resulting two-point correlation functions obtained using the $\geq 3.5\sigma$ as well as the $\geq 3.0\sigma$ catalogues for the ELAIS N2 and Lockman Hole fields are shown in Figure 2.8. The bin sizes used were $\delta\theta = 35''$ and $30''$, respectively, both of which roughly corresponds to two times the MAMBO

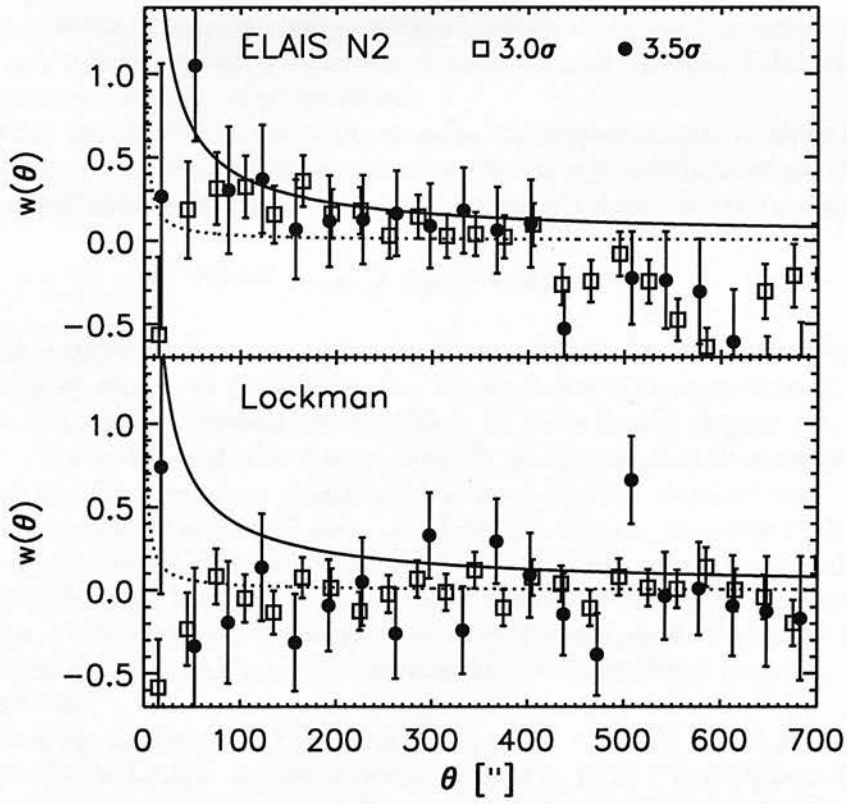

Figure 2.8: Angular two-point correlation function for ELAIS N2 (top) and the Lockman Hole (bottom). The two-point correlation function based on the $\geq 3.0\sigma$ sample (empty squares) uses a bin size of $30''$, while the correlation function based on the $\geq 3.5\sigma$ catalogue (filled circles) is derived using a bin size of $35''$. The solid line is the best-fit power-law correlation function found by Daddi et al. (2000) for EROs with $R - K > 5$ and $K < 18.5$. The dotted line represents the correlation function for LBGs as determined by Giavalisco & Dickinson (2001). The errors are given by $\delta w(\theta) = \left(\frac{1+w(\theta)}{\langle DD \rangle}\right)^{1/2}$.

beam and furthermore ensures an adequate number of sources in each bin. It is seen from Figure 2.8 that the two-point correlation function for the Lockman Hole is consistent with zero within the error bars at all angular scales. In the ELAIS N2 field, however, the correlation function has a gradient, showing a slight excess correlation at small angular scales and an anti-correlation at scales of $\sim 500''$. The correlation functions based on the $\geq 3.5\sigma$ and $\geq 3.0\sigma$ catalogues both show this trend. The correlation seen at $\theta \lesssim 100''$ seems to be apparent by looking at the map, from which it appears that the sources are distributed in 'clusters', one of which is located $\sim 200''$ south-west of the map centre, and another $\sim 350''$ south-east from centre. Within these clusters, the sources are typically separated by ~ 20–$80''$, which could explain the excess correlation seen on these scales. The anti-correlation at $\theta \sim 500''$ is reflected in the overall distribution of sources in the ELAIS N2 field which shows the sources to be distributed around a void slightly north-east of the map centre. A similar void, although less significant, is seen south-east of the centre of the Lockman Hole map. These voids appear to be real: not only are there no sources detected in these regions with SCUBA, but the μJy radio population also seems to have a similar spatial

distribution (chapter 3). The good correspondence between these three populations suggests that the structure seen is real large-scale structure. A more detailed analysis of this will be presented in a future paper (Greve et al., in preparation).

An alternative test for clustering is the so-called nearest-neighbour analysis (Scott & Tout 1989). This considers the distribution of nearest neighbour separations, θ, of sources on a sphere. For a random distribution of sources, the probability density function can be shown to be:

$$P(\theta)d\theta = \frac{N-1}{2^{N-1}} \sin\theta(1+\cos\theta)^{N-2}d\theta, \tag{2.8}$$

where N is the number of objects in the sample — see Scott & Tout (1989) for details. We performed a nearest-neighbour analysis on the $\geq 4.0\sigma$ source catalogues in each field, and the resulting nearest-neighbour distributions are shown as black lines in Figure 2.9. First of all, it is notable that the nearest-neighbour distributions for the two fields look remarkably similar. In particular, both distributions show a significant peak at angular scales of $\sim 23''$. Changing the bin size to values in the range 11–17″ does not alter the overall appearance of the distributions significantly, and the over-density of sources in the 15–30″ bin remains. In order to compare the angular distribution of MAMBO sources with a random distribution, we used the same 500 $\langle RR \rangle$-catalogues which were used in connection with the two-point correlation function. The ensemble-averaged nearest-neighbour distributions for these simulated maps are shown as grey curves in Figure 2.9.

It is seen that the random distributions do not peak at ~15–30″ but at $\theta \simeq 60''$ which is in accordance with the probability density function in eq. 2.8. From a Kolmogorov-Smirnoff (K–S) test we find that in both fields the probability of the $\langle DD \rangle$ and $\langle RR \rangle$ distributions being drawn from the same underlying distribution is about 10 per cent. In other words, there is a 10 per cent chance of a random distribution yielding a more paired distribution than that observed for the MAMBO sources. A similar analysis on the $\geq 3.5\sigma$ sample shows a similar significant peak at ~15–30″.

Thus, while we haven't found a significant clustering signal from the two-point correlation function, there is tentative evidence from the nearest-neighbour analysis that MAMBO sources are not randomly distributed but tend to come in pairs. This is qualitatively in agreement with a recent study which utilises the results from the spectroscopic survey of radio-bright SMGs to search for pairs and/or triplets of sources in redshift space. This has yielded a significant detection of the clustering of SMGs and has constrained the correlation length to $r_0 \simeq 6.1 \pm 2.1 h^{-1}$ Mpc (Blain et al. 2004; Smail et al. 2003).

2.7 Comparison with the SCUBA UK 8 mJy Survey

While a detailed analysis of the properties of the MAMBO sources at radio and optical/near-IR wavelengths shall be presented in Paper II (Greve et al., in preparation), it is appropriate here to compare the MAMBO and SCUBA maps. Such a comparison is meaningful since as we saw in section 2.5 both surveys reach very similar integral counts, and a 'typical' $z \sim 2.5$ starburst SED will hit the flux limit in both surveys almost simultaneously.

2.7.1 The reliability of (sub)mm surveys

First of all, such a cross-check between the MAMBO and SCUBA catalogues will allow us to assess the reliability of (sub)mm surveys. As already mentioned, (sub)mm surveys in general have adopted detection thresholds at low signal-to-noise ratios (typically 3.0–3.5σ - see e.g. Eales

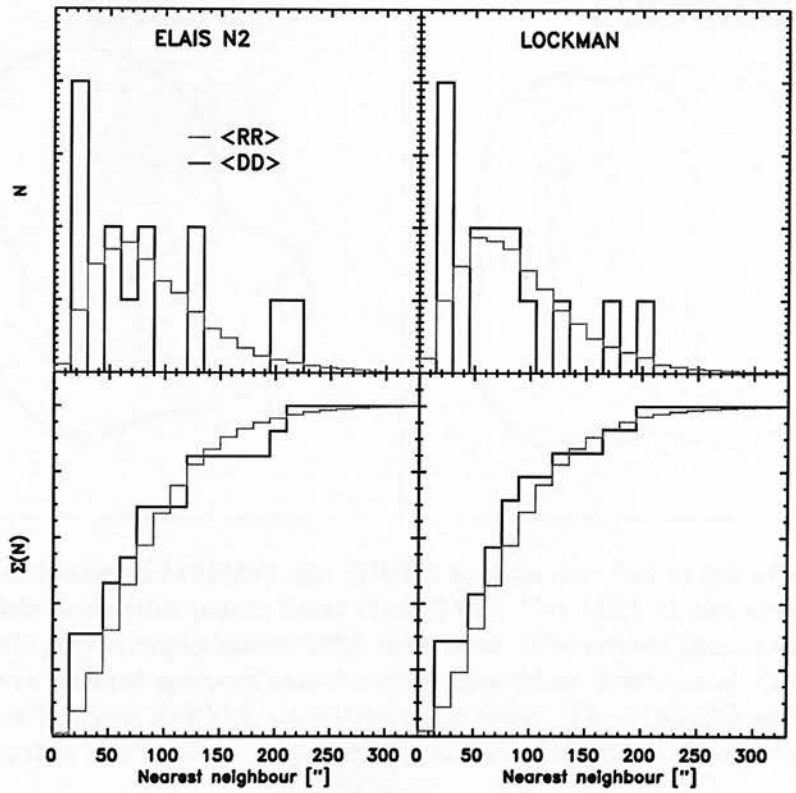

Figure 2.9: Distributions of nearest-neighbours in the ELAIS N2 (left column) and the Lockman Hole (right column). The black curves represent the actual data (the $\geq 4.0\sigma$ source catalogues), while the grey curves are the ensemble averaged distributions obtained from 500 simulated maps of the two fields.

et al. 2000; Scott et al. 2002; Webb et al. 2003; this work), and confusion has been a major issue for these surveys. In addition, different surveys have used different data-reduction software, and widely differing source extraction techniques have been adopted.

The comparison between the MAMBO and SCUBA $\geq 3.5\sigma$ source catalogues is shown in Figure 2.10, which shows the outline of the MAMBO and SCUBA maps with the $\geq 3.5\sigma$ 850 μm sample as given by Scott et al. (2002) and the $\geq 3.5\sigma$ 1200 μm sources presented in this paper overplotted. It is seen immediately that four SCUBA sources in ELAIS N2 are unambiguously detected at 1200 μm, while in the Lockman Hole eight SCUBA sources have been confirmed with MAMBO.

It is interesting to see how these MAMBO identifications are distributed in terms of signal-to-noise and whether the identification rate increases if we lower the source detection threshold to 3.0σ. In order to do so, we have compared the 4.0, 3.5, and 3.0σ SCUBA source lists of Scott et al. with our corresponding MAMBO source catalogues, and for each SCUBA source we computed the distance to the nearest MAMBO source. The resulting distributions are shown in Figure 2.11. For both fields the distribution is seen to peak at offsets smaller than $10''$. In fact, both distributions seem to show that a cutoff in positional offset of $< 10''$ is a natural selection criterion as to whether a MAMBO source is a genuine counterpart to a SCUBA source or not.

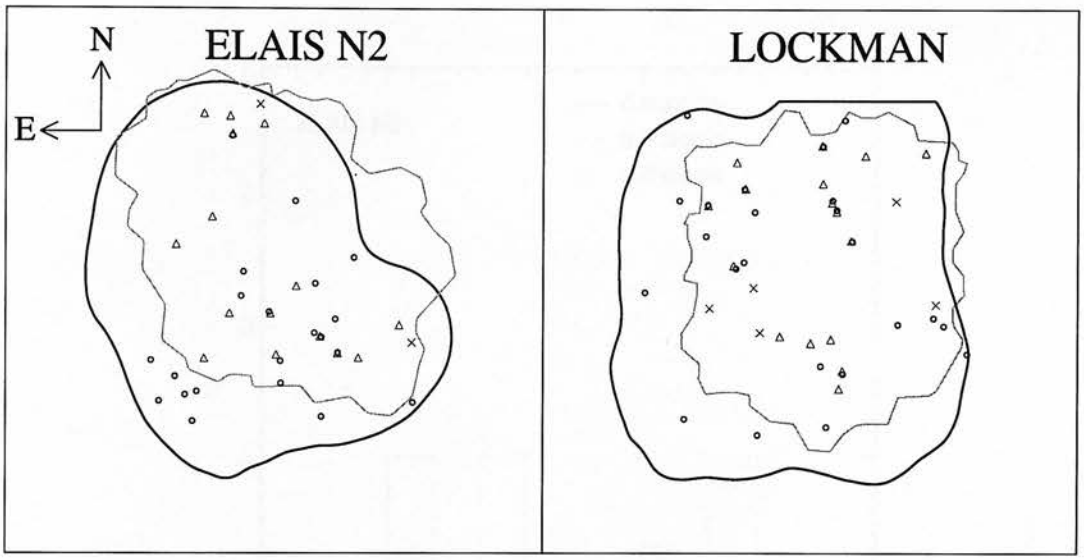

Figure 2.10: Distribution of MAMBO and SCUBA sources detected at $\geq 3.5\sigma$ in the ELAIS N2 and Lockman Hole fields (this paper; Scott et al. 2002). The black circles are sources detected by MAMBO while grey triangles are SCUBA detections. The crosses denote the seven SCUBA sources which were deemed spurious and therefore rejected by Ivison et al. (2002) due to their lack of radio identifications and high associated noise levels. The MAMBO and SCUBA survey regions are outlined in black and grey, respectively, see also Figure 2.1. The boxes are $21\farcm7 \times 21\farcm7$.

This is in line with what we would expect given the FWHMs of the MAMBO and SCUBA beams. Adopting this criterion and using the $\geq 3.0/3.5/4.0\sigma$ catalogues from both surveys, we confirm 6/4/3 out of 36/17/7 SCUBA sources in the ELAIS N2 field and 9/8/5 out of 36/21/12 SCUBA sources in the Lockman Hole, respectively. Thus, the identification rate clearly increases with signal-to-noise, from 17–25 per cent for the 3.0σ-catalogues to 43 per cent in ELAIS N2 and 42 per cent in the Lockman Hole for the 4.0σ-catalogues. At face value, our MAMBO survey thus confirms about half of the most significant SCUBA sources.

An additional 24 hr of 850 μm data — not used in the original 8 mJy Survey — resulted in a slightly different source catalogue than that given in Scott et al. (2002). With the inclusion of the new data, the significance of N2 850.17 drops from 3.5σ to 3.3σ, with a new flux density of 5.3 ± 1.7 mJy, while N2 850.16 disappears (see chapter 3). At the position of N2 850.17 in the MAMBO map, we detect a source at the 2.7σ significance level, suggesting that N2 850.17 is a real source, even though it is just below the formal 3.5σ detection threshold of the 8 mJy Survey. N2 850.16, however, is not detected at 1200 μm at greater than 1σ significance, confirming that this was a spurious source in the original Scott et al. map.

Based on extremely deep radio imaging of the 8 mJy fields, Ivison et al. (2002) concluded that six of the original SCUBA sources in the ELAIS N2 and Lockman Hole fields were likely to be fake sources. Not only were they extracted from extremely noisy regions, but they also lacked a radio counterpart despite being amongst the brightest SMGs in the sample. The sources in question were LE 850.9, LE 850.10, LE 850.11, LE 850.15, LE 850.20, and N2 850.14. From Figure 2.10 it is seen that none of these sources, which are denoted by grey crosses, coincide with a $\geq 3.5\sigma$ MAMBO source. In fact, the highest significance 1200 μm detection of the above

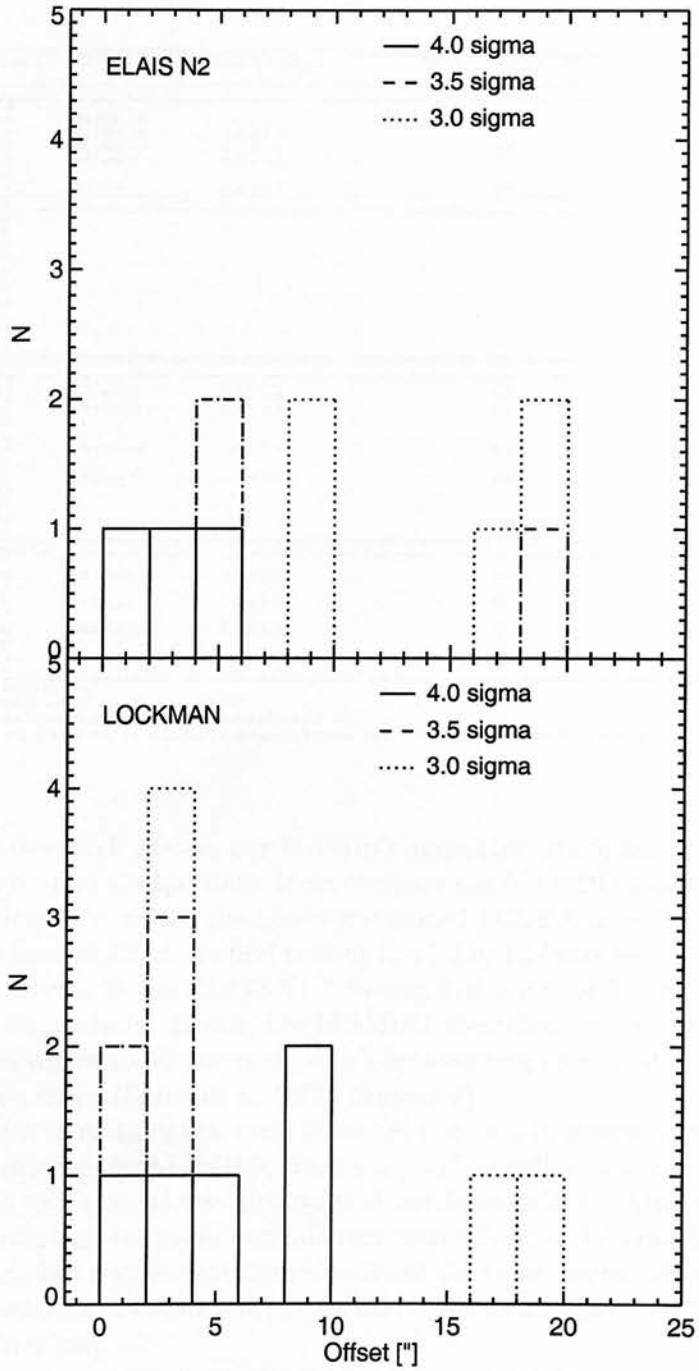

Figure 2.11: Distribution of offsets between SCUBA sources and their nearest MAMBO counterpart in the ELAIS N2 (top panel) and Lockman Hole fields (bottom panel). The 4.0, 3.5, and 3.0σ MAMBO samples are compared with the 4.0, 3.5, and 3.0σ SCUBA samples of Scott et al. (2002), and the corresponding distributions are shown as solid, dashed and dotted curves, respectively.

Table 2.4: MAMBO and VLA radio identifications of the SCUBA 8 mJy Survey $\geq 3.5\sigma$ source catalogue (Scott et al. 2002). The 850 μm and 1.4 GHz radio flux densities are from Scott et al. (2002) and Ivison et al. (2002), respectively.

SCUBA ID	$S_{850\mu m} \pm \sigma_{850\mu m}$ mJy	MAMBO ID	$S_{1200\mu m} \pm \sigma_{1200\mu m}$ mJy	SCUBA/MAMBO Offset $''$	RADIO	$S_{1.4GHz} \pm \sigma_{1.4GHz}$ μJy
$\sigma \geq 4.0$ Detections						
N2 850.1	11.2 ± 1.6				yes	45 ± 16
N2 850.2	10.7 ± 2.0	N2 1200.39	3.4 ± 1.1	8.4	yes	92 ± 16
N2 850.3	8.5 ± 1.6	N2 1200.19	2.9 ± 0.8	5.1	no	< 44
N2 850.4	8.2 ± 1.7	N2 1200.10	3.1 ± 0.7	4.5	yes	221 ± 17
N2 850.5	8.5 ± 2.2	N2 1200.3	3.9 ± 0.8	1.0	yes	77 ± 31
N2 850.6	9.2 ± 2.4				no	38 ± 19
N2 850.7	9.0 ± 2.4	N2 1200.4	3.4 ± 0.7	4.0	yes	159 ± 27
$4.0 > \sigma \geq 3.5$ Detections						
N2 850.8	5.1 ± 1.4				yes	74 ± 29
N2 850.9	9.0 ± 2.5				yes	33 ± 12
N2 850.10	5.4 ± 1.5				no	58 ± 24
N2 850.11	7.1 ± 2.0				no	< 44
N2 850.12	5.5 ± 1.6				no	32 ± 17
N2 850.13‡	6.3 ± 1.9				yes	99 ± 23
N2 850.14*	11.2 ± 3.3				no	< 44
N2 850.15	5.0 ± 1.5				no	31 ± 20
N2 850.16†	12.9 ± 3.9				no	< 44
N2 850.17††	5.3 ± 1.7				no	< 44
$\sigma \geq 4.0$ Detections						
LE 850.1	10.5 ± 1.6	LE 1200.5	3.4 ± 0.6	5.1	yes	73 ± 10
LE 850.2	10.9 ± 2.4	LE 1200.1	4.8 ± 0.6	1.3	yes	29 ± 11
LE 850.3	7.7 ± 1.7	LE 1200.11	2.9 ± 0.7	6.2	yes	98 ± 12
LE 850.4	8.3 ± 1.8				no	19 ± 8
LE 850.5	8.6 ± 2.0				no	< 25
LE 850.6	11.0 ± 2.6	LE 1200.10	2.9 ± 0.7	7.7	yes	54 ± 14
LE 850.7	8.1 ± 1.9				yes	135 ± 13
LE 850.8	5.1 ± 1.3	LE 1200.14	2.4 ± 0.6	3.9	yes	58 ± 12
LE 850.9*	12.6 ± 3.2				no	< 23
LE 850.10*	12.2 ± 3.1				no	< 25
LE 850.11*	13.5 ± 3.5				no	26 ± 12
LE 850.12	6.2 ± 1.6				yes	278 ± 12
$4.0 > \sigma \geq 3.5$ Detections						
LE 850.13	9.8 ± 2.8				no	18 ± 11
LE 850.14	9.5 ± 2.8	LE 1200.3	3.6 ± 0.6	2.0	yes	72 ± 12
LE 850.15*	11.7 ± 3.4				no	< 21
LE 850.16	6.1 ± 1.8	LE 1200.6	2.8 ± 0.5	2.6	yes	41 ± 12
LE 850.17	9.2 ± 2.7				no	< 23
LE 850.18	4.5 ± 1.3	LE 1200.12	3.3 ± 0.8	3.1	yes	47 ± 10
LE 850.19	5.5 ± 1.6				no	< 27
LE 850.20*	10.3 ± 3.1				no	< 24
LE 850.21	4.5 ± 1.3				yes	21 ± 10

‡ Detected with MAMBO at the 2.8σ level.
* Excluded from the refined 8 mJy sample of Ivison et al. (2002).
† This source vanished with the inclusion of an additional 24 hr of SCUBA data.
†† This source dropped from 3.5 to 3.3σ with the inclusion of additional SCUBA data. It is detected with MAMBO at 2.7σ.

sources was at the 1.6-σ level. Hence, our MAMBO maps strengthen the conclusion of Ivison et al. (2002) that these sources are spurious. If we compare the MAMBO catalogue with the refined SCUBA source catalogue, in which the above mentioned SCUBA sources (including N2 850.16 and N2 850.17) have been omitted, we find that at the $\geq 3.0/3.5/4.0\sigma$ level, we confirm 6/4/3 out of 33/14/7 SCUBA sources in the ELAIS N2 field and 9/8/5 out of 31/16/9 SCUBA sources in the Lockman Hole, respectively. Hence, the MAMBO identification rate of SCUBA sources in the Lockman Hole increases to 56 per cent, which is becoming comparable to fraction of SMGs detected in deep radio maps (Smail et al. 2000; chapter 3).

An important point to make in this context is that Figure 2.10 clearly shows that while not all SCUBA sources are detected by MAMBO, there is a good overall spatial correspondence between SCUBA and MAMBO sources, as was also pointed out in section 2.6. One way to interpret this result is that the two surveys represent two different realisations of the same large-scale structure. From two independent but similar (sub)mm surveys of the same region, we would expect to find the most significant sources in both surveys, but this is not necessarily true of the fainter sources near the detection threshold.

Deep radio observations provide an alternative route to reliably identify SMGs. About two thirds of SMGs are detected in the radio where the ratio of submm to radio flux detection thresholds is above $\sim$400 (Smail et al. 2000; chapter 3). However, it remains an open question whether the third of the population which are radio-blank are SMGs at very high redshifts ($z >> 3$), or cooler, less-far-IR-luminous objects at similar redshifts as the bulk of the population, or simply spurious sources. All three scenarios would explain the lack of radio counterparts.

In Table 4 we list all the $\geq 3.5\sigma$ SCUBA sources with a MAMBO counterpart detected at $\geq 3.0\sigma$ significance within $10''$, along with their positional offsets and flux densities at 1200 and

Table 2.5: The number (and percentage) of SCUBA sources identified by MAMBO divided into radio and non-radio ID categories. Note, that all the number in this table are based on the comparison with the $\geq 3.5\sigma$ 8 mJy Sample of Scott et al. (2002) and the $\geq 3.0\sigma$ MAMBO sample presented in this paper.

Field	MAMBO ID			No MAMBO ID		
	Radio ID	No Radio ID	Total	Radio ID	No Radio ID	Total
ELAIS N2	4	1	5	4	8	12
Lockman	8	0	8	3	10	13
Total	12 (92%)	1 (8%)	13	7 (28%)	18 (72%)	25

850 μm. Of the 12 $\geq 3.5\sigma$ SCUBA sources in the ELAIS N2 field which were not detected by MAMBO, only four had a radio identification. Of the eight radio-blank SCUBA sources, only one — N2 850.3 — was confirmed by MAMBO, indicating that it could be cool, or lie at $z >> 3$. In the Lockman Hole, *none* of the radio-blank SCUBA sources were detected at 1200 μm, and only three of the 11 radio-identified SCUBA sources were not detected by MAMBO.

Since the depth of the MAMBO maps at 1200 μm is comparable to that of the SCUBA maps at 850 μm it is hard to conceive of a way in which an 850 μm source with no radio counterpart could fail to be detected at 1200μ m. The only plausible explanations require that the sources are spurious or confused.

In Table 5 we have summarised the above findings. They suggest strongly that the fraction of robust SCUBA sources, i.e. sources confirmed by MAMBO, which are not detected in the radio is low: 20 per cent (1/5) in ELAIS N2 and 0 per cent in the Lockman Hole. These findings suffer from small number statistics and we await a comparison between the much larger map of the Lockman Hole being obtained with MAMBO (Bertoldi et al. in prep.) and the SCUBA map of that region which is being obtained as part of SHADES (see *http://www.roe.ac.uk/ifa/shades/*). In the light of current and future (sub)mm surveys, our findings underline the importance of multi-wavelength follow-up in order to establish the reality of (sub)mm sources, and the dependence only on the most robust samples to draw meaningful statistical conclusions (cf. Dannerbauer et al. 2004).

2.7.2 The 850/1200 μm flux density ratio

Another valuable piece of information which can be gleaned from a comparison of the MAMBO and SCUBA maps is the 850/1200 μm flux ratios for a large sample of (sub)mm galaxies. Beyond $z \geq 3$ this flux ratio becomes a strong function of redshift, and can thus be used as a crude discriminator between low- and high-redshift sources (Eales et al. 2003), much in the same way that the radio-to-submm spectral index acts as a redshift estimator for sources at $z \lesssim 3$ (Carilli & Yun 1999, 2000). Thus, the two redshift estimators complement each other, and if used in combination can potentially be used to probe the redshift distribution of (sub)mm sources. However, both of these redshift estimators suffer from the $T_{\rm d} - z$ degeneracy first pointed out by Blain (1999), which implies that a low-redshift source with a cold dust temperature is indistinguishable from a warm source at high redshift.

The distribution of 850/1200 μm flux ratios for the 13 $\geq 3.5\sigma$ SCUBA sources which were robustly identified by our MAMBO survey are plotted in Figure 2.12a, along with the ratios for a sample of SCUBA-observed MAMBO sources by Eales et al. (2003). Using SCUBA in its photometry mode, they observed 21 MAMBO-selected sources from the MAMBO Deep Field Survey (Bertoldi et al., in preparation). While there is a considerable overlap between the two distributions, the latter has a significant over-density at low values which is not reproduced by our sample. From our sample we find a median value of $S_{850}/S_{1200} = 2.6 \pm 0.6$, marginally higher than the median value of 2.1 ± 0.7 found by Eales et al. (2003), although within the scatter.

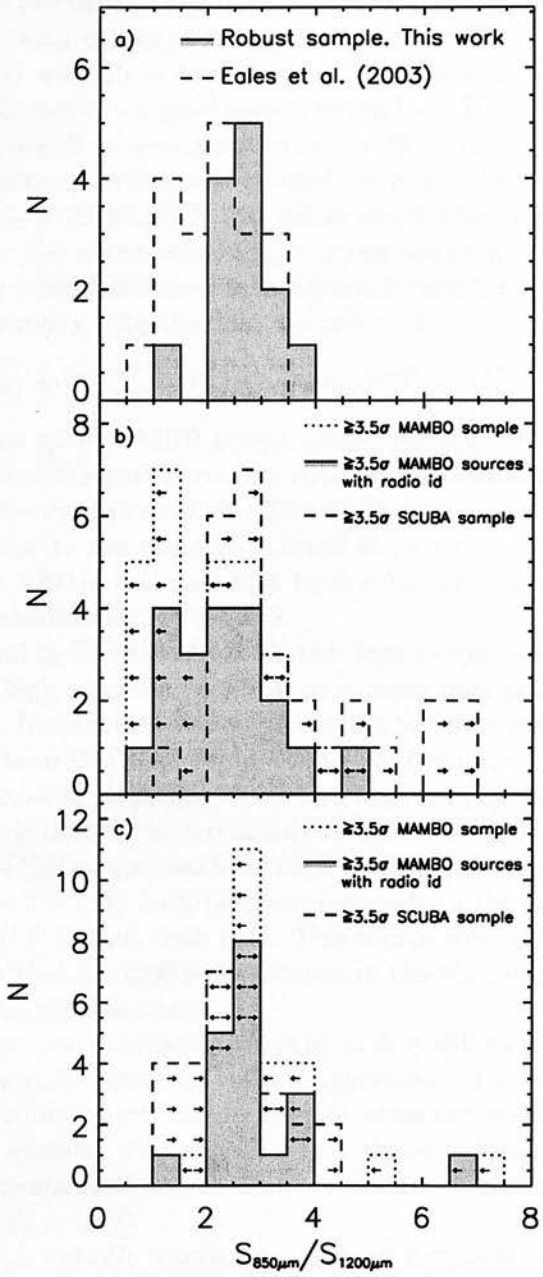

Figure 2.12: **a)** The distribution of 850/1200 μm flux ratios for the 13 $\geq 3.5\sigma$ SCUBA sources identified with MAMBO in this paper (light-grey shaded area), and for the sample presented by Eales et al. (2003) (dashed line). **b)** The dotted histogram is the flux ratio distribution for all the $\geq 3.5\sigma$ MAMBO sources within the SCUBA regions, including the ones which were not detected by SCUBA. In the latter case upper flux limits were estimated as the peak flux within an aperture of radius 10″centered on the MAMBO position in the SCUBA map. The distribution of flux ratios for all the $\geq 3.5\sigma$ SCUBA sources (dashed histogram) were obtained in a similar manner by measuring the peak flux in the MAMBO map within a 10″radius of the SCUBA position. The light-grey shaded histogram represents the distribution for the subset of MAMBO sources which were robustly identified in the radio. **c)** The same as b) except more conservative upper flux limits ($2\sigma + F$) were adopted, see text for details.

In Figure 2.13 we have plotted the measured 850/1200 μm flux ratios of our sample and the Eales et al. sample along with curves showing the predicted 850/1200 μm flux density ratios against redshift for an SED with $T_{\rm d} = 45\,{\rm K}$ and $\beta = +1.5$, and an SED with $T_{\rm d} = 35.6\,{\rm K}$ and $\beta = +1.3$. The former SED provides a good match to the local ULIRG, Arp 220, while the latter is based on the average $T_{\rm d}$ and β values derived from the SCUBA Local Universe Galaxy Survey (Dunne et al. 2000). In addition, we have also plotted the $S_{850\mu{\rm m}}/S_{1200\mu{\rm m}}$–$z$ relationship for a set of SEDs with $\beta = 1$ and $T_d = 20, 30...70\,{\rm K}$, i.e. SEDs which have very different dust properties from local ULIRGs. Note, the above dust temperatures are at a redshift of zero. In order to account for the increasing cosmic microwave background radiation (CMBR) temperature with redshift and its thermal coupling with the dust we have used

$$T_d(z) = \left(T_{d,z=0}^{4+\beta} + T_{\rm CMBR}^{4+\beta}\left[(1+z)^{4+\beta} - 1\right]\right)^{1/(4+\beta)}, \tag{2.9}$$

where $T_{\rm CMBR}$ is the present epoch CMBR temperature, (see e.g. Eales & Edmunds 1996). The effect is only significant when the dust is cold relative to the CMBR temperature, and therefore becomes more important at very high redshifts. The slight downward trend in the $S_{850\mu{\rm m}}/S_{1200\mu{\rm m}}$ curves at low redshifts is due to the negative spectral slope ($\alpha = -0.7$) of the radio continuum emission which boosts the 1200 μm flux relative to the flux at 850 μm. However, this effect is completely negligible at redshifts beyond $z \sim 0.5$.

The low flux ratios found by Eales et al. (2003) led them to conclude that a significant fraction of SMGs must lie at very high redshifts ($z >> 3$) or possess dust properties different from low-redshift starburst galaxies. In contrast, we find no conflict between our measured $S_{850\mu{\rm m}}/S_{1200\mu{\rm m}}$ ratios and SEDs based on local ULIRGs. From a subset of five sources which have been targeted spectroscopically by Chapman et al. (2003, 2004), and thus are placed at their correct redshift in Figure 2.13, we can conclude that the observed flux ratios for at least four of the five sources are consistent with the range of SEDs expected from local ULIRGs. The one exception is the outlying point at $S_{850\mu{\rm m}}/S_{1200\mu{\rm m}} = 3.8$ This data point corresponds to the source LE 850.6/LE 1200.10 which has another source (LE 1200.9) close to it. This source was detected by MAMBO but not by SCUBA, and it is likely that LE 1200.9 contributes to the 850 μm flux of LE 850.6, leading to an artificially high flux ratio for this source.

Our sample is taken from two unbiased surveys at slightly different (sub)mm wavelengths and is thus independent of any radio selection bias. Furthermore, it is clear from Figure 2.13 that the SMG without a radio counterpart (circled symbol) does not have a lower 850/1200 μm flux ratio than the rest of the sample. This suggests that the source is blank in the radio because it is a cooler, less-far-IR-luminous object at similar redshifts to the bulk of the population, not because it lies at a very high redshift.

Candidates for very-high-redshift sources, i.e. 850 μm dropouts, should be sought amongst sources detected by MAMBO but not SCUBA. From Figure 2.10 it is seen that 9 MAMBO sources in the ELAIS N2 field and 9 in the Lockman Hole fall within the regions observed by SCUBA, yet are not detected at $\geq 3.5\sigma$ significance at 850 μm. Upper limits on the flux densities at 850 μm of these sources were measured, taking the peak flux in a 10″radius aperture region of the SCUBA map coincident with the MAMBO position. These limits were then merged with the 850 μm fluxes of the robust sample, resulting in 850 μm flux estimates (or upper limits) for all the 9+9+13=31 MAMBO sources which lie within the SCUBA regions. The resulting distribution of 850-to-1200 μm flux ratios is shown as the dotted curve in Figure 2.12b. The distribution appears to have two peaks, one at $S_{850\mu{\rm m}}/S_{1200\mu{\rm m}} \sim 1$ which reproduces the low-end tail of Eales et al. (2003) rather well and is almost entirely due to the MAMBO sources not detected by SCUBA, and another at ~ 2.5 which stems from the 13 sources robustly identified at both 1200 μm and 850 μm.

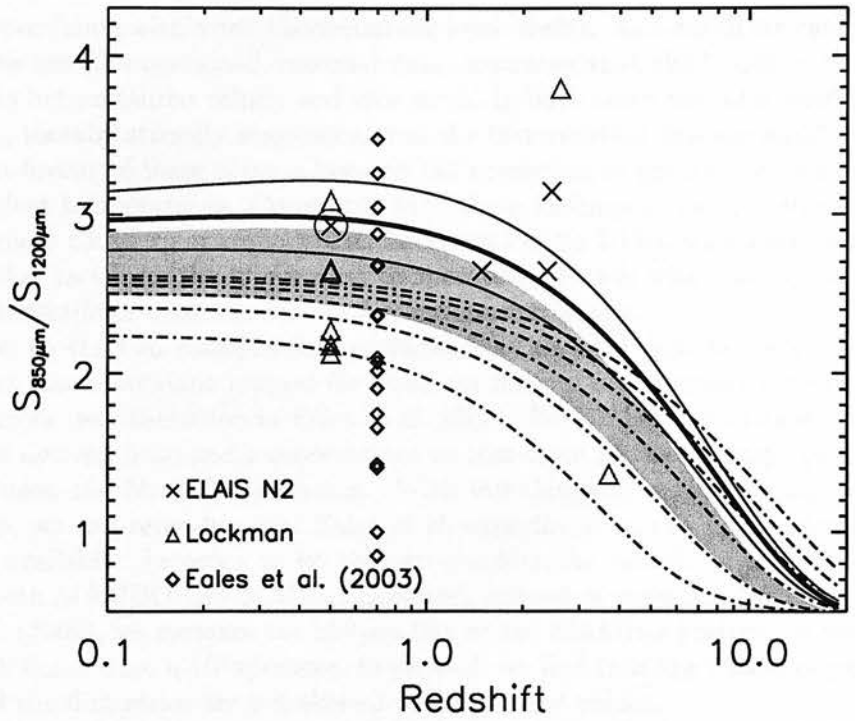

Figure 2.13: The 850/1200 μm flux density ratio for SCUBA sources detected by MAMBO in the ELAIS N2 (crosses) and Lockman Hole (triangles). Six of the sources have spectroscopic redshifts (see Chapman et al. 2003, 2004), while the remainder have been placed at $z = 0.5$. The encircled source has no radio counterpart. Shown as diamonds are the 850/1200 μm flux ratios for the sample of Eales et al. (2003). The thick solid curve represents the expected flux ratio for an optically thin modified blackbody with $T_{\rm d} = 45\,{\rm K}$ and $\beta = +1.5$, typical for a local ULIRG. This curve is enveloped by two thin solid curves which correspond to changes in the dust temperature and spectral index of $\Delta T_{\rm d} = \pm 5\,{\rm K}$ and $\Delta\beta = \pm 0.2$. The light-grey shaded area corresponds to a modified blackbody with $T_{\rm d} = (35.6 \pm 5.0)\,{\rm K}$ and $\beta = (+1.3 \pm 0.2)$. The dot-dashed curves corresponds to SEDs with $\beta = 1.0$ and $T_d = 20...70\,{\rm K}$ in steps of 10 K with the 850/1200 μm ratio increasing with temperature.

In order to make a fair comparison with the flux ratios of the SCUBA sample, we estimated 1200 μm fluxes for all the SCUBA sources. This was done in an identical fashion as above, i.e. upper 1200 μm flux limits were derived for the SCUBA sources not detected with MAMBO using the peak flux within a 10″radius aperture region of the MAMBO map centered on the SCUBA position, and concatenated with the robust sample. This distribution is shown as the dashed histogram in 2.12b.

The dotted and dashed distributions appear to be distinct, and in order to determine the probability of the two samples being drawn from the same parent distribution, we have employed the standard 'survival analysis' tests (Feigelson & Nelson 1985), which are appropriate in the case where the samples contain upper or lower limits (censored data). This included the Gehan, log rank, Peto-Peto, and Peto-Prentice tests, the latter being perhaps the most conservative and least sensitive to differences in the censoring patterns. However, common to all the tests is that they are unable to compare samples with mixed censor indicators, i.e. one cannot compare a sample

containing upper limits with a sample containing lower limits. As a result we ran the tests where only one of the samples contained censored data, assuming that the limits in the other sample were not limits but measured values, and vice versa. In both cases the tests yielded probabilities less than 0.01, thereby strongly suggesting that the two distributions are significantly different. This argues in favour of there being a low-end tail consisting of galaxies at either high redshifts or with cool dust temperatures. Consistent with these findings is the distribution of MAMBO sources with radio counterparts (shaded histogram in Figure 2.12b) which shows that few of the sources with flux ratios $\lesssim 1.5$ are identified in the radio. This is what one would expect if they were at high redshifts or cool, not very far-IR luminous systems.

In addition to the two astrophysical explanations (i.e. cold dust or high redshift) Eales et al. also suggest more mundane reasons for their low flux ratios, the most important of which is astrometric errors (see discussion in Eales et al. 2003). For all but five of their 21 sources, they used positions derived from radio observations or mm-wave interferometry. For the remaining sources they used the MAMBO positions. With our dataset, in conjunction with the 8 mJy Survey images, we can reproduce the Eales et al. experiment in the case where only MAMBO positions are available. In order to do this we consider the sample of 13 sources which were detected by both MAMBO and SCUBA. However, instead of using the 850 μm fluxes reported by Scott et al. (2002), we measure the 850 μm flux at the MAMBO position in the SCUBA map using the peak flux within a 10″aperture. In general, we find that the effects of positional errors are small, and the flux ratios are not skewed towards lower values.

Finally, it is possible that contamination by spurious or flux-boosted MAMBO sources is responsible for at least some of the low flux ratios observed. However, based the Monte Carlo simulations in section 2.4.2 we expect no more than 2 sources to be spurious in each of the MAMBO maps. This is an upper limit, given that the overlap between the SCUBA and MAMBO regions is only about 68 per cent of the areas covered by MAMBO.

While the above analysis suggests that astrometrical errors and spurious/flux-boosted sources are unable to account for the 12 MAMBO sources with $S_{850\mu m}/S_{1200\mu m} \lesssim 1.5$, we caution that the low flux ratio could be due to the way we have estimated the upper flux limits. Simply adopting the peak flux within a 10″aperture might in some cases result in too low flux estimates and would tend to bias the MAMBO and SCUBA distributions towards lower and higher flux ratios, respectively. In Figure 2.12c we have adopted a more conservative approach in which the upper limits on the fluxes were estimated by adding $2 \times \sigma$ to the peak flux, where σ is the local rms noise. Clearly, the overlap between the two distributions is now much greater, and the two distributions appear to be indistinguishable. This is confirmed by the 'survival analysis' tests which yield probabilities in the range 0.22 (log rank) to 0.11 (Peto-Prentice) and similar for the reverse comparison, i.e. comparing the SCUBA distribution with the uncensored MAMBO distribution. Thus, adopting what is arguably more realistic upper flux limits we find no evidence for SMGs with unusually low 850-to-1200 μm flux ratios as reported by Eales et al. (2003). If this is the case, the major implication is that, beyond the few completely unrepresentative submm-loud AGN at $z > 4$, there is no significant population of SMGs at very high redshifts. The redshift distribution of radio-identified SCUBA sources, as determined by Chapman et al. (2003, 2004), would be applicable to virtually all of the (sub)mm population.

However, while we find no conclusive evidence for '850 μm-dropouts' a handful of MAMBO sources do seem to be good candidates for SMGs at $z >> 5$. In particular, LE 1200.2 is one of the brightest sources in our survey, yet it is not detected by SCUBA nor is it seen in the radio. Pointed SCUBA photometry observations of this source would provide an accurate accurate estimate of its 850 μm flux and confirm or dismiss its status as a '850 μm-dropout'. Furthermore, with the completion of the MAMBO Deep Field Survey and the SCUBA Half Degree Extragalactic Survey,

which will not only provide us with much larger samples but also a multitude of observations at complementary wavelengths, we should be able to obtain a much better census of the high-redshift tail of (sub)mm sources.

2.8 Conclusions

In this paper we have presented results from a MAMBO 1200 μm blank-field survey of the ELAIS N2 and Lockman Hole fields, covering a total of 357 arcmin^2 to a rms level of $\sim$0.8 mJy beam^{-1}. We detect 27 sources at $\geq$4.0σ significance, and more than 40 sources at $\geq$3.5σ.

From the $\geq$3.5σ catalogue we have derived accurate number counts over the flux range 3–5.5 mJy, and find tentative evidence for a break at $S_{1200\mu m} \simeq 4$ mJy. This corresponds to a far-IR luminosity of $\sim 10^{13}\,L_{\odot}$ for a modified blackbody with $T_{\rm d} = 40$ K and $\beta = +1.5$ at $z = 2.5$. The observed 1200 μm source counts can be successfully reproduced by a simple parametric model for the evolution the local ULIRG population. Furthermore, this model also fits the 850 μm source counts which suggests that the MAMBO and SCUBA sources are drawn from the same population of dust-enshrouded starburst at high redshift. Although a firm conclusion on this issue will have to await a future comparison between much larger surveys currently being undertaken with SCUBA and MAMBO.

Two independent tests were carried out with the aim of detecting clustering in the MAMBO population. Although the angular two-point correlation function showed no evidence of clustering, a nearest neighbour analysis suggests that the most significant MAMBO sources are not randomly distributed but come in pairs, typically separated by 23″. Furthermore, the spatial distribution of sources appears to be non-random, with sources tending to reside in clusters surrounding large voids. The reality of these structures is strengthened by the good overall spatial correlation between the SCUBA, MAMBO and μJy-level radio sources. This suggests that co-spatial surveys at the two slightly different (sub)mm wavelengths skim the brightest members of a numerous but faint population, yielding two similar but low-signal-to-noise visualisations of the true (sub)mm sky.

Our MAMBO survey confirms roughly half of the refined $\geq$3.5σ SCUBA 8 mJy Survey sample (Scott et al. 2002; chapter 3). This is comparable to the radio identification rate of SCUBA and MAMBO sources. As a by-product of this analysis, we have produced a extremely robust sub-sample of 13 SMGs detected at $\geq$3.5σ by both SCUBA and MAMBO. We find that only one ($\sim$8 per cent) has no radio counterpart, a significantly lower fraction than the third which the radio-blank SMGs have generally been believed to constitute. Our results thus suggest that the population of SMGs which are detected by both SCUBA and MAMBO has no significant tail at $z >> 3$. This conclusion is further strengthened by the observed distribution of 850/1200 μm flux density ratios for the 13 sources in our sample. We find their flux density ratios to be consistent with the SEDs found for local ULIRGs and in agreement with the spectroscopic redshift distribution of SMGs as determined by Chapman et al. (2003, 2004).

Finally, we have identified 18 MAMBO sources within the SCUBA UK 8-mJy regions which are not detected at 850 μm at greater than 3.0σ significance. Any high-redshift SMGs should be sought amongst this population of '850 μm-dropouts'. However, using conservative upper flux limits we find that the distribution of 850-to-1200 μm flux ratios for these sources is statistically indistinguishable from that of the sources identified robustly in both wavelengths.

Acknowledgements

TRG acknowledges support from the Danish Research Council and from the European Union RTN Network, POE. We are grateful to Robert Zylka for providing us with the MOPSI package and for useful discussions concerning MOPSI. We are also grateful to Ian Smail for helpful comments on the paper. Finally, we thank Ernst Kreysa and his team for providing MAMBO.

References

Barger, A.J., Cowie, L.L., & Sanders, D.B. 1999, ApJ, 518, 5L.
Benson, A.J., Frenk, C.S., Baugh, C.M., Cole, S., & Lacey, C.G. 2001, MNRAS, 327, 1041.
Bertoldi, F., Menten, K.M., Kreysa, E., Carilli, C.L., & Owen, F. 2000, 24th meeting of the IAU, Joint Discussion 9, Manchester, England.
Blain, A.W. & Longair, M.S. 1993, MNRAS, 265, L21.
Blain, A.W. 1999, MNRAS, 309, 955.
Blain, A.W., Barnard, V.E., & Chapman, S. C. 2003, MNRAS, 338, 733.
Blain et al. 2004, ApJ, in press.
Borys, C., Chapman, S., Halpern, M., & Scott, D. 2003, MNRAS, 344, 385.
Carilli, C.L. & Yun, M.S. 1999, ApJ, 513, L13.
Carilli, C.L. & Yun, M.S. 2000, ApJ, 530, 618.
Chapman, S.C., Scott, D., Borys, C., Fahlman, G.G. 2002, MNRAS, 330, 92.
Chapman, S.C., Blain, A.W., Ivison, R.J., Smail, I.R. 2003, Nature, 422, 695.
Chapman et al. 2004, ApJ, submitted.
Cole, P. & Lucchin, F. 2002, 'Cosmology, the Origin and Evolution of Cosmic Structure', John Wiley & Sons, ltd.
Daddi, E., Cimatti, A., Pozzetti, L., Hoekstra, H., Röttgering, H.J.A., Renzini, A., Zamorani, G., & Mannucci, F. 2000, A&A, 361, 535.
Dannerbauer, H., Lehnert, M.D., Lutz, D., Tacconi, L., Bertoldi, F., Carilli, C., Genzel, R., & Menten, K.M. 2004, ApJ, in press.
Dunlop, J.S. 2001, UMass/INAOE conference proceedings on 'Deep millimeter surveys', eds.J.Lowenthal and D.Hughes, World Scientific.
Dunne, L., Eales, S., Edmunds, M., Ivison, R., Alexander, P., & Clements, D.L. 2000, MNRAS 315, 115.
Dunne, L., Eales, S.A., Edmunds, M.G. 2003, MNRAS, 341, 589.
Eales, S.A. & Edmunds, M.G. 1996, MNRAS, 280, 1167.
Eales, S., Lilly, S., Webb, T., Dunne, L., Gear, W., Clements, D., & Yun, M. 2000, AJ, 120, 2244.
Eales, S., Bertoldi, F., Ivison, R., Carilli, C., Dunne, L., & Owen, F. 2003, MNRAS, 344, 169.
Feigelson, E.D. & Nelson, P.I. 1985, ApJ, 293, 192.
Fox, M.J., Efstathiou, A., Rowan-Robinson, M., et al. 2002, MNRAS, 331, 839.
Giavalisco, M. & Dickinson, M. 2001, ApJ, 550, 177.
Hasinger, G., Altieri, B., Arnaud, M. et al. 2001, A&A, 365, L45.
Hauser, M.G., et al. 1998, ApJ, 508, 25.
Hughes, D.H., Serjeant, S., Dunlop, J., et al. 1998, Nature, 394, 241.
Ivison, R.J., Smail, I., Le Borgne, J.-F., Blain, A.W., Kneib, J.-P., Bezecourt, J., Kerr, T. H., & Davies, J. K. 1998, MNRAS, 298, 583.
Ivison, R.J., Smail, I., Barger, A.J., Kneib, J.-P., Blain, A.W., Owen, F.N., Kerr, T.H., & Cowie, L. L. 2000, MNRAS, 315, 209.
Ivison, R.J., Greve, T.R., Smail, I., et al. 2002, MNRAS, 337, 1.

Jameson, A. 1999, PhD Thesis, Univ. of Cambridge.
Kreysa, E., Gemuend, H.-P., Gromke, J., Haslam, et al. 1998, Proc SPIE 3357, 319.
Landy, S.D. & Szalay, A.S. 1993, ApJ, 412, 64L.
Manners, J.C., Johnson, O., & Almaini, O. 2003, MNRAS, 343, 293.
Saunders, W., Rowan-Robinson, M., Lawrence, A., Efstathiou, G., Kaiser, N., Ellis, R.S., & Frenk, C.S. 1990, MNRAS, 242, 318.
Scott, D. & Tout, C.A. 1989, MNRAS, 241, 109.
Scott, S.E., Fox, M.J., Dunlop, J.S., et al. 2002, MNRAS, 331, 817.
Serjeant, S., Dunlop, J.S., Mann, R.G., et al. 2003, MNRAS 344, 887.
Smail, I., Ivison, R.J., & Blain, A.W. 1997, ApJ, 490, L5.
Smail, I., Ivison, R.J., Owen, F.N., Blain, A.W., & Kneib, J.-P. 2000, ApJ, 528, 612.
Smail, I., Ivison, R.J., Blain, A.W., & Kneib, J.-P. 2002, MNRAS, 331, 495.
Smail, I., Chapman, S.C., Blain, A.W., & Ivison, R.J. 2003, ESO/USM Venice Conference Proceedings.
Webb, T.M., Eales, S.A., Lilly, S.J., et al. 2003, ApJ, 587, 41.
Zylka, R. 1998, Pocket Cookbook for the MOPSI Software (www.iram.es).

Chapter 3

Deep radio imaging of the SCUBA 8-mJy survey fields: sub-mm source identifications and redshift distribution

Abstract The SCUBA 8-mJy survey is the largest submillimetre (submm) extragalactic mapping survey undertaken to date, covering 260 arcmin^2 to a 4σ detection limit of $\simeq 8$ mJy at 850 μm, centred on the Lockman Hole and ELAIS N2 regions. Here, we present the results of new 1.4-GHz imaging of these fields, of the depth and resolution necessary to reliably identify radio counterparts for 18 of 30 submm sources, with possible detections of a further 25 per cent. Armed with this greatly improved positional information, we present and analyse new optical, near-infrared (IR) and *XMM-Newton* X-ray imaging to identify optical/IR host galaxies to half of the submm-selected sources in those fields. As many as 15 per cent of the submm sources detected at 1.4 GHz are resolved by the 1.4″ beam and a further 25 per cent have more than one radio counterpart, suggesting that radio and submm emission arise from extended starbursts and that interactions are common. We note that less than a quarter of the submm-selected sample would have been recovered by targeting optically faint radio sources, underlining the selective nature of such surveys. At least 60 per cent of the radio-confirmed optical/IR host galaxies appear to be morphologically distorted; many are composite systems — red galaxies with relatively blue companions; just over one half are found to be very red ($I-K>3.3$) or extremely red ($I-K>4$); contrary to popular belief, most are sufficiently bright to be tackled with spectrographs on 8-m telescopes. We find one submm source which is associated with the steep-spectrum lobe of a radio galaxy, at least two more with flatter radio spectra typical of radio-loud active galactic nuclei (AGN), one of them variable. The latter is amongst four sources ($\equiv 15$ per cent of the full sample) with X-ray emission consistent with obscured AGN, though the AGN would need to be Compton thick to power the observed far-IR luminosity. We exploit our well-matched radio and submm data to estimate the median redshift of the $S_{850\mu\mathrm{m}} \sim 8$ mJy submm galaxy population. If the radio/far-IR correlation holds at high redshift, and our sample is unbiased, we derive a conservative limit of $<z> \geq 2.0$, or ≥ 2.4 using spectral templates more representative of known submm galaxies.

3.1 Introduction

The nature of the sources detected in deep submm and mm surveys remains controversial. All SCUBA surveys agree as to the high surface density of 850-μm sources detected at the mJy level (Smail, Ivison & Blain 1997; Hughes et al. 1998; Barger, Cowie & Sanders 1999a; Eales et al. 1999; Chapman et al. 2002a; Borys et al. 2002; Webb et al. 2002b) but their exact distances, luminosities and their power source all remain contentious subjects.

Ivison, R.J., Greve, T.R., Smail, I., Dunlop, J.S., Roche, N.D., Scott, S.E., Page, M.J., Stevens, J.A., Almaini, O., Blain, A.W., Willott, C.J., Fox, M.J., Gilbank, D.G., Serjeant, S., & Hughes, D.H. (2002), MNRAS, 337, 1.

Most of the far-IR/submm background detected by the *DIRBE* and *FIRAS* experiments (Puget et al. 1996; Fixsen et al. 1998; Hauser et al. 1998; Schlegel, Finkbeiner & Davis 1998) has already been resolved into discrete sources by SCUBA (Blain et al. 1999b; Smail et al. 2002a; Cowie et al. 2002) implying that the cosmic energy budget in the early Universe was dominated by hitherto undetected dust-enshrouded systems, either starbursts with star-formation rates $\gg 100\,\mathrm{M}_\odot\,\mathrm{yr}^{-1}$, sufficient to construct a giant elliptical galaxy in $\lesssim 1$ Gyr, or Compton-thick AGN associated with the formation of super-massive black holes (SMBH).

If the submm galaxy population lies at high redshift, $z \sim 3$, and is predominantly powered by star formation, then its star-formation rate density is higher than that deduced from optical/ultraviolet observations of the more numerous Lyman-break galaxies (Steidel et al. 1999), a population with which there appears to be little overlap (Peacock et al. 2000; Chapman et al. 2000; Webb et al. 2002a; cf. Adelberger & Steidel 2000). In this scenario, the properties of SCUBA galaxies (e.g. space density, redshift distribution, etc.) would need to be reproduced by any successful model of galaxy formation. Equally, if the bulk of the bolometric luminosity of this population derives from gravitational accretion onto black holes then they clearly represent a crucial phase in the formation of SMBH and the evolution of QSOs and powerful radio galaxies (Archibald et al. 2001; Page et al. 2001). The apparently tight relation seen locally between the masses of bulges and the those of their resident SMBH suggests that both of these scenarios may contain elements of truth, indicating a complex interplay between obscured star formation, AGN activity and feedback in the early evolution of spheroids and SMBH (Silk & Rees 1998; Fabian 1999; Archibald et al. 2002).

While there has been significant progress in detailing the observational properties of the SCUBA population, theoretical interpretation has lagged behind. The standard framework for the theoretical understanding of this population relies upon hierarchical models which employ the cold dark matter (CDM) paradigm. These have successfully described the properties of the galaxies and large-scale structure in the local Universe (e.g. Cole et al. 2000) but the gradual growth of the characteristic mass of galaxies leads these models to predict that the most massive galaxies have formed only recently, $z \lesssim 1$ (Kauffmann & Charlot 1998), even in a low-density λCDM cosmology. Semi-analytic models of galaxy formation, developed within the hierarchical framework, predict that these massive galaxies form primarily through mergers, where the attendant starburst activity can be sufficient to power the prodigious luminosities seen in local ultraluminous IR galaxies (ULIRGs — Baugh et al. 2001). However, the strong decline in the number density of massive galaxies with redshift means that these models predict relatively modest median redshifts for the most massive mergers, $z \lesssim 1$, unless the physical nature of the systems evolves radically (Blain et al. 1999a, 1999c), or the efficiency of high-mass star formation is greater in bursts than in the quiescent mode seen in local disks. The most natural prediction of these models is therefore a low median redshift for galaxies selected by SCUBA. If it is shown that submm galaxies lie predominantly at high redshift, $z \gg 1$, and that they represent massive gas-rich mergers (most probably associated with the formation epoch of massive ellipticals, Eales et al. 1999) then this will require a radical overhaul of the treatment of high-redshift star formation in CDM-based hierarchical models. Hence an estimate of the redshift distribution, $N(z)$, for a complete, robust and well-characterised sample of submm-selected galaxies provides one important test of current theoretical galaxy formation models. In addition, the $N(z)$ is crucial for estimating the true 3-dimensional clustering of the submm population from the projected 2-dimensional clustering of sources in panoramic SCUBA surveys. The strength of the clustering of submm galaxies reflects the mass (and bias) of these systems and provides a further test of the predictions from galaxy formation models. For these reasons, determining the $N(z)$ of complete samples of submm galaxies is one of the highest priorities for researchers working on this

enigmatic population (e.g. Blain et al. 1999c, 2000; Smail et al. 2000, 2002a).

Unfortunately, if the majority of the submm population have no plausible optical counterparts, as has been widely reported, then traditional optical spectroscopy is not a viable option for determining $N(z)$ (e.g. Barger et al. 1999b). The faintness of near-IR counterparts to submm sources gives little hope to IR spectroscopists either and attention has focussed on redshift engines of one sort or another or on broadband photometric techniques (e.g. Townsend et al. 2001; Hughes et al. 2002; Aretxaga et al. 2002).

One potentially profitable route exploits the well-known radio/far-IR correlation (Dickey & Salpeter 1984; de Jong et al. 1985; Helou, Soifer & Rowan-Robinson 1985) as a redshift estimator using deep radio observations of submm sources. The submm flux density, S_ν, goes as $\nu^{\sim 3.5}$, while for the optically thin synchrotron emission in the radio, $S_\nu \propto \nu^{-0.7}$ (Condon 1992). $S_{850\mu\mathrm{m}}/S_{1.4\,\mathrm{GHz}}$ is thus a sensitive function of redshift, initially rising as $(1+z)^{\gtrsim 4}$ (Carilli & Yun 1999). Observations at 1.4 GHz thus complement submm surveys perfectly, being similarly sensitive to star-forming galaxies, although only at $z \lesssim 3$ with present facilities (at $z \gtrsim 3$, the positive K correction at 1.4 GHz overcomes the available sensitivity).

Given the preponderance of possible optical counterparts at the $I \leq 26$ level, the other crucial role of radio observations is to exploit their superior resolution to tie down the positions of submm sources: $\sigma \sim 0.3''$ compared to $4''$ for SCUBA (e.g. Ivison et al. 1998, 2000b, 2001). Moreover, a single radio image can cover $\sim 500\,\mathrm{arcmin}^2$ with high sensitivity and $\sim 1''$ resolution (for 25-m antennas separated by ~ 30 km at 1.4 GHz) enabling many of the sources in even the largest submm surveys to be identified in a single radio map. In addition, the large field of view allows the radio coordinate frame to be aligned accurately with the optical/IR frame (see §2.3). This means that only the positions of the most distant galaxies, those undetected in the radio, need then be laboriously determined on a case-by-case basis, via mm-wave continuum interferometry at the Owens Valley Radio Observatory (e.g. Frayer et al. 2000) and at Plateau de Bure (e.g. Downes et al. 1999; Lutz et al. 2001).

Radio observations also act as a useful probe of AGN, regardless of the level of obscuration, via the identification of lobe-like morphologies or deviations of the radio spectral index (α, where $S_\nu \propto \nu^\alpha$) from the -0.7 expected for star-forming galaxies (e.g. SMM J02399−0136, Ivison et al. 1999), or via anomalously high radio fluxes (e.g. SMM J14009+0252, Ivison et al. 2000b).

Previous radio imaging of submm samples has been extremely successful, identifying robust optical/IR counterparts (Ivison et al. 1998, 2000b, 2001; Smail et al. 1999) and providing evidence that submm-selected galaxies are extremely distant, $z \geq 2$–2.5 (Smail et al. 2000, 2002a; cf. Lawrence 2001). To date, however, the approach has been limited by small-number statistics, by the narrow, deep nature of the Smail et al. (2002a) survey, which has a median lensing-corrected flux of 4.0 ± 0.7 mJy, and by the need to spread observing time across many fields (although this was mitigated by the achromatic amplification of the sample by foreground clusters).

Some of us have recently completed a large unbiased extragalactic submm survey (Scott et al. 2002; Fox et al. 2002; hereafter S02, F02) covering $260\,\mathrm{arcmin}^2$ at 450 and 850 μm. S02 detected 38 850-μm sources at the $\geq 3.5\,\sigma$ level ($N_{\geq 8\,\mathrm{mJy}} = 320^{+80}_{-100}\,\mathrm{deg}^{-2}$) in the ELAIS N2 and Lockman Hole East regions. This survey is very well-suited for determining the radio/submm spectral indices of SCUBA sources, and hence estimating the redshift distribution of the bright submm population. While the redshifts of individual sources are unlikely to be strongly constrained, the $N(z)$ can be determined statistically for a sufficiently large sample. At an 850-μm detection threshold of ~ 8 mJy, many sources will be detected by deep 1.4-GHz imaging. Moreover, any ~ 8-mJy submm source *not* detected at radio wavelengths can be ascribed a relatively robust and potentially exciting redshift constraint of $z \geq 3$. The redshifts of the more distant fraction can be constrained further using flux ratios that are more effective at $z \gtrsim 3$, e.g. $S_{850\mu\mathrm{m}}/S_{1.25\mathrm{mm}}$

(Eales et al. 2002; see also Hughes et al. 2002).

F02 presented shallow, $\sim 12''$-resolution radio data from Ciliegi et al. (1999) and de Ruiter et al. (1997) for the 8-mJy survey regions. With noise levels of $\sim 30\,\mu$Jy beam^{-1}, limits of $z \gtrsim 1$ could be set for most of the bright submm galaxy population. In the next section, we describe deep, high-resolution imaging (σ = 5–9 μJy beam^{-1}, 1.4″ FWHM) of the 8-mJy survey regions. In §3 we use these maps to successfully identify robust radio counterparts for 60 per cent of the submm sources, and to refine the original submm sample via the excision of six sources which (in line with statistical expectation) appear to be the result of confusion. Next, in §4, we exploit the improved positional information provided by the 1.4-GHz maps to identify optical and/or near-IR host galaxies in new images, and to exclude possible counterparts where the radio data indicate blank fields ($V, R, I \gtrsim 26$, $K \gtrsim 21$). We go on to determine the redshift-sensitive submm-to-radio spectral indices for an unbiased sample of 30 sources from the $\geq 3.5\,\sigma$ 8-mJy sample. Finally, in §5 we discuss the implications of the results of this multi-frequency follow-up study for the nature and redshift distribution of the luminous submm galaxy population.

Throughout we adopt a flat cosmology, with $\Omega_m = 0.3$, $\Omega_\Lambda = 0.7$ and $H_0 = 70\,\mathrm{km\,s^{-1}\,Mpc^{-1}}$.

3.2 Imaging and Data reduction

3.2.1 Submm data

The 850-μm observations and data reduction are described fully by S02. To summarise, SCUBA (Holland et al. 1999) was used to map a total of 260 arcmin^2, split evenly between two fields, to a uniform noise level of $\sim$ 2.5 mJy beam^{-1}. The data were reduced using both the standard SURF software (Jenness 2000) and an IDL-based reduction routine (Serjeant et al. 2002). These methods have some common tasks (i.e. combining the positive and negative beams, flatfielding and extinction correction). The difference lies in the final binning procedure: the IDL-based method bins the signal into 1″ pixels, creating 'zero-footprint' maps with a corresponding noise value determined from the signal variance. The term 'zero-footprint' is an analogy with the drizzling algorithm (Fruchter & Hook 1997). A standard shift-and-add technique takes the flux in a given pixel and places its flux into the final map over an area equivalent to one detector pixel projected on the sky. Drizzling, on the other hand, takes the flux and places it into a smaller area in the final map. Simulations have shown that this helps preserve information on small angular scales, provided that there are enough observations to fill the resulting gaps. The area in the coadded map receiving the flux from one detector pixel is termed the *footprint*. The method is an extreme example of drizzling: data are taken from each 14″ (FWHM) bolometer beam and the signal is placed into a very small footprint (a 'zero-footprint'), 1″ square. Unlike the standard SURF reduction, there is no smoothing or interpolation between neighbouring pixels, so the signal-to-noise in the drizzled maps is low and the peaks must be found from Gaussian-convolved images. Although there is some degree of correlation between pixels in the output zero-footprint *signal* maps, the corresponding pixel *noise* values represent individual measurements of sky noise averaged over the full integration time at a specific point on the sky and are therefore statistically independent of their neighbours.

These uncorrelated noise maps enable a maximum-likelihood method to be employed to measure simultaneously the statistical significance of each peak in the maps, leading to well-quantified uncertainties for the flux densities of all potential sources. The final sample (Table 1) differs slightly from the catalogue of S02 due to an additional 24 hr of 850-μm data. The best-fit flux density of source N2 850.17 dropped from 5.7 ± 1.7 mJy to 5.3 ± 1.7 mJy (where the error budget includes absolute calibration), corresponding to a drop in significance from $3.5\,\sigma$ to $3.3\,\sigma$. Source

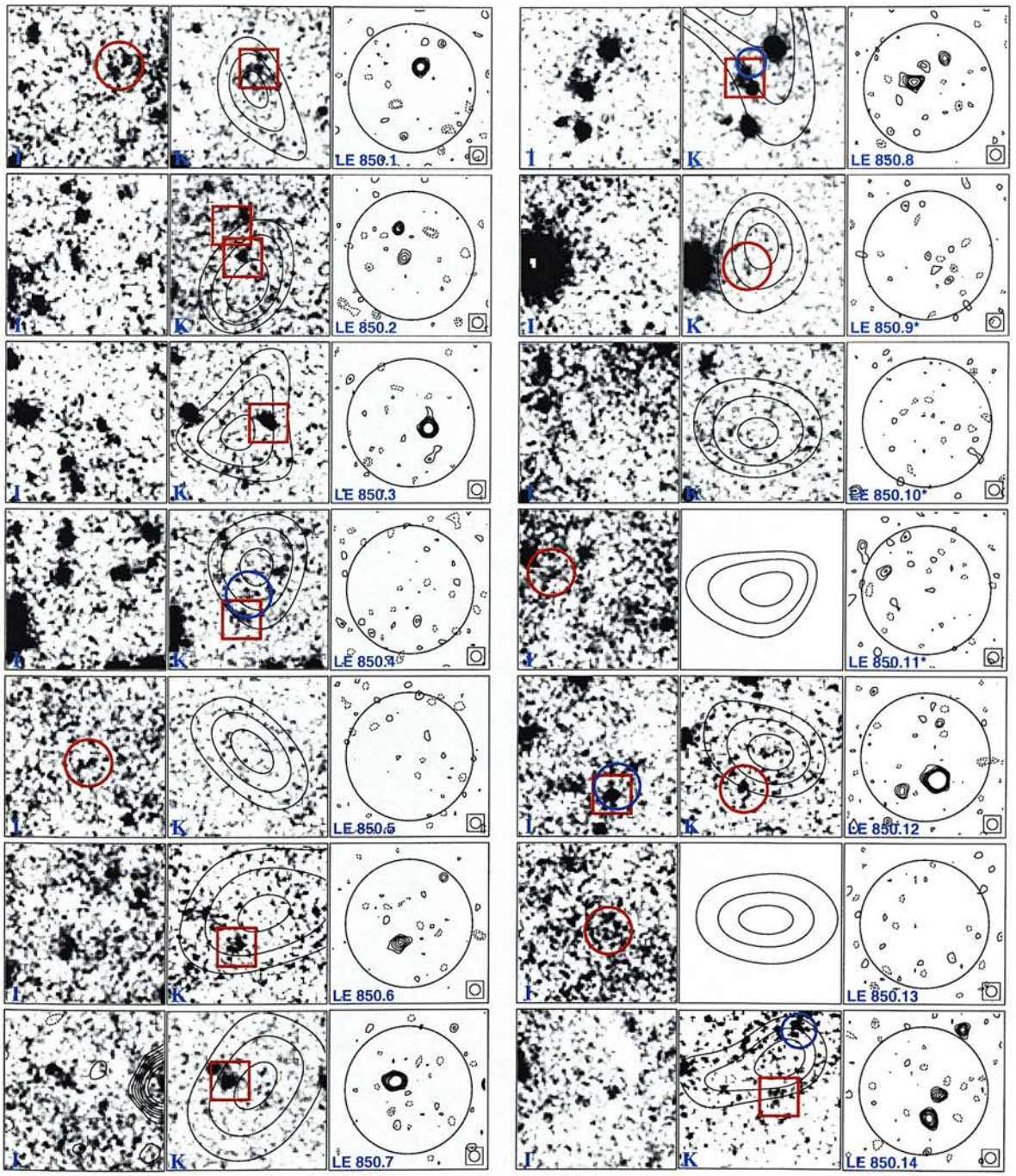

Figure 3.1: Postage stamps ($20'' \times 20''$) of the fields containing the twenty-one sources in the Lockman East region. For each submm source we show three images: *left*, I-band greyscale image, smoothed with a $0.3''$ FWHM Gaussian; *middle*, K-band greyscale, smoothed with a $0.3''$ FWHM Gaussian (with 850-μm contours at arbitrary levels); *right*, 1.4-GHz contours plotted at $-3,-2,2,3,4,5,6,8,10 \times\sigma$, where σ ranges from 4.3–5.3 μJy beam^{-1}; the circle represents the region of 95 per cent positional confidence ($\sim 8''$ radius). Sources within small red boxes are considered *robust* identifications (§4.2) and assigned photometric magnitudes in Table 2; those within small red circles are considered *plausible* identifications; blue circles represent X-ray detections via *XMM-Newton*. The radio data for LE 850.21 have been smoothed to a FWHM of $2''$ and the contours plotted on the I-band images of LE 850.7 represent 4.9-GHz emission. In §3.3 we refine the sample, excising those objects labelled with a star.

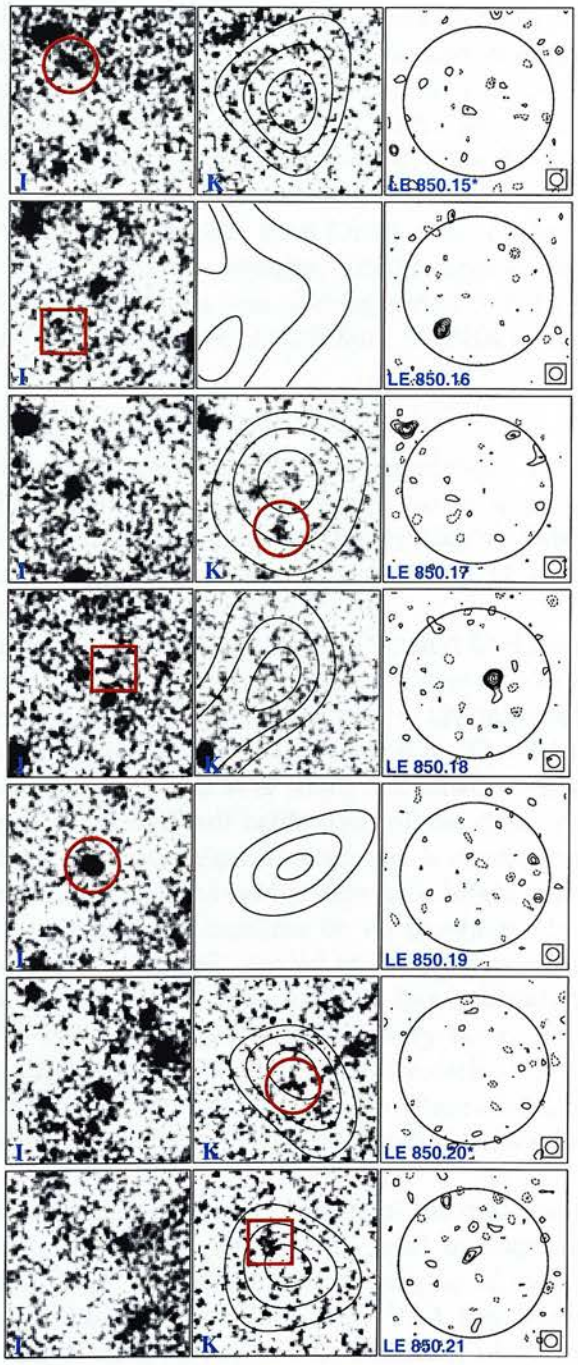

Figure 3.1: continued...

N2 850.16, originally in a noisy area of the map, has disappeared. This confirms that sources in 'non-uniform' regions of the maps (four, in addition to N2 850.16) are the least secure. No new sources were revealed at the $> 3.5\,\sigma$ level by the new data.

In order to assess the likely contamination from spurious and confused sources, a series of simulated images for each of the two survey fields were created, examples of which may be found in S02. Fake sources, arising purely from noise, were found to be in good agreement with Gaussian statistics, with only one spurious source found at the $\geq 3.5\,\sigma$ level. Confusion of fainter sources, however, can lead to catalogues being contaminated with false, brighter sources. At a 850-μm flux limit of ≥ 8 mJy, our simulations implied that 20 per cent of the objects recovered at $\geq 3.5\,\sigma$ could not be identified with a source brighter than 5 mJy. Most of these 'false bright sources' are real but are significantly fainter than the catalogues would suggest. Only minor modifications to the counts were required since our simulations also suggested that 15 per cent of 'real' ≥ 8-mJy sources are not recovered. The situation worsens if faint SCUBA galaxies are clustered.

3.2.2 Radio data

The process of obtaining and reducing deep, high-resolution, wide-field 1.4-GHz images is complicated by bandwidth smearing, necessitating the use of spectral-line, pseudo-continuum correlator modes at the National Radio Astronomy Observatory's[1] (NRAO) VLA, by interference (man-made and solar), and by the presence of dozens of bright (often structurally complex) sources in the primary beam.

For the two fields under consideration here, ELAIS N2 and Lockman Hole East, the problems encountered during data reduction were very different. The ELAIS N2 field is crowded with bright sources (the central 100 arcmin^2 field contains a ~ 120-mJy radio galaxy (Willott et al. 2002) as well as six structurally complex FR I/II sources). The field also has relatively poor nearby phase/amplitude calibrators, the best of which is resolved on some baselines. Fortunately, the presence of bright sources allowed self calibration of the data, correcting the poor initial phase/amplitude calibration. Lockman East, in contrast, is devoid of strong radio sources; self calibration was thus more difficult but the field is close to a bright, unresolved phase/amplitude calibrator so the initial calibration was excellent on all baselines. In detail: data were taken every 5 s in 3.25-MHz channels, 28 in total, centred at 1.4 GHz, recording left-circular and right-circular polarisations. 3C 84 and 3C 286 were used for flux calibration. The phase/amplitude calibrators, 1625+415 and 1035+564, were observed every hour. During 2001 January–May, 20 hr of integration was obtained for each field — 15 hr each in A configuration (maximum baseline, 27 km), during 2001 January; 5 hr each in B configuration (maximum baseline, 9 km). A further 55 hr of integration (A configuration) was obtained for the Lockman field during 2002 March.

After standard spectral-line calibration and editing of the data and their associated weights, using AIPS, the wide-field imaging task, IMAGR, was used to map the central $10' \times 10'$ fields of ELAIS N2 and Lockman East with simultaneous imaging of over 40 satellite fields known to contain bright sources via inspection of the NRAO VLA Sky Survey (NVSS — Condon et al. 1998). These maps, made with ROBUST = 0 weighting of the visibilities, were used to position CLEAN boxes around the sources, and IMAGR was re-run with 10,000 interations of the CLEAN algorithm (Högbom 1974; Clark 1980). The CLEAN components thus produced were used as a model for self calibration (in phase only) using CALIB with a relatively long integration time ($\sim$ 1–2 min) and a low signal-to-noise threshold (3–4 σ). Mapping was then repeated, after

[1] NRAO is operated by Associated Universities Inc., under a cooperative agreement with the National Science Foundation.

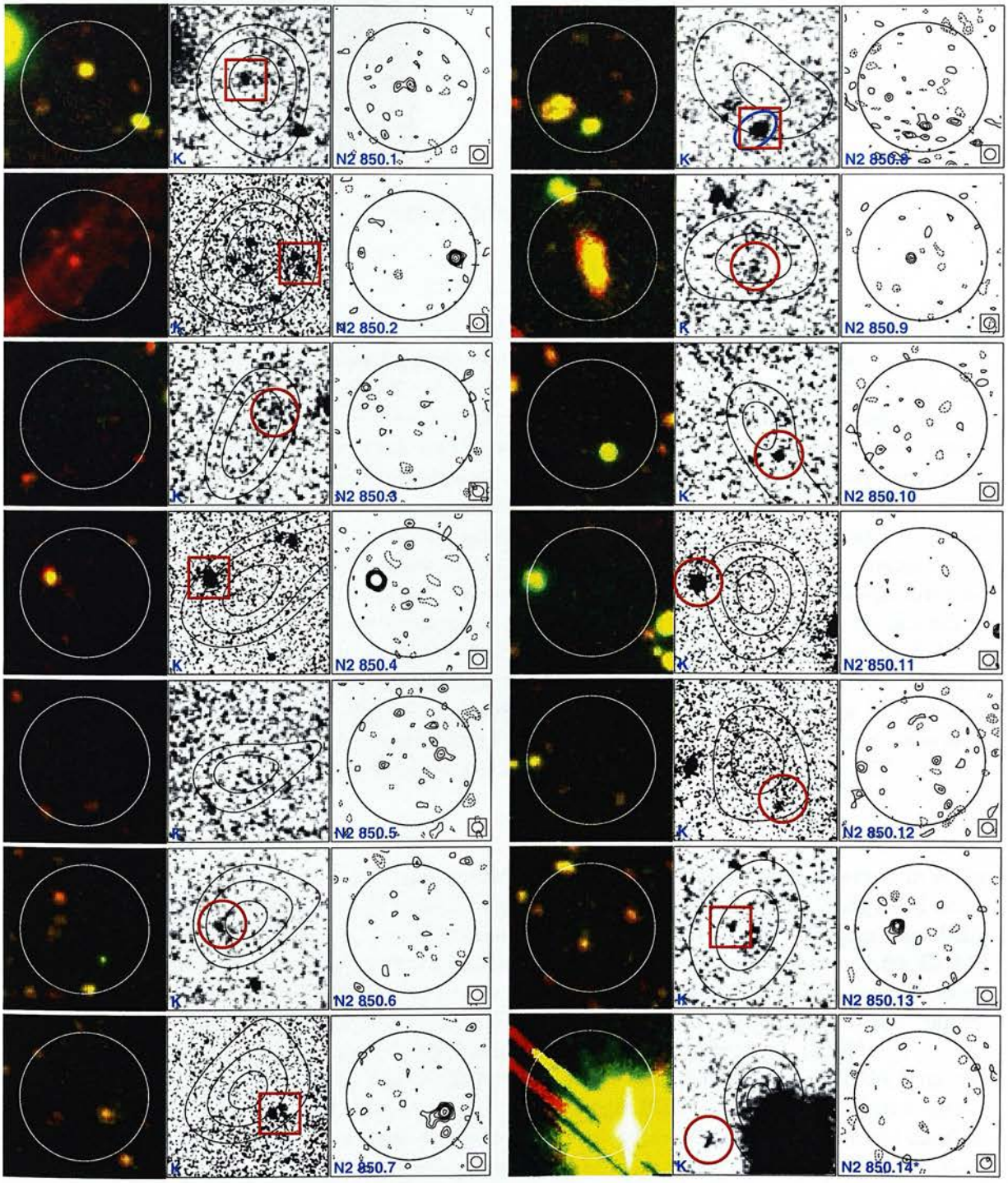

Figure 3.2: Postage stamps ($20'' \times 20''$) of the fields surrounding the submm sources in the ELAIS N2 region. For each submm source we show three images: *left*, VRI-band colour image, the circle representing 95 per cent positional confidence ($\sim 8''$ radius); *middle*, K-band greyscale, smoothed with a $0.3''$ FWHM Gaussian (with 850-μm contours at arbitrary levels); *right*, 1.4-GHz contours plotted at $-3,-2,2,3,4,5,6,8,10 \times\sigma$, again with a circle representing 95 per cent positional confidence. Sources within small red boxes are considered *robust* identifications (§4.2) and assigned photometric magnitudes in Table 2; those within small red circles are considered *plausible* identifications; the blue ellipse represents an X-ray detection by *Chandra*. In §3.3 we refine the sample, excising N2 850.14.

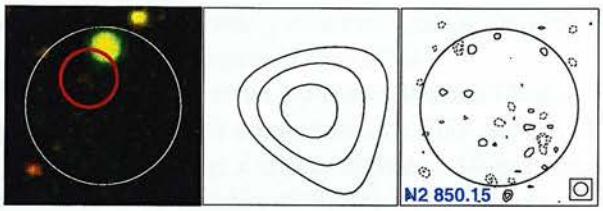

Figure 3.2: continued...

checks on the CLEAN boxes. The new CLEAN components were subtracted from the visibilities and the data were clipped to remove spikes, then added back to the CLEAN components. The IMAGR/CALIB loop was then repeated a further four times (though without further clipping), steadily decreasing the integration time and increasing the signal-to-noise threshold, the final pass of CALIB including both amplitude and phase (with the mean gain modulus of the applied calibration set at unity). This iterative method resulted in the loss of less than 5 per cent of the data. The A- and B-configuration data were dealt with separately and then co-added prior to imaging. The entire process involved several months of computer processing but produces images of very high quality. The resulting maps of Lockman East and ELAIS N2 have average noise levels of 4.8 and 9.2 μJy beam^{-1}, with 1.4″ resolution. Only the central 10′ × 10′ fields are used here, after correction for the primary beam response function of the VLA antennas using PBCOR.

Continuum data were also obtained at 4.9 GHz in the Lockman field using the VLA in its C configuration: a mosaic of seven overlapping positions, each separated by half the primary beam. These were reduced following the standard AIPS recipe. After correction for the primary beam response, the resulting maps were stitched together using FLATN, resulting in a noise level of $\sim 11\,\mu$Jy beam^{-1} in the central portion of the map and a FWHM resolution of $\sim 5.5''$.

3.2.3 IR/Optical imaging data

Our IR data for ELAIS N2 consist of a mosaic of 16 contiguous fields, each observed in K for 2 hr using the United Kingdom IR Telescope's (UKIRT[2]) UFTI Imager, a 1024^2 HgTeCd array with 0.091″ pixels. Three 1-hr UFTI integrations were also obtained in the Lockman East field, covering four submm sources. In addition, images through a K_s filter were obtained for ELAIS N2 (1.5-hr integrations) and Lockman East (1-hr integrations covering 17 submm sources) using the William Herschel Telescope's (WHT[3]) INGRID camera, a 1024^2 device with 0.237″ pixels. The IR data for ELAIS N2 and their reduction are described by Roche et al. (2002).

R-band imaging of ELAIS N2 was obtained with the Prime Focus Camera (PFC) on the WHT during 1999 May. At that time the PFC used a single EEV 4096 × 2048 detector with a pixel scale of 0.236″ and a field of view of $\sim 8' \times 16'$. Two adjacent pointings were obtained to cover a field of view of $16'^2$ with integration times of 1 hr each. The data were reduced using standard methods of bias subtraction, flat-fielding, de-fringing, extinction correction, registration and co-addition. The astrometric solution was obtained by comparison with the positions of stars in the United States Naval Observatory (USNO) A2.0 catalogue. The measured seeing is 0.7″.

[2] UKIRT is operated by the Joint Astronomy Centre on behalf of the United Kingdom Particle Physics and Astronomy Research Council (PPARC).

[3] Based on observations made with the WHT operated on the island of La Palma by the Isaac Newton Group in the Spanish Observatorio del Roque de los Muchachos of the Instituto de Astrofisica de Canarias

Photometric calibration was performed using observations of Landolt standard stars. The 3σ limiting magnitude in a $4''$-diameter aperture is $R = 26.0$.

I- and V-band imaging of ELAIS N2 was obtained with the Mosaic PFC on the WHT during 2000 June and 2001 May. This instrument comprises two EEV 4096×2048 detectors with $0.236''$ pixels and a field of view of $16'^2$. In the I filter, eighteen 10-min exposures were obtained at a variety of pointing positions: a total area of $370'^2$, with the central $140'^2$ receiving the full integration time of 3 hr. In V, a total of 1 hr of integration was obtained: twelve 5-min exposures dithered by $20''$ east–west. The data were reduced as described above and have seeing of $0.9''$ (I) and $0.7''$ (V). The 3σ limiting magnitudes are $I = 25.4$ and $V = 25.9$.

I-band imaging of the Lockman Hole was obtained with the PFC on the WHT during 2000 November: twelve 6-min exposures, dithered east-west by $20''$. The combined data have a measured seeing of $0.8''$ and a 3σ limiting magnitude of $I = 25.0$.

We have chosen to measure magnitudes (Table 2) and colours for galaxies from our optical/IR frames using a $4''$-diameter photometry aperture — equivalent to ~ 50 kpc at the likely redshifts of the submm sources, corresponding to effective total magnitudes. In this we differ from the standard procedure for faint galaxy photometry which usually relies on applying an aperture correction to photometry of sources taken with a small diameter, 2–3× FWHM, aperture. Our choice introduces a penalty in the precision of our photometry but it does guarantee that we obtain representative total magnitudes and colours for even the most extended counterparts to our submm sources (e.g. Lutz et al. 2001).

3.2.4 X-ray imaging

The Lockman Hole was observed by *XMM-Newton* during its performance verification phase, and the data are presented in Hasinger et al. (2001). Five observations were made, each with slightly different pointing centres and roll angles. For this analysis we have reprocessed the data with a more recent versions of the *XMM-Newton* Science Analysis System (SAS) taking advantage of the improved calibration data now available. After screening out periods of high particle background, the total exposure time is just over 100 ks. Data from all three EPIC cameras, in all five observations, were transformed to a common astrometric system and the combined data were used to produce images in the energy bands 0.2–0.5 keV, 0.5–2 keV, 2–5 keV and 5–12 keV. Energy channels contaminated by the strong instrumental emission lines (Lumb et al. 2002) were excluded from the images. The images were source-searched using the latest (SAS 5.3) versions of the SAS detection tasks EBOXDETECT and EMLDETECT, and images in all bands were searched simultaneously. Background maps for use in the source detection were constructed for each instrument, in each observation, and for each energy band, by performing a maximum likelihood fit of a vignetted (photon) and unvignetted (instrumental) background to the images after excising all detected sources. Several iterations of source detection followed by background determination were used to optimise the background model and thereby the sensitivity. All of the Lockman East submm sources lie within the combined *XMM-Newton* images, although LE 850.5 and LE 850.11 are so far off axis that they are only covered by the MOS cameras. We discuss the source properties in §4.3.

Chandra X-ray observations of the ELAIS N2 field are described in Manners et al. (2002). The field was observed using the 2×2 array of ACIS-I CCDs during 2000 August for 75 ks to a flux limit of 5×10^{-16} erg s^{-1} cm^{-2} (0.5–10.0 keV). Our optical imaging was also used to secure the X-ray astrometry to an accuracy of $\simeq 0.5''$ rms. Full details of the X-ray catalogue, source counts and hardness ratios can be found in Manners et al. (2002). The optical/IR identifications, photometry and preliminary spectra can be found in González-Solares et al. (2002) and Willott

Table 3.1: Radio counterparts with integrated flux densities above 30 (15) μJy within the 95 per cent confidence limit on the position of the 8-mJy ELAIS N2 (Lockman East) submm samples.

Source name[1]	Submm position α_{J2000} h m s	Submm position δ_{J2000} ° ′ ″	$S_{850\mu m}$ /mJy	Radio position α_{J2000} h m s	Radio position δ_{J2000} ° ′ ″	$S_{1.4GHz}$ /μJy	$S_{4.9GHz}$ /μJy	Radio-submm offset ″	P^2	Direction relative to submm centroid and other comments
LE 850.1	10 52 01.4	57 24 43	10.5 ± 1.6	10 52 01.25	57 24 45.7	73 ± 10	56 ± 37	3.1	0.014	compact source to NNW
LE 850.2	10 52 38.2	57 24 36	10.9 ± 2.4	10 52 38.30	57 24 35.8	29 ± 11	$5\sigma < 266$	1.0	0.003	central
				10 52 38.39	57 24 39.5	24 ± 9	$5\sigma < 266$	4.0	0.058	to NNE
LE 850.3	10 51 58.3	57 18 01	7.7 ± 1.7	10 51 58.02	57 18 00.3	98 ± 12	109 ± 26	2.8	0.007	compact source to W
				10 51 57.98	57 17 56.5	19 ± 13		5.5	0.104	to SW; 3σ peak
LE 850.4	10 52 04.1	57 25 28	8.3 ± 1.8	10 52 04.00	57 25 24.1	19 ± 8	$5\sigma < 60$	4.1	0.085	to S, 3σ peak
LE 850.5	10 51 59.3	57 17 18	8.6 ± 2.0			$5\sigma < 25$	$5\sigma < 300$			
LE 850.6	10 52 30.6	57 22 12	11.0 ± 2.6	10 52 30.73	57 22 09.5	54 ± 14	60 ± 35	2.8	0.018	to S, resolved
LE 850.7	10 51 51.5	57 26 35	8.1 ± 1.9	10 51 51.69	57 26 36.0	135 ± 13	$5\sigma < 60$	2.2	0.003	resolved? to NE; §3.1
				10 51 51.66	57 26 30.4	15 ± 9	$5\sigma < 60$	4.9	0.096	to SSE; 3σ peak
LE 850.8	10 52 00.0	57 24 21	5.1 ± 1.3	10 52 00.26	57 24 21.7	58 ± 12	57 ± 32	2.6	0.012	to NEE
				10 51 59.76	57 24 24.8	22 ± 11	$5\sigma < 60$	4.5	0.080	to NNW; 4σ peak
(LE 850.9)	10 52 22.7	57 19 32	12.6 ± 3.2			$5\sigma < 23$	$5\sigma < 90$			
(LE 850.10)	10 51 42.4	57 24 45	12.2 ± 3.1			$5\sigma < 25$	$5\sigma < 120$			
(LE 850.11)	10 51 30.6	57 20 38	13.5 ± 3.5	10 51 31.30	57 20 40.2	26 ± 12	$5\sigma < 400$	7.2	0.102	to NEE, resolved
LE 850.12	10 52 07.7	57 19 07	6.2 ± 1.6	10 52 07.49	57 19 04.0	278 ± 12	380 ± 28	3.7	0.004	to SSW; variable
				10 52 08.06	57 19 02.6	27 ± 11	$5\sigma < 200$	5.6	0.086	to SE, 4σ peak
LE 850.13	10 51 33.6	57 26 41	9.8 ± 2.8	10 51 33.14	57 26 36.7	18 ± 11	$5\sigma < 100$	6.3	0.109	to SW; 3σ peak
LE 850.14	10 52 04.3	57 26 59	9.5 ± 2.8	10 52 04.22	57 26 55.4	72 ± 12	30 ± 18	3.7	0.021	to S
				10 52 04.06	57 26 58.5	36 ± 12		2.4	0.017	to SW; 6σ peak
(LE 850.15)	10 52 24.6	57 21 19	11.7 ± 3.4			$5\sigma < 21$	$5\sigma < 60$			
LE 850.16	10 52 27.1	57 25 16	6.1 ± 1.8	10 52 27.58	57 25 12.4	41 ± 12	32 ± 22	6.0	0.061	to SE, resolved?
LE 850.17	10 52 16.8	57 19 23	9.2 ± 2.7			$5\sigma < 23$	$5\sigma < 90$			
LE 850.18	10 51 55.7	57 23 12	4.5 ± 1.3	10 51 55.47	57 23 12.7	47 ± 10	38 ± 19	2.4	0.013	to W
LE 850.19	10 52 29.7	57 26 19	5.5 ± 1.6			$5\sigma < 27$	$5\sigma < 67$			
(LE 850.20)	10 52 37.7	57 20 30	10.3 ± 3.1			$5\sigma < 24$	$5\sigma < 90$			
LE 850.21	10 52 01.7	57 19 16	4.5 ± 1.3	10 52 01.73	57 19 17.1	21 ± 10	$5\sigma < 125$	1.1	0.002	central
N2 850.1[3]	16 37 04.3	41 05 30	11.2 ± 1.6	16 37 04.34	41 05 30.3	45 ± 16		0.7	0.002	to W, 4σ peak
				16 37 04.48	41 05 30.1	31 ± 14		2.6	0.021	to E, 3σ peak
						76 ± 20				total flux for double
N2 850.2[3]	16 36 58.7	41 05 24	10.7 ± 2.0	16 36 58.19	41 05 23.8	92 ± 16		7.7	0.032	compact source to W
N2 850.3	16 36 58.2	41 04 42	8.5 ± 1.6			$5\sigma < 44$				
N2 850.4	16 36 50.0	40 57 33	8.2 ± 1.7	16 36 50.43	40 57 34.5	221 ± 17		6.5	0.010	compact source to NEE
				16 36 50.08	40 57 31.1	30 ± 16		2.2	0.023	to S, 3σ peak
N2 850.5	16 36 35.6	40 55 58	8.5 ± 2.2	16 36 35.28	40 55 59.2	77 ± 31		4.9	0.021	to W, 4σ peak
				16 36 35.30	40 55 59.5	50 ± 23		4.8	0.032	to NW, 3σ peak
N2 850.6	16 37 04.2	40 55 45	9.2 ± 2.4	16 37 04.49	40 55 39.2	38 ± 19		7.2	0.085	to SSE, $2\text{–}3\sigma$ peak
N2 850.7	16 36 39.4	40 56 38	9.0 ± 2.4	16 36 39.01	40 56 35.9	159 ± 27		6.3	0.014	to SW; 7σ; tail to SE
N2 850.8	16 36 58.8	40 57 33	5.1 ± 1.4	16 36 58.78	40 57 28.1	74 ± 29		4.9	0.033	to S; 4σ peak
N2 850.9	16 36 22.4	40 57 05	9.0 ± 2.5	16 36 22.54	40 57 04.8	33 ± 12		2.0	0.014	to E, $4\text{–}5\sigma$ peak
				16 36 22.34	40 57 08.3	40 ± 19		3.4	0.033	to NW, 2σ peak
N2 850.10	16 36 48.8	40 55 54	5.4 ± 1.5	16 36 49.29	40 55 50.8	58 ± 24		8.0	0.055	double to SE, 3σ peak
N2 850.11	16 36 44.5	40 58 38	7.1 ± 2.0			$5\sigma < 44$				
N2 850.12	16 37 02.5	41 01 23	5.5 ± 1.6	16 37 02.26	41 01 19.1	32 ± 17		5.3	0.067	to SW, 3σ peak
N2 850.13	16 36 31.2	40 55 47	6.3 ± 1.9	16 36 31.47	40 55 46.9	99 ± 23		4.1	0.011	to E, resolved? 6σ peak
(N2 850.14)	16 36 19.7	40 56 23	11.2 ± 3.3			$5\sigma < 49$				
N2 850.15	16 37 10.2	41 00 17	5.0 ± 1.5	16 37 10.42	41 00 23.0	31 ± 20		6.8	0.096	to NNE; 2σ peak

Notes: (1) Sources in parentheses are excluded from further analysis on the basis of large $\sigma_{850\mu m}$ values (see §3.3). (2) Probability that the radio source is *not* associated with the submm emission (see §3.2); (3) Photometry-mode observations at the radio positions give $S_{850\mu m} = 9.1 \pm 1.5$ mJy and $S_{450\mu m} = 24 \pm 9$ mJy for N2 850.1, $S_{850\mu m} = 10.4 \pm 1.7$ mJy and $S_{450\mu m} = 50 \pm 16$ mJy for N2 850.2. Errors include an uncertainty of 10 per cent for the absolute flux scale.

et al. (2002). Details of the X-ray/sub-mm coincidence and cross-correlation can be found in Almaini et al. (2002).

3.2.5 Positional ambiguity between reference frames

There has been a tendency in the past to ignore potential offsets of up to $\sim 1''$ between the radio/mm and optical/IR coordinate frames (e.g. Georgakakis et al. 1999). Unfortunately, this offset corresponds to the spatial scale expected for moderate and strong lensing (Chapman et al. 2002b) and identifying such offsets is therefore significant for interpreting the association of submm sources with optically bright galaxies. This situation is inevitable in mm interferometry, where the primary beam has a FWHM of only $\sim 20''$ and contains only the source of interest (Downes et al. 1999; Bertoldi et al. 2000; Frayer et al. 2000; Gear et al. 2000; Lutz et al. 2001; Dannerbauer et al. 2002) but at radio wavelengths the primary beam is sufficiently large ($\sim 30'$ at 1.4 GHz for the VLA) to permit investigation of potential offsets.

For this analysis, we used the Lockman East I-band and 1.4-GHz maps. Our optical/IR images were astrometrically calibrated using stars from the USNO A2.0 catalogue (Monet et al. 1998; see also Assafin et al. 2001). Seventy stars were used to calibrate the I-band image to the USNO reference frame, with an rms of $0.05''$. The positions of the radio sources on our VLA map are defined relative to a nearby type-A primary phase calibrator (i.e. unresolved, with a position known to $< 0.02''$). The brightest 32 1.4-GHz sources ($> 8\,\sigma$ at their peak) were selected from the radio image; of those, 17 had bright, compact optical counterparts (a few more had faint counterparts but these were ignored). Positions for these sources were measured using 2-D

Gaussian fits.

The mean offsets between the radio and optical frames were $\alpha_{\rm rad-opt} = -0.34 \pm 0.29''$, $\delta_{\rm rad-opt} = -0.35 \pm 0.24''$, i.e. the radio image was slightly south and west of the optical image. A similar analysis was performed for the ELAIS N2 R-band and radio images, finding offsets of $\alpha_{\rm rad-opt} = -0.39 \pm 0.28''$, $\delta_{\rm rad-opt} = -0.18 \pm 0.28''$. In the analysis that follows, and the plots, positional information has always been corrected to the radio coordinate frame, using the AIPS tasks LGEOM, HGEOM and OHGEO.

In terms of our confidence in assigning optical/IR host galaxies to radio sources, we now have several uncertainties to be added in quadrature: a) the uncertainty in the measured radio position, often given as $\sigma_{\rm rad} \sim {\rm fwhm}/({\rm s/n})$ (where FWHM is the source or beam size at full width at half maximum and S/N is the signal-to-noise ratio); b) the uncertainty in the alignment of the frames ($\sigma_{\rm align} \sim 0.3''$) and c) the uncertainty in the measured optical position, $\sigma_{\rm opt} \sim {\rm fwhm}/({\rm s/n})$. For the faintest optical/1.4-GHz sources, the total error budget is $\sim 0.8''$ (after the frames have been aligned); for the brightest sources this drops to $\sim 0.3''$.

3.3 Submm–radio associations and sample refinement

3.3.1 Selection of candidate radio counterparts

The HAPPY source detection routine developed for the FIRST survey (Faint Images of the Radio Sky at Twenty centimetres — White et al. 1997) was used initially, followed by more detailed analysis of the sources thus extracted. A radio source peaking at $\geq 4\,\sigma$ in the $1.4''$ or smoothed $2''$ images, with an integrated flux density in excess of $30\,\mu$Jy ($15\,\mu$Jy for Lockman), is considered a *robust* detection. Fainter sources, where the definition is relaxed to only the integrated flux (again $\geq 30\,\mu$Jy, or $\geq 15\,\mu$Jy in the Lockman field), were also catalogued.

For each sub-mm source we have searched for a potential radio (1.4 GHz) counterpart out to a radius of $8''$ from the nominal SCUBA position deduced by S02 (see Figs 3.2 and 3.2). This relatively large search area ($200''^2$ around each source) is required to ensure that ≤ 5 per cent of real associations are missed, given the angular size of the JCMT beam at $850\,\mu$m ($14''$ FWHM) and the fact that the majority of the SCUBA detections have S/N$\simeq$3.5–4.0. Fortunately, as demonstrated by the calculations described below, this large search radius for radio counterparts can be tolerated without compromising the statistical significance of genuine associations. This is because, even at the extreme depths reached by the radio imaging reported here, the cumulative surface density of radio sources is only $\simeq 2.5\,{\rm arcmin}^{-2}$.

Of the 36 submm sources in the sample, ten have no candidate radio counterparts, 20 have clearly detected candidate radio counterparts and the remaining six have faint candidate radio counterparts. The flux densities and positions of all candidate radio counterparts are listed in Table 1.

3.3.2 Statistical significance of submm–radio associations

To quantify the formal significance of each of the potential submm–radio associations listed in Table 1 we have used the method of Downes et al. (1986). This corrects the raw Poisson probability that a radio source of the observed flux density could lie at the observed distance from the submm source for the number of ways that such an apparently significant association could have been uncovered by chance (given the limiting search radius, the limiting depth of the available radio data and the flux density of the radio detection). This correction is extremely important for the present study due to the large search radius adopted above. Based on the

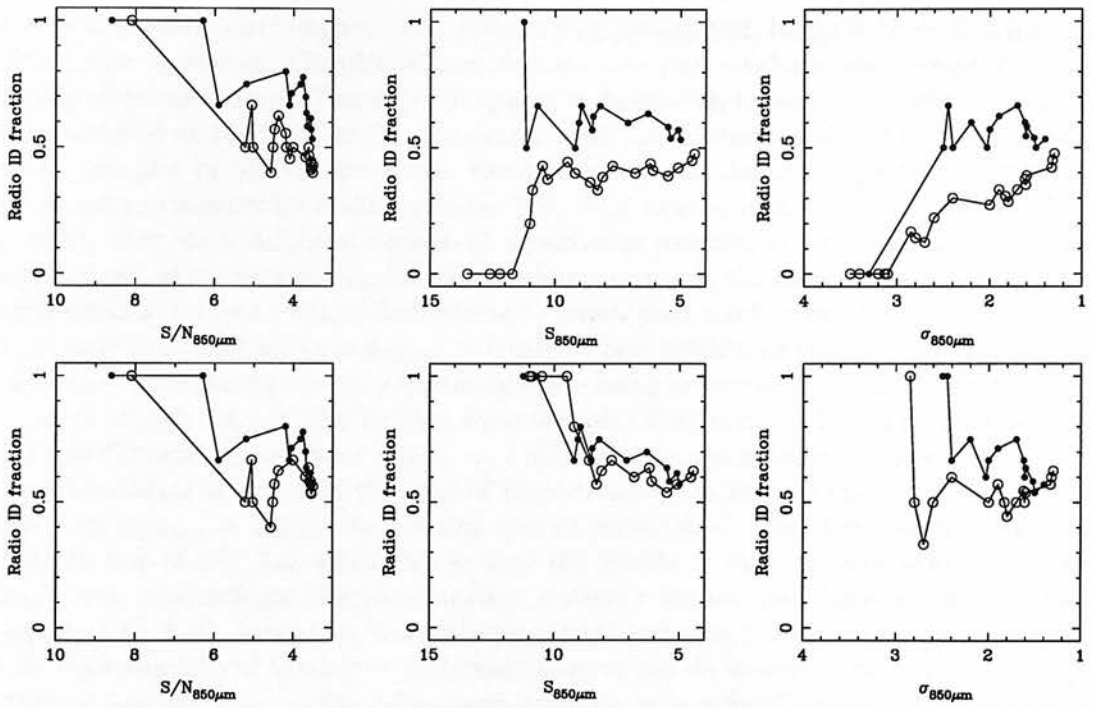

Figure 3.3: *Top row:* Plots of running (cumulative) average radio-identified fraction for the Lockman Hole East submm sample (open circles) and the ELAIS N2 submm sample (filled circles) against submm signal-to-noise ratio (*left*), 850-μm flux density (*middle*) and local 850-μm noise level (*right*). The unexpected failure to identify the radio counterparts to the four brightest Lockman submm sources, obvious in the middle plot, is shown in the right-hand plot to be due to the fact that all of these sources were extracted from the noisiest regions of the original submm maps. Based on the top-right plot we have rejected all six sources with $\sigma_{850\mu\mathrm{m}} > 3\,\mathrm{mJy}$ from the sample on the basis that they are probably produced by source confusion and/or severe submm flux boosting (as anticipated by S02). *Bottom row:* same plots after removal of the six unreliable sources. The observed trends now appear more sensible; moreover, they are statistically consistent between both fields, asymptoting to a final radio identification rate of 60 per cent.

$S_{850\mu\mathrm{m}} < 5\,\mathrm{mJy}$. In particular, from simulations using the real noise maps of the 8-mJy survey fields, S02 predicted that at the $3.5\,\sigma$ level, $\simeq$20 per cent of the Lockman Hole 8-mJy 'sources', and $\simeq$15 per cent of the ELAIS N2 8-mJy 'sources' could be expected to arise from confusion.

This raises an obvious question: how might one identify which sources these are? One clear prediction is that such 'fake' 8-mJy submm sources will not have detectable radio counterparts. However, it would be foolish to assume that all nine of the submm sources from the 36-source parent sample which lack a possible radio counterpart in the maps presented here are not real — genuine sources could also evade radio detection, either because they lie close to the flux limit of the submm survey or because they lie at extreme redshift. In this section we therefore explore what can be learned about the submm sources without radio counterparts by examining trends in radio identification rate.

In Fig. 3.3 we have plotted, in the top row, the running (i.e. cumulative) average radio identification rate for the submm sources from the ELAIS N2 and Lockman Hole sub-samples as

a function of submm source significance, submm flux density and, lastly, submm flux uncertainty. These plots are revealing. The plot of identification rate versus submm source significance shows some drop off towards $3.5\,\sigma$. This does not appear to be serious, in the sense that the identification fraction achieved at the $3.5\,\sigma$ level is consistent with that already achieved for sources at $>4\,\sigma$. However, the plot of identification rate versus submm flux density is peculiar, with the four brightest submm sources from the Lockman Hole field lacking a radio identification. This must mean either that these brightest sources lie at extreme redshift, or that they are not real. The third plot shows that the latter explanation is almost certainly the correct one. This plot — radio source identification rate versus submm noise — shows that the four brightest submm sources in the Lockman Hole field all have $\sigma_{850\mu\mathrm{m}} > 3\,\mathrm{mJy}$. Their brightness therefore simply reflects the fact that they have passed the $3.5\,\sigma$ threshold while being extracted from unusually noisy regions of the original map. It can also be seen from this plot that another Lockman Hole source, and one ELAIS N2 source, also have $\sigma_{850\mu\mathrm{m}} > 3\,\mathrm{mJy}$ and also lack radio counterparts. The most conservative course of action in the light of these trends is to assume that all six of the submm sources with $\sigma_{850\mu\mathrm{m}} > 3\,\mathrm{mJy}$ are not real and to excise them from the sample. As shown in the bottom row of Fig. 3.3, when this is done the trends in radio identification rate are more plausible and, interestingly, the identification statistics for the two fields are now statistically consistent, with both survey regions yielding a final radio-source identification rate of 60 per cent. In the remainder of this paper we therefore reject the six sources with $\sigma_{850\mu\mathrm{m}} > 3\,\mathrm{mJy}$ from the original sample, and confine subsequent analyses to a refined sample of 30 sources which should not be seriously biased by erroneous radio blank fields. The six sources rejected on this basis are LE 850.9, LE 850.10, LE 850.11, LE 850.15, LE 850.20 and N2 850.14.

We stress that the rejection of these sources is consistent with expectations based on the the simulations performed by S02. Specifically, based on these simulations S02 predicted that four of the $21 > 3.5\,\sigma$ Lockman Hole sources, and two of the original $17 > 3.5\,\sigma$ ELAIS N2 sources would likely be the result of confusion. Here, on the basis of the trends shown in Fig. 3.3, we have rejected five sources from the Lockman Hole sample, and one source from the ELAIS N2 sample. Interestingly, the only other source in the original ELAIS N2 sample which had $\sigma_{850\mu\mathrm{m}} > 3\,\mathrm{mJy}$ was N2 850.16, which we have already rejected in the light of additional 850-μm data. The simulations also predict that submm source confusion should only be capable of producing fake sources as bright as $S_{850\mu\mathrm{m}} > 8\,\mathrm{mJy}$ if the local submm map noise level is $\sigma_{850\mu\mathrm{m}} \simeq 3\,\mathrm{mJy}$ or greater. Thus it is to be expected that the 'fake' sources should turn out to be found among the apparently brightest sources selected from the noisiest regions of the original submm images (generally close to the edge of the maps).

In summary, we have exploited the observed trends in radio identification rate to decide on a criterion ($\sigma_{850\mu\mathrm{m}} > 3\,\mathrm{mJy}$) for rejecting those sources from the parent 36-source submm sample which appear to be the result of source confusion and/or severe submm flux boosting by noise. The number of sources rejected on this basis (i.e. six) is in line with expectations based on the simulations of S02 and therefore does not affect the source-count estimates derived in that paper. However, their excision from the sample under study here is important because otherwise it would be erroneously concluded that their non-detection at radio wavelengths implies they lie at very high redshift. Their removal thus avoids a potentially serious bias being introduced into our best estimate of the redshift distribution of the 8-mJy population (see §4.5).

3.4 Source characteristics

We now discuss the radio and optical/IR information gathered for the SCUBA sources in the refined 30-source 8-mJy sample. The optical/IR morphologies and colours of the proposed

Table 3.2: Magnitudes and morphologies for confirmed and plausible optical/IR host galaxies in the 8-mJy submm sample.

Source name[1]	Optical/IR[3] morphology	K mag[4]	R mag[4]	I mag[4]	V mag[4]	Comments
LE 850.1	M	19.8 ± 0.2	—	$3\sigma > 25.0$	—	ERO[5]
LE 850.2	M	20.32 ± 0.24	—	23.26 ± 0.16	—	Central object. VRO to N
LE 850.3	M	18.86 ± 0.09	—	23.24 ± 0.15	—	ERO
LE 850.4[2]	F	*19.56± 0.15*	—	*3σ > 25.0*	—	*ERO*
LE 850.5	F	*3σ > 20.6*	—	*24.29± 0.29*	—	*Faint, extended optical galaxy?*
LE 850.6	M	19.22 ± 0.16	—	22.71 ± 0.07	—	Obvious double in I and K; VRO
LE 850.7	M	17.93 ± 0.06	—	22.56 ± 0.10	—	Radio lobe; blue galaxy/ERO[6] pair
LE 850.8	M	18.82 ± 0.09	—	21.59 ± 0.03	—	Mags include both components
(LE 850.9)	*B (F?)*	*3σ > 20.5*	—	*3σ > 25.0*	—	*Very faint K near submm centroid?*
(LE 850.10)	*F*	*3σ > 20.6*	—	*3σ > 25.0*	—	*Blank field*
(LE 850.11)	F	$3\sigma > 20.6$	—	24.35 ± 0.40	—	Red/blue pair?
LE 850.12	C	$3\sigma > 20.6$	—	22.66 ± 0.08	—	Radio indicates AGN
LE 850.13	*F*	$3\sigma > 20.6$	—	*24.44± 0.39*	—	*Faint I-band emission?*
LE 850.14	F	20.34 ± 0.39	—	23.67 ± 0.24	—	Faint I and K emission; VRO
(LE 850.15)	*M*	*3σ > 20.4*	—	*23.28± 0.14*	—	*Tadpole-shaped I counterpart?*
LE 850.16[2]	F	*19.35± 0.05*	—	*23.94± 0.27*	—	*ERO + blue/ERO[7] pair*
LE 850.17[2]	*F*	*19.78± 0.18*	—	*3σ > 25.0*	—	*ERO/blue galaxy pair*
LE 850.18	M	$3\sigma > 20.4$	—	24.59 ± 0.39	—	Complex optical system
LE 850.19	*C*	*19.09± 0.03*	—	*22.17± 0.04*	—	*Bright compact source?*
(LE 850.20)	*M*	*20.28± 0.44*	—	*22.66± 0.07*	—	*Faint I and K emission?*
LE 850.21	M	19.73 ± 0.17	—	24.09 ± 0.25	—	ERO/blue pair (faint radio)
N2 850.1	C	19.48 ± 0.24	22.93 ± 0.02	21.99 ± 0.03	23.19 ± 0.03	Lens? (Chapman et al. 2002b)
N2 850.2	M	19.77 ± 0.06	25.42 ± 0.43	24.48 ± 0.20	$3\sigma > 25.9$	ERO
N2 850.3	*F*	*21.18± 0.14*	*25.07± 0.20*	*24.14± 0.19*	*25.22± 0.26*	*Red/blue galaxy pair*
N2 850.4	M	18.43 ± 0.02	22.28 ± 0.01	21.83 ± 0.02	22.40 ± 0.03	Blue galaxy/VRO pair.
N2 850.5	B	$3\sigma > 20.7$	$3\sigma > 26.0$	$3\sigma > 25.0$	$3\sigma > 25.9$	
N2 850.6	*M*	*19.54± 0.24*	*24.21± 0.07*	*23.29± 0.08*	*24.23± 0.12*	*Blue/red galaxy pair*
N2 850.7	M	19.54 ± 0.06	23.46 ± 0.03	22.44 ± 0.03	23.68 ± 0.06	Blue/red galaxy pair
N2 850.8	M (C?)	18.15 ± 0.09	22.49 ± 0.02	21.55 ± 0.02	22.79 ± 0.03	X-ray AGN; VRO
N2 850.9	M	17.9 ± 0.4	20.7 ± 0.2	19.4 ± 0.2	20.7 ± 0.2	Large-aperture mags
N2 850.10	*C*	*19.56± 0.24*	*20.96± 0.10*	*20.41± 0.01*	*21.23± 0.03*	*Compact blue counterpart?*
N2 850.11	*C*	*17.26± 0.01*	*20.93± 0.01*	*19.44± 0.01*	*21.78± 0.03*	*Compact counterpart, or blank?*
N2 850.12	*F (M?)*	*20.57± 0.14*	*24.96± 0.10*	*23.84± 0.12*	*24.62± 0.14*	*VRO*
N2 850.13	B	21.00 ± 0.64	$3\sigma > 26.0$	$3\sigma > 25.0$	$3\sigma > 25.9$	Blue galaxy/ERO pair
(N2 850.14)	*F*	*19.47± 0.17*	—	—	—	Optical images saturated
N2 850.15	*F*	—	*25.18± 0.12*	*24.13± 0.12*	*25.82± 0.40*	*Several possible faint counterparts*

Notes: (1) Details in italics refer to *plausible* counterparts (those circled Figs ?? and ??). Sources with robust submm–radio associations (§3.2) have their names in bold. Sources excluded from further analysis on the basis of large $\sigma_{850\mu m}$ values (see §3.3) are named in parentheses. (2) Sources with well-determined positions on the basis of extreme colours and/or weak radio emission. (3) Morphologies are categorised as: B, blank; F, very faint; C, compact; M, multiple/distorted; —, unknown. (4) Magnitudes were measured in 4″-diameter apertures. (5) Lutz et al. (2001) showed LE 850.1 to be a clumpy ERO. (6) Magnitudes for the red component: K=18.43 ± 0.05, I=22.93 ± 0.12. (7) ERO to the NW has $I - K > 4.76$.

identifications are listed in Table 2. To quantify the classification of the colours of the optical/IR identifications, we note that the general field galaxy population brighter than $K = 21$ has a median $(I - K) = 2.6$, with 6 per cent of the galaxies redder than $(I - K) = 4$ and 20 per cent redder than $(I - K) = 3.3$. Hence in the following we adopt the standard definition of an extremely red object, ERO, of $(I - K) > 4$, and in addition use the term "very red object" (VRO) to denote galaxies with $(I - K) > 3.3$.

3.4.1 Notes on individual sources

LE 850.1: the submm–radio association is unambiguous and statistically significant, and in this case confirmed by 1.3-mm interferometry in the detailed study of this object presented by Lutz et al. (2001). Deep IR imaging, also presented by Lutz et al., permits the submm galaxy to be identified with a complex red object offset to the east of the faint I-band emission circled in Fig. 3.2 ($I = 23.7 \pm 0.2$).

LE 850.2: at least two potential 1.4-GHz counterparts, seemingly confirmed in the lower resolution 4.9-GHz image and in a smoothed version of the 1.4-GHz map (3″ FWHM). There is an equally complex picture in the optical/IR: faint I-band components stretch from the submm centroid towards the N and NNE; K emission is associated with several of them, with an extremely red object (ERO) and a very red object (VRO) close to, but not coincident with, two of the optical sources — composite blue/red systems, both with radio emission ($I - K > 4.8$ and $I - K > 3.9$, respectively). However, statistically the correct radio identification is clear, and the corresponding optical identification is the more central optical source.

LE 850.3: a strong, and statistically compelling radio counterpart is found to be aligned with an ERO, a distorted/multi-component galaxy in the I-band image, typical of submm host galaxies (Smail et al. 1998, 1999). A very close resemblence to LE 850.7 led us to check for nearby sources: another 1.4-GHz source lies 14.5″ to the east. Both have I-band counterparts (Fig. 3.4) and we

view an association with a twin-lobed radio galaxy to be unlikely in this case. The radio spectral index, $\alpha = +0.1 \pm 0.3$, indicates a probable AGN contribution.

LE 850.4: A complex field, but an ERO to the south (detected at 1.4 GHz) is probably the galaxy responsible for the submm emission (although the formal significance of the submm–radio association falls just above the $P = 0.05$ level). A faint *XMM-Newton* 2–5-keV counterpart is detected, coincident with the submm source position. The position of the X-ray source is just consistent with that of the ERO/μJy radio source. The absence of any X-ray emission below 2 keV means this is likely an obscured AGN, with a column density of $> 10^{23}\,\mathrm{cm}^{-2}$.

LE 850.5: the one faint potential submm-radio association is not statistically convincing. At optical/IR wavelengths this is a blank field although there is a hint of I-band emission at the position of the submm centroid.

LE 850.6: this source is unambiguously associated with a faint, resolved radio source with a faint, similarly-shaped distorted/multi-component VRO visible in I and K. The 850-μm contours in Fig. 3.2 suggest another submm source lies to the west. Further investigation revealed a $3.48\,\sigma$ source (R.A. $10^{\mathrm{h}}52^{\mathrm{m}}27.1^{\mathrm{s}}$, Dec. $+57°22'21''$, J2000, 10.2 ± 3.1 mJy) not included in the original S02 catalogue, with a robust 1.4-GHz counterpart but no optical or IR emission (Fig. 3.5). Both 1.4-GHz sources have faint emission at 4.9 GHz, so there is no evidence that these are steep-spectrum sources as found for LE 850.7, and no sign of a flat-spectrum core between them.

LE 850.7: apparently a carbon copy of LE 850.3, even with regard to position angle. This seems at first to be a straightfoward case: a bright, compact and statistically compelling radio source is found within a few arcseconds of the submm position, with a faint, seemingly disturbed, optical counterpart — an ERO. In fact, the 1.4-GHz emission seen in Fig. 3.2 has an extremely steep spectrum (steeper than $S_\nu \propto \nu^{-1.2}$). Examining the 1.4- and 4.9-GHz data closely (Fig. 3.6), another source is apparent, with an inverted spectrum, to the west of the submm source (R.A. $10^{\mathrm{h}}51^{\mathrm{m}}50.12 \pm 0^{\mathrm{s}}.06$, Dec. $+57°26'35.6 \pm 0''.5$, J2000); a weaker steep-spectrum source is visible beyond that. These are the characteristics of a double-lobed radio galaxy. The core has flux densities of 163 ± 18 and $269 \pm 26\,\mu$Jy at 1.4 and 4.9 GHz and has an obvious optical counterpart (Fig. 3.6). With such a steep spectrum, it seems implausible that the radio component at the submm position could be responsible for the optical emission via the synchrotron mechanism (the extrapolated flux density in the I-band is many orders of magnitude too low, and the counter lobe has no optical counterpart). We suggest instead that the optical galaxy is part of a system undergoing an intense burst of star formation triggered by a jet from a neighbouring radio galaxy. LE 850.3 and LE 850.12 (possibly LE 850.14 and LE 850.18) are other systems plausibly associated with radio-loud AGN.

LE 850.8: a statistically robust radio counterpart is aligned with the faint north-eastern extension of a complex galaxy or group of galaxies visible in I. Probably the site of highly obscured star formation, with a less obscured companion (see Ivison et al. 2001). A highly significant *XMM-Newton* counterpart is detected in all but the 0.2–0.5-keV image, $2''$ NNE of the submm source position, and just consistent with the brighter radio source position. This X-ray source was also detected in the *Rosat* Ultra Deep HRI survey by Lehmann et al. (2001), who propose that the northernmost optical/IR source in Fig. 3.2 is the optical counterpart, an AGN at $z = 0.974$. The position we derive from *XMM-Newton* is *not* consistent (at 90 per cent confidence) with this proposed optical counterpart, although it is consistent with the HRI position. The X-ray colours suggest that the source is intrinsically absorbed by a column density of $> 10^{22}\,\mathrm{cm}^{-2}$.

LE 850.12: a very bright and statistically compelling radio counterpart is found which, at first glance appears aligned with a compact optical source. There is, in fact, a significant offset between their positions, although it is plausible that the optical source is closely related to the submm/radio emission. Faint optical emission extends $\sim 5''$ to the NW and NE. The 1.4-GHz

emission appears to be variable, dropping from 345 μJy in 2001 January to 278 μJy in 2002 March. The 4.9-GHz emission is as strong as that at 1.4 GHz, leading us to conclude that this is an AGN, most likely a radio-loud quasar. This conclusion is supported by the detection of an *XMM-Newton* 2–5-keV counterpart coincident with the radio source. The ratio of the 2–5 keV to 0.5–2 keV flux suggests the X-ray source is intrinsically absorbed by a column density of order $10^{23}\,\mathrm{cm}^{-2}$ or more. A fainter 1.4-GHz source lies to the east, also with the suspicion of 4.9-GHz emission, coincident with a faint optical/IR galaxy (circled in Fig. 3.2). However, statistically the presence of this second radio source is not surprising.

LE 850.13: the one faint potential submm–radio association is not statistically convincing. At optical/IR wavelengths this is a blank field, although there is evidence for faint I-band emission at the position of the submm centroid.

LE 850.14: with reference to LE 850.7, this appears at first glance to be another twin-lobed AGN, the northern component representing the core. Another weak 1.4-GHz source further to the north (above the 95 per cent confidence circle) would represent the counter lobe, although it has a faint optical counterpart, and a 2–5-keV *XMM-Newton* counterpart, unlike the stronger southern 'lobe'. The weak central component is also aligned with I-band emission. However, faint 4.9-GHz emission is associated with the southern component ($S_{1.4\mathrm{GHz}} = 72 \pm 12\,\mu\mathrm{Jy\,beam}^{-1}$, $S_{4.9\mathrm{GHz}} = 30 \pm 18\,\mu\mathrm{Jy\,beam}^{-1}$), and this 4.9-GHz emission argues against this being a steep-spectrum lobe (we expect $S_{1.4\mathrm{GHz}}/S_{4.9\mathrm{GHz}} \simeq 2.4$ for a starburst; here we have 2.4 ± 1.5). Whatever the true explanation, in this case the most likely statistical identification is with the central radio source which also coincides with the faint I-band and K-band emission. Nevertheless, the additional presence of the brighter radio source to the south is also not expected by chance, suggesting some sort of physical association.

LE 850.16: a clear radio source, aligned with an ERO. The formal significance of the submm-radio association falls just above $P = 0.05$; however, inspection of Fig. 3.2 suggests that the submm centroid appears to be closer to the radio source than suggested by the position derived by S02 and even a slight move in this direction would be enough to make the submm–radio association statistically convincing. The brightest I-band source and another ERO to the NW — a plausible blue/red galaxy association — have no radio counterparts.

LE 850.17: conceivably the 1 ± 1 expected source with a submm position in error by more than $8''$. Within the adopted error circle this is one of only three definite radio blank fields, but a clear radio source, associated with a bright galaxy, lies $10''$ to the NE. However, the IR image reveals an ERO close to the submm centroid. It is not detected at 1.4 GHz but we consider this the more likely source of the submm emission.

LE 850.18: a clear and statistically compelling radio counterpart, roughly aligned with the faintest part of what may be a complex multi-component galaxy visible in I. Deep IR imaging and optical/IR spectroscopy may yield a robust counterpart and a redshift, but caution is advised since the lessons learnt through the case of LE 850.7 show that the 1.4-GHz emission could plausibly be lobe of a radio galaxy, the other lobe being to the NE at R.A. $10^{\mathrm{h}}51^{\mathrm{m}}58.91 \pm 0.^{\mathrm{s}}04$, Dec. $+57°23'30.1 \pm 0.''3$ (J2000).

LE 850.19: a radio blank field, but a fairly bright object lies close to the submm centroid, with $I - K \sim 3.1$ — a plausible host galaxy.

LE 850.21: a typical counterpart consisting of a pair of galaxies, one blue faint I-band galaxy and one red, radio-detected ERO a few arcseconds to the east. Despite the relative faintness of the submm source, the submm-radio association is statistically compelling.

N2 850.1: three potential radio counterparts, none of which are expected by chance. This object has been discussed in depth by Chapman et al. (2002b). Spectroscopy with Keck-II/ESI revealed a redshift of 0.84 for the bright, compact optical galaxy aligned with the brightest knot of radio

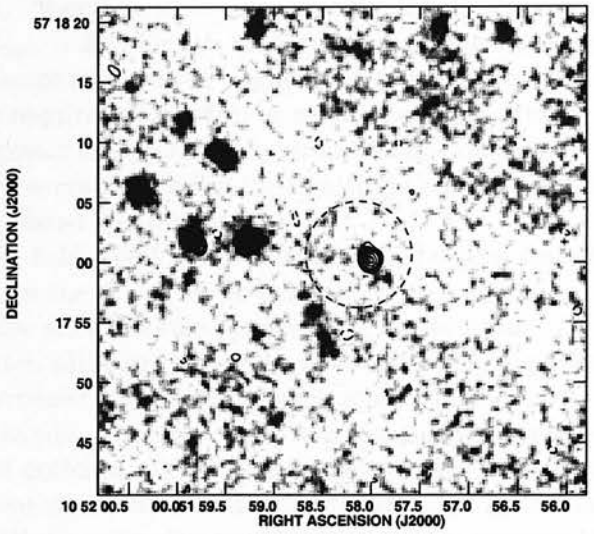

Figure 3.4: Radio and optical properties of LE 850.3: $40'' \times 40''$ greyscale of the I-band emission, smoothed with a $0.3''$ FWHM Gaussian, centred on LE 850.3, with 1.4-GHz contours at $-3,3,4,5,6,8,10 \times 9\,\mu\mathrm{Jy\,beam^{-1}}$. We identify a bright radio counterpart aligned with an ERO, which shows a distorted/multi-component morphology in the I-band image, indicative of a merging or dust-obscured system. The dashed circle represents the 95 per cent submm positional confidence ($\sim 8''$ radius).

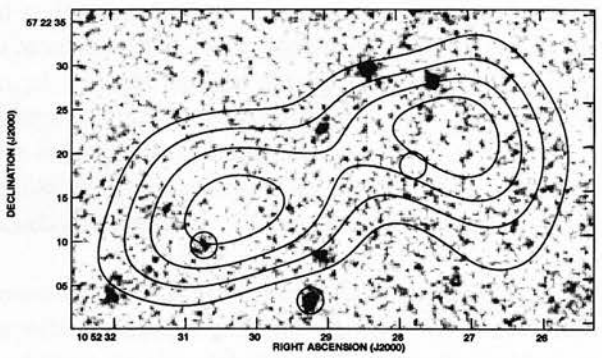

Figure 3.5: K and 850-μm properties of LE 850.6 and the $3.48\,\sigma$ source to the west: greyscale of the K emission, smoothed with a $0.3''$ FWHM Gaussian, with 850-μm contours at 3,4,5,6 $\times$ 2.5 mJy beam^{-1}. The radio source is aligned with faint, similarly-shaped distorted/multi-component galaxy visible in I- and K-bands. The 850-μm contours show a $3.48\,\sigma$ source missed in the original S02 catalogue, with a robust 1.4-GHz counterpart but no optical or IR emission. Small ($2''$) circles represent robust sources detected at 1.4 GHz.

emission (Chapman et al. 2002c). A weak K-band extension was detected in the direction of the extended radio emission. Together with unreasonable 450-/850-μm and submm/radio spectral indices (which require $T_{\rm dust} \sim 23\,{\rm K}$ for $z = 0.845$), this was taken as strong evidence for lensing of the faint background submm source by a bright foreground galaxy (see also Dunlop et al. 2002). CO observations will be required to confirm or refute the association.

N2 850.2: a strong, compact and statistically robust radio counterpart with no optical counterpart to the limits of our observations in VRI, but with rather complex, multi-component K-band emission — an ERO, or class-I counterpart.

N2 850.3: a radio blank field. Very faint emission can be seen near the submm centroid, becoming steadily brighter in the $R \rightarrow I \rightarrow K$ bands.

N2 850.4: two alternative submm-radio associations, the brighter of which is more statistically significant than the fainter, although the latter is also formally significant and lies closer to the submm centroid. The favoured identification is a strong, compact radio source with well-aligned emission in the optical bands. Emission in K is more morphologically complex and is slightly offset from the radio and optical ($\sim 0.5''$) — a composite blue/red galaxy pair.

N2 850.5: two alternative weak, but apparently statistically significant radio counterparts, but no clear sign of optical/IR emission. Deeper IR imaging may uncover the counterpart.

N2 850.6: an extremely complex field in the radio, with many 2 and $3\,\sigma$ peaks near the submm position, but with none of these individually representing a formally significant submm–radio association. Similarly complicated in the optical bands, although the presence of faint VRI emission just to the east of the submm centroid, with the K-band offset by a few arcseconds, suggests that the counterpart is a composite blue/red galaxy pair.

N2 850.7: a clear and statistically unambiguous radio counterpart, slightly resolved at 1.4 GHz, with well-aligned (if complex) optical and IR emission.

N2 850.8: a weak but statistically significant radio counterpart to the south is coincident with a compact galaxy (also detected by *Chandra* at X-ray energies — Almaini et al. 2002). The ring galaxy to the SE cannot be ruled out as the submm source and may well be related to the *Chandra* galaxy.

N2 850.9: two potential radio counterparts, both formally significant, with the more significant source just east of the submm centroid being statistically favoured as the correct ID. This source is aligned with the centre of a bright optical galaxy. The galaxy's optical morphology is not well reproduced in the IR, where the surface brightness is low. Spectroscopy and CO observations are required to confirm or refute the association.

N2 850.10: a weak possible radio counterpart to the SE of the submm position which just falls above the $P < 0.05$ association threshold. The only obvious optical object does not coincide with this radio peak.

N2 850.11: at radio wavelengths this is a blank field within the adopted error circle. This is possibly a second source with a submm position in error by more than $8''$, since a bright radio source, associated with a bright and morphologically-complex optical galaxy $11''$ to the SW.

N2 850.12: a very weak potential radio counterpart, but not a formally significant radio–submm association. However a plausible red ($R - K \sim 4.3$) counterpart is present, with several $3\,\sigma$ 1.4-GHz peaks in the vicinity.

N2 850.13: an obvious and statistically unambiguous radio counterpart, aligned well with a faint ERO. Spectroscopy of an optical system to the west, which appears to possess several related components, may yield the redshift of the SCUBA galaxy if this is a composite blue/red system similar to SMM J14011+0252, as suggested for the blue and ERO counterparts to SMM J14009+0252 (Ivison et al. 2000b, 2001).

N2 850.15: only a single, statistically unconvincing radio peak is found within the error circle.

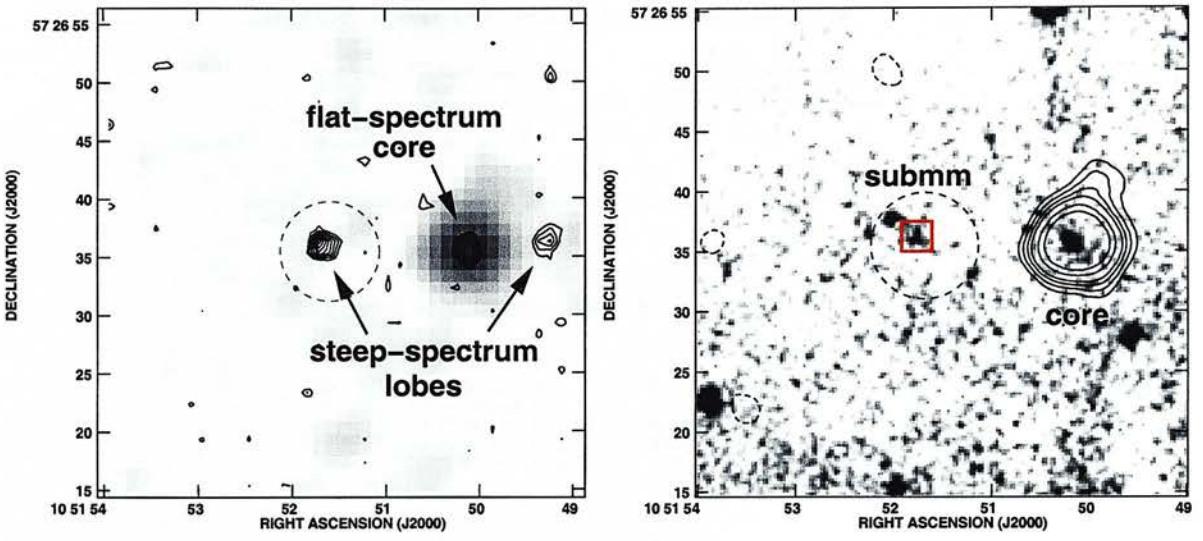

Figure 3.6: Radio and optical properties of LE 850.7: *left*, $40'' \times 40''$ greyscale of the 4.9-GHz emission, centred on LE 850.7, with 1.4-GHz contours at 2,3,4,5,6,8,10 $\times\sigma$; *right*, $40'' \times 40''$ greyscale of the I-band emission, smoothed with a $0.3''$ FWHM Gaussian, with 4.9-GHz contours plotted at $-3,3,4,5,6,8,10 \times 9\,\mu\mathrm{Jy\,beam^{-1}}$. The dashed circle represents the 95 per cent submm positional confidence ($\sim 8''$ radius) and the red box contains the ERO portion of the counterpart pair of blue and red galaxies. Morphologically, this system appears very similar to LE 850.3, with the submm source associated with an optically faint counterpart. However, in this case the 1.4-GHz emission has an extremely steep spectrum and another source is apparent, with an inverted spectrum, to the west of the submm source, with a further weaker steep-spectrum source visible beyond that: the characteristics of a double-lobed radio galaxy. See text for discussion.

No convincing optical identification, and no K-band data currently available.

3.4.2 Summary of Optical/IR characteristics

Of the 30 sources in our refined sample, 18 have statistically robust radio identifications. We robustly identify another one counterpart based on a combination of extreme optical/IR colours and faint radio emission (LE 850.4). A further source, LE 850.17, is blank in the radio but has an ERO counterpart which we consider the correct identification. Finally, a minor and very plausible shift in the submm centroid for LE 850.16 (see Fig. 3.1), a radio-detected ERO, would make its submm–radio association very much more significant. In total, therefore, we have localised the submm emission for 21 of the 30 sources in our sample. We list the basic properties of the sources in our two fields in Table 3.

For the seven other sources with statistically uncompelling radio associations and the two remaining radio blank fields we find only one counterpart, N2 850.12, with a colour/morphology which supports the identification. It is difficult to identify the correct counterpart in the absence of a well-determined position for the submm emission and so for those systems (at least those without unusually red counterparts) it is not possible to conclude reliably that they are truly blank, or whether the sources simply have colours indistinguishable from those of the field galaxy population.

Table 3.3: Fractions of sample in different categories.

Category /Field	Radio classification[1]			Optical/IR counterparts to robust radio associations		
	Robust	Faint	Blank	Normal	E/VRO	Blank
Lockman	10	5	1	4	6	0
ELAIS	8	4	2	3	4	1
Total	18	9	3	7	10	1

Notes: (1) LE 850.16 is classified as 'faint' here, adopting the S02 submm position for consistency.

Table 3.4: Classification of host galaxies.

Class	Optical/IR Magnitude	Description
0	$I > 26$ and $K > 21$	No plausible counterpart
I	$I > 26$ and $K \leqslant 21$	$I - K > 5$ (ERO)
II a	$I \leqslant 26$ and $K \leqslant 21$	Pure starburst
II b	$I \leqslant 26$ and $K \leqslant 21$	Type-II (narrow-line) AGN
II c	$I \leqslant 26$ and $K \leqslant 21$	Type-I (broad-line) AGN

For the 21 sources with *reliable* radio identifications, or extreme colours, we can make a complete inventory of the optical/IR properties of their host galaxies. For these galaxies we show in Fig. 3.7 the distribution of radio-confirmed host galaxies on the $(I-K)$–K colour-magnitude plane. This figure demonstrates the wide variety of colours and magnitudes seen for the host galaxies of submm sources, spread across a factor of 15× in their IR fluxes (compared to only a factor of 3× in their submm fluxes) and encompassing a broad range in colours, similar to that seen for the field population, although typically slightly redder. In terms of the classification scheme for SCUBA galaxies (Table 4) we see that most of the galaxies are scattered across the Class I/II boundaries — more so than the Smail et al. (2002a) submm lens sample, partly because our large-diameter photometric apertures result in less extreme colours. In particular, several sources occupy the $(I-K) = 4$–5 region, conspicuously blank previously. These class as EROs using the colour definition adopted here, but are not quite Class-I sources. Our optical and IR data are not sufficiently deep to encroach on Class-0 territory. Among the potentially interesting statistics to be gleaned from this exercise is the fraction of submm sources with host galaxies which exhibit very red optical/IR colours, and the fraction of these red galaxies that have no radio counterparts, i.e. those with potentially large redshifts.

The IR and optical data for ELAIS N2 are reasonably well matched in terms of conclusively identifying VRO/ERO counterparts, although both datasets would need to be 1–2 magnitudes deeper to match the statistics available for the lensed Smail et al. (2002a) sample. Based on the photometry in Table 2 we conclude that at least two of the ELAIS submm sources are EROs: N2 850.2 and N2 850.13. N2 850.4 has a VRO component offset slightly from the radio and optical emission; N2 850.8 and N2 850.12 also classify as VROs. In Lockman, Lutz et al. (2001) show that LE 850.1 is an ERO, the complex morphology of which is confirmed by deep K-band imaging from the Gemini telescope (Dunlop et al., in preparation). LE 850.3, LE 850.4, LE 850.7, LE 850.16, LE 850.17 and LE 850.21 are also EROs. The LE 850.2 field contains an ERO and a VRO, but only the latter is within the 95 per cent positional confidence region. Of all the VROs and EROs, only LE 850.17 and N2 850.12 are undetected in our deep radio images (though note that LE 850.16 has two plausible ERO host galaxies, only one of which is radio-detected). These may prove to be amongst the most distant sources in the sample, although N2 850.12 is a relatively faint submm source. Hence, at least 43 per cent of submm galaxies imaged to $K = 20.5$–21 are associated with VROs or EROs. Most of these are detected at radio wavelengths. Of the 18 submm galaxies with accurate radio positions, 33 [55] per cent have ERO

[and/or VRO] counterparts, the vast majority with $K < 20$. We would have expected only two EROs (5 per cent) to fall within $8''$ of our submm centroids by chance (Smith et al. 2002).

For the sample with robust submm–radio associations we find a relatively small fraction of submm sources which are blank in the optical/IR – only one example (6 per cent). However, trying to determine the proportion of submm sources in the full sample which are blank in the optical/IR is much more difficult in the absence of a well-determined position for the submm source. Thus, in principle, all of the radio-undetected submm sources could be fainter than our detection limit in the optical/IR – raising the proportion of blank fields for the full population to a possible maximum of 43 per cent.

In summary, we find that almost a third of our sample of submm sources have ERO counterparts. In terms of the breakdown of counterparts between those which are detected in the optical, but have unremarkable colours, and those which are blank, we can only reliably estimate this for the radio-detected subsample: we find that 39 per cent have blue, optically bright ('normal') counterparts and 6 per cent are blank. These represent lower limits on the proportions in the full population. We conclude that the proportions of optically bright, ERO and blank counterparts in our sample are: 39–72:22–27:6–43 per cent, where the ranges reflect the uncertainty of identifying the host galaxies to the radio-undetected or IR-unobserved submm sources. Clearly the uncertain nature of the radio-undetected fraction of the submm population dominates our conclusions. These proportions should be compared to the 20:20:60 per cent split between optically bright, EROs and blank counterparts in the smaller sample of (typically fainter) lensed submm galaxies from Smail et al. (2002a).

In terms of the morphological properties of the sample, of the 21 sources for which we possess reliable positions based on radio detections and/or extreme colours we have the following breakdown of optical characteristics:

- six are blank fields, or too faint ($I \gtrsim 24$) to be categorised morphologically;
- twelve are distorted or close multiple systems;
- two are compact;
- one galaxy appears to be a bright, low-redshift spiral, with another bright galaxy $9''$ to the north: N2 850.9, although we note that this is the configuration most commonly associated with galaxy-galaxy lens candidates (Chapman et al. 2002b). We categorise this latter source, in a distance-independent manner, as another multiple system.

We thus find that 60 per cent of the radio-detected sub-sample are distorted/multiples, 30 per cent are very faint/blank, and the remaining 10 per cent are compact. The data also reveal a strong tendency for submm sources to have plausible optical sources very close *but not coincident* with the strongest 1.4-GHz emission (e.g. LE 850.1, LE 850.8, LE 850.12, LE 850.14, N2 850.13). Many of these systems appear to be composite obscured/unobscured mergers: relatively blue galaxies with faint very red or ERO components aligned with the 1.4-GHz emission in cases where it is detected (LE 850.1, LE 850.3, LE 850.7, LE 850.8, LE 850.17, LE 850.21, N2 850.4, N2 850.13). Looking at clustering of the field galaxies in our I-band images we estimate that typical $I = 22$–25 galaxies have a companion within $5''$, compared to the 2–$3''$ separation of the components in the 'composite' host galaxies we have noted. We therefore expect that most of these pairs represent real physical systems, although it is conceivable that the optical counterparts in a small number represent foreground galaxies lensing the more distant submm source (Chapman et al. 2002d). However, we expect most are related galaxy pairs and these systems thus resemble the well-studied SCUBA galaxies SMM J02399−0136 and SMM J14011+0252, where Ivison et al. (2001b)

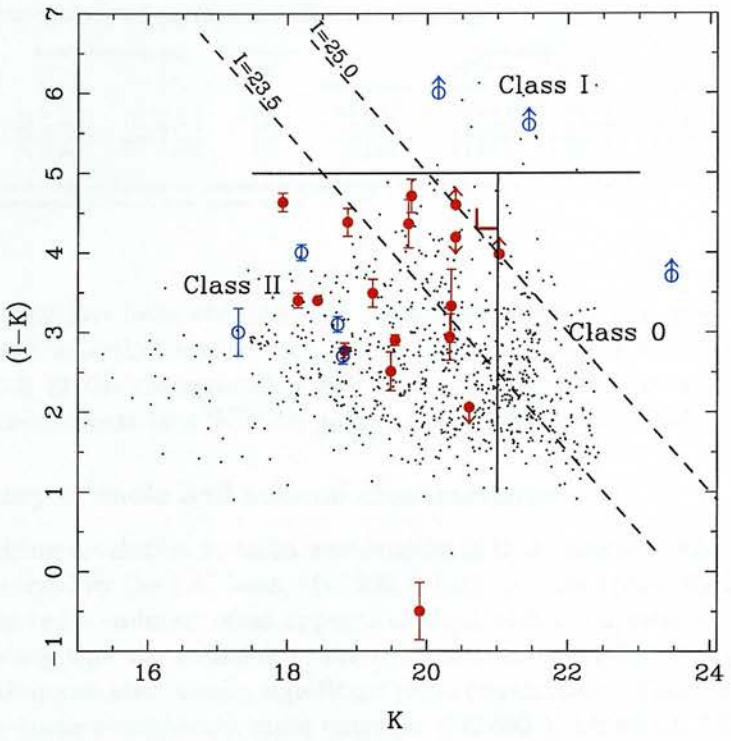

Figure 3.7: Colour-magnitude $(I-K)$–K plane showing the radio-identified host galaxies from the 8-mJy survey (red) and the submm lens survey (blue — Smail et al. 2002a). The latter have been corrected for lens amplification. For comparison, we have plotted the distribution of a deep K-selected field sample (black — L. Cowie, priv. comm.). The host galaxies to the SCUBA galaxies in our sample are highly diverse, exhibiting a wide range of (typically red) optical/IR colours and magnitudes. The boundaries of the counterpart classification scheme proposed by Ivison et al. (2000a) and Smail et al. (2002a) are delineated.

argued that the diverse optical/IR properties of the host galaxies arises from a complex mix of obscuration and star formation. Our adoption of a large-diameter aperture for our photometric measurements means that the colours of these systems in Table 2 are less extreme than would have been measured for the reddest components in each galaxy (cf. Smail et al. 2002a).

One effect of these composite sources is to increase the fraction of distorted/pairs at the expense of faint or blank fields. This leaves essentially a 65:25:10 per cent split between distorted/multiple sources, faint/blank fields, and compact sources, which may mean that virtually all of them will be found to be distorted/multiple sources once deeper optical/IR data become available.

Another important consequence of the frequency of blue/red galaxy pairs is that a large fraction of the radio-detected 8-mJy sample is sufficiently bright to permit spectroscopy on 8-m class telescopes. Around 90 per cent of those detected in the radio have optical ($I \lesssim 25$) or IR ($K \lesssim 20$) host galaxies. The case for conventional spectroscopy grows stronger still when one takes in to account the spectroscopic properties of known SCUBA-selected galaxies (Ivison et al. 1998, 2000; Chapman et al. 2001a), i.e. bright, spatially extended Lyman α emission lines, often with extremely large equivalent widths (Chapman et al. 2002c). It should also be stressed

Table 3.5: Potential X-ray counterparts to Lockman East submm sources.

Source name	X-ray position (J2000) α h m s	δ ° ′ ″	Positional error[1] ″	Band fluxes[2] /10^{-15} erg s^{-1} cm^{-2} $S_{0.2-0.5\,\mathrm{keV}}$	$S_{0.5-2\,\mathrm{keV}}$	$S_{2-5\,\mathrm{keV}}$	$S_{5-12\,\mathrm{keV}}$	Significance in 2-5 keV band
LE 850.4	10 52 04.11	+57 25 28.1	3.0	0.1 ± 0.2	0.0 ± 0.3	0.9 ± 0.3	2.7 ± 20.0	3.7
LE 850.8	10 52 00.09	+57 24 23.2	1.0	0.2 ± 0.1	1.2 ± 0.2	2.6 ± 0.5	15.2 ± 4.8	9.5
LE 850.12	10 52 07.37	+57 19 04.2	2.3	0.0 ± 0.5	0.5 ± 0.2	1.5 ± 0.6	6.4 ± 6.1	3.9
LE 850.14	10 52 03.95	+57 27 06.8	2.0	0.0 ± 0.4	0.2 ± 0.1	1.2 ± 0.4	0.8 ± 17.0	4.9

Notes: (1) 90 per cent statisitical uncertainty on the position. Residual systematic offsets ($\leq 1''$) between the X-ray and radio astrometric frames have not been included. (2) Count rates were converted to fluxes assuming power-law X-ray spectra with $S_\nu \propto \nu^{-0.7}$.

that once spectroscopy has been obtained for these host galaxies it is possible to confirm the relationship between the optical and submm sources by searching for strong CO emission in the mm/radio wavebands at the corresponding redshift. This provides the only reliable test of the identification of a counterpart to a SCUBA galaxy (e.g. Frayer et al. 1998, 1999).

3.4.3 Summary of radio and submm characteristics

The most surprising revelation at radio wavelengths is that several of the most obvious radio counterparts are resolved by the 1.4″ beam (N2 850.7, LE 850.6, and possibly LE 850.8, N2 850.13 and LE 850.16). The radio emission often appears to align with the optical/IR morphology of the counterpart, suggesting that the emission in the two wavebands is related. As noted in §3.2, five sources have more than one statistically significant radio counterpart. There is a suspicion in four further cases of low-surface-brightness radio emission (N2 850.5, LE 850.4, LE 850.9, LE 850.17): several 2–3 σ features covering tens of arcsec^2. We created smoothed 1.4-GHz images (2″, 2.5″, 3″ FWHM) to investigate this further but cannot confirm their reality with any authority.

Resolved sources point to radio-emitting regions within the galaxies on scales of $\sim 1''$, equivalent to $\gtrsim 10$ kpc at $z \geq 1$. The implication is that the submm emission from these galaxies also extends over similar scales, either as multiple bright components or as a more uniform region. In our view, the spatial extent of this emission argues strongly that the submm emission from these galaxies is powered by a widespread starburst with an intensity and spatial scale far larger than that seen in local starbursts. This conclusion is supported by the similarity of the morphology of the radio and optical/IR emission in several cases.

Perhaps less surprisingly, given the supposed diversity of the submm population (Ivison et al. 2000), three sources have spectral indices more consistent with radio-loud AGN cores or lobes than with star-forming galaxies (LE 850.3, LE 850.7 and LE 850.12). A further two (LE 850.14 and LE 850.18) are plausibly related to radio-loud AGN. We note that this acts as a warning against extrapolating from shorter wavelengths (typically 4.9 GHz) before attempting to estimate redshifts from the submm/radio spectral indices (e.g. Eales et al. 1999). We comment later on the possible prevalence of AGN in the 8-mJy sample based on radio and X-ray properties.

The discovery of resolved radio counterparts has consequences for any surveys at this resolution, or higher, that intend to address $N(z)$ for the submm galaxy population using the radio/submm spectral index discussed in the next sub-section. Adopting upper limits set using the standard 3 σ recipe, where σ is the rms noise level, may risk underestimating the flux limit in a significant number of cases, thus overestimating the true redshift limits. To test the possible extent of this problem we have compared the fluxes of the most extended radio sources in our deep map (1.4″ FWHM) against those measured using *only* B-configuration data (5″ FWHM). Comparing sources common to both maps we find that compact sources have similar fluxes but that the largest sources — those with deconvolved angular sizes above 6″ — have fluxes which can be as much as 30 per cent higher in the low-resolution map. Checking the radio fluxes of our brightest submm counterparts, we find no correction is necessary. Our approach, nevertheless,

has been to set radio upper limits on faint or undetected sources at $5\,\sigma$ from the deep radio map to mitigate against the possible flux bias effect. We note that the only sure method to ensure maximum sensitivity to large structures in the radio maps is by taking data on short baselines — a difficult task given the prevalence of radio-frequency interference, both man-made and solar.

Related to previous discussion of extended radio emission, if a significant fraction of submm sources are extended on scales of tens of kpc then the interplay of heating/cooling mechanisms may yield different characteristic dust temperatures, probably lowering $T_{\rm dust}$. One of the most important addenda to the technique of redshift estimation discussed in the next section has been the realisation that there is a degeneracy between redshift and $T_{\rm dust}$ (Blain 1999): it is impossible to differentiate between a cool $z = 0.5$ galaxy ($T_{\rm dust} \sim 20\,{\rm K}$) and a warmer galaxy at $z = 2$ ($T_{\rm dust} \sim 40\,{\rm K}$), for example (the degeneracy is effective up to $\sim 60\,{\rm K}$ — Blain et al. 2002). Hence, if the typical dust temperatures in the submm sources are lower (Efstathiou & Rowan-Robinson 2002) or higher (Blain & Phillips 2002) than expected, this will impact on redshift estimates based on inappropriate spectral templates. The most common template SED has been that of the local ULIRG, Arp 220, which lies $1\,\sigma$ above the mean temperature for galaxies from the local *IRAS*-selected survey by Dunne et al. (2000b). If one adopts an Arp 220-like template SED then the resulting redshift distribution will be biased to the high end if there is a significant population of cool submm-selected galaxies, as hinted by the discovery of luminous, cold galaxies amongst a 175-μm-selected *FIRBACK*, SCUBA-detected sample (Chapman et al. 2002d). This bias would arise because the 850-μm selection band falls longward of the dust's spectral peak (Eales et al. 2000). We return to this point in the next section.

In conclusion, the existence of resolved radio counterparts can be taken as evidence that the submm galaxy population may be bi- or tri-modal: a combination of warm, compact ULIRG-related systems, a scattering of dust-obscured radio-loud AGN and, finally, a population of extended starbursts. A sizeable population of cool, spatially-extended starbursts (e.g. Eales et al. 2000; Chapman et al. 2002d) would require alterations to the templates used to calculate redshifts from radio/submm spectral indices, shifting $N(z)$ considerably and possibly forcing a re-evaluation of the use of local ULIRGs as templates for studying the distant SCUBA population.

3.4.4 Summary of X-ray characteristics

Four potential X-ray counterparts were found, to the sources LE 850.4, LE 850.8, LE 850.12 and LE 850.14, and details are given in Table 5. N2 850.8 was detected by *Chandra* and is discussed by Almaini et al. (2002). The X-ray emission near LE 850.14 is associated with a radio source to the north and is not likely to be the correct identification of the submm source, although it could be related. All the *XMM-Newton* counterparts were detected in the 2–5 keV band with $> 3.5\,\sigma$ significance, but they were not all detected in the other energy bands. They have fluxes of $1 - 3 \times 10^{-15}\,{\rm erg\,s^{-1}\,cm{-}2}$ and show a deficit of soft X-ray flux which implies that their X-ray emission is absorbed by significant column densities.

3.4.5 Redshift constraints from the radio/submm spectral index

As we have stressed, a fair fraction of the 8-mJy sample (especially the radio-detected sources) have optical counterparts which can be realistically targeted with efficient spectrographs on 8-m class telescopes. However, there is currently no published optical spectroscopy on any of these host galaxies. While we look forward to correcting this situation, we are currently restricted in our analysis to using cruder redshift estimators – in particular the radio/submm spectral index, $\alpha^{850\mu{\rm m}}_{1.4{\rm GHz}}$. Hughes et al. (1998) and Carilli & Yun (1999, 2000, hereafter CY) were the first to point out that the ratio of radio-to-submm flux density is a strong function of redshift, at least out

Table 3.6: Redshifts for the refined 30-source 8-mJy sample derived from the radio/submm spectral index using three SED templates.

Source name	Mean $z \pm \sigma$ (DCE)	Mean $z \pm \sigma$ (CY)	Mean $z \pm \sigma$ (RT)
LE 850.1	$2.2^{+0.4}_{-0.3}$	$2.7^{+1.3}_{-0.9}$	$3.4^{+1.1}_{-0.9}$
LE 850.2	$3.5^{+0.9}_{-0.7}$	$4.6^{+3.2}_{-1.7}$	$5.3^{+1.5}_{-1.3}$
LE 850.3	$1.7^{+0.4}_{-0.4}$	$1.9^{+0.9}_{-0.6}$	$2.6^{+0.9}_{-0.7}$
LE 850.4	≥ 3.2	≥ 4.3	≥ 5.0
LE 850.5	≥ 3.3	≥ 4.4	≥ 5.1
LE 850.6	$2.5^{+0.6}_{-0.4}$	$3.2^{+1.8}_{-1.1}$	$4.0^{+1.3}_{-1.0}$
LE 850.7	$1.6^{+0.4}_{-0.4}$	$1.8^{+0.9}_{-0.6}$	$2.4^{+0.8}_{-0.6}$
LE 850.8	$1.8^{+0.4}_{-0.4}$	$2.0^{+1.0}_{-0.7}$	$2.7^{+0.9}_{-0.7}$
LE 850.12	$0.8^{+0.2}_{-0.1}$	$1.0^{+0.5}_{-0.4}$	$1.4^{+0.5}_{-0.4}$
LE 850.13	≥ 3.5	≥ 4.7	≥ 5.4
LE 850.14[1]	$1.8^{+0.4}_{-0.4}$	$2.0^{+1.0}_{-0.7}$	$2.7^{+0.9}_{-0.7}$
LE 850.16	$2.2^{+0.4}_{-0.3}$	$2.7^{+1.4}_{-0.9}$	$3.5^{+1.1}_{-0.9}$
LE 850.17	≥ 3.4	≥ 4.6	≥ 5.3
LE 850.18	$1.8^{+0.4}_{-0.4}$	$2.1^{+1.0}_{-0.7}$	$2.8^{+0.9}_{-0.7}$
LE 850.19	≥ 2.6	≥ 3.4	≥ 4.2
LE 850.21	≥ 2.4	≥ 3.0	≥ 3.8
N2 850.1	$2.2^{+0.4}_{-0.3}$	$2.7^{+1.4}_{-0.9}$	$3.5^{+1.1}_{-0.9}$
N2 850.2	$2.0^{+0.4}_{-0.3}$	$2.4^{+1.2}_{-0.8}$	$3.1^{+1.0}_{-0.8}$
N2 850.3	≥ 2.4	≥ 3.1	≥ 3.9
N2 850.4[1]	$0.9^{+0.3}_{-0.2}$	$1.2^{+0.6}_{-0.4}$	$1.7^{+0.6}_{-0.4}$
N2 850.5[1]	$1.5^{+0.4}_{-0.4}$	$1.8^{+0.8}_{-0.6}$	$2.4^{+0.8}_{-0.6}$
N2 850.6	≥ 2.5	≥ 3.2	≥ 4.0
N2 850.7	$1.4^{+0.4}_{-0.3}$	$1.6^{+0.8}_{-0.5}$	$2.2^{+0.7}_{-0.6}$
N2 850.8	$1.5^{+0.4}_{-0.4}$	$1.8^{+0.9}_{-0.6}$	$2.4^{+0.8}_{-0.6}$
N2 850.9[1]	$2.0^{+0.4}_{-0.3}$	$2.4^{+1.2}_{-0.8}$	$3.2^{+1.1}_{-0.8}$
N2 850.10	$1.8^{+0.4}_{-0.4}$	$2.1^{+1.0}_{-0.7}$	$2.8^{+0.9}_{-0.7}$
N2 850.11	≥ 2.2	≥ 2.8	≥ 3.6
N2 850.12	≥ 2.0	≥ 2.4	≥ 3.2
N2 850.13	$1.5^{+0.4}_{-0.4}$	$1.7^{+0.8}_{-0.6}$	$2.3^{+0.8}_{-0.6}$
N2 850.15	≥ 2.0	≥ 2.3	≥ 3.0

Note: (1) For sources with more than one radio counterpart, we have used the combined fluxes of all radio detections with $P < 0.05$ in Table ??, consistent with our policy of generating a conservative $N(z)$.

to $z \sim 3$. The technique has since been revised, adapted or commented upon by Blain (1999), Barger, Cowie & Richards (2000), Dunne, Clements & Eales (2000a, hereafter DCE), Rengarajan & Takeuchi (2001, hereafter RT) and Yun & Carilli (2002).

We have estimated the redshifts for the 8-mJy galaxies from their 850-μm and 1.4-GHz flux densities. For radio non-detections, or sources weaker than 45 μJy (25 μJy in Lockman), we have used a conservative $5\,\sigma$ limit at 1.4 GHz. This was intended to take into account the possibility that some sources have fallen below the formal detection threshold because they are extended relative to the beam, as discussed in §4.3: our intention is to produce a conservative redshift distribution, building on the fact that mis-identifications and AGN-related radio emission both tend to skew $N(z)$ to lower values, as will the excision of six bright sources from our sample (§3.3). In Fig. 3.8 we show the three different models for the behaviour of the 850-μm/1.4-GHz spectral index as a function of redshift which were used, including the semi-analytic model by CY. The DCE and RT models are based on a complete sample of 104 empirical spectral energy distributions (SEDs) from the SCUBA Local Universe Galaxy Survey (SLUGS — Dunne et al. 2000b). The latter model takes into account free-free self-absorption and the effect of the far-IR luminosity, $L_{\rm FIR}$, on the 850-μm/1.4-GHz spectral index. The redshift ranges for the 8-mJy sources, as allowed by the rms uncertainties of the three models considered here, are summarized in Table 6. There is a significant overlap between the different redshift estimators, but individual redshifts are clearly not well constrained, especially in the light of the large scatter seen in current spectroscopically-confirmed submm samples (Fig. 3.9).

The cumulative redshift distribution, $\Sigma N(z)$, for the 8-mJy sample is shown in Fig. 3.9 for the mean CY redshift estimator (solid black line). For clarity we have left out the corresponding distributions based on the DCE and RT models, but they display a similar overall shape and agree within the raw statistical errors. The CY model predicts that 0:23:43:34 per cent of the

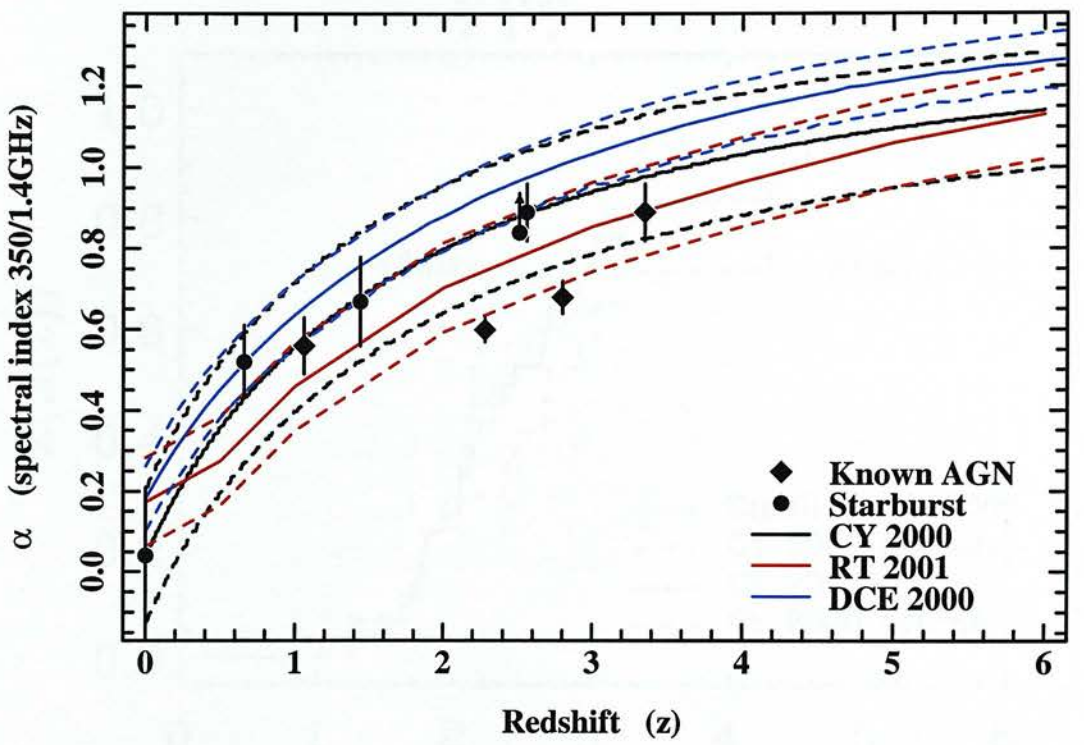

Figure 3.8: Spectral index between 1.4 GHz and 850 μm ($\alpha_{1.4\mathrm{GHz}}^{850\mu\mathrm{m}}$) as a function of redshift, z, as predicted by the work of Carilli & Yun (2000) [black], Dunne et al. (2000) [blue] and Rengarajan & Takeuchi (2001) [red]. Dashed lines represent the rms uncertainties; filled circles represent dusty starbursts with known redshifts (e.g. Dey et al. 1999; Ivison et al. 2000); filled diamonds represent AGN (e.g. Ivison et al. 1998; Ledlow et al. 2002). Those submm galaxies with reliable redshift measurements clearly follow the trend to higher spectral indices at higher redshifts in the manner predicted by the models. However, the large spread in redshift at a fixed spectral index highlights the care which must be taken when interpreting redshift constraints from this technique.

sources lie at $z < 1$, $1 \leq z < 2$, $2 \leq z \leq 3$ and $z > 3$. The median redshifts for the 8-mJy sample based on the DCE, CY and RT models are 2.0, 2.4, and 3.2, respectively. While the CY and DCE models predict that 20–40 per cent of submm-selected galaxies lie at $z \leq 2$, the RT estimator yields < 10 percent. The most important effect on the predicted $\Sigma N(z)$ is thus revealed as the SED template. The order of progression from the lowest to the highest redshift distributions (DCE $\rightarrow$ CY $\rightarrow$ RT) is not surprising since the model templates derived by the three groups are based on SEDs that are progressively more luminous. This is illustrated by the fact that the CY and RT curves are in closest agreement with the measured spectral indices of spectroscopically identified starbursts in Fig. 3.8, although again we stress the large scatter and the potential biases in these comparisons from selection effects.

The fundamental conclusion, reached on the basis of the *most conservative* radio/submm constraints, i.e. using $5\,\sigma$ limits and the DCE spectral template, is that the bright submm galaxy population lies at $< z > \geq 2.0$. Using spectral templates more representative of known submm galaxies yields $< z > \geq 2.4 \pm 0.5$ (where the error includes the bootstrap estimate of the uncer-

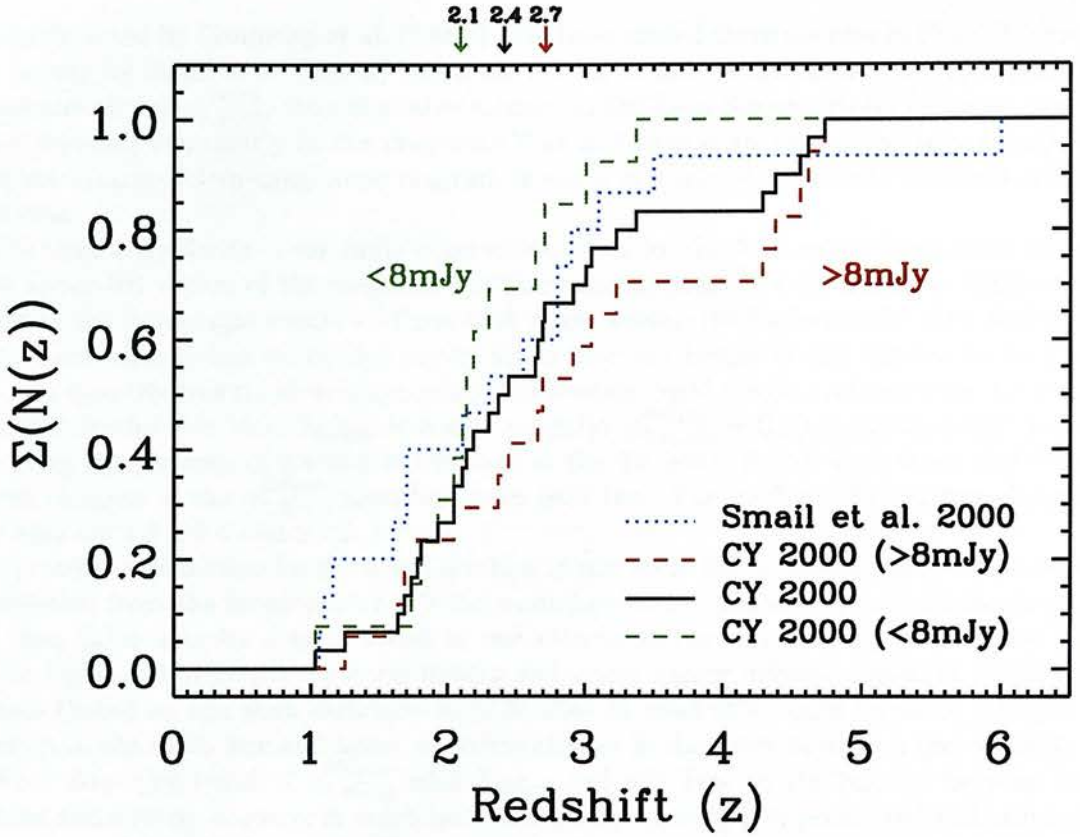

Figure 3.9: Cumulative redshift distribution, $\Sigma N(z)$, of the 8-mJy sample as deduced from the spectral index between 1.4 GHz and 850 μm using the CY redshift estimator from Fig. 3.8 [solid black]. For comparison, $\Sigma N(z)$ for the complete SCUBA lens survey by Smail et al. (2000, 2002a) has also been plotted [dotted blue]. $\Sigma N(z)$ for ≥ 8 and $\leq$8-mJy submm sources are plotted as red and green dashed lines, respectively (assuming the CY model): those we expect to be more luminous based on our tentative interpretation of Fig. 3.10 are seen to have a distribution skewed to significantly higher redshifts than the overall sample.

taintly in the median redshift of the sample, ± 0.3, but is dominated by systematic errors arising from the choice of SED, which we conservatively estimate to be ± 0.4). It is worth noting that if we had refined our sample more severely in §3.3, e.g. excising sources with $\sigma_{850\mu m} > 2.5$ mJy, $<z>$ would remain unchanged. In the next section we discuss apparent differences in the median redshift of the submm population as a function of 850-μm flux density.

3.5 Discussion

3.5.1 Trends in source properties

In Fig. 3.10 we present the submm/radio colour-magnitude diagram (CMD) for the 8-mJy survey. Arrows indicate lower limits on the submm/radio ratio at 5σ radio detection thresholds. We also plot sources from the surveys by Hughes et al. (1998), Smail et al. (2002a), Serjeant et al. (2002), and the 13 radio-selected sources in the HDF with submm counterparts brighter than

3.5 mJy detected by Chapman et al. (2002e). We have circled three sources in Fig. 3.10 from the Lens Survey by Smail et al. (2002a) which are known to host AGN. As one would expect, these sources have lower $\alpha_{1.4\mathrm{GHz}}^{850\mu\mathrm{m}}$ than the other sources in the Lens Survey. Note, however, that they do not separate out clearly in the diagram. This indicates that, except for very strong AGN, the submm/radio colour-magnitude diagram is not a powerful discriminant between AGN and starbursts.

The sensitivity limits of the radio observations used in Fig. 3.10 define a selection boundary in the upper-left region of the diagram, but there also appears to be a deficit of bright submm sources in the lower-right region — those with a low submm/radio flux ratio. Any such sources should have been picked up by our survey since they are bright in the submm as well as the radio. To quantify this trend we have calculated bootstrapped median values of the 1.4-/850-μm spectral index for two bins, $S_{850\mu\mathrm{m}} < 8$ and > 8 mJy: $\alpha_{1.4\mathrm{GHz}}^{850\mu\mathrm{m}} = 0.83 \pm 0.03$ and 0.91 ± 0.04 — confirming the presence of a trend in the data at the $2\,\sigma$ level. Errors were estimated from 100 random samples of the $\alpha_{1.4\mathrm{GHz}}^{850\mu\mathrm{m}}$ distribution in each bin. The median 850-μm flux densities in these bins are 4.8 ± 0.4 and 9.2 ± 0.3 mJy.

A possible explanation for the trend is a bias in our radio flux measurements due to resolving out emission from the larger sources. If the more luminous submm sources have larger angular sizes then there may be a weak trend in our measurements which would make these appear to have higher submm/radio spectral indices and hence higher inferred redshifts. However, we estimate (based on the work described in §4.3) that at most this would result in a 20 per cent reduction in the radio flux and hence a modest change in the spectral indices ($\delta\alpha \sim 0.03$).

What does this trend of $\alpha_{1.4\mathrm{GHz}}^{850\mu\mathrm{m}}$ with $S_{850\mu\mathrm{m}}$ tell us? Due to the balance between cosmic dimming and a steep, negative K correction, submm flux density is expected to be almost entirely independent of redshift for $z \gtrsim 1$. The submm flux thus provides us with a gauge of L_{FIR}. The trend we see therefore reflects differing behaviour in the intrinsically low- and high-luminosity SCUBA populations. As discussed earlier, the 1.4-GHz/850-μm spectral index is sensitive to both redshift and the form of the dust SED of the galaxy, parameterised in terms of T_{dust} and dust emissivity index, β. There are thus several possible causes of this trend: 1) 1.4-GHz/850-μm spectral indices mostly reflect differences in the form of the dust SEDs, with a decreasing T_{dust} at higher luminosities or equivalently a decrease in β; 2) a bias in submm surveys in favour of colder objects at a given L_{FIR} and z; 3) 1.4-GHz/850-μm spectral indices are tracking the source redshifts and we are seeing a tendency for the most luminous submm sources to lie at higher redshifts.

Taking the first possible cause, we note that locally there appears to be little evidence for systematic variations in the properties of obscured galaxies: the scatter of 0.2 dex in the observed radio/far-IR correlation (Helou et al. 1985) can be accounted for by the dispersion in T_{dust} and β. This is supported by results for the SLUGS sample of bright *IRAS* galaxies (DCE), where the radio/far-IR correlation was found to be independent of L_{FIR} and T_{dust}. Although it has been pointed out (CY; DCE) that in the rest frame there is a strong dependence of $\alpha_{1.4\mathrm{GHz}}^{850\mu\mathrm{m}}$ on L_{FIR}, for sources at $z \gtrsim 1$ the effect is likely to be small since submm observations probe the far-IR regime. Furthermore, any effect of L_{FIR} on the spectral index may be compensated by a decrease in radio emission due to self-absorption in luminous sources. The main concern about this findings is that the strong constraints really only apply to dusty galaxies with FIR luminosities of $\log L_{\mathrm{FIR}} = 9$–$11\,\mathrm{L}_{\odot}$, lower than those expected for the galaxies in our sample. Therefore there remains the possibility that the most luminous, obscured galaxies have a strong luminosity–temperature relation which is driving the trend in Fig. 3.10.

If, instead, we ascribe the trend to redshift, we have a situation where the *apparently* brightest sources are also the most distant. This rather unusual situation would reflect very strong

luminosity evolution in the submm-selected galaxy population, with a model where high-redshift sources are typically more luminous than local sources. This trend may also be reflected in Fig. 3.9 where the cumulative redshift distribution of ≥ 8-mJy sources is plotted in red (assuming the CY model). The sources which we expect to be more luminous based on our tentative interpretation of Fig. 3.10 are seen to have a distribution skewed towards higher redshifts than the overall sample: $<z> = 2.7$ for ≥ 8 mJy, cf. $<z> = 2.4$ for all sources and $<z> = 2.1$ for <8 mJy (close to the distribution found for the faint Cluster Lens Survey — Smail et al. 2000, 2002a). Similar behaviour was predicted by Chapman et al. (2002e) who reproduced the submm/radio CMD using a mock population of 50-K SEDs and adopting a luminosity function $\Phi(L,\nu) = \Phi_0(L/g(z), \nu(1+z))$, with a power-law evolution function $g(z) = (1+z)^4$ out to $z = 3$ and $g(z) = (1+z)^{-4}$ for $z > 3$.

To distinguish between these scenarios we look for other supporting evidence in the properties of the host galaxies to the submm sources in our survey. We plot in Figs 3.11, 3.12 and 3.13, the variation in the key observables for the submm population: K-band magnitude, $(I-K)$ colour and K-band-to-1.4-GHz flux ratio. For each of these figures we compare the distributions of submm galaxies with 850-μm fluxes above and below 8 mJy.

We start by examining the distribution of sources in Fig. 3.11. There appears to be a very weak correlation between K magnitude and spectral index, with the fainter counterparts typically having higher spectral indices. This tentative correlation arises primarily because of the absence of bright K-band counterparts ($K < 19$) for submm sources with high spectral indices, $\alpha_{1.4\mathrm{GHz}}^{850\mu\mathrm{m}} > 0.85$. This deficit contrasts with the distribution seen for sources with $\alpha_{1.4\mathrm{GHz}}^{850\mu\mathrm{m}} < 0.85$ where over half of the K-band counterparts are brighter than $K \sim 19$. Looking next at the distribution of the sources divided on the basis of morphology or submm flux density, there is no strong differentiation between the classes (apart from the trivial conclusion that faint/blank-field sources have faint K-band magnitudes). The main conclusion from this figure is that submm sources with higher spectral indices are generally fainter at K, suggesting that these galaxies are either more distant (in support of our earlier hypothesis) or more obscured.

Next we look at the variation in $(I-K)$ colour with spectral index in Fig. 3.12. For simple stellar populations, $(I-K)$ increases monotonically with redshift, providing a crude redshift estimate (Lilly et al. 1999). The first thing to note is that the submm counterparts are generally redder than the $(I-K) = 2.6$ typically seen for the field population at $K < 21$, suggesting again that they are either more distant or more obscured than galaxies in the field. However, beyond that, the impression gained from Fig. 3.12 is that there is no strong correlation between $(I-K)$ and $\alpha_{1.4\mathrm{GHz}}^{850\mu\mathrm{m}}$, either for the whole sample, or when divided into submm flux bins. We suggest that the mix of dust and young and old stellar populations expected in these systems makes the interpretation of their optical-IR colours complex and highly model-dependent (e.g. Ivison et al. 2001). This is illustrated by the broad distribution shown by the dominant population of distorted/multiple host galaxies. These composite systems, are by their nature, unlikely to be well-described by a simple stellar population model. However, two of the other morphological classes do warrant mention: two of the bluest sources have very compact morphologies, suggestive of the presence of an AGN; the two faint galaxies which, from the radio and submm observations are expected to be at the highest redshifts ($\alpha_{1.4\mathrm{GHz}}^{850\mu\mathrm{m}} \sim 1.1$) are also the two reddest galaxies in the sample, $(I-K) > 5.2$. We conclude that the simplest interpretation of the $(I-K)$ colours of the submm host galaxies points to a complex and diverse population.

Finally, we investigate the variation in IR-to-radio fluxes as a function of spectral index, Fig. 3.13. The 2.2-μm/1.4-GHz flux density ratio is relatively insensitive to source redshift since the spectral slope in both wavebands is very similar. Instead, this ratio should provide a good measure of the relative flux in the optical and far-IR, and hence a redshift-independent measure

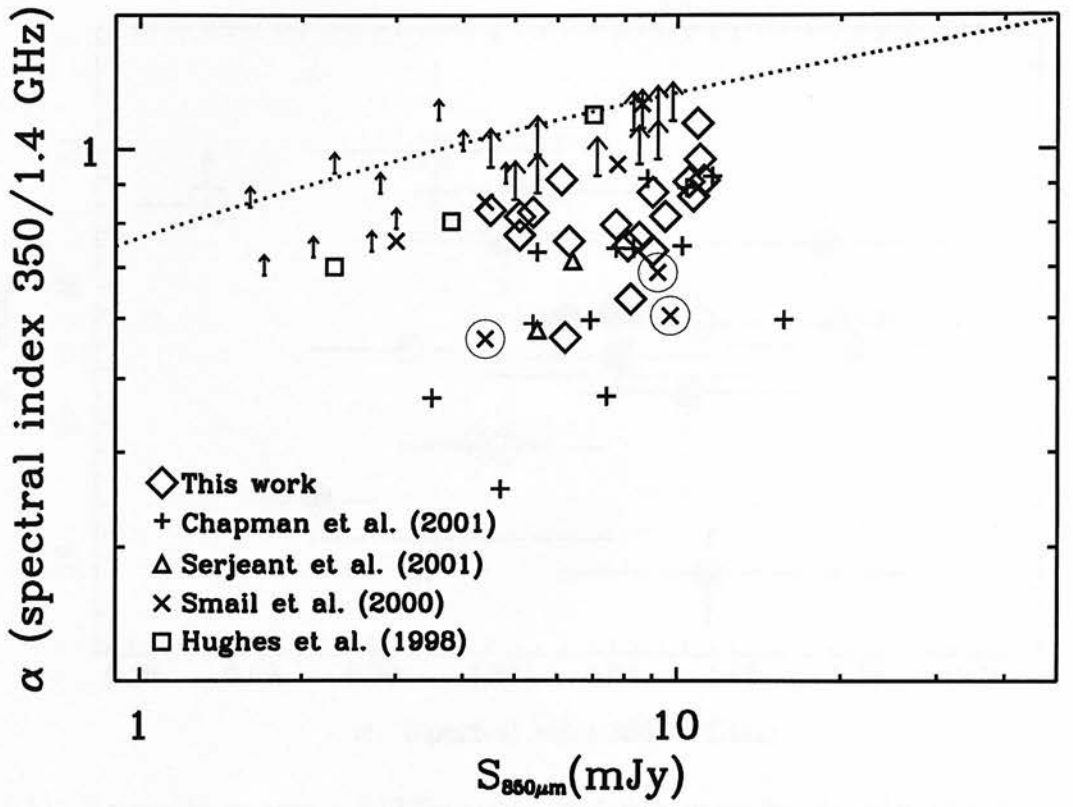

Figure 3.10: Spectral index between 1.4 GHz and 850 μm ($\alpha_{1.4\mathrm{GHz}}^{850\mu\mathrm{m}}$) versus $S_{850\mu\mathrm{m}}$ colour-magnitude diagram for the 8-mJy survey [large arrows for lower limits]. Also plotted are sources from the HDF submm field (Hughes et al. 1998; Serjeant et al. 2002; Dunlop et al. 2002; Chapman et al. 2001b, 2002e) and the Cluster Lens Survey (Smail et al. 2000, 2002a) [small arrows for lower limits]. Some of the brightest 850-μm objects (circled) are known to host radio-loud AGN (Ivison et al. 1998, 2000). The dotted line represents the 3σ limit of our radio survey in Lockman.

of the obscuration (Soifer, Houck & Neugebauer 1987). In Fig. 3.13 we find that submm sources with distorted or multi-component morphologies cover a broad region in the centre of the figure, with a hint that those with brighter submm fluxes typically have lower values of 2.2-μm/1.4-GHz. This suggests that the more luminous systems are more obscured than the fainter sources. Looking at the remainder of the population, those sources that are faint or blank in K span a similar range in 2.2-μm/1.4-GHz flux ratio to the morphologically complex sources but typically have higher $\alpha_{1.4\mathrm{GHz}}^{850\mu\mathrm{m}}$, indicating that they are probably more distant (but similarly obscured) analogues of the multi-component sources. The lack of large variations in the distribution of sources on this plane (with either K-band magnitude or submm flux) suggests that obscuration is not responsible for the trend seen in Fig. 3.11 and that instead this must reflect redshift differences.

In summary, due to the small number of sources and the large scatter in the population, one cannot unambigously say that Figs 3.11, 3.12 and 3.13 confirm the luminosity evolution scenario suggested above. However, looking at the optical and IR properties of the submm galaxies we do find some differences which are consistent with high-spectral-index sources lying at higher

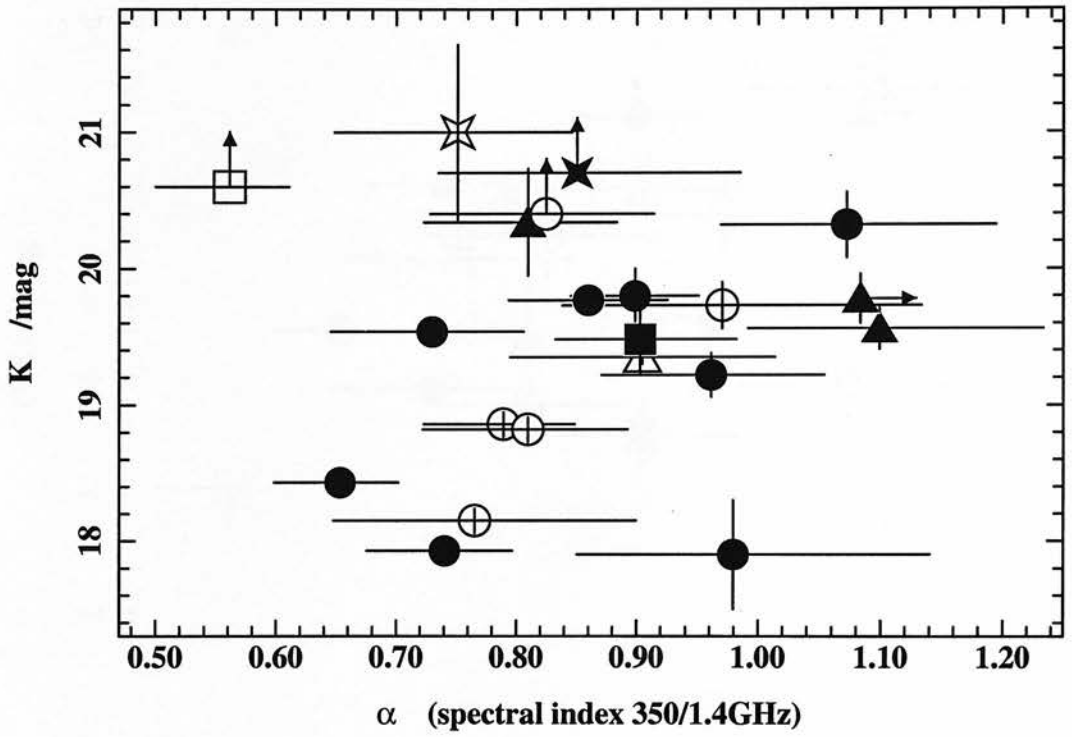

Figure 3.11: K magnitude versus 1.4-/850-μm spectral index for the fraction of the 8-mJy sample with robust counterparts. Symbols represent different morphologies and 850-μm flux densities: circles are multiple/distorted; squares are compact; triangles are very faint; stars are blank fields; $S_{850\mu m} \geq 8\,\mathrm{mJy}$ [solid]; $S_{850\mu m} < 8\,\mathrm{mJy}$ [open].

redshifts, as required by the luminosity evolution model.

3.5.2 Comparison with galaxy-formation models

How do these results compare to current theoretical expectations? Several groups working with semi-analytic galaxy-formation models are attempting to include the effects of dust obscuration and hence predict the properties of galaxies selected in SCUBA surveys. One self-consistent and well-developed model is that discussed by Lacey et al. (2002). This model incorporates the GRASIL dust code of Silva et al. (1998) and Granato et al. (2000) in the galaxy-formation framework of Cole et al. (2000). The original Cole et al. model had difficulty producing enough luminous submm sources (as discussed in §1); however, by tuning it so that it can fit the submm counts, it has provided useful insights into the characteristics necessary to successfully reproduce the SCUBA population. The main changes made to the model to allow it to fit the counts of SCUBA sources are: (i) increase the amount of gas in mergers at high redshifts (Blain et al. 1999a) by adopting a longer timescale for star formation in disks at high redshifts than in the Cole et al. model and (ii) adopt a top-heavy IMF for the starbursting phase (Blain et al. 1999c). With these two changes, the model can reproduce the observed number counts at 850 μm from 0.5–10 mJy as well as the integrated flux in the background seen by *COBE* (Lacey et al. 2002).

The model predicts that dusty starbursts undergoing major mergers dominate the submm

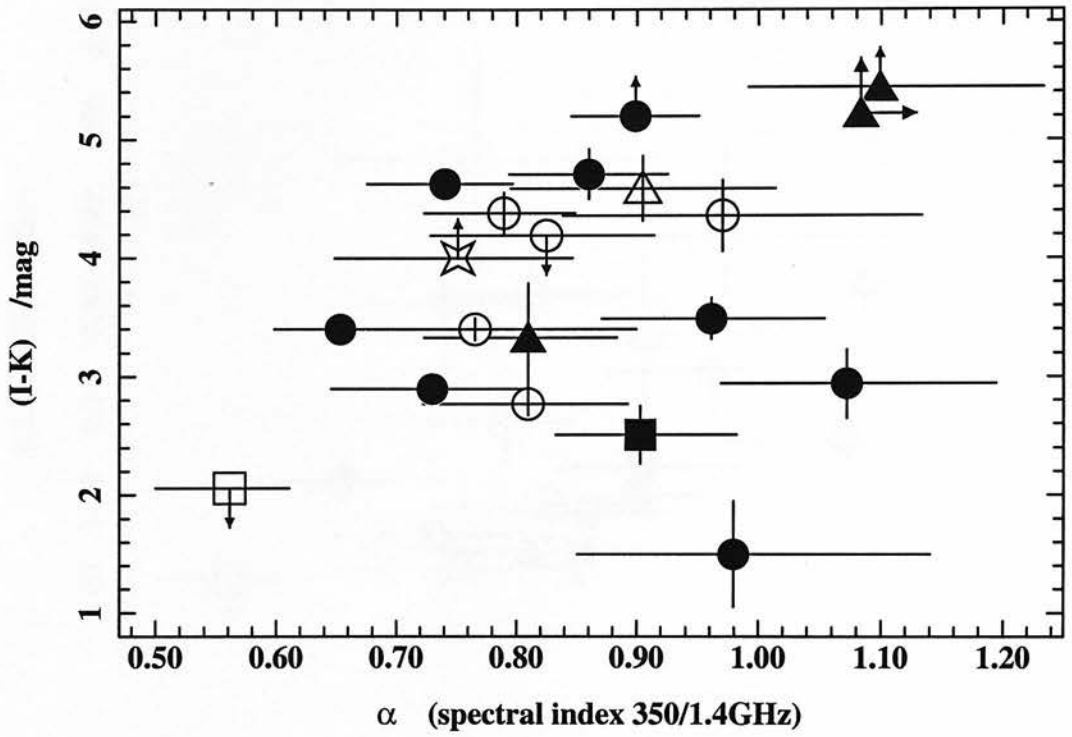

Figure 3.12: $(I - K)$ colour versus 1.4-/850-μm spectral index for the fraction of the 8-mJy sample with robust counterparts. Symbols are explained in Fig. 3.11.

counts at ≥ 0.3 mJy. In particular, for a sample limited at an 850-μm flux density of 8 mJy the model predicts a median redshift of $z = 2.5$ with a width of $\delta z = \pm 1$ (Lacey et al. 2002). This is in reasonable agreement with the results we find in §4.5, providing some support for the model. However, there is little change in the median redshift of the population with submm flux between ~ 0.1 and 8 mJy, in contrast to the results presented in §4.5 and Fig. 3.9. An advantage of the semi-analytic models is that they provide a framework to interpret the relationship between different classes of galaxies at high and low redshifts. For example, in this model the SCUBA galaxies are expected to evolve into typically massive galaxies lying in the highest density regions seen in the local Universe, i.e. luminous ellipticals in rich clusters. In terms of the high-redshift populations, we are most interested in the relationship between the SCUBA and Lyman-break (LBG) populations. Here, Lacey et al. (2002) suggest that these represent a time sequence — both classes arise from merger-induced starbursts: SCUBA sources represent the earliest dust-obscured phase, $\lesssim 50$ Myr, and the LBGs represent more evolved post-burst systems. There are also small differences in the halo and stellar masses of the typical members of the two populations, with SCUBA galaxies on average being 3–10$\times$ more massive and residing in dark matter halos with masses of 1–2 $\times 10^{12}\,M_{\odot}$ (consistent with dynamical estimates from CO observations, Frayer et al. 1998, 1999).

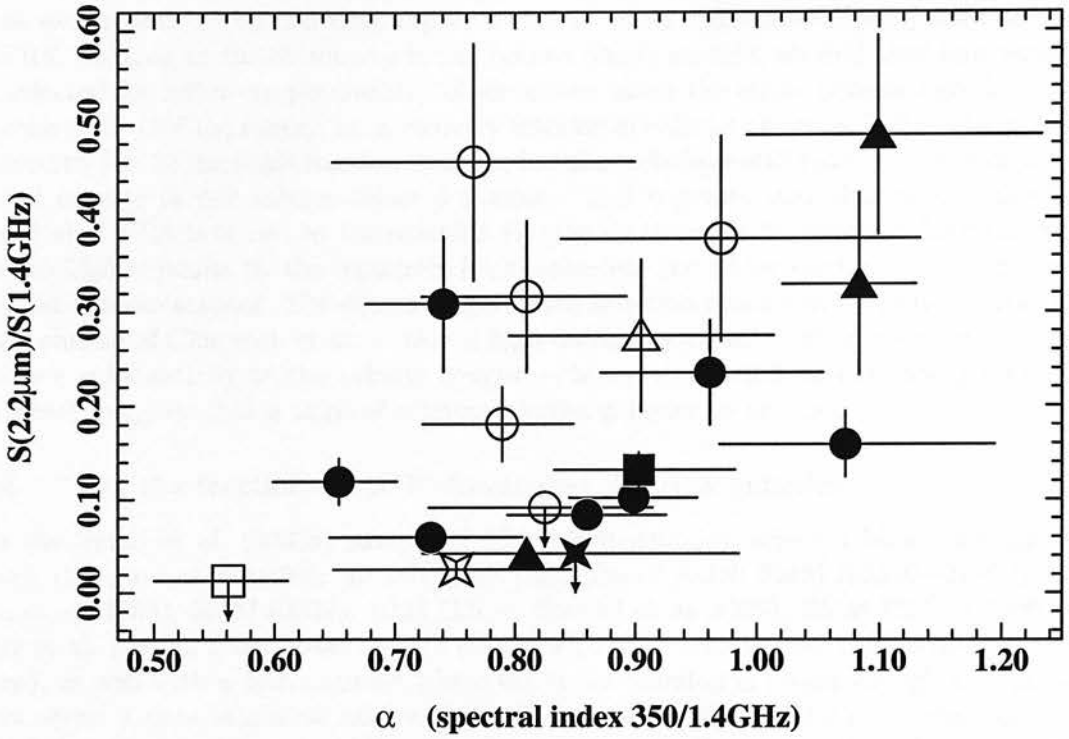

Figure 3.13: 2.2-μm/1.4-GHz flux density ratio versus 1.4-/850-μm spectral index for the robust sub-sample of 8-mJy sources. Symbols are explained in Fig. 3.11.

3.5.3 Comparison to radio-pre-selected SCUBA samples

Barger et al. (2000) and Chapman et al. (2001b) discuss a technique designed to improve the detection rate of submm galaxies: pre-selection of optically faint radio sources (OFRS, $S_{1.4\mathrm{GHz}} \geq 40\,\mu$Jy, $I > 25$ within $2''$), which exploits SCUBA's time-saving photometry mode. Chapman et al. (2001b) argue that their sample is representative of the 850-μm population brighter than 5 mJy with $z \leq 3$, and that the redshift distribution ($<z>\sim 2$), arrived at via the radio/submm technique employed in §4.3, is inconsistent with the existence of a high-redshift ($z > 4$) population of primeval galaxies contributing substantially to the submm counts. This conclusion is, of course, heavily dependent on the fraction of the blank-field submm counts that are recovered by the OFRS selection technique. If the fraction is low, then conclusions based on OFRS samples are not necessarily relevant to the entire submm-selected galaxy population. Chapman et al. (2001b) estimate that around 75 per cent of bright submm sources are typically recovered through radio pre-selection (cf. Chapman et al. 2002f), based on a comparison of their counts with those in blank-field surveys, although there is considerable uncertainty in this fraction.

The 8-mJy survey together with the radio imaging presented here give us the ideal tool to deduce the typical recovery fraction: measurements of the same fields at submm and radio wavelengths. In what follows, we search within $8''$ of the 8-mJy sample submm positions for radio sources peaking above $4\,\sigma$ with integrated fluxes above $30\,\mu$Jy ($15\,\mu$Jy for Lockman), then check for optical counterparts, $R < 25.5$ or $I < 25$. A submm source without a radio counterpart (or a

submm source with an optical counterpart within 2″ of its radio counterpart) does not class as an OFRS. Looking at the 30 sources in the refined 8-mJy sample, we find that four would have been selected for follow-up photometry observations using the strict criteria laid down for the Chapman et al. (2001b) survey, i.e. a recovery fraction of only 13 per cent. If the I-band criterion is relaxed to $I > 24$ then this fraction doubles, but the technique still recovers $\lesssim$ half of the radio-detected sources in our submm-selected sample. This suggests that the redshift distribution deduced via OFRS is biased to *low* redshifts ($z \leq 3$) by to the radio selection function, but also biased to *high* redshifts by the 'optically faint' criterion, the latter accounting for the loss of $\gtrsim$ half of the submm sources. The effects of the OFRS selection process are clearly far from simple. The conclusion of Chapman et al. — that a high-redshift population of primeval galaxies cannot contribute substantially to the submm counts — is not supported by our radio/submm-based $N(z)$ which suggests that a third of submm-selected galaxies lie at $z > 3$.

3.5.4 On the fraction of AGN-dominated SCUBA galaxies

In the Smail et al. (2002a) sample of 15 submm galaxies, selected blind through lensing clusters, there are at least four unambiguous examples of AGN: SMM J02399−0136 (L1/L2 — Ivison et al. 1998), SMM J02399−0134 (L3 — Soucail et al. 1999), SMM J22471−0206 (P4 — Barger et al. 1999b), SMM J04431+0210 (the ERO, N4 — Smail et al. 1999; Frayer et al. 2002, in prep), as well with a fifth example where the radio emission is bright enough to raise serious doubts about a pure starburst nature, SMM J14009+0252 (the ERO J5 — Ivison et al. 2000, 2001). The AGN fraction, even without the ability to probe Compton-thick AGN, is at the $\sim$30 per cent level.

Three submm sources (LE 850.4, LE 850.8 and LE 850.12) have 2–5 keV X-ray counterparts detected with *XMM-Newton*; another, N2 850.8, was detected by *Chandra*. All show a deficit of soft X-ray flux which implies that their X-ray emission is absorbed by significant column densities. Assuming the sources are at $z > 1$, and making no correction to the 2–5-keV fluxes for absorption, all of them have 2–10-keV luminosities in excess of $10^{42.6}$ erg s^{-1}. The X-ray emission almost certainly comes from obscured AGN, because such luminosities exceed by more than a factor of 10 that of the most X-ray luminous starburst currently known (NGC 3256; Moran, Lehnert & Helfand 1999), and because the lack of soft X-ray flux rules out a substantial contribution from superwinds, which are ubiquitous in luminous starburst galaxies (Read & Ponman 1998).

Assuming that about 5 per cent of an AGN's bolometric luminosity is emitted between 2 and 10 keV (Elvis et al. 1994), the weakness of the observed X-ray emission implies that even though AGN are present, they are not capable of powering the far-IR emission unless they are Compton thick, i.e. unless their X-ray emission is attenuated by column densities $> 10^{24}$ cm^{-2}. If they have column densities $< 10^{24}$ cm^{-2} then even at $z = 5$ their X-ray emission would imply AGN bolometric luminosities that fall short of their far-IR luminosities. Furthermore, the radio-loud AGN population includes a much larger proportion of luminous X-ray sources than the radio-quiet population (Ciliegi et al. 1995); the presence of radio-loud AGN amongst the submm-selected galaxies therefore indicates that they may contain relatively powerful AGN rather than low-luminosity Seyfert galaxies.

We note that half of our sources are either resolved in the radio or have more than one counterpart. This immediately suggests that the emission from these sources is due to starbursts on kpc scales rather than heating by AGN. We also note that even the most obvious AGN in the Smail et al. (2002a) sample is gas rich, with the gas playing a dynamically important role (Frayer et al. 1998). However, we have determined that at least three galaxies from the 8-mJy sample, possibly as many as five, have radio emission consistent with radio-loud AGN. An analogy with

radio surveys of X-ray-selected samples, where less than 10 per cent of AGN are found to be radio loud (e.g. Ciliegi et al. 1995), implies that a very large fraction of the submm-selected galaxies here may contain AGN.

If the AGN fraction of our submm-selected sample can feasibly be approaching unity, contamination by AGN-heated dust is clearly an issue that must be addressed since it will impact directly on our view of cosmic star-formation history. However, the ubiquity of SMBH in the most massive local galaxies, and the scaling of their mass with that of their host bulge, indicates that the formation of a black hole — which will result in AGN activity — may be an important signature of the formation phase of the most massive galaxies at high redshifts. Indeed, the important issue is not the *presence* of an AGN in a SCUBA galaxy, but its contribution to the bolometric luminosity of the system. In this regard, our *XMM-Newton* results suggest that even when an AGN is present, it rarely dominates the bolometric luminosity of the galaxy (Frayer et al. 1998; Alexander et al. 2002). This is consistent with what is known about the energetics of ULIRG-like events in the local Universe, where again emission from the AGN rarely dominate.

In all the cases for which an AGN component has been detected in X-rays, the relative weakness of the X-ray emission below 2 keV implies significant X-ray absorption. The association between X-ray-absorbed AGN and submm sources is also found when following up X-ray sources in the submm: Page et al. (2001) found that 50 per cent of luminous, X-ray-selected, X-ray-absorbed AGN are also submm sources. This is particularly relevant because some models for the formation of SMBH and their host galaxies (e.g. Fabian 1999) predict that X-ray-absorbed AGN will be a generic feature of young spheroidal galaxies. However, the predominance of X-ray absorption amongst the current small sample of X-ray-detected submm sources is completely compatible with what is found in the local Universe (80 per cent absorbed AGN; Maiolino & Rieke 1995). Therefore, at present, X-ray absorption expected during spheroid formation cannot be distinguished from the X-ray absorption expected from AGN unification schemes.

We conclude, following Ivison et al. (1998, 2000), that the fraction of SCUBA galaxies hosting AGN may be high; however, current evidence suggests that AGN rarely dominate the bolometric emission. We are therefore confident that the bolometric luminosities of the SCUBA population primarily reflect dust-obscured massive star formation.

3.5.5 Star-formation history inferred from submm and radio observations

Numerous attempts have been made to derive the cosmic star-formation history. These efforts were originally restricted to deep UV/optical surveys (e.g. Lilly et al. 1996; Connolly et al. 1997; Madau et al. 1996; Cowie, Songaila & Barger 1999; Steidel et al. 1999) and relied on several assumptions: that the IMF is universal; that the emitted UV light is proportional to the SFR; that extinction by dust is neglible or, in later attempts, can be corrected for. The existence of a heavily obscured galaxy population is clear from the energy in the submm extragalactic background, which is comparable to the background at UV and optical wavelengths. Locally the ratio between the amount of light emitted by galaxies in the far-IR and optical wavebands is significantly smaller than that measured from the background, suggesting an early period of dust-enshrouded star formation (cf. Adelberger & Steidel 2000). With the data presented here, we can begin to quantify this star formation.

Given the large number of sources in our sample we can afford to divide the sample into redshift bins and determine the star-formation rate (SFR) in each co-moving volume element. Next, we need to estimate the SFR for each source. The radio and far-IR luminosities of a starburst galaxy provide two independent estimates of the SFR. The power emitted at radio wavelengths — a tiny fraction, $< 10^{-4}$, of the bolometric luminosity — is mainly non-thermal

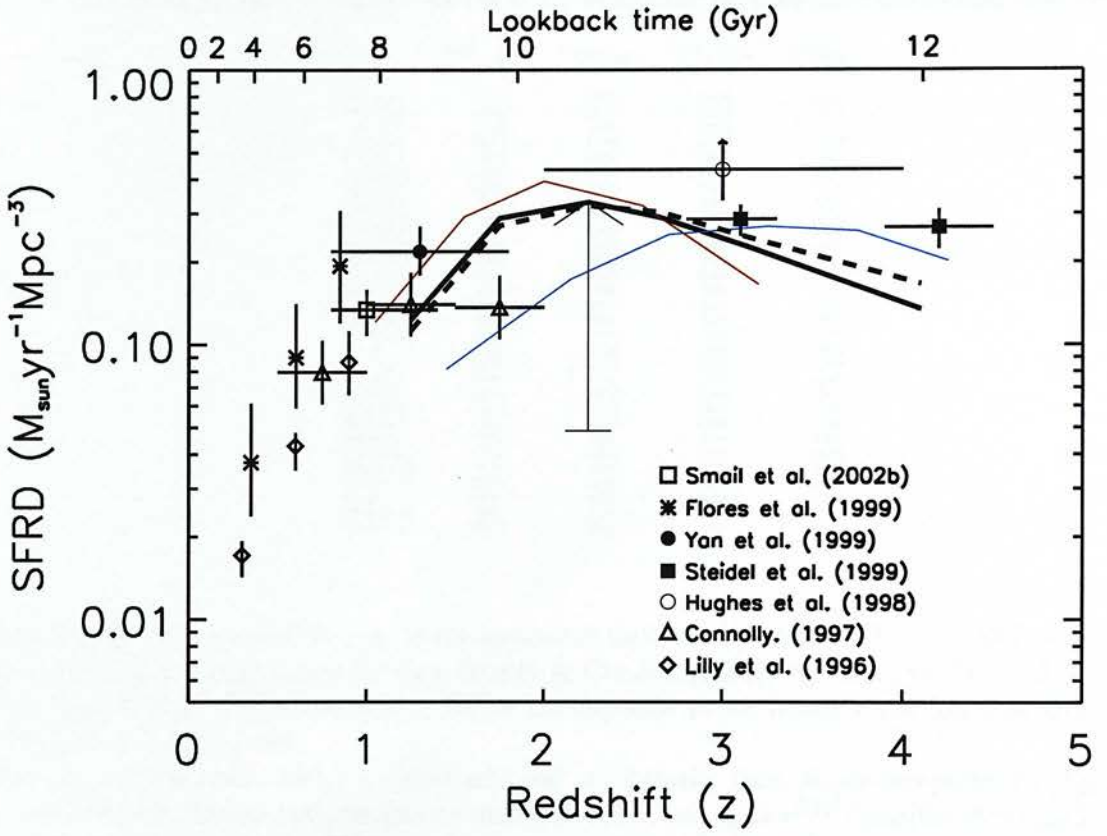

Figure 3.14: Co-moving star-formation rate density (SFRD) versus redshift for an $\Omega_M = 0.3$, $\Omega_\Lambda = 0.7$ and $H_0 = 70\,\mathrm{km\,s^{-1}\,Mpc^{-1}}$ cosmology. The black, red and blue solid lines are the submm-derived SFRDs based on the CY, DCE and RT redshift estimators, respectively. The dashed line indicates the SFRD derived from the radio observations using the CY redshift estimator. Also shown are results derived from optical and IR (Lilly et al. 1996; Connolly et al. 1997; Flores et al. 1999; Yan et al. 1999), radio (Smail et al. 2002b) and submm studies (Hughes et al. 1998). The arrow indicates the extrapolation from the $\sim$8-mJy population down to $\gtrsim$1 mJy.

synchrotron radiation emitted by relativistic electrons accelerated by Type II and Ia supernova remnants. L_{radio} and the SFR are thus linked via massive stars, $\geq 5\,\mathrm{M}_\odot$, and L_{radio} consequently probes very recent star formation (e.g. Condon 1992; Yun & Carilli 2001). L_{FIR} constitutes most of the bolometric luminosity for dust-enshrouded starbursts: almost all the radiation from young OB stars is absorbed by dust and re-radiated, giving a measure of star formation that is largely invisible at optical/UV wavelengths. Combining deep radio and submm observations is therefore a very powerful way of tracing the co-moving star-formation rate density (SFRD) as a function of redshift: with a determination of $N(z)$, it allows for two independent estimates of the SFRD, sensitive to star formation at practically all redshifts. However, since we have used our submm and radio data to derive $N(z)$, the radio- and submm-based SFR measurements are not independent.

In the following, rest-frame 1.4-GHz radio luminosities, $L_{1.4\mathrm{GHz}}$, were computed assuming a spectral index of $\alpha = -0.8$, i.e. $L_{1.4\mathrm{GHz}} = 4\pi D_L^2(z) S_{1.4\mathrm{GHz}} (1+z)^{-(\alpha+1)}\,\mathrm{W\,Hz^{-1}}$, where $D_L(z)$ is

Table 3.7: Star-formation rates in $M_\odot\,yr^{-1}$ for the 8-mJy sample derived from radio and submm observations.

Source name	$SFR_{1.4GHz}$ (CY)	$SFR_{850\mu m}$ (DCE)	$SFR_{850\mu m}$ (CY)	$SFR_{850\mu m}$ (RT)
LE 850.1	1700	1600	1600	1600
LE 850.2	2200	1700	1700	1700
LE 850.3	1100	1200	1200	1200
LE 850.4	1600	1300	1300	1300
LE 850.5	1700	1300	1300	1300
LE 850.6	1900	1700	1700	1700
LE 850.7	1200	1200	1200	1300
LE 850.8	700	800	800	800
LE 850.12	700	700	800	900
LE 850.13	2000	1500	1500	1500
LE 850.14	1300	1400	1500	1500
LE 850.16	1000	900	900	900
LE 850.17	1900	1400	1400	1400
LE 850.18	600	700	700	700
LE 850.19	1000	900	800	800
LE 850.21	800	700	700	700
N2 850.1	1800	1700	1700	1700
N2 850.2	1700	1600	1700	1600
N2 850.3	1500	1300	1300	1300
N2 850.4	1000	900	1100	1200
N2 850.5	1200	1200	1300	1300
N2 850.6	1600	1400	1400	1400
N2 850.7	1200	1300	1300	1400
N2 850.8	700	700	800	800
N2 850.9	1400	1400	1400	1400
N2 850.10	800	800	800	800
N2 850.11	1200	1100	1100	1100
N2 850.12	800	800	900	800
N2 850.13	800	900	900	1000
N2 850.15	800	800	800	800

the luminosity distance and $S_{1.4GHz}$ is the measured flux density at 1.4 GHz. The SFR was then calculated using the calibration by Yun, Reddy & Condon (2001): $SFR(M_\odot\,yr^{-1}) = 5.9 \pm 1.8 \times 10^{-22} L_{1.4GHz}\,W\,Hz^{-1}$. The conversion factor corresponds to an initial mass function $\psi(M) \propto M^{-2.35}$ for $0.1 < M_\odot < 100$.

For our submm-based SFRs we have adopted an optically thin, single-temperature ($T_{dust} = 45\,K$) modified blackbody with emissivity index, $\beta = 1.2$, i.e. $S_\nu \propto \nu^{3+\beta}/[\exp(0.048\nu/T_{dust}) - 1]$, where ν is in GHz. Using this SED template we compute L_{FIR} for each source by integrating the rest-frame spectral luminosity over the wavelength range 40–500 μm. SFRs were then calculated from $SFR = L_{FIR}/5.8 \times 10^9\,M_\odot\,yr^{-1}$, after Kennicutt (1998) who estimates an uncertainty of 20 per cent in the calibration.

For each source, we computed a radio-based SFR using the CY redshift estimator. Submm-based SFRs were found using all three redshift estimators (CY, DCE, and RT). The results are outlined in Table 7. SFRs range from a few hundred to more than a thousand $M_\odot\,yr^{-1}$. Note that the derived SFRs are sensitive to the adopted SED template, in particular to T_{dust}. An increase of 10 per cent in T_{dust} increases the SFR by one third. The SFRDs computed in this way should be taken as lower limits since we are dealing with a survey that skims the top 10 per cent of the submm counts, leaving room for a substantial contribution from less luminous submm sources. To account for this, a correction has been applied to the SFRDs. Assuming that the differental number counts of submm sources are well described by $dN/dS(deg^{-2}\,mJy^{-1}) = 3.0 \times 10^4 S^{-3.2}$ (Barger et al. 1999a), we find a correction factor of ~ 12 down to $S_{850\mu m} > 1$ mJy. In Fig. 3.14 we present the co-moving SFRD as a function of redshift based on the 8-mJy survey. Blue and red lines correspond to submm-based SFR estimates using the most extreme redshift estimators (DCE and RT) whilst the solid and dashed lines use the CY redshift estimator: submm- and radio-based estimates respectively. For comparison we have plotted the SFRD as estimated from μJy radio observations of a sample of EROs in the redshift range 0.8–1.4 (Smail et al. 2002b) and several other optical-, IR- and radio-based estimates. These are consistent with our measurement of the cosmic SFRD and point to a picture in which significant star formation takes place beyond $z \geq 1$. We find star-formation activity in the $z = 1$–4 range at a similar level to extinction-corrected estimates for LBGs (Steidel et al. 1999).

3.6 Concluding remarks

(1) We describe deep 1.4-GHz imaging of the 8-mJy survey regions in ELAIS N2 and Lockman East. These detect 60 per cent of the 30 submm-selected galaxies in our sample, enabling us to constrain the positions of these sources to better than $1''$ and thereby identify host galaxies in other wavebands.

(2) We present new optical and IR imaging and, based on the new positional information from the radio map, we find robust counterparts to 90 per cent of the radio-detected galaxies. Identifications based on colour are made for several more.

(3) At least 60 per cent of the radio-detected optical/IR host galaxies display highly-structured or distorted morphologies, suggestive of merging or interacting systems.

(4) Almost one half of the optical/IR host galaxies are found to contain very or extremely red components. In addition, as many as ten of the optical/IR counterparts are composite systems comprising blue and red components separated by a few arcsec (tens of kpc at the relevant redshifts). The strong internal colour gradients within these systems may be indicative of patchy dust obscuration.

(5) Contrary to popular belief, virtually all of the host galaxies to the radio-detected population are sufficiently bright to justify spectroscopic observations with 8-m telescopes. We caution that redshifts require confirmation via CO detections before optical/IR host galaxies can be considered robust associations.

(6) *XMM-Newton* X-ray data for Lockman are presented, as well as *Chandra* data for ELAIS N2. We detect four submm-selected galaxies, only one of which would have been identified as an AGN via its radio characteristics.

(7) The diversity of the submm galaxy population is highlighted. We identify a beguiling mixture of sources, including eight EROs (one associated with the lobe of a radio galaxy) and two sources with flat-spectrum radio emission.

(8) We find that less than a quarter of the sample would have been recovered by targeting optically faint radio sources, underlining the selective nature of such surveys.

(9) We exploit the radio/far-IR correlation using our well-matched radio and submm data, finding a *conservative* lower limit of $<z>\geq 2.0$ for the median redshift of bright submm-selected galaxies, or $<z>\geq 2.4$ using spectral templates more representative of known submm galaxies.

(10) We find tentative evidence for luminosity evolution, with the brightest sources ($\geq 8\,\mathrm{mJy}$) tending to be the most distant.

(11) Employing our estimated redshift distribution, we find that submm galaxies with $S_{850\mu\mathrm{m}} \sim 8\,\mathrm{mJy}$ play an important role in cosmic star-formation history. They are responsible for a higher star-formation-rate density at $z \sim 1$–4 than the entire galactic zoo manages at $z \sim 0$, and for a similar density as the $z \sim 3$–4 LBG population when extrapolated to $S_{850\mu\mathrm{m}} > 1\,\mathrm{mJy}$.

Acknowledgements

We would like to thank Frazer Owen, Chris Carilli and Bob Becker for their patient and invaluable help during the reduction of the data presented here and the VLA data analysts for their ceaseless endevours. We thank Graham Smith for providing time to gather some of the observations presented here. We acknowledge useful discussions with Carlton Baugh, Carlos Frenk and Cedric Lacey. We are also grateful for data received from the WHT service programme. JSD, CJW, SES, NDR and MJF acknowledge the UK PPARC for funding. DGG acknowledges funding from the Leverhulme Trust. IRS acknowledges support from Royal Society and Leverhulme Fellowships. TRG acknowledges support from the Danish Research Council and from the European Union RTN network, POE.

References

Adelberger K.L., Steidel C.C., 2000, ApJ, 544, 218.
Alexander D.M., Bauer F.E., Brandt W.N., Hornschemeier A.E., Vignali C., Garmire G.P., Schneider D.P., 2002, ApJ, in preparation Almaini O. et al., 2002, MNRAS, in press (astro-ph/0108400).
Archibald E.N., Dunlop J.S., Hughes D.H., Rawlings S., Eales S.A., Ivison R.J., 2001, MNRAS, 323, 417.
Archibald E.N., Dunlop J.S., Friaca A., Jimenez R., McLure R.J., 2002, MNRAS, in press (astro-ph/0108122).
Aretxaga I., Hughes D.H., Chapin E.L., Gaztañaga E., Dunlop J.S., 2002, MNRAS, submitted (astro-ph/0205313).
Assafin M. et al., 2001, ApJ, 552, 380.
Barger A.J., Cowie L.L., Sanders D.B., 1999a, ApJ, 518, L5.
Barger A.J., Cowie L.L., Smail I., Ivison R.J., Blain A.W., Kneib J.-P., 1999b, AJ, 117, 2656.
Barger A.J., Cowie L.L., Richards E.A., 2000, AJ, 119, 2092.
Baugh C.M., Benson A.J., Cole S., Frenk C.S., Lacey C.G., 2001, in 'QSO hosts and their environments', Granada, in press.
Bertoldi F. et al., 2000, A&A, 360, 92.
Blain A.W., 1999, MNRAS, 309, 955.
Blain A.W., Jameson A., Smail I., Longair M.S., Kneib J.-P., Ivison R.J., Kneib J.-P., 1999a, MNRAS, 309, 715.
Blain A.W., Kneib J.-P., Ivison R.J., Smail I., 1999b, ApJ, 512, L87.
Blain A.W., Smail I., Ivison R.J., Kneib J.-P., 1999c, MNRAS, 302, 632.
Blain A.W., Phillips T.G., 2002, MNRAS, 333, 222.
Blain A.W., Smail I., Ivison R.J., Kneib J.-P., Frayer D.T., 2002, Physics Reports, in press (astro-ph/0202228).
Borys C., Chapman S., Halpern M., Scott D., 2002, MNRAS, 330, L63.
Carilli C.L., Yun M.S., 1999, ApJ, 513, L13.
Carilli C.L., Yun M.S., 2000, ApJ, 530, 618 [CY].
Chapman S.C. et al., 2000, MNRAS, 319, 318.
Chapman S.C., Lewis, G.F., Scott D., Richards E., Borys C., Steidel C.C., Adelberger K.L., Shapley A.E., 2001a, ApJ, 548, L17.
Chapman S.C., Richards E.A., Lewis G.F., Wilson G., Barger A.J., 2001b, ApJ, 548, L147.
Chapman S.C., Scott D., Borys C., Fahlman G.G., 2002a, MNRAS, 330, 92.
Chapman S.C., Smail I., Ivison R.J., Blain A.W., 2002b, ApJ, submitted (astro-ph/0204086).
Chapman S.C., Blain A.W., Smail I., Ivison R.J., 2002c, Nature, submitted.
Chapman S.C., Smail I., Ivison R.J., Helou G., Dale D.A., Lagache G., 2002d, ApJ, 573, 66.

Chapman S.C., Lewis G.F., Scott D., Borys C., Richards E.A., 2002e, ApJ, in press (astro-ph/0111157).
Chapman S.C. et al., 2002f, ApJ, submitted.
Ciliegi P., Elvis M., Wilkes B.J., Boyle B.J., McMahon R.G., Maccacaro T., 1995, MNRAS, 277, 1463.
Ciliegi P. et al., 1999, MNRAS, 302, 222.
Clark B.G., 1980, A&A, 89, 377.
Cole S.M., Lacey C.G., Baugh C.M., Frenk C.S., 2000, MNRAS, 319, 168.
Condon J.J., 1992, ARAA, 30, 575.
Condon J.J., Cotton W.D., Greisen E.W., Yin Q.F., Perley R.A., Taylor G.B., Broderick J.J., 1998, AJ, 115, 1693.
Connolly A.J., Szalay A.S., Dickinson M., Subbarao M.U., Brunner R.J., 1997, ApJ, 486, L11.
Cowie L.L., Songaila A., Barger A.J., 1999, AJ, 118, 603.
Cowie L.L., Barger A.J., Kneib J.-P., 2002, AJ, 123, 2197.
Dannerbauer H., Lehnert M., Lutz D., Tacconi L., Bertoldi F., Carilli C., Genzel R., Menten K., 2002, ApJ, submitted (astro-ph/0201104).
de Jong T., Klein U., Wielebinski R., Wunderlich E.W., 1985, A&A, 147, L6.
de Ruiter H.R. et al., 1997, A&A, 319, 7 Dey A., Graham J.R., Ivison R.J., Smail I., Wright G.S., Liu M., 1999, ApJ, 519, 610.
Dickey J.M., Salpeter E.E., 1984, ApJ, 284, 461.
Downes A.J.B., Peacock J.A., Savage A., Carrie D.R., 1986, MNRAS, 218, 31.
Downes D. et al., 1999, A&A, 347, 809.
Dunlop J.S. et al. 2002, MNRAS, submitted (astro-ph/0205480).
Dunne L., Clements D.L., Eales S.A., 2000a, MNRAS, 319, 813 [DCE].
Dunne L., Eales S.A., Edmunds M.G., Ivison R.J., Alexander P., Clements, D., 2000b, MNRAS, 315, 115.
Eales S.A, Lilly S.J., Gear W.K., Dunne L., Bond J.R., Hammer F., Le Fèvre O., Crampton D., 1999, ApJ, 515, 518.
Eales S., Lilly S., Webb T., Dunne L., Gear W., Clements, D., Yun M., 2000, AJ, 120, 2244.
Eales S.A, Ivison R.J., Carilli C., Bertoldi F., Dunne L., 2002, MNRAS, in preparation.
Efstathiou A., Rowan-Robinson M., 2002, MNRAS, submitted.
Elvis M. et al., 1994, ApJS, 95, 1.
Fabian A.C., 1999, MNRAS, 308, L39.
Fixsen D.J., Dwek E., Mather J.C., Bennett C.L., Shafer R.A., 1998, ApJ, 508, 123 Flores H. et al., 1999, ApJ, 517, 148.
Fox M.J. et al., 2002, MNRAS, 331, 839 [F02].
Frayer D.T., Ivison R.J., Scoville N.Z., Yun M., Evans A.S., Smail I., Blain A.W., Kneib J.-P., 1998, ApJ, 506, L7.
Frayer D.T. et al., 1999, ApJ, 514, L13.
Frayer D.T., Smail I., Ivison R.J., Scoville N.Z., 2000, AJ, 120, 1668.
Frayer D.T. et al., 2002, ApJ, in preparation.
Fruchter A., Hook R.N., 1997, in Applications of Digital Image Processing, ed Tescher A.G., Proc. SPIE Vol. 3164, p. 120.
Gear W.K., Lilly S.J., Stevens J.A., Clements D.L., Webb T.M., Eales S.A., Dunne L., 2000, MNRAS, 316, L51.
Georgakakis A., Mobasher B., Cram L., Hopkins A., Lidman C., Rowan-Robinson M., 1999, MNRAS, 306, 708.
González-Solares E. et al., 2002, MNRAS, in preparation.

Granato G.L., Lacey C.G., Silva L., Bressan A., Baugh C.M., Cole S., Frenk C.S., 2000, ApJ, 542, 710.
Hasinger G. et al., 2001, A&A, 365, L45.
Hauser M.G. et al., 1998, ApJ, 508, 25.
Helou G., Soifer B.T., Rowan-Robinson M., 1985, ApJ, 298, L7.
Högbom J.A., 1974, A&AS, 15, 417.
Holland W.S. et al., 1999, MNRAS, 303, 659.
Hughes D.H. et al., 1998, Nature, 394, 241.
Hughes D.H. et al., 2002, MNRAS, submitted (astro-ph/0111547).
Ivison R.J., Smail I., Le Borgne J.-F., Blain A.W., Kneib J.-P., Bézecourt J., Kerr T.H., Davies J.K., 1998, MNRAS, 298, 583.
Ivison R., Smail I., Blain A., Kneib J.-P., Frayer D., 1999, ApSS, 266, 285.
Ivison R.J., Dunlop J.S., Smail I., Dey A., Graham J.R., Liu M.C., 2000a, ApJ, 542, 271.
Ivison R.J., Smail I., Barger A., Kneib J.-P., Blain A.W., Owen F.N., Kerr T.H., Cowie L.L., 2000b, MNRAS, 315, 209.
Ivison R.J., Smail I., Frayer D.T., Kneib J.-P., Blain A.W., 2001, ApJ, 561, L45.
Jenness T., 2000, JCMT Technical Report 84, http://www.jach.hawaii.edu/JACdocs/JCMT/tr/001/84/tr0084.html.
Kauffmann G., Charlot S., 1998, MNRAS, 294, 705.
Kennicutt R.C., 1998, ApJ, 498, 541.
Lacey C. et al., 2002, MNRAS, in preparation.
Lawrence A., 2001, MNRAS, 323, L147.
Ledlow M.J., Smail I., Owen F.N., Keel W.C., Ivison R.J., Morrison G.E., 2002, ApJ, submitted.
Lumb D.H., Warwick R.S., Page M., De Luca A., 2002, A&A, 389, L93.
Lutz, D. et al. 2001, A&A, 378, L70.
Manners J.C. et al., 2002, MNRAS, submitted.
Monet D.G. et al., 1998, USNO-A2.0, United States Naval Observatory, Washington.
Madau P., Ferguson H.C., Dickinson M.E., Giavalisco M., Steidel C.C., Fruchter A., 1996, MNRAS, 283, 1388.
Maiolino R., Rieke G.H., 1995, ApJ, 454, 95.
Moran E.C., Lehnert M.D., Helfand D.J., 1999, ApJ, 526, 649.
Lilly S.J., Le Fevre O., Hammer F., Crampton D., 1996, ApJ, 460, L1.
Page M.J., Stevens J.A., Mittaz J.P.D., Carrera F.J., 2001, Science, 294, 2516.
Peacock J.A. et al., 2000, MNRAS, 318, 535.
Puget J.-L., Abergel A., Bernard J.-P., Boulanger, F., Burton W.B., Desert F.-X., Hartmann D., 1996, A&A, 308, L5.
Read A.M., Ponman T.J., 1998, MNRAS, 297, 143.
Rengarajan T.N., Takeuchi T.T., 2001, PASJ, 53, 433 [RT].
Roche N.D., Almaini O., Dunlop J.S., Ivison R.J., Willott C.J., 2002, MNRAS, submitted (astro-ph/0205259).
Schlegel D.J., Finkbeiner D.P., Davis M., 1998, ApJ, 500, 525.
Scott S.E. et al., 2002, 331, 817 [S02].
Serjeant S. et al., 2002, MNRAS, submitted (astro-ph/0201502).
Silk J., Rees M.J., 1998, A&A, 333, L1.
Silva L., Granato G.L., Bressan A., Danese L., 1998, ApJ, 509, 103.
Smail I., Ivison R.J., Blain A.W., 1997, ApJ, 490, L5.
Smail I., Ivison R.J., Blain A.W., Kneib J.-P., 1998, ApJ, 507, L21.
Smail I., Ivison R.J., Kneib J.-P., Cowie L.L., Blain A.W., Barger A.J., Owen F.N., Morrison G., 1999, MNRAS, 308, 1061.

Smail I., Ivison R.J., Owen F.N., Blain A.W., Kneib J.-P., 2000, ApJ, 528, 612.
Smail I., Ivison R.J., Blain A.W., Kneib J.-P., 2002a, MNRAS, 331, 495.
Smail I., Owen F.N., Morrison G.E., Keel W.C., Ivison R.J., Ledlow M.J., 2002b, MNRAS, submitted.
Smith G.P. et al. 2002, MNRAS, 330, 1.
Soifer B.T., Houck J.R., Neugebauer G., 1987, ARAA, 25, 187.
Soucail G., Kneib J.-P., Bézecourt L., Metcalfe L., Altieri B., Le Borgne J.-F., 1999, A&A, 343, L70.
Steidel C.C., Adelberger K.L., Giavalisco M., Dickinson M., Pettini M., 1999, ApJ, 519, 1.
Townsend R.H.D., Ivison R.J., Smail I., Blain A.W., Frayer D.T., 2001, MNRAS, 328, L17.
Yan L., McCarthy P.J., Freudling W., Teplitz H.I., Malumuth E.M., Weymann R.J., Malkan M.A., 1999, ApJ, 519, L47.
Yun M.S., Carilli C.L., 2002, ApJ, 568, 88.
Yun M.S., Reddy N.A., Condon J.J., 2001, ApJ, 554, 803.
Webb T.M.A., Eales S.A., Lilly S.J., Clements D.L., Dunne L., Gear W.K., Flores H., Yun M., 2002b, ApJ, submitted (astro-ph/0201180).
Webb T.M.A. et al., 2002a, ApJ, submitted (astro-ph/0201181).
White, R.L., Becker R.H., Helfand D.J., Gregg M.D., 1997, ApJ, 475, 479.
Willott C.J. et al., 2002, MNRAS, submitted.

Chapter 4

The Large Velocity Gradient Model

Abstract. We have developed a numerical Large Velocity Gradient (LVG) code in order to simulate the non-LTE excitation conditions for the rotational transitions of CO in a spherical molecular cloud of H_2. The model includes the first 20 rotational transitions of CO, using theoretically calculated collisional rate constants for $J \leq 9$ (Green & Chapman 1978) and extrapolated values for the higher transitions. We discuss how observed line ratios of CO in conjunction with the LVG model can be used to constrain physical properties such as density and kinetic temperature of the gas. We have explored how the observed line intensities and line ratios predicted by the model are affected by an increase of cosmic microwave background (CMB) temperature ($T_{\rm CMB}$) in order to learn more about CO emission lines from high redshift objects. It is found that the population levels are shifted towards higher J-levels as a result of the higher CMB temperature. This suggest that the high-J CO lines are better suited for high-z detections that the lower level lines - although, that might not be the case if large reservoirs of cold and/or sub-thermal molecular gas are lurking around such objects.

4.1 Introduction

About half of the gas in our Galaxy is contained in giant molecular clouds (GMCs), which act as nurseries in which stars are born. Typically, GMCs have masses in the range $10^5 - 10^7\,M_\odot$ and diameters greater than 20 pc, and they are the only phase of the interstellar medium (ISM) which can become gravitationally bound, unlike the other phases of the ISM which are in pressure-equilibrium with their surroundings. While GMCs consist almost entirely of H_2, the unfavorable energy spacing of the the rotational levels (the lowest $J = 2 - 0$ transition energy corresponds to a temperature of 509 K), makes it very hard to excite and thus observe H_2 in typical cloud environments where the kinetic temperature is much lower. Furthermore, the symmetry of the H_2 molecule makes electric dipole transitions strictly forbidden, and as a result only the much weaker quadropole transitions can occur. Only in the vicinity of HII regions where the molecular gas is heated to $\sim$ 1000 K can one hope to detect H_2 via its mid-IR vibrational lines. Hence, one has to rely on other molecules such as CO, CS, HCN and others to trace the H_2 in the cool molecular phase of the ISM. It turns out that CO traces the bulk of the molecular ISM best due to a fortunate combination of three parameters: the abundancy of CO, its small permanent electric dipole moment, and its small rotational-energy spacing (van Dishoeck & Black 1987). Studies of CO in our own Galaxy have been highly successful in determining the molecular gas masses of GMCs and the physical conditions prevailing in them. For the remainder of this thesis we shall use CO observations together with an empirical linear relation between the measured CO line intensity and H_2 content to derive H_2 gas masses in galaxies. We therefore briefly outline three independent ways in which this relation has been calibrated in our own Galaxy.

Virialised clouds A heurestic estimate of the conversion factor can be made by assuming that a) the CO traces individual clouds, meaning that the integrated flux is proportional to the

filling factor of clouds of a constant flux, b) the emission is optically thick and thermalised, and c) the clouds are virialised. The velocity-integrated ^{12}CO $J = 1 - 0$ line emission is

$$I_{^{12}\mathrm{CO}} = \frac{1}{\Omega_B} \int\int\int (T_{ex} - T_{CMB})\, dv d\Omega, \tag{4.1}$$

where T_{ex} and T_{CMB} are the Rayleigh-Jeans temperatures corresponding to the CO $J = 1 - 0$ excitation temperature and the 2.7 K cosmic microwave background, respectively, and Ω_B is the beam solid angle. The CO $J = 1 - 0$ excitation temperature is $T_{ex} = \frac{h\nu_{10}}{k} [\ln(3n_1/n_0)]^{-1}$, and in the vast majority of cases $T_{ex} >> T_{CMB}$ since at the $\tau_{10} \simeq 1$ surface in typical clouds the hydrogen density will be so high that the $J = 1 - 0$ line is thermalised and therefore $T_{ex} = T_{kin}$. This means eq. 4.1 reduces to $I_{^{12}\mathrm{CO}} = T_{ex} f(v) \Delta v_{source} = T_{ex} f' \Delta v_{cloud}$, where $f(v)$ is the cloud filling factor at velocity v and $f' = f(v)\Delta v_{source}/\Delta v_{cloud}$ is the filling factor of clouds in the ensemble, which move around the center of the galaxy with an overall velocity width Δv_{source}. The velocity width of each individual cloud is Δv_{cloud} and is determined by the virial equilibrium that each cloud is in.

The assumption that the clouds are in virial equilibrium means that they obey the scalar virial theorem: $2E_{kin} + E_{pot} = 0$ or simply $\langle v^2 \rangle = GM/R$. Recalling that in an ideal gas the mean square velocity is $\langle v^2 \rangle 3kT_{kin}/\langle m \rangle$, we find that

$$\frac{GM}{3R} = \sigma^2_{cloud} + kT_{kin}/\langle m \rangle, \tag{4.2}$$

where $\langle m \rangle$ is the mean mass per hydrogen molecule, and σ^2_{cloud} is the contribution from the intrinsic cloud motion to the mean square velocity. In fact, the latter is by far the dominant term, and we can therefore write $GM/3R \simeq \sigma^2_{cloud} = (\Delta v_{cloud}/2.35)^2$.

The average H_2 column density for the cloud-ensemble within the beam is $\langle N(\mathrm{H_2}) \rangle = f' N(\mathrm{H_2})_{cloud} = f' 2R \langle n(\mathrm{H_2}) \rangle$. From the above equations it is then straightforward to derive the following expression for the conversion factors

$$X_{\mathrm{CO}} = \frac{\langle N(\mathrm{H_2}) \rangle}{I_{^{12}\mathrm{CO}}} = 3 \times 10^{20} \left(\frac{8\,\mathrm{K}}{T_{ex}} \right) \left(\frac{\langle n(\mathrm{H_2}) \rangle}{200\,\mathrm{cm^{-3}}} \right)^{1/2} \tag{4.3}$$

Inserting values for T_{ex} and $n(\mathrm{H_2})$ typical for GMCs (Scoville & Sanders 1987) we find a convertion factor, X_{CO}, which is in agreement (within a factor of 2) with estimates obtained using the alternative methods described in this section. The main result of the above exercise, however, is that eq. 4.1 shows how X_{CO} depends on the temperature and density of the cloud: $X_{\mathrm{CO}} \propto T^{-1} n(\mathrm{H_2})^{1/2}$. Thus, it is clear that the conversion factor *does* depends on the environment and is likely to vary between different types of clouds.

Observations of CO isotopes A second method involves observing line emission from CO isotopes such as ^{13}CO, C^{18}O and C^{17}O against regions with high visual extinction. Such lines are typically optically thin (low abundances), and as a result the column densities of these isotopes can be directly measured, which in turn can be used to derive the ^{12}CO column density subject to the following assumptions: a) the measured ^{12}CO line temperature is equal to the excitation temperature; b) the same same excitation temperature applies to ^{13}CO; and c) the $n(^{12}\mathrm{CO})/n(^{13}\mathrm{CO})$ ratio is known. The column density of H_2 is inferred from from measurements of the visual extinction (e.g. from star counts) through the cloud and assuming a standard gas/extinction ratio. The measured $N(\mathrm{H_2})$ is then compared directly with the $I_{^{12}\mathrm{CO}}$.

Diffuse γ-ray emisssion High-energy γ-rays are produced by cosmic rays colliding with hydrogen nuclei. Thus, by measuring the diffuse γ-ray background and its variation on the sky,

the number of hydrogen nuclei can be determined in volumes across the Galaxy. This is provided that the process in which the γ-rays are produced is well calibrated (i.e. how many γ-rays are produced per collision), In practice, the conversion factor is estimated by comparing maps of the Galaxy in γ-rays and at 21 cm (which measures the line emission from neutral hydrogen), as well as ^{12}CO $J = 1 - 0$ maps, and simultaneously solving for the distribution of cosmic rays, the distribution of gas density, and the value of $N(H_2)/I(CO)$. The advantage of this method is that it is independent of abundance ratio, excitation conditions and the structure of the cloud.

The above methods all give conversion factors which agree to within a factor of 2 or so. The typically adopted value for this Galactic conversion factor is X_{CO}= $4.8\,M_\odot$ $(\mathrm{K\,km\,s^{-1}\,pc^2})^{-1}$. However, in starburst galaxies, where intense UV radiation fields dominate, the concept of isolated molecular clouds breaks down due to the strong tidal fields which tends to disrupt stable clouds. In this case the CO traces an extended, diffuse medium – bound by the overall potential of the galaxy – in which massive stars are embedded, and the line width is therefore determined by the total dynamical mass in the region (gas and stars). The net result is that in order to derive molecular gas masses from CO observations of starburst galaxies, one must adopt a conversion factor which is about 6× smaller than the Galactic value, i.e. X_{CO}= $0.8\,M_\odot$ $(\mathrm{K\,km\,s^{-1}\,pc^2})^{-1}$ (Downes, Solomon & Radford 1993).

Observed molecular lines widths from Galactic molecular clouds indicate that large velocity gradients exist in such clouds which exceed thermal velocities by a large margin. The inferred velocity gradients range from $1\,\mathrm{km\,s^{-1}}$ to $\sim 50\,\mathrm{km\,s^{-1}}$ while the rms thermal velocities of interstellar molecules typically are of the order $\sim 0.1\,\mathrm{km\,s^{-1}}$. Explaining such large velocity gradients by supersonic turbulence poses a number of problems. First of all isotopes of the same molecular species (^{13}CO and ^{12}CO, say) show very similar line shapes, but different intensities, meaning that the optical depth is different for the two species. The fact that the line shapes are the same would require the turbulence to be constant at different depths of the cloud. Furthermore, the lines often display the same variation with position across the cloud (Green & Chapman 1978). Finally, to maintain turbulence in a cloud requires a significant source of mechanical energy, and it is not obvious what the nature of such a source might be.

Alternatively, it has been suggested that a large systematic velocity gradient across the cloud may account for the observations. The typically low temperatures of dense clouds suggest that thermal pressure is inadequate to maintain the clouds in hydrostatic equilibrium, and since we have argued that turbulent pressure can be neglected it follows that the clouds must be in a state of gravitational collapse. This supports the idea of the presence of an overall velocity gradient across the cloud. Furthermore, the source function across an emission line is determined by the velocity field within the cloud, i.e. the emission at a specific frequency originates from a small segment along the line of sight. If the velocity field is dominated by a large systematic gradient, it would explain why lines of different molecular species have similar line profiles.

In order to study CO emission from cosmological object we need to have an idea of how the emission is influenced by the physical conditions in molecular clouds. In particular, we need to understand how the population levels of the CO molecule are affected by density ($n(H_2)$), kinetic temperature (T_k), CO abundance (X_{CO}), and the cosmic microwave background temperature (T_{CMB}) which increases with redshift. To solve this problem generally is not trivial and requires a 3D, geometry-dependent numerical code which simultaneously solves the radiative transfer equation and the chemical network included (e.g. Silk & Spaans 1997; Gnedin et al. 2001). Such detailed modeling is justified in situations where a host of different molecular species have been observed. However, the LVG-model more than often provide an adequate insight into the overall

physical conditions in cases where only a few molecular lines have been observed. The latter scenario is typically the case in extragalactic objects, and the LVG-model has found widespread usage in these situations. The drawback here of course is that the CO emission is not emitted from a single molecular cloud but rather from an ensemble of clouds with a wide range of different physical properties. In most cases, therefore, extragalactic CO observations and subsequent LVG-analysis should only be interpreted as the ensemble-averaged physical conditions.

We will adopt the LVG approximation as a reference model with which we can get an idea of CO emission from molecular clouds with varying physical conditions.

4.2 Outline of the model

The LVG model adopted here is reminiscent to the one described by Goldreich & Kwan (1974), but other very similar models can be found in e.g. de Jong et al. (1975) and Goldsmith et al. (1983). Common to all models is that they consider a pressure-free spherical cloud consisting of H_2 and ^{12}CO only. Uniform density and kinetic temperature throughout the cloud is assumed. Hence, the cloud is in a state of free gravitational collapse, and its in-fall velocity field can be described by

$$v(r) = \sqrt{\frac{2GM}{R^3}} \cdot r, \tag{4.4}$$

where M and R is the mass and radius of the cloud, respectively. The line of sight velocity, v_z, at a projected distance, p, from the center is easily seen to be

$$v_z = \mp \sqrt{\frac{2GM}{R}} \cdot \left(\frac{r^2 - p^2}{R^2} \right)^{1/2}. \tag{4.5}$$

The key assumption of the LVG approach is that the large-scale velocity gradient is the dominant mechanism for line broadening, in other words the velocity field given by eq. 4.5 is assumed to exceed the thermal velocities, v_T. This implies that photons emitted at some point in the cloud can only be re-absorbed within a region of size $l \sim (R/v)v_T$ of the point; otherwise the photon will escape the cloud. Apart from collisional excitation, molecules can only be excited by photons which were emitted within a Doppler width away or by CMB photons which have leaked into the cloud. As a result the population levels of the CO molecule are the same throughout the cloud, and it is sufficient to solve the equations of radiative transfer and statistical equilibrium locally in order to derive population levels and brightness temperatures.

4.2.1 Radiative transfer in a spherical LVG model

As pointed out above it is the velocity gradient which allows us to decouple the equations for the level populations from the radiative transfer. In order to do so we introduce the escape probability, $\beta_{ij}(r)$, which is the probability that a photon emitted in the transition $i \rightarrow j$ at a radius r will escape the cloud. In this section we shall derive an analytical expression for $\beta_{ij}(r)$ in the case of a spherical cloud. The spherical symmetry of the problem greatly simplifies the equation of radiative transfer in that it becomes a one-dimensional problem. The change of specific line intensity, I_ν, along an infinitesimal radial element, dr, through the cloud is given by

$$dI_\nu(r)dr = \epsilon_\nu(r)dr - \kappa_\nu(r)I_\nu(r)dr, \tag{4.6}$$

where ϵ_ν and κ_ν are the emission and absorption coefficients. ϵ_ν and κ_ν are given by

$$\kappa_\nu = \frac{h\nu}{4\pi}\left(n_i B_{ij} - n_j B_{ji}\right)\phi(\nu) \tag{4.7}$$

$$\epsilon_\nu = \frac{h\nu}{4\pi} n_j A_{ji}\phi(\nu), \tag{4.8}$$

where n_i, n_j are the volume densities of the molecules in the upper and lower states of the transition. The Einstein coefficients B_{ij} and B_{ji} give the rates per second per molecule for stimulated radiative processes. Similarly, A_{ij} is the rate of decay of n_i by spontaneous radiative transitions. $\phi(\nu)$ is the normalised line profile and as already mentioned is determined by the large-scale velocity gradient of the cloud. Having introduced the concept of the escape probability we can write down the average radiation field inside the cloud:

$$\langle J_\nu \rangle = (1 - \beta_{ij})\, S_\nu + \beta_{ij} B_\nu(T_{\rm CMB}), \tag{4.9}$$

where $B_\nu(T_{\rm CMB})$ is the cosmic microwave background (CMB). S_ν is the source function and is defined as

$$S_\nu = \frac{\epsilon_\nu}{\kappa_\nu} = \frac{2h\nu^3}{c^2}\left[\frac{g_i n_j}{g_j n_i} - 1\right]^{-1} = \frac{2h\nu^3}{c^2}\left[\exp\left(\frac{h\nu}{kT_{ex}}\right) - 1\right]^{-1}. \tag{4.10}$$

Clearly, if all the photons escape the cloud ($\beta = 1$) the average radiation field will simply be that of the CMB. If every photon is absorbed within the cloud ($\beta = 0$) then $\langle J_\nu \rangle$ is equal to the source function S_ν.

Now consider a point P(r) in the cloud (Figure 4.1). At this point, the optical depth at

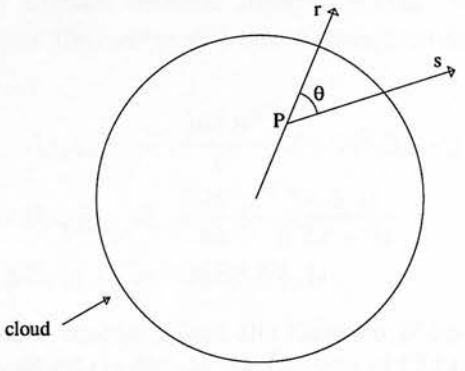

Figure 4.1: Schematic illustration of the LVG model. s is the directions towards the observer.

frequency ν as seen for an observer in the direction $\vec{s}$ is given by

$$\tau(\nu, r, \mu) = \int_0^\infty \kappa_0(r, \vec{s}, \mu)\phi\left(\nu - \nu_0 + \frac{\nu_0}{c}\alpha s\right) ds, \tag{4.11}$$

where $\kappa_0 = \frac{h\nu_0}{4\pi}(n_j B_{ji} - n_i B_{ij})$ is the absorption coefficient at the centre of the line, and α is the velocity gradient $\frac{dv(r)}{dr} = \sqrt{\frac{2GM}{R^3}}$ (Castor 1970; de Jong & Dalgarno 1975). The line shape function, ϕ, is sharply peaked at zero which corresponds $s = \frac{-(\nu-\nu_0)}{\alpha\nu_0/c}$. Thus, if the velocity gradient is very large $s \simeq 0$, and we get

$$\tau(\nu, r, \mu) = \kappa_0(r, \mu)\int_0^\infty \phi\left(\nu - \nu_0 + \frac{\nu_0}{c}\alpha s\right) ds = \kappa_0(r, \mu)\frac{c}{\alpha\nu_0}\int_{-x}^\infty \phi(x')dx', \tag{4.12}$$

where we have made the following substitutions $x = \nu - \nu_0$ and $x' = -x + \alpha\nu_0 s/c$. The probability for a photon to escape from the point P in any direction is then given by

$$\beta_{ij}(r) = \frac{1}{4\pi}\int_{4\pi}\int_{-\infty}^{\infty}\phi(x)e^{-\tau(x,r,\mu)}dxd\Omega = \frac{1}{2}\int_{-1}^{1}\frac{1-e^{-\tau_{ij}}}{\tau_{ij}}d\mu = \frac{1-e^{-\tau_{ij}}}{\tau_{ij}}, \tag{4.13}$$

where $\tau_{ij} = \frac{\kappa_0 c}{\nu_0 \alpha} = \frac{A_{ij}c^3 n_i}{8\pi\nu_{ij}^3}\left(\frac{n_j g_i}{n_i g_j} - 1\right)\alpha$ is the optical depth for the entire line $i \rightarrow j$ (Castor 1970; de Jong & Dalgarno 1975).

4.2.2 The rate equations

Next we turn to the equations of statistical equilibrium, or rate equations, which govern the population levels. In its full generality the multi-level rate equation for level i is given by

$$n_i\left[\sum_{k\neq i}(C_{ik} + \langle J_\nu\rangle B_{ik}) + \sum_{k<i}A_{ik}\right] = \sum_{i\neq k}n_k\left[C_{ki} + \langle J_\nu\rangle B_{ki}\right] + \sum_{k>i}A_{ki}n_k, \tag{4.14}$$

where $\langle J_\nu\rangle = \int_{4\pi} I_\nu d\Omega/4\pi$ is the average radiation field (line plus continuum) at the frequency of the transition. C_{ij} are the collision rate coefficients and are equal to the collision partner density, n, which in our case is H_2, times the velocity-integrated cross-section, i.e. $C_{ij} = n(H_2)\langle\sigma_{ij}v\rangle$.

We will now write down the equations of statistical equilibrium in a form which is adequate for our LVG model, i.e. a spherical cloud consisting of H_2 and CO. Fortunately, eq. 4.14 is simplified considerably by the fact that due to the permanent electric dipole moment of the CO molecule rotational transitions are only allowed between adjacent states. Furthermore, we note that the Einstein A and B coefficients and the energy difference corresponding to the transition $J+1 \rightarrow J$ can be written as

$$A_{J+1,J} = \frac{16hB^3}{c^2}(J+1)^3 B_{J+1,J} \tag{4.15}$$

$$B_{J+1,J} = \frac{32\pi^4\mu^2}{3h^2c}\frac{(J+1)}{((2J+3)} \tag{4.16}$$

$$\Delta E_{J+1,J} = 2hB(J+1), \tag{4.17}$$

where B is the molecular rotation constant (not the Einstein B coefficient), and μ is the electric dipole moment of CO. Finally, we let n_J denote the fraction of CO molecules in the Jth rotational level divided by the degeneracy for that level, i.e. the Gaunt factor $g_J = 2J+1$. In doing so we find that the rate equation for the Jth level is given by

$$\begin{aligned} 0 = {} & \beta_{J+1,J}A_{J+1,J}\left(\frac{2J+3}{2J+1}\right)\left[n_{J+1} - \frac{n_J - n_{J+1}}{\exp(\frac{2hB(J+1)}{kT_{\rm CMB}}) - 1}\right] - \beta_{J,J-1}A_{J,J-1}\left[n_J - \frac{n_{J-1} - n_J}{\exp(\frac{2hBJ}{kT_{\rm CMB}}) - 1}\right] \\ & + \sum_{L=J+1}^{\infty}(2L+1)C_{LJ}\left[n_L - n_J\exp\left(\frac{hB}{kT_k}\left[J(J+1) - L(L+1)\right]\right)\right] \\ & + \sum_{L=0}^{J-1}(2L+1)C_{JL}\left[n_J - n_L\exp\left(\frac{hB}{kT_k}\left[L(L+1) - J(J+1)\right]\right)\right], \end{aligned} \tag{4.18}$$

(Goldreich & Kwan 1974). In deriving eq. 4.18 we have made use of eqs. 4.9 and 4.10, as well as the standard relations between the Einstein A and B coefficients. The first two terms in eq. 4.18 account for the spontaneous emission from the transitions $J+1 \rightarrow J$ and $J \rightarrow J-1$, respectively. The only continuum source present is the CMB, and the absorption and stimulated emission which

the CMB photons cause are included in the radiative terms. The first collisional term includes the collisional de-excitations from levels above J and collisional excitations from the J level to levels above it. Similarly, the second collisional terms describes collisional de-excitations from the J level to lower levels and excitations from lower levels to the J level.

4.2.3 Collision rate constants

In contrast to the Einstein radiative rate constants which only require the electrical dipole moment of the CO molecule to be known, collision rate constants are much more difficult to estimate, experimentally as well as theoretically, and furthermore depends on the kinetic temperature of the gas. The most reliable results have come about from theoretical calculations of the interaction potential of the exciting particle and CO (e.g. Green & Thaddeus 1976). The problem is particular simple if the exciting particle in its ground state has a spherical shape. This is the case for molecular hydrogen in its lowest rotational state $J = 0$; this state is called para-H_2 as opposed to ortho-H_2 which has $J = 1$. Goldsmith et al.(1983) found that collision rate constants between ortho-H_2 and CO where J is decreasing by 2, i.e. $\Delta J = -2$, are about 50% larger than the corresponding collision rates for para-H_2. Assuming a 3:1 ratio of ortho-H_2 and para-H_2 they showed that the effect of the different collision rates on the derived H_2 densities from LVG computations is no larger than 25%.

In the model presented here, only para-H_2 is included since in cold molecular clouds, the bulk of the H_2 molecules are expected to be para-H_2, i.e. in their lowest rotational level. The downward collision rates were adopted from Green & Chapman (1978), who provide cross sections for para-H_2 and CO collisions involving rotational levels up to $J = 9$. However, for higher transitions no collision rates exist in the literature. This was a problem since in order for the CO lines to be detectable above the CMB at very high redshifts, the excitation temperature and thereby also the kinetic temperature of the cloud has to be correspondingly high. This means that also the higher rotational levels will be significantly populated, and must be included in the computations. It was decided to approximate the collision rates for $J > 9$ using an extrapolation scheme similar to that of de Jong et al. (1975), which consist of fitting an empirical expression to the known collision rates and extrapolate it to higher levels. The formulae adopted by de Jong et al. (1975) is

$$\langle \sigma v \rangle_{JI} = a_{JI} \frac{g_I}{g_J} \left(1 + \frac{\Delta E_{JI}}{kT_k}\right) \exp\left(-b_{JI} \left(\frac{\Delta E_{JI}}{kT_k}\right)^{1/2}\right), \tag{4.19}$$

where a_{JI} and b_{JI} are the parameters to be fitted. For a given transition eq. 4.19 was fitted to the collision rates for all the kinetic temperatures considered by Green & Chapman (1978), namely $T_k = 10, 20, 30, 40, 50, 60, 80$, and 100 K. The resulting fits are shown in figure 4.2. However, such fits could only be done for transitions which implied a change in J less than or equal to 9. For transitions where J is changed by 10 or more, e.g. $J = 18 \rightarrow 7$, the collision rates were estimated by extrapolating the a_{JI} and b_{JI} coefficients found for $\Delta J \leq 9$ to $\Delta J \geq 10$. Figure 4.3 shows that indeed there seems to be a systematic trend in a_{JI} and b_{JI} with ΔJ. The dashed curves mark the best-fit power law and a straight line to the a_{IJ} and b_{JI} points, respectively. Hence, from the extrapolations described above we obtained collision rates for all transitions $J \leq 20$ at the various kinetic temperatures given above. Figure 4.4 (left panel) shows the Green & Chapman (1978) collision rates for transitions from $J = 9$ to lower levels for various kinetic temperatures, while the extrapolated collision rates for transitions from $J = 19$ to lower levels are shown in the right panel of figure 4.4. As expected the overall collision rates decrease as ΔJ becomes bigger since the probability of a transition across several rotational levels is low. A dependence

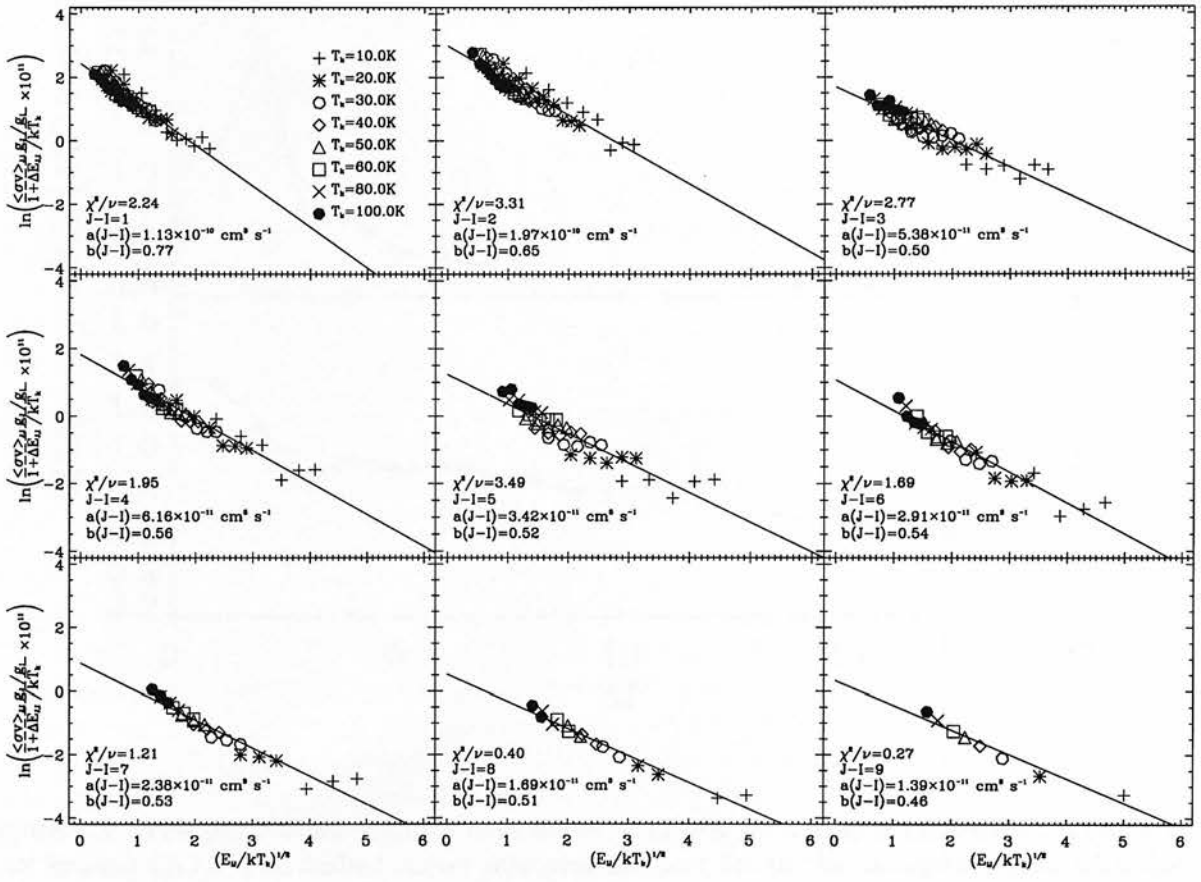

Figure 4.2: The panels show the quantity $\ln\left(\frac{\langle\sigma v\rangle_{IJ} g_J / g_I}{1+\Delta E_{IJ}/kT_k} \times 10^{11}\right)$ vs. $(\Delta E_{IJ}/kT_k)^{1/2}$, where $\langle\sigma v\rangle_{IJ}$ are the collision rates from Green & Chapman (1978). Each panel corresponds to different steps of the rotational ladder of CO - starting with $J - I = 1$ in the upper left corner. The solid lines represent best fits of eq. 4.19 to the data.

on kinetic temperature is also clear from the plots, and seems to indicate that the collision rates increase with kinetic temperature.

4.2.4 Implementation

A program called `lvg.x` was written in `C++` which solves the 20 non-linear equations in eq. 4.18 using a globally convergent version of the Newton-Raphson method adopted from Press et al. (1985). For a given kinetic temperature, CMB temperature, hydrogen density, CO abundance, and velocity gradient, the program solves for the population levels of the CO molecules, and from those it calculates the excitation temperature, optical depth and brightness temperature for the various transitions. The excitation temperature for the $J + 1 \rightarrow J$ transition is given by the familiar definition: $T_{ex,J+1\rightarrow J} = \frac{2hB(J+1)}{k \ln(n_J/n_{J+1})}$. Expressing the line intensities in terms of the

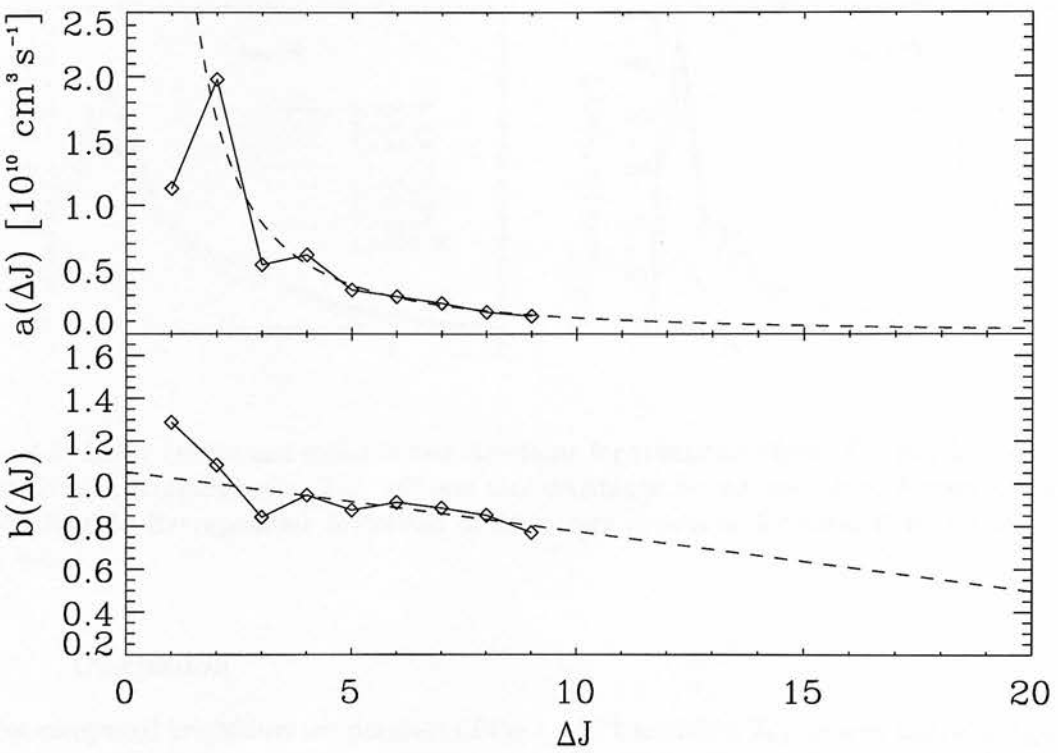

Figure 4.3: The parameters a and b determined from Figure 4.2 as a function of rotational level spacing (ΔJ). The dashed curves represent the best fits to the data-points (but with the data-point at $\Delta J = 1$ excluded). These curves were used to extrapolated a and b coefficients to $\Delta J \geq 10$.

equivalent Rayleigh-Jeans temperature the brightness temperatures become

$$T_{b,J+1\rightarrow J} = (T_{ex,J+1\rightarrow J} - T_{\mathrm{CMB},J+1\rightarrow J})(1 - e^{-\tau_{J+1\rightarrow J}}), \tag{4.20}$$

$$T_{b,J+1\rightarrow J} = \frac{2hB(J+1)}{k}\left(\frac{1}{\exp(\frac{2hB(J+1)}{kT_{ex,J+1\rightarrow J}}) - 1} - \frac{1}{\exp(\frac{2hB(J+1)}{kT_{\mathrm{CMB},J+1\rightarrow J}}) - 1}\right)(1 - e^{-\tau_{J+1\rightarrow J}}) \tag{4.21}$$

Note that excitation temperatures for different transitions are in general not equal, e.g. $T_{ex,2\rightarrow 1} \neq T_{ex,1\rightarrow 0}$ in general. $T_{\mathrm{CMB},J+1\rightarrow J}$ is the equivalent Rayleigh-Jeans temperature of the $T_{\mathrm{CMB}} = 2.73\,\mathrm{K}$ Cosmic Microwave Background for the $J+1 \rightarrow J$ transition.

For a given kinetic temperature, CMB temperature, and for densities $10^2\,\mathrm{cm}^{-3} \leq n(\mathrm{H}_2) \leq 10^5\,\mathrm{cm}^{-3}$ and CO abundances $10^{-9}(\mathrm{km\,s^{-1}pc^{-1}})^{-1} \leq X_{\mathrm{CO}}(dv/dr)^{-1} \leq 10^{-4}(\mathrm{km\,s^{-1}pc^{-1}})^{-1}$, the code computes relative population numbers, optical depths, and excitation and brightness temperatures for all rotational levels $J = 0, \ldots, 19$. Computations were done for $T_k = 10, 20, 30, 40, 50, 60, 70, 80$, and $100\,\mathrm{K}$ and $T_{\mathrm{CMB}} = 2.73, 5, 8, 10, 15, 20, 25$, and $30\,\mathrm{K}$. The wide ranges of values for the different parameters allowed us to study CO excitation under very different conditions.

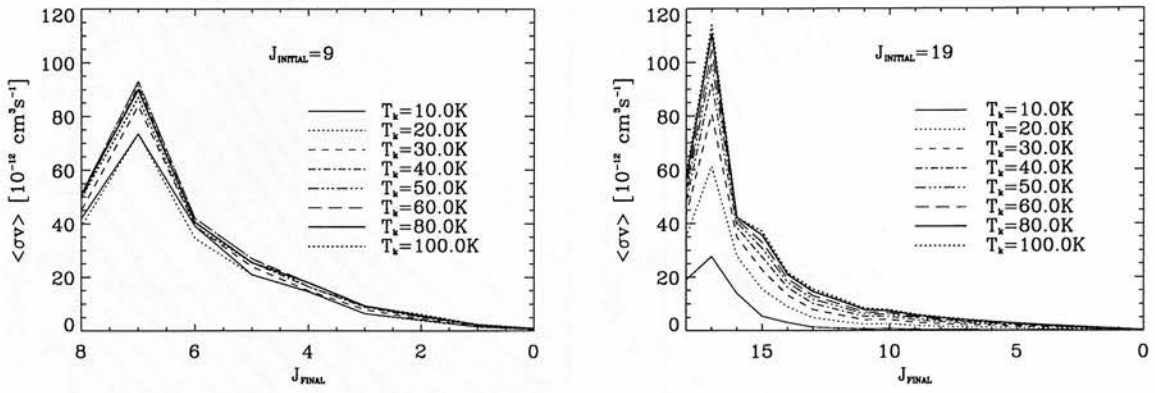

Figure 4.4: **Left:** Downward collision rate constants for transitions from $J = 9$ to levels below for various kinetic temperatures. The collision rate constants are adopted from Green & Chapman (1978). **Right:** Extrapolated downward collision rate constants for transitions from $J = 19$ to levels below.

4.3 Discussion

The computed brightness temperature of the $1 \rightarrow 0$ transition, $T_{b,1\rightarrow 0}$, and the ratio $T_{b,2\rightarrow 1}/T_{b,1\rightarrow 0}$ are shown in figure 4.5 as contours against molecular hydrogen density and abundance of CO per unit velocity gradient. In both the left and right hand side plot the CMB temperature is 2.73 K while the kinetic temperatures are $T_k = 10\,\mathrm{K}$ and $T_k = 20\,\mathrm{K}$, respectively. From figure 4.5 it is seen that $T_{b,1\rightarrow 0}$ increases with increasing molecular hydrogen density and CO abundance. This is as expected since an increase in $n(\mathrm{H_2})$ and/or X_{CO} means more collisional $J = 1 \rightarrow 0$ excitations and hence a higher brightness temperature for that transition. For $T_{b,2\rightarrow 1}/T_{b,1\rightarrow 0} < 1$ we see that when X_{CO} is increased the molecular hydrogen density has to drop in order to keep the brightness temperature ratio constant. For $T_{b,2\rightarrow 1}/T_{b,1\rightarrow 0} > 1$ the molecular hydrogen density must increase in order to keep $T_{b,2\rightarrow 1}/T_{b,1\rightarrow 0}$ constant. Figure 4.5 also shows that for $n(\mathrm{H_2}) > 10^4\,\mathrm{cm^{-3}}$ and $n(\mathrm{H_2}) < 10^{2.5}\mathrm{cm^{-3}}$ it becomes increasingly difficult to derive accurate $n(\mathrm{H_2})$-estimates from the $T_{b,2\rightarrow 1}/T_{b,1\rightarrow 0}$ curves, due to the steepness of the curves. Comparing plots with same CMB temperature but different kinetic temperatures it is seen that for a given kinetic temperature, the molecular hydrogen density needed to maintain a certain brightness temperature ratio is less than what is required at lower kinetic temperatures. Hence, as expected higher kinetic temperatures results in the higher rotational levels being populated on account of the lower levels.

Provided that the kinetic temperature of the cloud is known, observations of the $J = 1 \rightarrow 0$ and $J = 2 \rightarrow 1$ line strengths and curves such as the ones shown in figure 4.5 can be used to derive the the molecular hydrogen density and CO abundance per unit velocity gradient. Furthermore, from line intensity of the lowest CO transition, i.e. $T_{b,1\rightarrow 0}$ a lower estimate of the total column density of CO can be obtained. For extragalactic work one often adopts the galactic value of X_{CO} and uses the observed line ratios to infer molecular hydrogen densities and kinetic temperatures of the extragalactic ISM. However, things are complicated by the fact that most of the time the beam filling factor of CO observations is unknown. As a result it is more convenient to compare observed and predicted line ratios instead of line intensities. Furthermore, since different combinations of $n(\mathrm{H_2})$ and T_{kin} can give the same LVG-model line ratios, at least

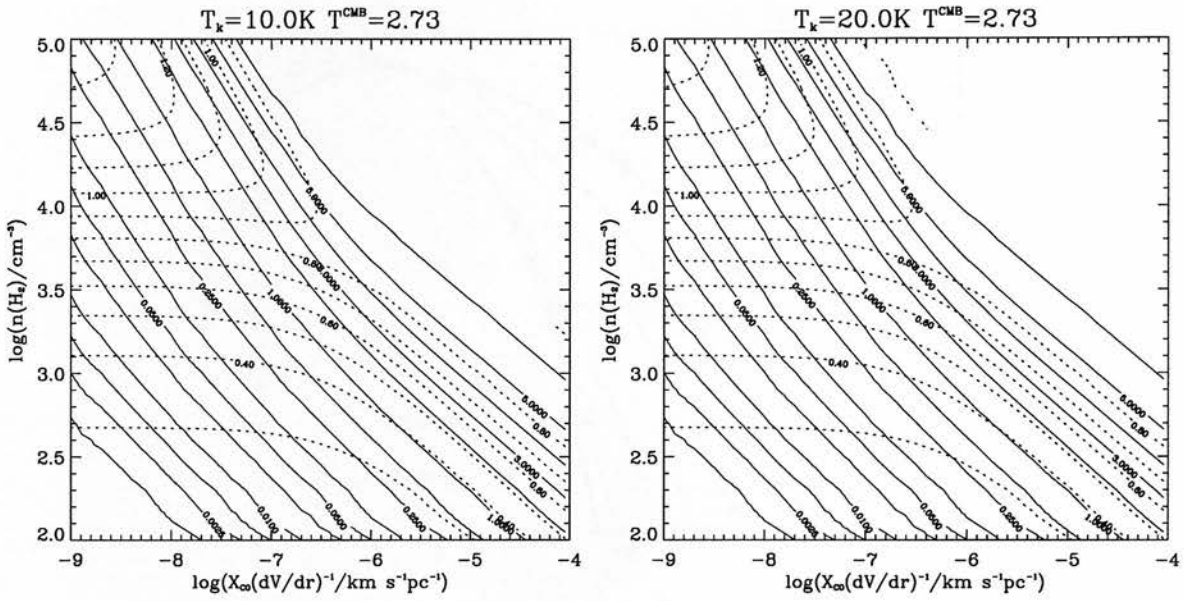

Figure 4.5: Curves of constant brightness temperature for the $J = 1 \rightarrow 0$ transition (solid lines) and constant ratios of $J = 2 \rightarrow 1$ to $J = 1 \rightarrow 0$ brightness temperatures (dashed line) for kinetic temperatures of $T_k = 10\,\mathrm{K}$ (left) and $T_k = 20\,\mathrm{K}$ (right) and $T_{\mathrm{CMB}} = 2.73\,\mathrm{K}$.

two line ratios, i.e. three CO transitions, need to be observed in order to properly constrain the physical conditions. Finally, in extragalactic studies the situation becomes if further complicated by the fact that observed CO emission is not emitted from a single molecular cloud but from a large ensemble of clouds with presumably a wide range of different physical conditions.

At high redshifts, the increase in CMB temperature leads to an enhancement of the high-J levels. This is illustrated in figure 6 where $(2J+1)n_J/n_{tot}$ has been plotted against J for various CMB temperatures. Note that due to the way n_J was defined in section 4.2, $(2J+1)n_J$, and not n_J, is the actual relative population number of level J. Hence, it follows that $n_{tot} = \sum_{J=0}^{J=19}(2J+1)n_J$. Clearly, at high redshifts the distribution is skewed towards higher levels. However, for a given kinetic temperature and redshift it is seen that $(2J+1)n_J/n_{tot} \leq ((2J+1)n_J/n_{tot})_{LTE}$ always holds. This comes about from the fact that the kinetic temperature of the gas can never be lower than the surrounding CMB temperature; at most they can be equal which happens at a given redshift and means that the gas is in LTE with the CMB background.

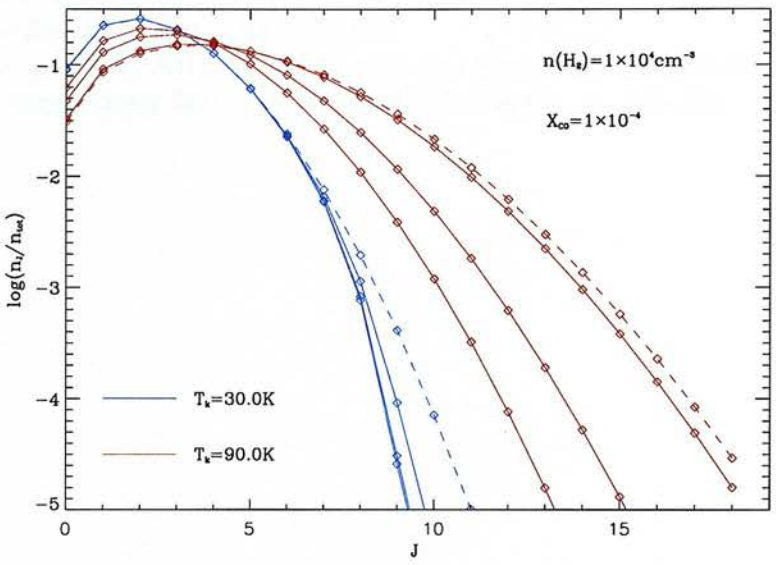

Figure 4.6: **Left:** CO rotational level population numbers for redshifts $z = 0, 2, 5$ and $T_k = 30\,\mathrm{K}$ (blue curves), and $z = 15, 20, 30$ and $T_k = 90\,\mathrm{K}$ (red curves). In all cases $n(\mathrm{H_2}) = 1.0 \times 10^4\,\mathrm{cm^{-3}}$ and $X_{\mathrm{CO}}(dv/dr)^{-1} = 1.0 \times 10^{-4}(\mathrm{km\,s^{-1}pc^{-1}})^{-1}$. The blue and red dashed curves are the LTE population numbers for $T_k = 30\,\mathrm{K}$ and $T_k = 90\,\mathrm{K}$, respectively.

References

Andreani, P., Cimatti, A., Loinard, L., & Röttgering, H. 2000, A&A, 354, L1.
Castor, J.I. 1970, MNRAS, 149, 111.
Cimatti, A., Andreani, P., Röttgering, H., & Tilanus, R. 1998, Nature, 371, 586.
de Jong, T., Chu, S.-I., & Dalgarno, A. 1975, ApJ, 199, 69.
Dey, A., Graham, J.R., Ivison, R.J., Smail, I.m Wright, G.S., & Liu, M. 1999, ApJ, 519, 610.
Downes, D., Solomon, P.M. & Radford, S.J.E. 1993, ApJ, 414, L13.
Genzel, R. 1990, p. 155 in Proceedings of the NATO Advanced Study Institute on The Physics of Star Formation and Early Stellar Evolution", Agia Pelagia, Greece, Eds. Lada, C.J. & Kylafis, N.D.
Gnedin, N.Y., Silk, J., & Spaans, M. 2001, MNRAS, submitted (astro-ph/0106110).
Goldreich, P. & Kwan, J. 1974, ApJ, 189, 441.
Goldsmith, P.F., Young, J., & Langer, W.D. 1983, ApJS, 51, 203.
Graham, J.R. & Dey, A. 1996, ApJ, 471, 720.
Green, S. & Thaddeus, P. 1976, ApJ, 205, 766.
Green, S. & Chapman, S. 1978, ApJS, 37, 169.
Hu, E.M. & Ridgway, S.E. 1994, AJ, 107, 1303.
Maloney, P. & Black, J.H. 1988, ApJ, 325, 389.
Press, W.H., Teukolsky, S.A., Vetterling, W.T., & Flannery, B.P. 1985, "Numerical Recipies in C", second edition, Cambridge University Press.
Scoville, N.Z. & Sanders, D.B. 1987, in "Interstellar Processes", Eds. Hollenbach, D. & Thronson, H., Reidel (Dordrecht(, p. 21.
Silk, J. & Spaans, M. 1997, ApJ, 488, L79.

Sobolev, V.V. 1960, "Moving Envelopes of Stars", Cambridge: Harvard University Press.
Young, J.S. & Scoville, N.Z. 1982, ApJ, 258, 467.
van Dishoeck, E.F. & Black, J.H. 1987, "Physical processes in interstellar clouds", Proceedings of the NATO Advanced Study Institute, Reidel Publishing Co., p. 241-274.

Chapter 5

Gas and Dust in the Extremely Red Object ERO J164502+4626.4

Abstract. We report the first detection of the lowest CO transition in a sub-millimetre bright galaxy and extremely red object (ERO) at $z = 1.44$ using the Very Large Array[4] . The total $J = 1 - 0$ line luminosity of ERO J164502+4626.4 is $(7 \pm 1) \times 10^{10}\,\mathrm{K\,km\,s^{-1}\ pc^2}$, which yields a total molecular gas mass of $\sim 6 \times 10^{10}\,M_\odot$. We also present a map of the 850-μm continuum emission obtained using SCUBA, from which we infer a far-IR luminosity and dust mass of $L_{FIR} \sim 9 \times 10^{12}\,L_\odot$ and $M_d \sim 9 \times 10^8\,M_\odot$. We find tentative evidence that the CO and sub-mm dust emission is extended over several tens of kpc. If confirmed by high-resolution imaging, this implies that ERO J164502+4626.4 is not simply a high redshift counterpart of a typical Ultra Luminous Infrared Galaxy (ULIRG).

5.1 Introduction

Observations of CO provide one of the most powerful methods of probing the interstellar medium (ISM) in galaxies – i.e. determining the amount of molecular gas available to fuel star formation and accretion onto active galactic nuclei (AGN), the two processes believed to generate the large far-infrared (far-IR) luminosities of star-forming galaxies (Sanders et al. 1991). The first detection of CO at high redshift (Brown & vanden Bout 1991) revealed its potential to trace metal-enriched molecular gas in the early Universe. CO is thus key to our understanding of galaxy formation and evolution.

Extremely red objects (EROs - usually defined as galaxies with $R - K \gtrsim 5.3$, e.g. Moriondo, Cimatti & Daddi 2000) constitute a bi-modal population - a combination of dusty, starbursting systems (Dey et al. 1999) and evolved ellipticals (Dunlop et al. 1996). While both types of objects appear similar in the optical/near-IR, the detection of sub-millimetre continuum emission and/or CO unambiguously pinpoints the dusty EROs. A significant fraction of the sub-mm-selected population of high-redshift dust-enshrouded starburst galaxies is believed to be associated with EROs (Smail et-al. 1999). Since the advent of large-format bolometer arrays such as SCUBA (Holland et al. 1999) and MAMBO (Kreysa et al. 1998), over a hundred sources have been detected in (sub)millimetre surveys (Smail et al. 1997; Hughes et al. 1998; Bertoldi et al. 2001). In cases where optical/IR counterparts of sub-mm galaxies are available, it is found that the sources typically are distorted, multi-component systems with one or more components being an ERO (chapter 3). The sub-mm population has a median redshift of $z \simeq 2.4$ (Chapman et al. 2003), and is widely believed to comprise the progenitors of present-day spheroids and

Greve, T.R, Ivison, R.J. & Papadopoulos, P.P. 2003, ApJ, 599, 839.

[4] The Very Large Array (VLA) is operated by the National Radio Observatory, which is a facility of the National Science Foundation, operated under cooperative agreement by Associated Universities, Inc.

massive ellipticals. At present, however, the molecular gas content of sub-mm selected galaxies remains largely unknown, and a systematic inventory of the molecular gas and its properties in these sources is required in order to properly address the question of their typical mass and evolutionary status. Of particular importance is the ratio of gas and dynamical masses in such objects, since it can help determine whether sub-mm galaxies are merely high-redshift analogues of local ultra luminous infra-red galaxies (ULIRGs) or massive, large-scale galaxy-formation events. The difficulties arise mainly because sub-mm selected galaxies have proved extremely difficult to identify in the optical (cf. Ivison et al. 1998, 2000). As a result only a handful of sub-mm selected galaxies have been detected in CO to date (Frayer et al. 1998; Frayer et al. 1999; Ivison et al. 2001; Downes & Solomon 2003; Genzel et al. 2003; Neri et al. 2003)

ERO J164502+4626.4 (Graham & Dey 1996) was amongst the first EROs discovered by Hu & Ridgway (1994). Deep near-IR and optical spectroscopy of J164502 put it at a redshift of $z = 1.44$ (Graham & Dey 1996; Dey et al. 1999), and the detection of the Hα line and the [O II]λ3726,3729 doublet in its spectrum suggested that J164502 is an actively star-forming galaxy, possibly containing an AGN, and not an evolved elliptical at $z = 2 - 4$ as initially suggested by Hu & Ridgway (1994). The presence of large amounts of dust was inferred from sub-mm observations by Cimatti et al. (1998) and Dey et al. (1999), the latter detecting J164502 in the continuum at 450, 850 and 1350 μm. These observations together with detections of CO $J = 2 - 1$ and $J = 5 - 4$ by Andreani et al. (2000), which revealed the presence of large quantities of molecular gas, unamibiguously demonstrated that J164502 is a gas-rich dust-enshrouded starburst galaxy.

Here we present observations of the CO $J = 1 - 0$ emission from J164502 using the VLA, providing the first detection of the lowest, and thus least excitation biased, CO line in a galaxy typical of the sub-mm population. We also present the 850-μm SCUBA map of this source. Throughout this paper we have assumed $H_0 = 65\,\mathrm{km\,s^{-1}\,Mpc^{-1}}$, $\Omega_M = 0.3$ and $\Omega_\Lambda = 0.7$. In this cosmology the luminosity distance of J164502 is 11.2 Gpc and $1''$ corresponds to 9.1 kpc.

5.2 Observations and data reduction

5.2.1 Very Large Array observations

At $z = 1.44$ the CO $J = 1 - 0$ line from J164502 falls within the VLA's Q-band at 0.7 cm. The line widths of the CO $J = 5 - 4$ and $J = 2 - 1$ lines were $\simeq 400\,\mathrm{km\,s^{-1}}$ FWHM (Andreani et al. 2000), and a similar line width could be expected for the $J = 1 - 0$ line. In order to cover the entire CO line, two adjacent 50 MHz IF pairs (left and right circular polarisation) were centred at 47.235 and 47.285 GHz giving $635\,\mathrm{km\,s^{-1}}$ of coverage. Measurements of J164502 in the radio have yielded $S_{20\,cm} \leq 300\,\mu$Jy and $S_{3.6\,cm} = (35 \pm 11)\,\mu$Jy (Frayer 1996). Fitting a power law spectrum to these data points yields a spectral index of $\alpha \geq -1.25$. Adopting a more conservative spectrum with $\alpha = -0.7$, we find that the extrapolated synchroton flux at 0.7 cm amounts to no more than 11 μJy. Furthermore, the dust contributes by less than 10 μJy at these wavelengths (Dey et al. 1999). Hence, any contribution from continuum emission is neglible and no continuum subtraction was necessary. Observations were obtained in D and C configurations (see Table 1). Due to bad weather, all the C-configuration data were of poor quality and discarded, leaving a total of 11.6 hr of observing time on source. The primary calibrator, 3C 286, was observed at the beginning and end of each observing run in order to fix the absolute flux density scale. Every 3-4 minutes the antennas were pointed toward a phase calibrator to ensure phase coherence throughout the run. This fast-switching technique resulted in a residual phase rms, after calibration, of less than $\sigma_\phi \sim 20^o$. Calibration and data reduction was done using standard recipes in the NRAO $\mathcal{AIPS}$ Cookbook. D-configuration data taken at different

times were combined using DBCON, weighting each dataset by its total gridded weight.

TABLE 5.1
VLA OBSERVATIONS

Date	Configuration	Frequency, (GHz)	Integration time, (hrs)
2001 Oct 9	D	47.235,47.285	5.2
2002 Oct 26	C	47.235,47.285	2.9
2002 Nov 14	C	47.235,47.285	2.4
2002 Dec 24	C	47.235,47.285	2.6
2003 Feb 21	D	47.235,47.285	2.6
2003 Mar 1	D	47.235,47.285	3.8

The astrometrical uncertainty in the final CO map is given by $\sigma^2 = \sigma^2_{cal} + \sigma^2_{res} + \sigma^2_{SNR}$, where σ_{cal} is the uncertainty of the assumed position of the phase calibrator, σ_{res} is the residual rms phase error after the phase correction, and σ_{SNR} is the positional error due to the presence of thermal noise. In our case the latter is by far the most dominant source of error and is given by $\sigma_{SNR} \simeq (FWHM/2)/SNR$. Adopting $FWHM \simeq 3''$ and $SNR \simeq 7$ (see Fig. 1) we find the total positional error in the final CO map to be $\sim 0.2''$.

5.2.2 Submillimetre observations

Imaging data at 450 and 850-μm were obtained for J164502 using the Submillimetre Common User Bolometer Array (SCUBA – Holland et al. (1999)) during periods of exceptionally low opacity at the James Clerk Maxwell Telescope (JCMT[5]) on Mauna Kea, Hawaii. Data for J164502 were acquired during 1998 July 28–30 and 1998 September 03–05, a total integration time of 28.8 ks using a 45″ east-west nod/chop. In brief, data were flat-fielded, corrected for atmospheric losses, edited both automatically and by hand, plotted onto an astrometric grid and flux calibrated using observations of planets and secondary calibration sources. The map was convolved with a Gaussian resulting in a resolution of 14″.

5.2.3 Near-IR Observations

Near-IR K-band imaging was obtained of J164502 in June 2002 using the United Kingdom IR Telescope's (UKIRT[6]) UFTI imager, a 1024^2 HgTeCd array with 0.091″ pixels. Nine individual frames taken during good to moderate seeing conditions were co-registered and combined yielding a total exposure time of 2700s. The seeing in the final image is $\sim 0.8''$. Using 5 stars also detected in the USNO A2.0 catalogue (Monet et al. 1998), the UKIRT image was calibrated on to the USNO reference frame to within 0.2″ rms. The CO map was aligned to the K-band frame using the tasks GEO and HGEOM in *AIPS* resulting in a relative positional accuracy between the two of $\sim 0.3''$.

[5] The JCMT is operated by the Joint Astronomy Centre on behalf of the United Kingdom Particle Physics and Astronomy Research Council (PPARC), the Netherlands Organisation for Scientific Research, and the National Research Council of Canada.

[6] UKIRT is operated by the Joint Astronomy Centre on behalf of the United Kingdom Particle Physics and Astronomy Research Council (PPARC)

5.3 Results

In order to sensitively search for possible faint extended CO $J = 1 - 0$ emission, at the expense of high spatial resolution, we used the compact D-configuration data tapered down using a Gaussian with a full-width of 60 kλ at 30 per-cent amplitude, yielding a synthesized beam of $3.1'' \times 2.8''$. The resulting CO map overlaid on the UKIRT K-band image is shown in Fig. 1. CO $J = 1 - 0$ emission is detected at the 7σ significance level in J164502. Assuming that we cover the entire $J = 1 - 0$ line with the two IFs, and that we have rectangular passbands, we estimate the velocity-integrated flux-density using

$$\int_{\Delta v} S_{\nu_{obs}} dv = 2\Delta\nu_{IF} \frac{c}{\nu_{obs}} \overline{S}_{CO}, \tag{5.1}$$

where $\Delta\nu_{IF}$ is the width of the IF and $\overline{S}_{CO} = (S_1 + S_2)/2$ is the average of the flux density measured in the two IFs. Using the task IMEAN to get the flux density of the source in the two IF maps we find $\overline{S}_{CO} = 1.0 \pm 0.2$ mJy which yields a velocity-integrated flux density of 0.6 ± 0.1 Jy km s^{-1}, where we have used $\nu_{obs} = 47.26$ GHz and an IF bandwidth of 45 MHz instead of 50 MHz due to bandpass rollover.

As first noted by Dey et al. (1999) using high-resolution HST WFPC2 images, J164502 in the optical has a reflected S-shaped morphology with two bright knots at each end. A comparison with Keck K-band imaging revealed that the bulk of the near-IR emission comes from the region between the two bright knots located $\sim 0.4''$ north of the brightest optical knot (Dey et al. 1999). As seen from Fig. 1, the peak intensity in the CO $J = 1 - 0$ map coincides with the peak in the UKIRT K-band image both of which are coincident with the region of low optical emission found by Dey et al. (1999). A similar offset between the HST position and the CO $J = 2 - 1$ emission was reported by Andreani et al. (2000). While the near-IR emission traces the dust-enshrouded stars in J164502, the optical emission corresponds to regions of low extinction, and it is therefore not surprising to see such an offset between the two types of emission. Since gas should be a good tracer of dust one would expect the CO to coincide with the K-band emission, as it appears to do within the limits of our astrometric errors. A Gaussian fit to the CO data in the image plane yields a deconvolved source size of $4.5'' \times 3.0''$, suggesting that even in the D-configuration we have resolved the CO emission, albeit marginally. Different weighting schemes and tapering functions were tried in order to see the effects on the extended emission. Using a less restrictive tapering function (FWHM= 200kλ) and a robust parameter of 2 instead of 5 (natural weighting), thereby increasing the weight of the long baselines, the source still appeared extended although at a lower significance due to the larger noise on the longest baselines (see Figure 1). In order to confirm or dismiss the reality of the extended emission we shifted the peak of the CO emission to the phase center, and then plotted the binned real and imaginary parts of the complex visibilities as a function of baseline distance, Fig. 1. The complex visibilities are the Fourier components of the source brightness distribution. Hence, for a Gaussian source brightness distribution the real part of the complex visibilities is a Gaussian while the imaginary part will be zero since a Gaussian is an even function. The dashed curves in Fig. 1 represents a least-squares fit of a circular Gaussian to the visibilities. The position of the Gaussian was fixed to the phase center during the fit and only the amplitude and width were allowed to vary. We find that the real part of the visibilities is consistent with a Gaussian source model with a $FWHM = 3.9''$ in agreement with the Gaussian fit in the image plane. The imaginary part is consistent with zero at all baselines within the limits of our residual rms phase error of $\sigma_\phi \sim 20^o$. The phase error would give rise to a dispersion around zero of $\sigma(Im(V)) = \sigma(S \sin\phi) \simeq S\sigma(\phi)$ =1.0 mJy $(20^o/180^o)\pi \simeq 0.3$ mJy which is close to the observed scatter. The 850-μm SCUBA map of J164502 is shown in Fig. 2, and is seen to

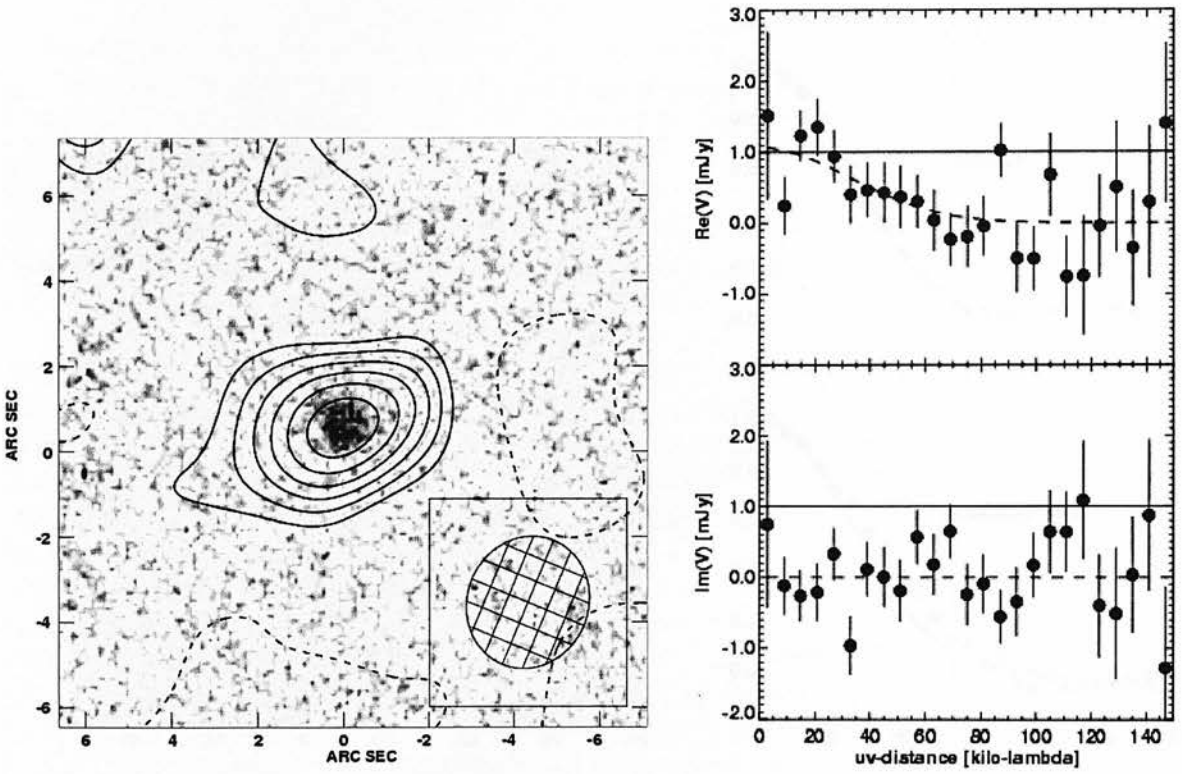

Figure 5.1: **Left:** Naturally weighted CO $J = 1 - 0$ contour map of J164502 overlaid on the UKIRT UFTI K-band image. The resolution of the CO map is $3.1'' \times 2.8''$ at $PA = 157^o$, see the insert. The contours are -2,2,3,4,5,6, and 7σ where $\sigma = 0.1\,\mathrm{mJy\,beam^{-1}}$. **Right:** The real (top panel) and imaginary (bottom panel) part of the complex visibilities vs. baseline. The visibilities have been binned. The solid line represents a point source with flux density of 1.0 mJy. The dashed curves represent a least-square fit of a Gaussian source model to the visibilities.

contain at least two statistically significant sources. A 7σ emission feature showing in the map is detected at a position which coincides with the near-IR and CO-detections of J164502, and we take this to unambiguously be the 850-μm SCUBA detection of J164502. Another source, marked as J164502-SMM1 in Fig. 2, detected at the 5σ level is seen $50''$ to the south, with faint emission at the 4σ level also seen just $\sim 20''$ south of J164502. We estimated the 850-μm flux density in four different ways. Two estimates were made by measuring the flux within apertures of $20''$ and $16''$ diameter. A third measurement was made by fitting a Gaussian to the emission, and a fourth by fitting a Gaussian with a fixed $FWHM$ of $15''$ to the emission. The values derived from each of these measurements are given in Table 2 for J164502 as well as J164502-SMM1. For J164502 we find $S_{850\mu\mathrm{m}} = 8 \pm 2\,\mathrm{mJy}$ where we have adopted the average of the four different measurements. While this is in good agreement with the 850-μm measurement by Cimatti et al. (1998), it is larger than the flux quoted by Dey et al. (1999). Both of these measurements were obtained using SCUBA in its photometry mode but the latter value is based on twice as large a data-set as the former, taken in excellent weather conditions and is therefore the most reliable estimate. If this is the case, the large discrepancy between the flux density derived from our map and the value derived from photometry-measurement by Dey et al. (1999) could be due to

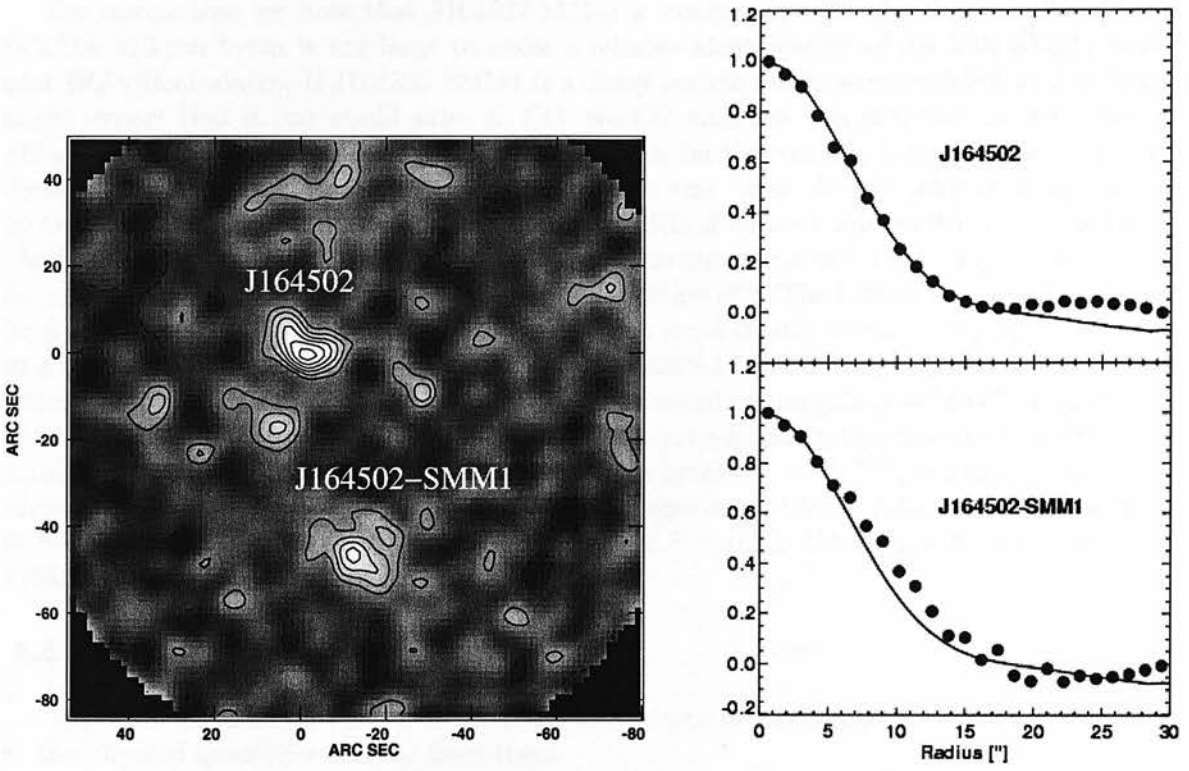

Figure 5.2: **Left:** SCUBA 850-μm jiggle-maps of J164502. The resolution is $FWHM = 14''$, and the rms noise level is 1.6 mJy beam^{-1}. Contours start at 2σ. J164502-SMM1 denotes a statistically significant detection of 850-μm emission about $50''$ south of J164502. Weak emission is also seen $20''$ south-east of J164502. **Right:** Radial profiles of J164502 and J164502-SMM1 (filled circles) compared with the radial profile of the PSF (solid curve).

extended emission from J164502 which would have been missed by the single pixel measurement.

From the 850-μm map in Fig. 2 it is seen that the emission from J164502 does in fact appear to be extended, with emission to the NE. The reality of this extended emission is strengthened by the high-resolution Keck K-band image obtained by Dey et al. (1999) which shows an emission feature extending in the same direction, albeit on a smaller scale of $\gtrsim 1''$ (see Fig. 2 of Dey et al. (1999)). However, the fact that the stars traced by the K-band emission is extended on scales of $\gtrsim$9 kpc means that cold dust is distributed on at least the same scales, and likely on much larger scales. Fitting a Gaussian to the SCUBA image yields a source size of $15.1''$ along the major axis, which is comparable to the $14''$ resolution of the map, though very tentatively suggestive of a slight extension. In Fig. 2 we compare the azimuthally averaged radial profiles of J164502 and J164502-SMM1 with the point spread function (PSF) of SCUBA at 850-μm derived from a beam map of a bright blazar obtained during the same observing run. The radial profile of J164502 agrees with the PSF out to $r \simeq 20''$ beyond which it displays excess emission over that of a point source. This bump in the radial profile is due to the 4σ emission feature $20''$ south ($\sim$ 180 kpc) of J164502. The reality of this emission feature is questionable but if real its close vicinity to J164502 could mean that it is a system in the process of merging with J164502. While there is thus tentative evidence that J164502 is extended, the large beam size of SCUBA

does not allow for a firm conclusion on this issue.

For comparison we note that J164502-SMM1 is consistent with the PSF at all radii. The SCUBA 850-μm beam is too large to make a reliable identification of J164502-SMM1 with an near-IR/optical source. If J164502-SMM1 is a dusty system at the same redshift as J164502 one might expect that it too would shine in CO. No CO emission was detected at the position of J164502-SMM1, however, and we set an upper limit on the velocity-integrated line flux using the equation $S_{\rm CO}\Delta v < 3\sigma(\delta v dv)^{1/2}$, where σ is the rms noise, δv the velocity resolution, and dv the line width which we assume to be equal to the $J = 2-1$ line width, i.e. $\sim 400\,{\rm km\,s^{-1}}$ (Andreani et al. 2000). The measured rms noise in the image is $\sigma \simeq 0.1\,{\rm mJy\,beam^{-1}}$ which yields $S_{\rm CO}\Delta v < 0.2\,{\rm Jy\,km\,s^{-1}}$ for a velocity- coverage of $635\,{\rm km\,s^{-1}}$. The failure to detect CO-emission from J164502-SMM1 does not rule out a association since cluster velocity dispersions can go up to $\gtrsim 1000\,{\rm km\,s^{-1}}$, and in some cases even closely associated CO-emitting regions can have velocity differences of $\sim 1000\,{\rm km\,s^{-1}}$ as was seen in the high redshift radio galaxy 4C 60.07 (Papadopoulos et al. 2000). The probability of finding by chance a source with a flux density brighter than or equal to 6 mJy within $r = 50''$ from J164502 is given by $P = 1 - e^{-\pi r^2 N}$, where N is the average surface density of sources with $S_{850\mu{\rm m}} \geq 6\,{\rm mJy}$ (Downes et al. 1986). Adopting a surface density of $N \sim 400\,{\rm deg^{-2}}$ (Borys et al. 2003) one finds that $P = 0.22$. On that basis we conclude that J164502-SMM1 is most likely unrelated to J164502.

5.4 Analysis & Discussion

Table 2 summarises the CO and sub-mm observations of J164502 and J164502-SMM1 as well as the physical quantities derived from them.

5.4.1 Molecular gas and dust in J164502

For an observed velocity-integrated line flux density of the $J+1 \rightarrow J$ CO line, the intrinsic CO line luminosity is given by

$$\mathrm{L_{CO_{J+1,J}}} = \frac{\mathrm{c}^2}{2\mathrm{k}\nu^2_{\mathrm{J+1,J}}} \frac{\mathrm{D_L^2}}{1+\mathrm{z}} \int_{\Delta \mathrm{v}} \mathrm{S}_{\nu_{\mathrm{obs}}} \mathrm{dv}, \tag{5.2}$$

where D_L is the luminosity distance, and $\nu_{J+1,J}$ is the rest-frame frequency of the CO transition. Inserting astrophysical units, the equation reads

$$\mathrm{L'_{CO_{J+1,J}}} = 2.43 \times 10^3 (\mathrm{J}+1)^{-2} (1+\mathrm{z})^{-1} \left(\frac{\mathrm{D_L}}{\mathrm{Mpc}}\right)^2 \left(\frac{\int_{\Delta \mathrm{v}} \mathrm{S}_{\nu_{\mathrm{obs}}} \mathrm{dv}}{\mathrm{Jy\,km\,s^{-1}}}\right), \tag{5.3}$$

where $\mathrm{L'_{CO_{J+1,J}}}$ is the so-called pseudo-luminosity which is measured in units of $\mathrm{K\,km\,s^{-1}\,pc^2}$. The observed CO $J = 1-0$ line flux density for J164502 implies an intrinsic CO luminosity of $L'_{\rm CO(1-0)} = (7 \pm 1) \times 10^{10}\,{\rm K\,km\,s^{-1}\,pc^2}$. From the CO $J = 1-0$ line the molecular gas mass can be found using the scaling relation $M({\rm H_2}) = {\rm X_{CO}} L'_{\rm CO(1-0)}$ where $X_{\rm CO} \simeq 5\,M_\odot\,({\rm K\,km\,s^{-1}\,pc^2})^{-1}$ is the standard Galactic CO-H_2 conversion factor. The standard conversion factor, $X_{\rm CO}$ has been calibrated using Giant Molecular Clouds (GMCs) in our Galaxy (Strong et al. 1988). However, the conditions of the interstellar medium in active starbursting galaxies such as ULIRGs is markedly different from that in our Galaxy, and applying the Galactic conversion factor would result in seriously underestimated gas masses. In particular, the concept of isolated and virialised GMCs breaks down, and instead the bulk of the CO emission is found to originate from a warm diffuse phase. In effect, this yields a lower conversion factor of $X_{\rm CO} = 0.8\,M_\odot\,({\rm K\,km\,s^{-1}\,pc^2})^{-1}$,

more appropriate for such extreme environments (Downes & Solomon 1998). It is reasonable to assume that in high-redshift starbursts similar conditions prevail and the aforementioned value of $X_{\rm CO}$ is also adopted for J164502. In doing so we estimate the molecular gas mass present in J164502 to be $M(\mathrm{H_2}) = (6 \pm 1) \times 10^{10}\,M_\odot$. This is in agreement with the $J = 2 - 1$ detection by Andreani et al. (2000), which yields a molecular gas mass of $\sim 4 \times 10^{10}\,M_\odot$ when converted to the cosmology adopted in this paper.

The CO $J = 1 - 0$ line luminosity and the implied molecular gas mass of J164502 is somewhat lower than those found in the quasars APM 08279+5255 and PSS 2322+1944, and in the high redshift radio galaxy 4C 60.07 ($L'_{\rm CO(1-0)} \sim 10^{11}\,\mathrm{K\,km\,s^{-1}\,pc^2}$ and $M(\mathrm{H_2}) \sim 10^{11}\,M_\odot$ - see Papadopoulos et al. 2001; Carilli et al. 2002; Greve et al. in preparation). This is not surprising since these objects are among the most luminous systems in the Universe, and might therefore be expected to contain more gas. Solomon et al. (1997) observed CO $J = 1 - 0$ in a sample of 37 local ULIRGs out to a redshift of $z = 0.3$, and found an average $J = 1 - 0$ luminosity of $L'_{\rm CO(1-0)} \simeq 8 \times 10^9\,\mathrm{K\,km\,s^{-1}\,pc^2}$ which is roughly the luminosity of Arp 220 and Mrk 231. The scatter on this result was only 30 per cent. A more recent survey of CO $J = 1 - 0$ observations of a complete sample of 60 ULIRGs selected from the SCUBA Local Universe Galaxy Survey (SLUGS - Dunne et al. (2000)) yielded similar results (Yao et al. 2003). Hence, we find that J164502 has a CO $J = 1 - 0$ luminosity and consequently a molecular gas mass which is about an order of magnitude larger than is found for local ULIRGs.

The dynamical mass of the system can be calculated from the observed size and line width of the source and assuming the gas is distributed in a disk with diameter L in Keplerian rotation, in which case it can be shown that the dynamical mass is given by

$$M_{dyn} \simeq \frac{\Delta V_{FWHM}^2 L}{2\alpha_d G} \frac{1}{\sin^2 i} \tag{5.4}$$

$$= 1.16 \times 10^9 \left(\frac{\Delta V_{FWHM}}{100\,\mathrm{km\,s^{-1}}}\right)^2 \times \left(\frac{R}{\mathrm{kpc}}\right) \frac{1}{\sin^2 i} M_\odot\,, \tag{5.5}$$

where i is the inclination angle of the disk, and α_d is a correction factor of order unity (Bryant & Scoville 1996). Adopting a line width of $\Delta V_{FWHM} = 400\,\mathrm{km\,s^{-1}}$ (Andreani et al. 2000), a source size of $\theta \lesssim \sqrt{4.5'' \times 3.0''} = 3.7''$, which corresponds to a maximum linear diameter of $L \sim 34\,\mathrm{kpc}$ at a redshift of $z = 1.44$ we estimate the enclosed dynamical mass within the CO-emitting region to be $M_{dyn} \lesssim 6.3 \times 10^{11} (\sin i)^{-2}\,M_\odot$. The inferred ratio of the molecular-to-dynamic mass for the system as a whole is then $M(\mathrm{H_2})/\mathrm{M_{dyn}} \gtrsim 0.1 \sin^2 \mathrm{i}$. Hence, geometrical factors aside, the amount of molecular gas accounts for at least 10 per cent of the total dynamical mass within the CO-emitting region. The dynamical mass should be considered an upper limit on the total amount of molecular gas present in J164502, and the two mass estimates would only coincide if the CO emission was concentrated within the inner $\sim 3\,\mathrm{kpc}$. Due to the higher spatial resolution and the fact that the $J = 1 - 0$ line provides an unbiased estimate of $M(\mathrm{H_2})$, our constraint on the molecular-to-dynamical mass ratio should be an improvement over that of Andreani et al. (2000). A gas mass fraction of $\gtrsim 10$ per cent is compatible with the range of gas mass fractions found for local ULIRGs (Downes & Solomon 1998) yet, unlike the latter, it is distributed over significantly larger scales.

The extrapolated synchroton radiation flux at 850-μm is less than 3 μJy, and it is therefore safe to assume that the observed 850-μm flux from J164502 is dominated by thermal dust emission, with the radio synchroton emission contributing a negligible amount. The dust mass can therefore be estimated using

$$M_d = \frac{S_{\nu_{\rm obs}} D_L^2}{(1+z)\kappa_d(\nu_{\rm rest})} \left[B(\nu_{\rm rest}, T_d) - B(\nu_{\rm rest}, T_{cmb}(z)\right]^{-1}\,, \tag{5.6}$$

where $\nu_{rest} = \nu_{obs}(1+z)$ is the rest-frame frequency, $T_{cmb}(z)$ is the CMB temperature at redshift z, and $\kappa_d \propto \nu^\beta$ is the dust absorption coefficient. The emissivity index, β, depends on the dust temperature, T_d, (Dunne et al. 2000) both of which are poorly constrained for high-redshift objects - typical values are $\beta = 1-2$. Dey et al. (1999) found the spectral energy distribution (SED) of J164502 to be well described by an optically thin modified black body law with a dust temperature of $T_d = 40\,\mathrm{K}$ and an emissivity law of $\beta = 1.5$, and we adopt those values here. In doing so we estimate the dust mass to be $M_{dust} \simeq 9 \times 10^8\,M_\odot$, where we have used a dust absorption coefficient of $\kappa_d(\nu_{rest}) = 0.11(\nu_{rest}/353\,\mathrm{GHz})^\beta\,\mathrm{m^2\,kg^{-1}}$ after Hildebrand (1983). The uncertainty in k_d is large, so we present this estimate for comparison only. We can estimate the total far-IR luminosity by integrating the thermal spectrum

$$L_{FIR} = 4\pi M_d \int_0^\infty \kappa_d(\nu) B(\nu, T_d) d\nu, \tag{5.7}$$

which yields a total far-IR luminosity of $L_{FIR} \simeq 9 \times 10^{12}\,L_\odot$. This almost puts J164502 in the class of hyperluminous infrared galaxies (HyLIRGs) which have $L_{FIR} \gtrsim 10^{13}\,L_\odot$. The dust masses and far-IR luminosities typically found in local ULIRGs are $M_{dust} \simeq 10^{7-8}\,M_\odot$ and $L_{FIR} \gtrsim 10^{12}\,L_\odot$ (Sanders & Mirabel 1996; Dunne et al. 2000), i.e. nearly an order of magnitude smaller than what we find for J164502. It is comparable, however, to what is found in high-redshift QSOs and HzRGs (Omont et al. 2003; Archibald et al. 2001) and, perhaps more importantly, similar to the dust masses and far-IR luminosities found in sub-mm-selected dust-enshrouded starbursts at high redshifts (Ivison et al. 1998, 2000). From the above we estimate the gas-to-dust mass ratio of J164502 to be $M(\mathrm{H_2})/\mathrm{M_{dust}} \simeq 67$ which is well within the range of 50-100 found for local ULIRGs. Note, however, that significant uncertainty is attached to the normalisation of κ_d, and values differing by as much as a factor of two has been reported (Draine & Lee 1984; Mathis & Whiffen 1989), which in turn could lead to a similar change in the dust mass but not in L_{FIR} which is independent of the normalisation value of the dust absorption coefficient. Using $\beta = 2.0$ instead of 1.5 would decrease the dust mass by nearly a factor of two, but increase L_{FIR} by a similar amount.

If the bulk of the far-IR emission can be ascribed to starburst activity the corresponding star formation rate is given by

$$SFR \simeq L_{FIR} 10^{-10} \delta_{IMF} \delta_{SB}\,L_\odot\,M_\odot\,\mathrm{yr^{-1}}, \tag{5.8}$$

where $\delta_{IMF} \sim 0.8-2$ is a function of the initial mass function, and δ_{SB} is the fraction of the FIR emission which is heated by the starburst (Omont et al. 2001). Assuming a conservative value of $\delta_{IMF} = 1$, we estimate the starformation rate in J164502 to be $SFR \simeq 900\delta_{SB}\,M_\odot\,\mathrm{yr^{-1}}$. It is possible that J164502 harbours an AGN in its center, so a significant fraction of the far-IR luminosity could be due to dust being heated by the AGN and not by the starburst. The derived value for the SFR could therefore be overestimated. However, the narrow linewidths seen in optical and NIR spectra of J164502 (Dey et al. 1999) favours young hot stars over an AGN as the main source of energy. Furthermore, as pointed out by Dey et al. (1999), J164502 deviates from the $60\,\mu$m - 6 cm relation obeyed by local star-forming galaxies by having almost an order of magnitude less radio emission at 6 cm, which is unlikely if an AGN dominated the energetics of the system (Dey & van Breugel 1994). In addition, it is found that the bulk of the far-IR emission from local ULIRGs is powered by starburst activity even though an AGN is present (Downes & Solomon 1998). Finally, if the sub-mm emission is extended it would strongly suggest that the main power source for the far-IR emission is a massive starburst since it is difficult to imagine the AGN heating the dust on scales of tens of kpc. The large quantity of molecular gas

TABLE 5.2
OBSERVED PROPERTIES OF J164502

Parameter	J164502	J164502-SMM1
α (J2000)	16:45:02.26	16:45:01.20
δ (J2000)	+46:26:26.50	+46:25:39.0
$z_{\rm CO}$	1.439	
$\int_{\Delta V} S_{\rm CO(1-0)} dV$ [Jy km s^{-1}]	0.6 ± 0.1	< 0.2
$S_{850\mu{\rm m}}$ [mJy]	$8 \pm 2^{\rm a}$	$6 \pm 2^{\rm b}$
$L'_{\rm CO}(1-0)$ [K km s^{-1} pc^{-1}]	$(7 \pm 1) \times 10^{10}$	$< 2 \times 10^{10{\rm c}}$
L_{FIR} [$L_\odot$]	9×10^{12}	$7 \times 10^{12{\rm c}}$

[a] The average of 7.5/7.9/7.3/9.8 mJy which was the flux densities obtained using the four different methods described in section 3.
[b] The average of 6.7/6.5/6.0/6.5 mJy which was the flux densities obtained using the four different methods described in section 3.
[c] This value assumes that J164502-SMM1 has a redshift of $z = 1.439$.

revealed by the CO detections in this system could provide the necessary fuel for such a massive starburst for a period of $\sim 10^7$ years.

The efficiency of star formation should be measured relative to the amount of molecular gas available to form stars. Such a measure of the star-formation efficiency is the rate of star formation per solar mass of molecular hydrogen, i.e. $L_{FIR}/M({\rm H_2})$. For J164502 we find $L_{FIR}/M({\rm H_2}) \simeq 150\, L_\odot\, {M_\odot}^{-1}$. Probably a better gauge of the star-formation efficiency is the continuum-to-line ratio $L_{FIR}/L'_{\rm CO}(1-0)$ since it is independent of $X_{\rm CO}$. Giant Molecular Cloud (GMCs) in our Galaxy typically have values of ~ 15 and similar ratios are found in nearby spirals (Mooney & Solomon 1988). Starburst galaxies and ULIRGs have $L_{FIR}/L'_{\rm CO}(1-0)$ ratios which are 10 times higher than this, ranging in values from 80 to 250 with a median of $160\, L_\odot\, ({\rm K\,km\,s^{-1}\,pc^2})^{-1}$ (Solomon et al. 1997). For J164502 we find $L_{FIR}/L'_{\rm CO}(1-0) \simeq 129\, L_\odot\, ({\rm K\,km\,s^{-1}\,pc^2})^{-1}$, i.e. in line with what is found for local ULIRGs. Recent studies of large samples of ULIRGs at low and intermediate redshifts have shown that the $L_{FIR}/L'_{\rm CO}(1-0)$ ratio increases with increasing L_{FIR} (Young et al. 1986; Tutui et al. 2000; Yao et al. 2003). Such behaviour can be explained if the more far-IR luminous galaxies, in addition to having more dust and gas which would just continue the linear relation between L_{FIR} and $L'_{\rm CO}(1-0)$, have higher dust temperatures due to extra heating by an AGN or a higher star-formation efficiency. Assuming that there is no contribution to L_{FIR} from an AGN, the derived $L_{FIR}/L'_{\rm CO}(1-0)$-ratio should probably be taken as a lower limit on the star-formation efficiency since in the extreme starburst regions dominating the emission from ULIRGs, the bulk of the CO luminosity comes from a diffuse inter-cloud medium, rather than from the dense gas gravitationally bound in clouds where the stars are formed (Downes et al. 1993; Solomon et al. 1997). The dense gas is better traced by HCN, and as shown by Gao et al. (1999) the $L_{FIR}/L_{\rm HCN}$-ratio is the same for GMCs to ULIRGs, indicating that anywhere in the Universe only the dense gas is relevant to star-formation. In ULIRGs the dense/diffuse gas mass ratio (roughly quantified by $L_{\rm HCN}/L_{\rm CO}$) is particularly high which is not a surprise given their merger status and the way the gas responds to a merger.

5.4.2 Excitation conditions of the molecular gas in J164502

The velocity/area-averaged brightness temperature ratio between CO $J+1 \rightarrow J$ and CO $1 \rightarrow 0$ is

$$r_{J+1,J} = \frac{T_b(J+1 \rightarrow J)}{T_b(1 \rightarrow 0)} = \frac{L'(J+1 \rightarrow J)}{L'(1 \rightarrow 0)}. \quad (5.9)$$

Andreani et al. (2000) estimated the CO $J = 2-1$ and $J = 5-4$ luminosities to be 4×10^{10} and $7 \times 10^9\,\mathrm{K\,km\,s^{-1}\,pc^2}$, respectively, where we have converted the luminosities to the cosmology adopted here. The line ratios estimated from eq. 9 are $r_{21} = 0.6 \pm 0.2$ and $r_{54} = 0.10 \pm 0.05$. The majority of high-redshift systems detected in CO to date are strongly gravitationally lensed. This makes estimating the excitation conditions in such systems complicated since differential magnification of the high-J lines compared to lower transitions may bias the line ratios significantly. There is nothing to suggest that J164502 is gravitationally lensed, and the above derived line ratios ought to represent the intrinsic excitation conditions of the gas, albeit still averaged over the entire galaxy.

We used the observed line ratios of $r_{21} = 0.6 \pm 0.2$ and $r_{54} = 0.10 \pm 0.05$ as constraints to a Large Velocity Gradient (LVG) code in order to gain some insight on the bulk properties of the molecular gas in J164502. A lower limit on gas temperature $\mathrm{T_{kin}} = 40\,\mathrm{K}$ is assumed since this value is deduced for the bulk of the dust (Dey et al. 1999) and $\mathrm{T_{kin}} \gtrsim \mathrm{T_{dust}}$ is expected for FUV-heated gas/dust (Tielens & Hollenbach 1999). A wide range of temperatures ($\mathrm{T_{kin}} = 60 - 90\,\mathrm{K}$) offers an acceptable fit to the aforementioned line ratios, with $\mathrm{T_{kin}} = 70\,\mathrm{K}$ being the optimal value. This wide range is due to the poor constraints offered by only two line ratios while the high gas temperatures may reflect the UV-intense environment of the molecular gas in J164502 and/or turbulent motions heating only the gas, a situation that has already been noted for molecular gas in the Galactic center (Rodriguez-Fernandezxi et al. 2001).

A common feature of all the LVG solutions is the low gas densities $\mathrm{n(H_2)} \sim 300\ \mathrm{cm^{-3}}$. This has already been noted when only the CO $(5-4)/(2-1)$ line ratio was available (Papadopoulos & Ivison 2002) and is a property often found for the bulk of the gas in extreme starbursts (Aalto et al. 1995; Downes & Solomon 1998). Interestingly for such low gas densities all CO $J+1 \rightarrow J$ transitions with $J+1 > 5$ have flux density ratios with respect to the lowest $1-0$ transition of $S(J+1-J)/S(1-0) = (J+1)^2\, r_{\mathrm{J+1\ J}} \lesssim 0.25$ for any plausible gas temperature ($\mathrm{T_{kin}} \sim 40 - 100\,\mathrm{K}$), thus no longer offering the advantage of a higher flux density with respect to the latter.

As a consequence, any estimate of the $\mathrm{H_2}$ mass based on the assumption of optically thick, thermalised high-J CO lines could be severely underestimated. Using the 5–4 line in J164502 only, and assuming it is optically thick and thermalised ($r_{54} \sim 1$), one would find a molecular gas mass which is an order of magnitude lower than that inferred from the $J = 1-0$ line. There is no significant flux advantage between the 2–1 and 1–0 lines, since $S_{\mathrm{CO}}(2-1)/S_{\mathrm{CO}}(1-0) = 4T_b(2-1)/T_b(1-0) > 1$ even for a very subthermal ratio of $r_{21} = 0.3$, say. This is consistent with the fact that we find the molecular masses derived from the two lines to be similar (section 4.1). The above demonstrates the importance of using low-J CO lines in order to infer the amount of molecular gas in a galaxy. This is particularly true at redshifts beyond 3, since at those redshifts the current mm-interferometers can only hope to detect CO $J+1 \rightarrow J$, $J > 2$, and the the excitation bias of the high-J lines could become very severe.

5.4.3 Comparison with high-redshift sub-mm galaxies

Although J164502 was originally selected as an ERO and not a (sub)millimetre galaxy, subsequent observations at optical/IR and sub-mm wavelengths have shown that it can in fact be

considered a typical sub-mm galaxy (Dey et al. 1999; see also Smail et al. 1999). Our detection of CO $J = 1 - 0$ in J164502 is therefore the first detection of this transition in a galaxy which is thought to be similar to the SCUBA population of dust-enshrouded galaxies at high redshifts. J164502 has a far-IR and CO luminosity about ten times that of the average values found in ULIRGs, and the amount of molecular gas present in J164502 is comparable to the median gas mass ($\sim 2 \times 10^{10} M_{\odot}$) of the five SCUBA galaxies detected in CO to date (Neri et al. 2003), although a thorough characterisation of the gas content of this population has to await CO observations of a large, unbiased sample of submm-selected galaxies. Hence, the observations presented here further supports that J164502 is more similar in its properties to sub-mm galaxies than a high-redshift analogue of Arp 220.

Recently, a subject of some debate has been whether the CO emission detected from high-redshift sub-mm galaxies originates from a huge, massive resevoir of molecular gas ~ 10 kpc in size or from a much more compact circumnuclear disk, typically of radius $r \sim 100$ pc, as seen in local ULIRGs such as Arp 220 (Ivison et al. 2001; Genzel et al. 2003; Downes & Solomon 2003). If, as the observations seem to suggest, the starburst in J164502 is extended over several tens of kpc that would set apart from the local ULIRG population and point toward the former scenario.

Acknowledgements

TRG acknowledges support from the Danish Research Council and from the EU RTN Network POE. PPP acknowledges a Marie Curie Individual Fellowship HPMT-CT-2000-00875. The authors wish to thank Ignas Snellen and Philip Best for useful advices on *AIPS*, and Omar Almaini for kindly providing us with the reduced UKIRT UFTI K-band image of J164502+4626.4. We also thank Jason Stevens and Andy Taylor for useful discussions.

References

Aalto, S., Booth, R. S., Black, J. H. & Johansson, L. E. B. 1995, A&A, 300, 369.
Andreani, P., Cimatti, A., Loinard, L. & Röttgering, H. 2000, A&A, 354, L1.
Archibald, E. N., Dunlop, J. S., Hughes, D. H., Rawlings, S., Eales, S. A. & Ivison, R. J. 2001, MNRAS, 323, 417.
Bertoldi, F., Menten, K.M., Kreysa, E., Carilli, C.L. & Owen, F. 2001, 24th meeting of the IAU, Manchester, England (astro-ph 0010553).
Borys, C., Chapman, S., Halpern, M. & Scott, D. 2003, MNRAS , in press, astro-ph/0305444.
Brown, R.L. & vanden Bout, P.A. 1991, A&A, 102, 1956.
Bryant, P.M. & Scoville, N.Z. 1996, ApJ, 457, 678.
Carilli, C.L., Cox, P., Bertoldi, F., Menten, K.M., Omont, A., Djorgovski, S.G., Petric, A., Beelen, A., Isaak, K.G. & McMahon, R.G. 2002, ApJ, 575, 145.
Chapman, S.C., Blain, A.W., Ivison, R.J. & Smail, I. 2003, Nature, accepted.
Cimatti, A., Andreani, P., Röttgering, H. & Tilanus, R. 1998, Nature, 392, 895.
Dey, A. & van Breugel, W. 1994, "Mass Transfer Induced Activity in Galaxies", Cambridge Univ. Press, ed. Shlosman, I.
Dey, A., Graham, J. R., Ivison, R. J., Smail, I., Wright, G. S. & Liu, M. C. 1999, ApJ, 519, 610.
Downes, A. J. B., Peacock, J. A., Savage, A., Carrie, D. R. 1986, MNRAS, 218, 31.
Downes, D., Solomon, P.M. & Radford, S.J.E. 1993, ApJ, 414, L13.
Downes, D. & Solomon, P.M. 1998, ApJ, 507, 615.
Downes, D. & Solomon, P.M. 2003, ApJ, 582, 37.
Draine, B. & Lee, H. 1984, ApJ, 285, 89.

Dunlop, J., Peacock, J., Spinrad, H., Dey, A., Jimenez, R., Stern, D. & Windhorst, R., Nature, 381, 581.
Dunne, L., Eales, S, Edmunds, M., Ivison, R.J., Alexander & P. Clements, D.L. 2000, MNRAS, 315, 115.
Frayer, D.T. 1996, PhD Thesis, University of Virginia.
Frayer, D.T., Ivison, R.J., Scoville, N.Z., Yun, M., Evans, A.S., Smail, I., Blain, A.W. & Kneib, J.-P. 1998, ApJ, 506, 7.
Frayer, D.T., Ivison, R.J., Scoville, N.Z., Evans, A.S., Yun, M.S., Smail, I., Barger, A.J., Blain, A.W. & Kneib, J.-P. 1999, ApJ, 514 L13.
Gao, Y., Solomon, P.M. & Philip, M. 1999, ApJ, 512, 99.
Genzel, R., Baker, A.J., Tacconi, L.J., Lutz, D., Cox, P., Guilloteau, S. & Omont, A. 2003, ApJ, 584, 633.
Graham, J. R. & Dey, A. 1996, ApJ, 471, 720.
Hildebrand, R. 1983, QJRAS, 24, 267.
Holland, W. S., Robson, E. I., Gear, W. K., Cunningham, C. R., Lightfoot, J. F., Jenness, T., Ivison, R. J., Stevens, J. A., Ade, P. A. R., Griffin, M. J., Duncan, W. D., Murphy, J. A. & Naylor, D. A. 1999, MNRAS, 303, 659.
Hu, E. M. & Ridgway, S. E. 1994, AJ, 107, 1303.
Hughes, D.H., Serjeant, S., Dunlop, J., Rowan-Robinson, M., Blain, A., Mann, R. G., Ivison, R., Peacock, J., Efstathiou, A., Gear, W., Oliver, S., Lawrence, A., Longair, M., Goldschmidt, P. & Jenness, T. 1998, Nature, 394, 241.
Ivison, R.J., Papadopoulos, P.P., Seaquist, E.R. & Eales, S.A. 1996, MNRAS, 278, 669.
Ivison, R.J., Smail, I., Le Borgne, J.-F., Blain, A.W., Kneib, J.-P., Bezecourt, J., Kerr & T.H., Davies, J.K. 1998, MNRAS, 298, 583.
Ivison, R.J., Smail, I., Barger, A.J., Kneib, J.-P., Blain, A.W., Owen, F.N., Kerr, T.H. & Cowie, L.L. 2000, MNRAS, 315, 209.
Ivison, R.J., Smail, I., Frayer, D.T., Kneib, J.-P. & Blain, A.W. 2001, ApJ, 561, L45.
Ivison, R.J., Greve, T.R., Smail, I., Dunlop, J., Roche, N., Scott, S., Page, M., Stevens, J., Almaini, O., Blain, A., Willott, C., Fox, M., Gilbank, D., Serjeant, S. & Hughes, D. 2002, MNRAS, 337, 1.
Kreysa, E., Gemuend, H.-P., Gromke, J., Haslam, C.G., Reichertz, L., Haller, E.E., Beeman, J.W., Hansen, V., Sievers, A. & Zylka, R. 1998, Proc SPIE 3357, 319.
Mathis, J. & Whiffen, G. 1989, ApJ, 341, 808.
Monet, D., Bird A., Canzian, B., Dahn, C., Guetter, H., Harris, H., Henden, A., Levine, S., Luginbuhl, C., Monet, A. K. B., Rhodes, A., Riepe, B., Sell, S., Stone, R., Vrba, F. & Walker, R. 1998, USNO-SA2.0 (U.S. Naval Observatory, Washington DC).
Mooney, T. & Solomon, P.M. 1988, ApJ, 334, L51.
Moriondo, G., Cimatti, A., Daddi, E. 2000, A&A, 364, 26.
Neri, R., Genzel, R., Ivison, R.J., Bertoldi, F., Blain, A.W., Chapman, S.C., Cox, P., Greve, T.R., Omont, A. & Frayer, D.T. 2003, ApJ, submitted.
Omont, A., Cox, P., Bertoldi, F., McMahon, R., Carilli, C., & Isaak, K. G. 2001, A&A, 374, 371.
Omont, A., Beelen, A., Bertoldi, F., Cox, P., Carilli, C. L., Priddey, R. S., McMahon, R. G. & Isaak, K. G. 2003, A&A, 398, 857.
Papadopoulos, P. P., Röttgering, H. J. A., van der Werf, P. P., Guilloteau, S., Omont, A., van Breugel, W. J. M. & Tilanus, R. P. J. 2000, ApJ, 528, 626.
Papadopoulos, P.P., Ivison, R.J., Carilli, C.L. & Lewis, G. 2001, Nature, 409, 58.
Papadopoulos, P. P. & Ivison, R.J. 2002, ApJ, 564, L9.
Rodriguez-Fernandez, N. J., Martin-Pintado, J., Fuente, A., de Vicente, P., Wilson, T. L., &

Hüttemeister, S. 2001, A&A, 365, 174.
Sanders, D.B., Scoville, N.Z. & Soifer, B.T. 1991, ApJ, 370, 158.
Sanders, D.B. & Mirabel, I.F. 1996, ARA&A, 34, 749.
Smail, I., Ivison, R.J. & Blain, A.W. 1997, ApJ, 490, L5.
Smail, I., Ivison, R.J., Kneib, J.-P., Cowie, L.L., Blain, A.W., Barger, A.J., Owen, F.N. & Morrison, G. 1999, MNRAS, 308, 1061.
Solomon, P.M., Downes, D., Radford, S.J.E. & Barrett, J.W. 1997, ApJ, 478, 144.
Strong, A. W., Bloemen, J. B. G. M., Dame, T. M., Grenier, I. A., Hermsen, W., Lebrun, F., Nyman, L.-A., Pollock, A. M. T. & Thaddeus, P. 1988, A&A, 201, 1.
Tielens, D.J. & Hollenbach, A.G.G.M. 1999, Rev. Modern Physics, 71, 174.
Tutui, Y., Sofue, Y., Honma, M., Ichikawa & T., Wakamatsu, K.-i. 2000, PASP. 52, 803.
Yao, L., Seaquist, E.R., Kuno, N. & Dunne, L. 2003, AJ, accepted.
Young, J.S., Schloerb, F.P., Kenney, J.D. & Lord, S.D. 1986, ApJ, 304, 443.

Chapter 6

Detection of CO $J = 1 - 0$ in the $z = 3.79$ Radio Galaxy 4C 60.07

Abstract. We report on the detection of the lowest CO $J = 1 - 0$ transition in the powerful high-redshift radio galaxy 4C 60.07 at $z = 3.79$. The CO emission is distributed in two spatially and kinematically distinct components as was previously known from the observations of the higher excitation CO $J = 4 - 3$ line. The total molecular gas mass in 4C 60.07 inferred from the CO $J = 1 - 0$ emission is $M(\mathrm{H_2}) \simeq 1.3 \times 10^{11}\, M_\odot$, sufficient to fuel the inferred star-formation rate of $\sim 1600\, M_\odot\ \mathrm{yr}^{-1}$ for 10^8 yrs. From our high-resolution CO $J = 1 - 0$ VLA maps we find the dynamical mass of 4C 60.07 to be comparable to that of a giant elliptical at the present time. A significant fraction of the mass is in the form of molecular gas suggesting that 4C 60.07 is in an early state of its evolution. The merging nature of 4C 60.07 along with its large dynamical mass imply that this system is a giant elliptical caught in its formative stages.

6.1 Introduction

High-redshift radio galaxies (HzRGs) are amongst the most luminous objects known, and are believed to serve as tracers of the peaks of the primordial density field around which giant elliptical galaxies and clusters of galaxies form (Kauffmann 1996; West et al. 1994). In the radio, HzRGs typically display a double-lobe morphology and large radio luminosities ($P_{178\,MHz} \sim 5 \times 10^{35}\,\mathrm{erg\,s^{-1}\,Hz^{-1}}$), indicating a highly active black hole.

Recently, evidence has been mounting that HzRGs are massive starburst galaxies. This has come about from sub-millimetre detections of a number of HzRGs, implying large rest-frame far-IR luminosities ($L_{FIR} \simeq 10^{13}\, L_\odot$) powered by intense star formation ($SFR \simeq 1000 - 2000\, M_\odot\ \mathrm{yr}^{-1}$ - Dunlop et al. 1994; Hughes et al. 1997; Ivison et al. 1998; Archibald et al. 2001). In a recent SCUBA survey of seven HzRGs and their surroundings, Stevens et al. (2003) not only found the star formation in the radio galaxies themselves to be extended on several tens of kilo-parsec scales but also found one or more previously undetected submm sources in the vicinity ($50 - 250$ kpc) of more than half of the targeted objects. It is difficult to see how the Active Galactic Nucleus (AGN) could power the far-IR luminosity on $\gtrsim 10$ kpc scales, and a massive starburst seems to be the natural explanation. Indeed, adequate "fuel" for such large star formation rates has been found in the four HzRGs which have been detected in CO to date (Papadopoulos et al. 2000; De Breuck et al. 2003a; De Breuck et al. 2003b). These observations revealed the presence of massive ($\sim 10^{11}\, M_\odot$) reservoirs of molecular gas, enough to fuel a $\sim 1000\, M_\odot\ \mathrm{yr}^{-1}$ starburst for $\sim 10^8$ yr, and in half of the cases the CO emission was found to be extended on tens of kpc scales (Papadopoulos et al. 2000; De Breuck et al. 2003a). Similar large molecular gas masses distributed in clumps on tens of kilo-parsec scales has been found in a number of QSOs at high redshifts (Carilli et al. 2002a; Carilli et al. 2002b). In general, HzRGs

Greve, T.R, Ivison, R.J. & Papadopoulos, P.P. 2004, A&A, 419, 99.

have the advantage over quasars that they are not gravitationally lensed since they are usually selected on the basis of extended lobe-emission whereas quasars are often found to be lensed. Furthermore, HzRGs are known to be associated with giant ellipticals in the local Universe (McLure & Dunlop 2000).

In this paper we present high-resolution observations of the CO $J = 1 - 0$ emission from 4C 60.07 at $z = 3.788$ using the Very Large Array[1] . Throughout we have assumed $H_0 = 65\,\mathrm{km\,s^{-1}\,Mpc^{-1}}$, $\Omega_M = 0.3$ and $\Omega_\Lambda = 0.7$. In this cosmology the luminosity distance of 4C 60.07 is 36.2 Gpc and $1''$ corresponds to 7.7 kpc.

6.2 4C 60.07

4C 60.07 is an ultra-steep-spectrum (USS) radio galaxy at redshift of $z = 3.788$ (Chambers et al. 1996; Röttgering et al. 1997). It displays a Fanaroff-Riley II (FR II) edge-brightened double-radio morphology (Fanaroff & Riley 1974). The radio morphology of 4C 60.07 is seen in Figure 6.1 which shows a VLA C-band (6 cm) archive image of 4C 60.07. The system consists of two main bright hot spots separated by about $9''$. The south-eastern component is further comprised of two components (B and C). Continuum emission is also seen from the radio core which is located $\sim 2''$ west-northwest of the C-component.

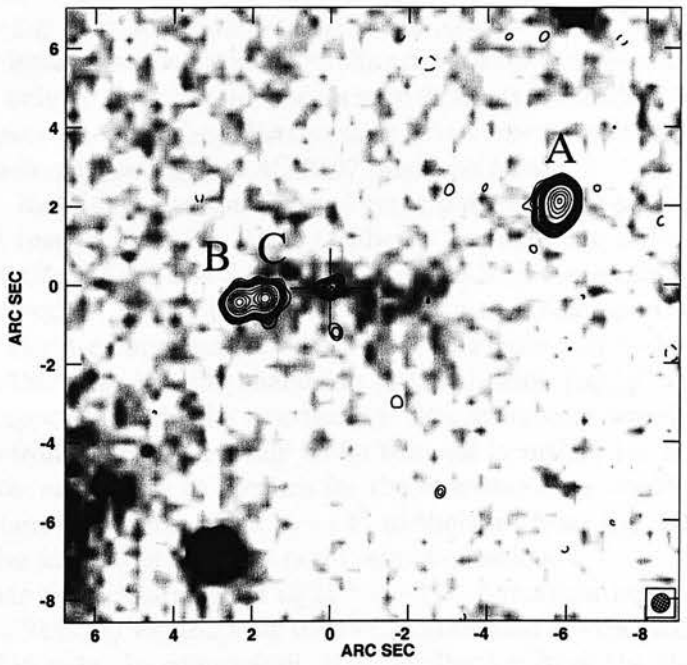

Figure 6.1: 6 cm VLA map of 4C 60.07 overlaid on an I-band image obtained with the William Herschel Telescope. The radio hot spots are denoted by A, B and C. The cross marks the position of the radio core: R.A.(J2000): $05^h12^m55\overset{s}{.}147$, DEC.(J2000): $+60^o30'51\overset{''}{.}0$. The insert in the bottom right corner shows the synthesized beam.

The CO $J = 4 - 3$ line and 1.25 mm continuum emission from 4C 60.07 have been imaged

[1] The Very Large Array (VLA) is operated by the National Radio Observatory, which is a facility of the National Science Foundation, operated under cooperative agreement by Associated Universities, Inc.

Table 6.1: VLA Observations.

Date	Configuration	t_{int}/hrs
2001 Oct 2	CD	1.4
2001 Oct 9	CD	1.7
2001 Oct 11	D	1.7
2001 Oct 19	D	2.8
2002 Nov 12	C	1.7
2002 Dec 20	C	1.5

using the IRAM Plateau de Bure Interferometer (Papadopoulos et al. 2000). The CO emission was found to emerge from two kinematically distinct components separated in velocity space by $\sim 700\,\mathrm{km\,s^{-1}}$. The component with the narrowest line profile ($FWHM \sim 150\,\mathrm{km\,s^{-1}}$) is offset by $V \simeq -224\,\mathrm{km\,s^{-1}}$ from the systemic velocity corresponding to $z = 3.788$ and spatially coincident with the position of the radio core. The broader component ($FWHM \geq 550\,\mathrm{km\,s^{-1}}$) peaks $\sim 7''$ ($\sim 30\,\mathrm{kpc}$) west of the radio core, and is offset by $\simeq 483\,\mathrm{km\,s^{-1}}$ from the systemic velocity. Such large offsets between the redshift of the optical emission lines and the CO emission has been observed in several other high redshift systems, and is commonly attributed to the optical lines originating in strong outflows and winds (Guilloteau et al. 1999; Cox et al. 2002). Strong gravitational lensing can be ruled out as the origin of the double source and large apparent luminosity since not only do the two components have different line widths but they are also offset in velocity with respect to each other. Furthermore, there are no indications from observations in the optical and radio suggesting that 4C 60.07 might be lensed.

In order to get a handle on the non-thermal contribution to the submm and CO fluxes, we used C and X band images from the VLA Archive to measure the radio fluxes of the various components in 4C 60.07 at 6 cm and 3.6 cm. In Figure 6.3 we have plotted the submm/far-IR spectral energy distribution (SED) of 4C 60.07 along with the radio spectra of the A-component and the radio core. The A-component (the dotted line in Figure 6.3) is the brightest component in the radio and furthermore has the shallowest spectral slope ($\alpha_{6\,cm}^{3.6\,cm} = -1.4$) which means it provides a strict upper limit on the non-thermal flux at submm wavelengths. The 1.25 mm continuum emission from 4C 60.07 is likely to be thermal in origin, i.e. from warm dust, since non-thermal processes are unable to account for the observed flux, see Figure 2. Furthermore, the 1.25 mm continuum emission is offset by $\sim 4''$ to the west from the radio core position, and does not appear to be associated with the non-thermal emission.

The radio core has a spectral slope of $\alpha_{6\,cm}^{3.6\,cm} = -1.7$. Extrapolating to the frequency of the CO $J = 1 - 0$ line ($\sim 24\,\mathrm{GHz}$) we find that the radio continuum is expected to contribute a non-neglible $S_{24\,\mathrm{GHz}} = 0.03\,\mathrm{mJy}$. In comparison, the contribution from the thermal dust spectrum seems completely neglible, see Figure 6.3.

6.3 Observations

The CO $J = 1 - 0$ line ($\nu_{rest} = 115.27\,\mathrm{GHz}$) from 4C 60.07 is redshifted into the VLA's K-band (1.3-cm) receivers. Since non-thermal continuum emission from the radio core was expected, we used two IF pairs (right- and left-hand circular polarisation) centred on the two kinematically distinct emission-line components, each pair set up such that one IF pair was centred on the line and the other pair was offset from this by 100 MHz to measure the continuum. The IF set-up for both the broad and narrow component is detailed in Figure 6.3. The broad-line component was

observed in continuum mode with a 50 MHz-wide IF centred at 24.035 GHz, which corresponds to a velocity coverage of 624 km s^{-1}. Not only does this not properly cover the broad component but, since the observations were done in continuum mode, no information on the line shape was available, and one therefore has to rely on the IRAM CO $J = 4 - 3$ observations to infer a line width for the broad component. The narrow component was observed in spectral-line mode with a 7-channel IF centered at 24.095 GHz, each channel being 3.125 MHz wide. This was to avoid under-resolving the narrow line in velocity space. However, the line datasets from the 2002 December 20 and 2003 March 09 are centred at 24.089 GHz, corresponding to a shift of two channels, in order to get a better spectral coverage at the low-frequency side of the line. Thus nine channels (denoted channels 1,..,9 in Figure 6.3) covered the line, corresponding to a velocity coverage of 350 km s^{-1}. 4C 60.07 was observed in the VLA's CD, D and C configurations (see Table 1). The D-configuration data, however, turned out not to have the spatial resolution required to properly separate the (B,C) component from the radio core, and was therefore discarded. The lack of D-array data is very unlikely to result in "filtering out" any extended CO emission since such emission would have to be extended over scales $\gtrsim 60''$ ($\gtrsim 460$ kpc). The fact that we do not find any change in total flux after including the D-array data verifies this point.

In total, after calibration overheads, we obtained 6.3 hr of integration time on source for both the broad and narrow components. Calibration and data reduction was done using standard recipes in the NRAO *AIPS* Cookbook. The amplitude was calibrated with the quasars 3C 48 and 3C 286 at the beginning and/or end of each transit. The phase drift was calibrated using a fast-switching technique in which we observed the nearby source 04494+63322 every few minutes. The data were obtained in good weather conditions, and the rms phase fluctuations after calibration was less than 10°. For the spectral-line mode observations of the narrow component, the bandpass of the system was calibrated using 0319+415. In all cases the bandpass calibration averaged over the 7 channels was better than 92%. Data taken at different times and in different configurations were combined using DBCON, weighting each dataset with the its total gridded weight.

6.4 Results & Analysis

The radio morphology of 4C 60.7 in the broad and narrow component IF set-ups is shown in Figure 6.4. Figure 6.4a and b show pure continuum emission and continuum emission plus the broad CO line emission, respectively; similarly for Figure 6.4c and d but for the narrow component.

In Figure 6.4a, which shows the continuum emission at 23.935 GHz, we recognise the two radio lobes seen in Figure 6.4, although we have failed to separate the B and C components from the radio core, let alone to resolve it into its two sub-components. The emission from the radio core is clearly stronger and more extended in IF2 which, in addition to the continuum, contains the CO-emission from the broad component (Figure 6.4b). A similar picture is seen for the narrow component in Figure 6.4c and d. Here, the radio core and B-component are separated in both IFs. The (large) negative spectral index ($\alpha \sim -1.7$) of the radio core rules out the possibility that the excess emission seen in the IF2-maps is due to an increase in continuum emission, since the IF2 maps are at a higher frequency than the IF1 maps. The B and C radio hot spots have even larger negative spectral indices (Carilli et al. 1997) and can therefore not be the cause of the increased emission either. This suggests that what we are seeing in the IF2 maps is continuum emission plus CO $J = 1 - 0$ emission from the emission features detected in the CO $J = 4 - 3$ maps.

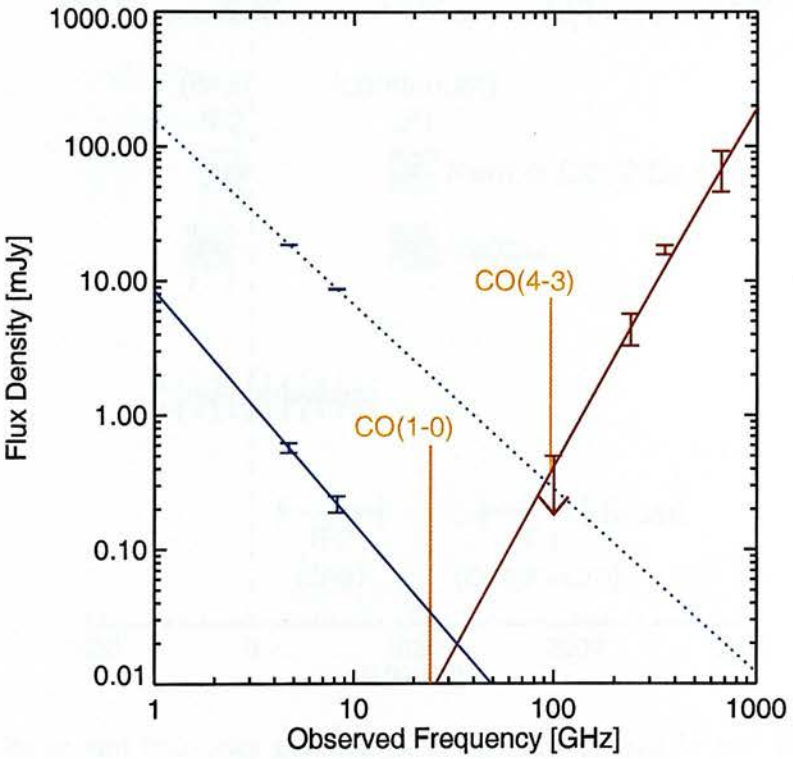

Figure 6.2: The submm/far-IR spectral energy distribution (SED) of 4C 60.07 (red line) along with the radio spectra of the A-component (blue dotted line) and the radio core (blue solid line). The submm points are taken from SCUBA observations by Archibald et al. (2001) while the IRAM 30m Telescope data-points at 252 GHz (1.25 mm) and 100 GHz (3 mm) are from Papadopoulos et al. (2000). The radio points are measured from C and X band data of 4C 60.07 from the VLA Archive. The positions and strengths of the CO $J = 1 - 0$ and $J = 4 - 3$ lines relative to the SED are shown in yellow (based on this paper and Papadopoulos et al. (2000)).

6.4.1 The Broad Line Component

In order to disentangle the broad CO emission from the continuum, a box was put around the entire system and a CLEAN-component model of the continuum emission shown in Figure 6.4a was constructed. The CLEANing was stopped when the rms of the residuals reached the noise level in the image. This was then subtracted in uv-space from the IF2 data using the *AIPS* task UVSUB, resulting in uv-data from which maps free of continuum emission could be produced. Figure 6.5a shows the resulting CO $J = 1 - 0$ map of the broad component. The lack of residual emission at the positions of the two radio lobes demonstrates the effectiveness of the continuum emission subtraction. The CO $J = 1 - 0$ emission is detected at 5σ, peaking at a position which is coincident with the radio core position but with emission appearing to extend $2 - 3''$ to the west. In comparison, the broad component of the CO $J = 4 - 3$ emission was found to peak $\sim 4''$ south-west of the radio core (Papadopoulos et al. 2000).

In Figure 6.5b we have overlaid the CO $J = 1 - 0$ contours on top of a gray-scale image of the $J = 4 - 3$ emission. The $1 - 0$ map has been tapered down to 60 kλ in order to better match

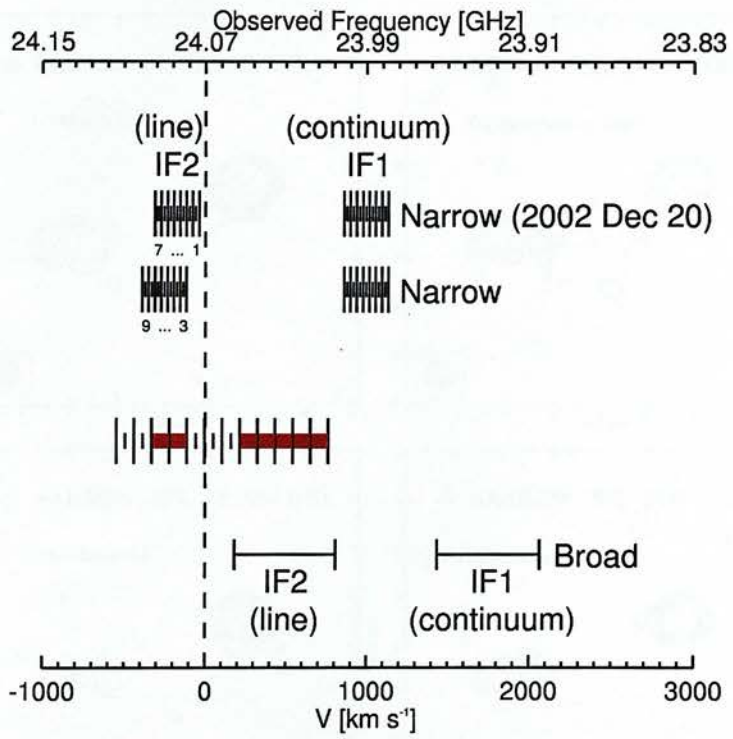

Figure 6.3: Velocity and frequency coverage of the IF set-up used in our VLA CO $J = 1 - 0$ observations. The dashed line outlines the systemic velocity corresponding to $z = 3.788$. In red is shown the velocity-channels of the IRAM PdBI observations of Papadopoulos et al. (2000); channels in which CO $J = 4 - 3$ emission was detected are marked in thick red.

the resolution of the $4 - 3$ data ($FWHM = 8\farcs9 \times 5\farcs5$). The offset between the centroids of the $1 - 0$ and $4 - 3$ emission is within the positional errors given the large $J = 4 - 3$ synthesized beam, and in general there is good spatial correspondence between the two.

Assuming that the IF covers the entire line, we can estimate the velocity-integrated $J = 1 - 0$ flux density using

$$\int_{\Delta v} S_{\nu_{obs}} dv = \Delta\nu_{IF} \frac{c}{\nu_{obs}} S_{CO}, \tag{6.1}$$

where $\Delta\nu_{IF}$ is the width of the IF and S_{CO} is the flux density. We find $S_{CO} = (0.27 \pm 0.05)$ mJy which yields a velocity-integrated flux density of (0.15 ± 0.03) Jy km s^{-1}, where we have used $\nu_{obs} =$ 24.035 GHz and an IF bandwidth of 45 MHz (560 km s^{-1}) instead of 50 MHz due to bandpass rollover. The CO $J = 1 - 0$ emission from the broad component in the uvtaper 200 map appears to be somewhat extended in the north-west direction, although the low signal-to-noise of the data does not warrant a firm conclusion on this issue.

6.4.2 The Narrow Line Component

The continuum subtraction in the case of the narrow-line emission was done in a similar fashion as for the broad component: a continuum model was constructed by combining all IF1 channels and then subtracted from the IF2 channels. Since channels 1 and 2 had a different uv-coverage than channels 3 to 7 which again had a different uv-coverage than channels 8 and 9, three

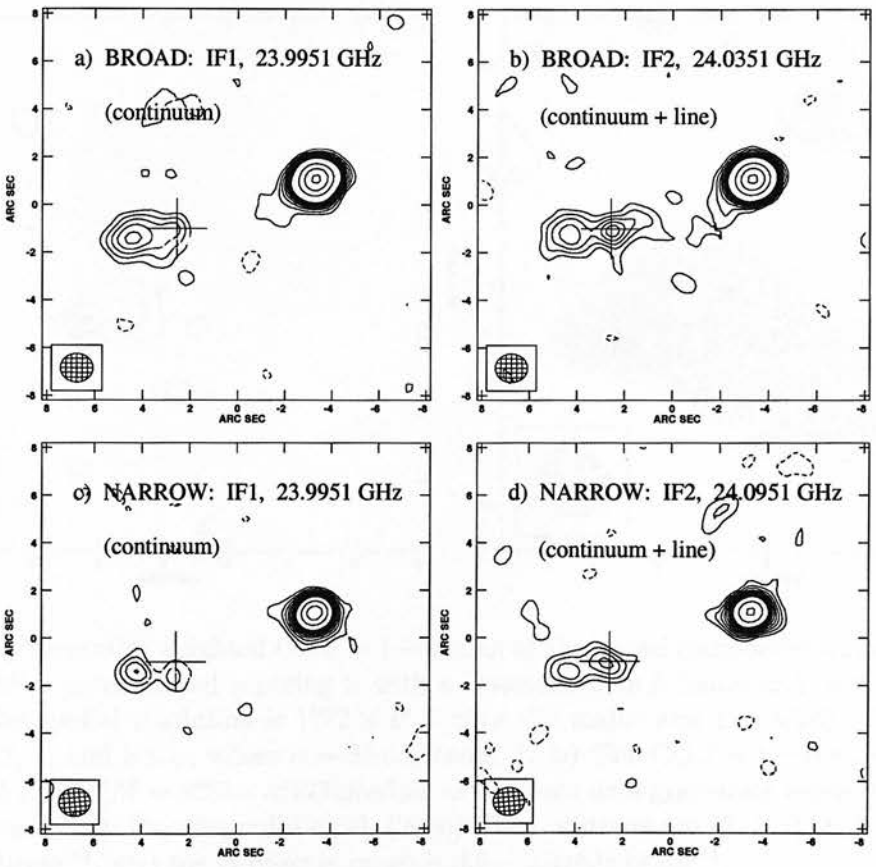

Figure 6.4: Naturally weighted, untapered maps, showing the morphology of 4C 60.07 in the two IF set-ups. **Top row:** The spatial resolution is $1\farcs36 \times 1\farcs19$ with the major axis P.A. $= 89^o$. The rms noise is $0.030\,\mathrm{mJy\,beam^{-1}}$. Contours are shown at -2, 2, 3, 4, 5, 6, 7, 8, 9, 10, 20, 30, and $40 \times 35\,\mu\mathrm{Jy\,beam^{-1}}$. **Bottom row:** The spatial resolution (FWHM) is $1\farcs32 \times 1\farcs17$ with the major axis P.A. $= 275^o$, and the rms noise level is $0.051\,\mathrm{mJy\,beam^{-1}}$. Contours are shown at -2, 2, 3, 4, 5, 6, 7, 8, 9, 10, 15, and $20 \times 60\,\mu\mathrm{Jy\,beam^{-1}}$. The cross marks the position of the radio core (R.A.(J2000): 05:12:55.147, DEC.(J2000): +60:30:51.0.

different continuum models had to be constructed, one for each of these three sets of channels. In order to increase the signal-to-noise ratio we averaged neighbouring channels during the imaging of the continuum-subtracted IF2 channels. We then searched for any residual emission at the expected position of the narrow component and used the task IMEAN to measure the flux. The resulting spectrum of the CO $J = 1 - 0$ emission is shown in Figure 6.6 where we have also plotted the velocity-coverage of the two IRAM PdBI channels in which $J = 4 - 3$ emission from the narrow component was detected. Note that channels 1-2 and 8-9 are somewhat more noisy than the other channels, since the corresponding integration time is less. We detect CO $J = 1 - 0$ emission in channels 3 to 6, which in velocity-space overlaps with the two IRAM PdBI channels in which the strongest CO $J = 4 - 3$ emission is detected. Only very weak CO $J = 4 - 3$ emission was found in the third IRAM PdBI channel at 96.3095 GHz which is in agreement with the $J = 1 - 0$ line profile. From a Gaussian fit to the line profile, we find the $1 \rightarrow 0$ spectrum to peak at $V \simeq (-220 \pm 40)\,\mathrm{km\,s^{-1}}$ offset from the systemic velocity of 4C 60.07 which is consistent with

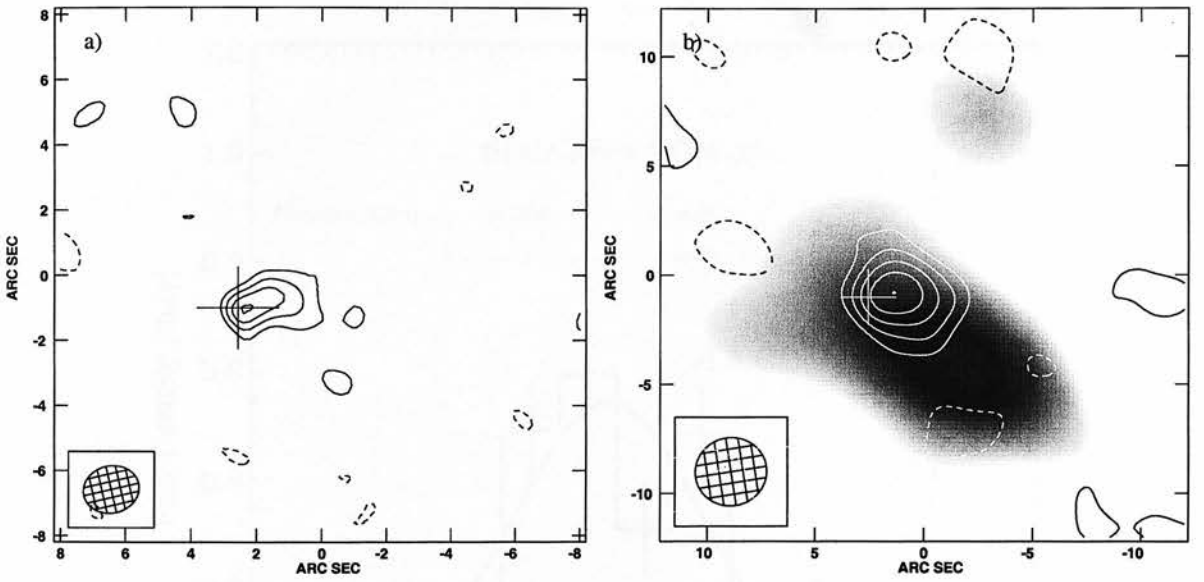

Figure 6.5: **a)** Naturally weighted CO $J = 1 - 0$ map of the broad component obtained by combining the entire data-set and tapering it with a Gaussian with a half-width at 0.30 amplitude of 200kλ. The spatial resolution is $1\farcs72 \times 1\farcs45$ with the major axis P.A.=283^o. The contours are at -2, 2, 3, 4, and $5 \times \sigma$, where $\sigma = 35\,\mu$Jy beam^{-1}. **b)** The CO $J = 1 - 0$ emission tapered down to 60kλ ($FWHM = 3\farcs33 \times 3\farcs12$) overlaid as contours on a gray-scale representation of the $J = 4 - 3$ emission by Papadopoulos et al. (2000). The contours are -2, 2, 3, 4, 5, and 6σ with $\sigma = 0.4$ mJy beam^{-1}, and the gray-scale range is $0.6 - 2.0$ mJy beam^{-1}.

that found for the $4 \rightarrow 3$ line given the large velocity bins. The formal linewidth is $\Delta V_{FWHM} \simeq (165 \pm 24)$ km s^{-1}, again in good agreement with that of the CO $J = 4 - 3$ line profile. The fit yields a velocity-integrated flux density of 0.09 ± 0.01 Jy km s^{-1}, see also Table 2.

Combining channels 3 to 6 we obtain the velocity-integrated CO $J = 1 - 0$ emission map shown in Figure 7a. In Figure 7b we have overlaid contours of the CO $J = 1 - 0$ emission on a gray-scale image of the $J = 4 - 3$ emission where the latter has been tapered down to 60 kλ. The $J = 1 - 0$ emission peaks at $\sim 0\farcs7$ east of the radio core which is consistent with the position of the narrow $J = 4 - 3$ component. Similar to what was found for the $J = 4 - 3$ line, in $J = 1 - 0$ the narrow component appears to be more compact and less extended than the broad component.

6.5 Discussion

6.5.1 CO Luminosity and Molecular Gas Mass

The observed CO $J = 1 - 0$ line fluxes for the broad and narrow components in 4C 60.07 imply intrinsic CO luminosities of $L'_{\rm CO(1-0)} = (1.0 \pm 0.2) \times 10^{11}$ K km s^{-1} pc^2 and $(6.0 \pm 0.7) \times 10^{10}$ K km s^{-1} pc^2, respectively. For the $4 - 3$ line Papadopoulos et al. (2000) found $L'_{\rm CO(4-3)} = (7 \pm 1) \times 10^{10}$ K km s^{-1} pc^2 and $L'_{\rm CO(4-3)} = (3.5 \pm 0.8) \times 10^{10}$ K km s^{-1} pc^2 for the broad and narrow component, respectively, where we have computed the luminosities in the cosmology adopted here. From the CO $J = 1 - 0$ line the molecular gas mass can be found using the well-known relation $M({\rm H_2}) = {\rm X_{CO}} L'_{\rm CO(1-0)}$ which relates the CO $J = 1 - 0$ luminosity with the molecular

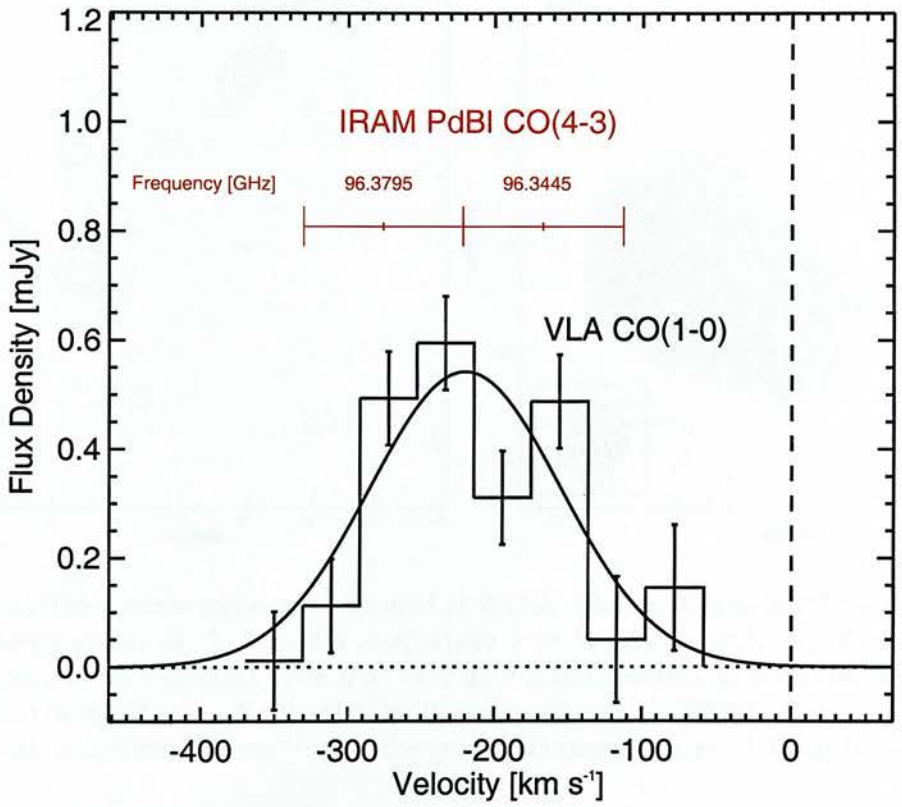

Figure 6.6: The spectrum of the narrow CO $J = 1 - 0$ component in 4C 60.07. All channels maps were tapered with a 200kλ Gaussian. The rms noise in channels 1-2 is 0.12 mJy beam^{-1} at a spatial resolution of $1\farcs4 \times 1\farcs3$; the noise in channels 3-6 is 0.086 mJy beam^{-1} at a spatial resolution of $1\farcs7 \times 1\farcs4$, and the noise in channels 7-8 is 0.09 mJy beam^{-1} at a spatial resolution of $1\farcs9 \times 1\farcs5$. Above the line-profile we have plotted the velocity coverage of the channels in which $J = 4 - 3$ emission was detected (Papadopoulos et al. 2000). The vertical dashed line corresponds to the systemic velocity ($z = 3.788$).

gas mass (e.g. Strong et al. 1988). $X_{\rm CO}$ is the CO $J = 1 - 0$ line luminosity to H_2-mass conversion factor which in the extreme UV-intense environments found in local Ultra Luminous Infra-Red Galaxies, and presumably also in high redshift galaxies such as 4C 60.07, has a value of about $0.8\,({\rm K\,km\,s^{-1}\,pc^2})^{-1} M_\odot$ (Downes & Solomon 1998). In doing so we find molecular gas masses of $M({\rm H_2}) \sim 8 \times 10^{10}\,M_\odot$ and $M(H_2) \sim 5 \times 10^{10}\,M_\odot$ for the broad and narrow CO emitting components, respectively. Hence, even for a conservative, non-Galactic value of $X_{\rm CO}$ we find that about $\sim 10^{11}\,M_\odot$ of molecular gas is associated with 4C 60.07. The estimated gas masses are in very good agreement with those of Papadopoulos et al. (2000).

The total gas mass in 4C 60.07 will of course be larger once the neutral hydrogen has been accounted for. Assuming a value of $M({\rm HI})/M({\rm H_2}) = 2$ which is typically found in IRAS galaxies (Andreani, Casoli, & Gerin 1995) we find a total gas mass of $M_{gas} = M({\rm H_2}) + 2M({\rm H_2}) = 2.4 \times 10^{11}\,M_\odot$ for the broad component and $1.5 \times 10^{11}\,M_\odot$ for the narrow component. In case that metal-poor gas is also present the gas mass can be even higher.

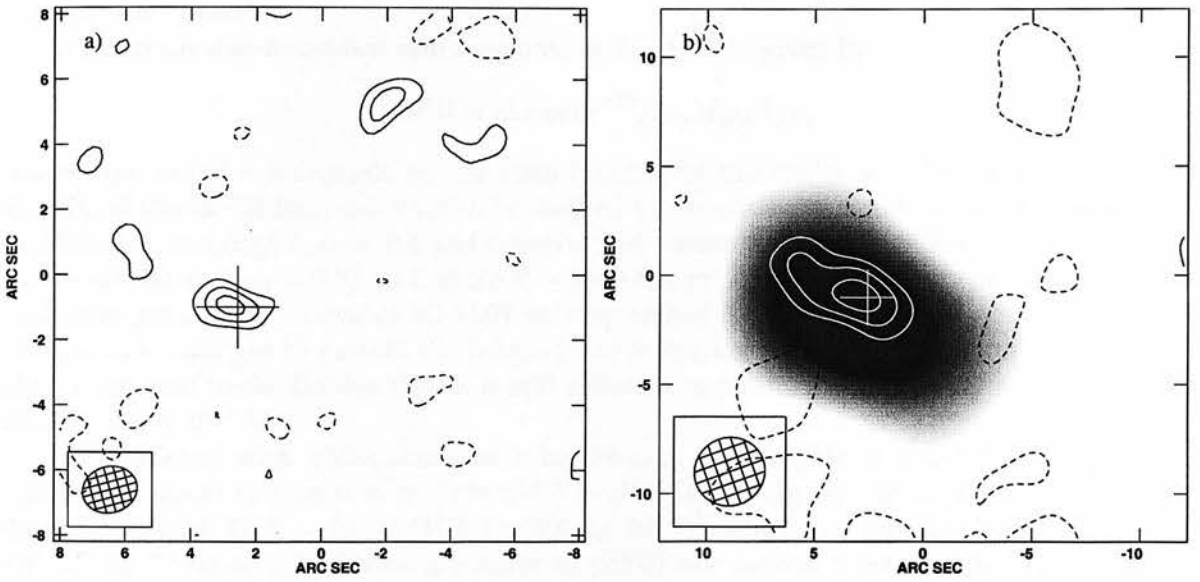

Figure 6.7: **a)** The narrow component tapered at 200kλ. The resolution is $1\farcs72 \times 1\farcs42$ at P.A. = 285^o. Contours are at -2, 2, 3, and $4 \times \sigma$, where $\sigma = 55\,\mu$Jy beam^{-1}. **b)** The CO $J = 1 - 0$ emission tapered down to 60kλ ($FWHM = 3\farcs22 \times 3\farcs07$) overlaid as contours on a gray-scale representation of the $J = 4 - 3$ detection by Papadopoulos et al. (2000). The contours are -2, 2, 3, and 4σ with $\sigma = 0.6$ mJy beam^{-1}, and the gray-scale range is $0.6 - 2.0$ mJy beam^{-1}.

Table 6.2: Observed and Derived Properties for 4C 60.07.

Parameter	4C 60.07 (broad)	4C 60.07 (narrow)
R.A.(J2000)	$05^h12^m54\fs75$	$05^h12^m55\fs30$
Decl.(J2000)	$+60^o30'50\farcs92$	$+60^o30'52\farcs29$
$S_{CO(1-0)}$ [mJy]	(0.27 ± 0.05)	(0.30 ± 0.10)
$S_{CO(1-0)}\Delta V$ [Jy km s^{-1}]	(0.15 ± 0.03)	(0.09 ± 0.01)
$L'_{CO(1-0)}$ [K km s^{-1} pc^2]	$(1.0 \pm 0.2) \times 10^{11}$	$(6.0 \pm 0.7) \times 10^{10}$
$M(H_2)$ [$M_\odot$]	8×10^{10}	5×10^{10}

6.5.2 FIR Luminosity and star-formation efficiency

In the case where the far-IR luminosity is powered by a starburst and not an AGN, and all the stellar radiation is absorbed by dust, the far-IR to CO luminosity ratio, L_{FIR}/L_{CO}, provides a rough measure of the integrated luminosity of massive stars responsible for heating the dust (L_{FIR}) relative to the amount of fuel available for star formation (L'_{CO}). We estimate the far-IR luminosity of 4C 60.07 to be $L_{FIR} \simeq 4 \times 10^{13}\,L_\odot$, where we have used the 850-μm flux measurement of Archibald et al. (2001) and adopted a dust temperature and spectral index of $T_d = 50$ K and $\beta = 1.5$, respectively. This yields a L_{FIR}/L_{CO} ratio of $\simeq (4 \times 10^{13} L_\odot)/(1.6 \times 10^{11}\,\mathrm{K\,km\,s^{-1}\,pc^2}) = 250\,L_\odot\,(\mathrm{K\,km\,s^{-1}\,pc^2})^{-1}$, which is similar to values found in ULIRGs (e.g. Solomon et al. 1997). Carilli et al. (2002a) found continuum-to-line ratios of 350 and 323 in the QSOs BRI 1202-0725 ($z = 4.70$) and BRI 1335-0417 ($z = 4.41$), respectively. A somewhat lower value of 200 was found in the $z = 4.12$ QSO PSS J2322+1944

(Carilli et al. 2002b).

The current star-formation rate measured in $M_\odot$ yr^{-1} is given by

$$SFR \simeq (L_{FIR} 10^{-10}/L_\odot) \delta_{MF} \delta_{SB}, \tag{6.2}$$

where $\delta_{MF} \sim 0.8 - 2$ depends on the mass function of the stellar population, and δ_{SB} is the fraction of the far-IR luminosity which is powered by the starburst and not the AGN (Omont et al. 2001). If we adopt $\delta_{MF} = 0.8$ and conservatively assume that only 50% of L_{FIR} is powered by the starburst ($\delta_{SB} = 0.5$) we find $SFR \sim 1600\, M_\odot$ yr^{-1}. Assuming that the total amount of molecular gas observed towards 4C 60.07 ends up as fuel for the starburst, we find that there is enough molecular gas to sustain the inferred star-formation rate for $\sim 8 \times 10^7$ yr. While this is short compared to the Hubble time it is still sufficient to produce a giant elliptical with a stellar mass of $M_* \simeq 10^{11}\, M_\odot$.

The efficiency with which stars are being formed, i.e. the rate of star-formation per solar mass of molecular hydrogen, is given by $SFE = SFR/M(\mathrm{H_2})$ or equivalently $L_{FIR}/M(\mathrm{H_2})$. For 4C 60.07 we find $SFE = L_{FIR}/M(\mathrm{H_2}) \simeq 300\, L_\odot\, {M_\odot}^{-1}$, which is somewhat higher than the $\sim 190\, L_\odot\, {M_\odot}^{-1}$ reported by Papadopoulos et al. (2000) who derived their value based on their flux density measurement of $S_{850\mu m} = 11$ mJy. Here we have used the measurement by Archibald et al. (2001) which yields a somewhat higher 850 μm flux density of 17 mJy, although still lower than the 22 mJy reported by Stevens et al. (2003). Local ULIRGs exhibit star-formation efficiencies comparable to that of 4C 60.07, once the same X_{CO}-factor has been used (Solomon et al. 1997). It is worth stressing that our detection of CO $J = 1 - 0$ enables us to make a direct comparison of SFEs with that of local ULIRGs since the same gas mass measure (the $J = 1 - 0$ line) is used for ULIRGs. The apparently high star-formation efficiencies found for the above systems, could be severely overestimated if the AGN contributes significantly to the far-IR luminosity. However, the detection of CO together with the fact that 4C 60.07 and other HzRGs appear extended on several tens of kilo-pc scales at submm-wavelengths (Ivison et al. 2000; Stevens et al. 2003) strongly suggests that the far-IR emission is powered by large-scale starburst and not the AGN. Here we must mention that while CO $J = 1 - 0$ may be a good indicator of the total metal-rich $\mathrm{H_2}$ gas resevoir, it may be a poor one regarding the dense gas phase ($n \geq 10^5$ cm^{-3}) that "fuels" star-formation. The latter could be particular true in the tidally disrupted giant molecular clouds (GMCs) expected in ULIRGs where a diffuse phase may dominate the CO $J = 1 - 0$ emission but has little to do with star formation. This could be the reason why the L_{FIR}/L'_{CO} ratio is found to be such a strong function of L_{FIR}, increasing for the merger systems associated usually with large far-IR luminosities. Interestingly, recent work shows that the SFE of dense gas, parametrised by the $L_{FIR}/L_{HCN(1-0)}$ ratio (the HCN $J = 1 - 0$ critical density is 2×10^5 cm^{-3}), remains constant from GMCs all the way to ULIRG system (Gao & Solomon 2003).

6.5.3 Excitation Conditions

From the detections of CO in 4C 60.07 we can infer the CO $(4 - 3)/(1 - 0)$ velocity/area-averaged brightness temperature ratio using $r_{43} = \mathrm{L'_{CO(4-3)}/L'_{CO(1-0)}}$. The global line ratio, i.e. the line ratio obtained by combining the flux from the two components, is $r_{43} = 0.7^{+0.3}_{-0.2}$. The line ratios for the broad and narrow components are $0.7^{+0.3}_{-0.2}$ and $0.6^{+0.2}_{-0.2}$, respectively. Hence, given the large uncertainties we find no significant difference in the excitation conditions between the two components. Thus in this case $\mathrm{H_2}$ mass estimates solely from CO $J = 4 - 3$ assuming full thermalisation and optical thickness of the latter (i.e. $r_{43} \simeq 1$) would not result in too large errors. However, the sub-thermal excitation of such high-J CO lines remains a possibility even in starburst environments (e.g. Papadopoulos & Ivison 2002; chapter 5).

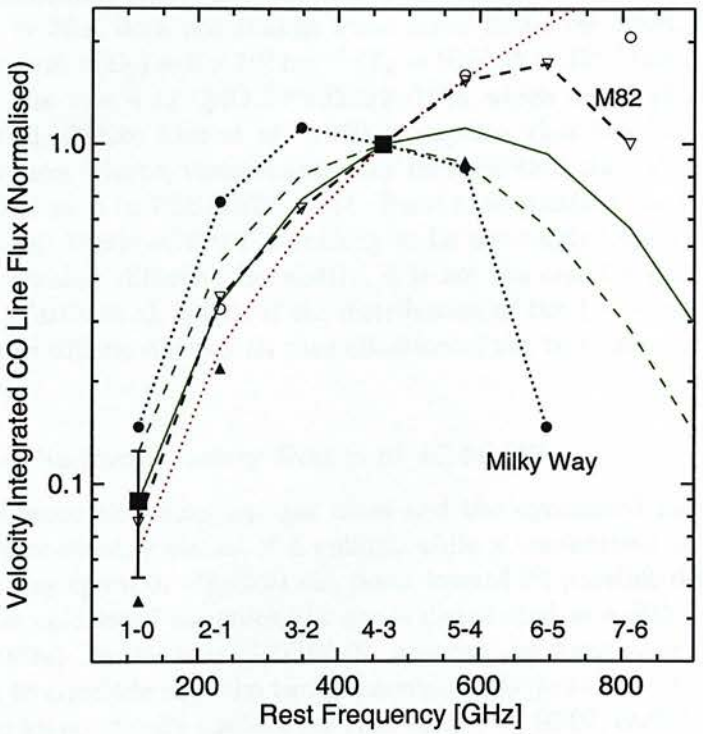

Figure 6.8: Velocity-integrated CO line flux densities from 4C 60.07 are shown as filled squares. The integrated line fluxes have been normalised to the $J = 4 - 3$ line. Also shown are the line fluxes from the $z = 4.12$ QSO PSS J2322+1944 (filled triangles - Carilli et al. 2002b; Cox et al. 2002), the $z = 4.69$ QSO BRI 1202-0725 (open circles - Omont et al. 1996; Carilli et al. 2002a), the local starburst galaxy M 82 (open triangles - Mao et al. 2000), and the integrated emission from within the solar radius of the the Milky Way (filled circles - Fixsen et al. 1999). The red dotted line shows the line flux increasing as frequency squared which is expected for optically thick conditions. The green lines show results from a LVG-model with $T_{kin} = 50\,\mathrm{K}$, $X_{\mathrm{CO}}/(dV/dr) = 10^{-5}\,(\mathrm{km\,s^{-1}\,pc^{-1}})^{-1}$, and $n(\mathrm{H_2})$ equal to $3.0 \times 10^3\,\mathrm{cm^{-3}}$ (solid line) and $2.2 \times 10^3\,\mathrm{cm^{-3}}$ (dashed line).

In Figure 6.8 we plotted the velocity-integrated CO line flux densities (normalised to $J = 4 - 3$) for the broad and narrow components in 4C 60.07 as well as the normalised line fluxes for PSS J2322+1944. We have used a standard single-component large velocity gradient (LVG) code to interpret the observed line ratio. In fact, given the large range compatible with our measurements we can only put a lower limit on the density. Indeed, for both components the upper values for r_{43} are compatible with LTE and optically thick emission where the ratio is no longer sensitive to the density.

A lower limit on the average gas density can be set by the lowest possible value of $r_{43} = 0.4$ allowed by the observations. Adopting a typical CO abundance $\Lambda = X_{\mathrm{CO}}/(dV/dr) = 10^{-5}\,(\mathrm{km\,s^{-1}\,pc^{-1}})^{-1}$, a $T_{CMB} = (1+z) \times 2.73\,\mathrm{K} = 13.07\,\mathrm{K}$ and a $T_{kin} = 50\,\mathrm{K}$, which is a typical dust temperature in starburst environments (Colbert et al. 1999; Hughes et al. 1997), we find $n(\mathrm{H_2}) \geq 2 \times 10^3\,\mathrm{cm^{-3}}$. Adopting a higher $\Lambda = 10^{-4}$ (unlikely in such kinematically violent,

UV-aggressive environments) lowers the aforementioned limit to $\sim 600\,\mathrm{cm}^{-3}$. A lower assumed temperature of $T_{kin} = 30\,\mathrm{K}$ does not change these lower limits by much. For the most likely value of $r_{43} = 0.7$ we find $n(\mathrm{H_2}) = 3 \times 10^3\,\mathrm{cm}^{-3}$ ($T_k = 50\,\mathrm{K}$, $\Lambda = 10^{-5}\,(\mathrm{km\,s^{-1}\,pc^{-1}})^{-1}$).

Comparing with the $z = 4.12$ QSO PSS J2322+1944 which has a (4-3)/(1-0) line ratio of 1.4 ± 0.6 (Carilli et al. 2002b; Cox et al. 2002) it appears that the excitation conditions in 4C 60.07 are less extreme. Hence, these results may indicate that the molecular gas in 4C 60.07 is not as dense as that seen in PSS J2322+1944. Such a comparison, however, is prone to the effects of strong lensing. While 4C 60.07 is unlikely to be a strongly lensed system because of its CO components with widely different line widths, it is not the case for PSS 2322+1944 which is known to be lensed (Carilli et al. 2003). If the distribution of the $1 \rightarrow 0$ and $J = 4 - 3$ emitting gas in the source plane differs, differential magnification of the two lines can result in erroneous intrinsic line ratios.

6.5.4 What is the Evolutionary Status of 4C 60.07?

A comparison between the molecular gas mass and the dynamical mass allows for the determination of the evolutionary status of a galaxy, while a comparison of its dynamical mass with that of present-day spiral or elliptical can point toward its possible descendant. Typically, dynamical masses are calculated assuming the gas is distributed in a disk in Keplerian rotation (e.g. Carilli et al. 2002a). In the case of 4C 60.07, however, we have sufficient spatial and kinematical information to conclude that the two gas components do not belong to such a structure. The detection of two kinematically distinct gas resevoirs in 4C 60.07, each with a large gas mass, suggest a major merger event. Hence, a more plausible scenario might be that the two clouds are part of spherical system in the process of collapsing. Assuming the system is virialised, one can apply the virial theorem to derive the following expression for the dynamical mass

$$M_{dyn} = 2.33 \times 10^9 \left(\frac{R}{\mathrm{kpc}}\right) \left(\frac{\Delta V_{FWHM}}{100\,\mathrm{km\,s^{-1}}}\right)^2 \left(\frac{1}{\alpha(1+q)}\right), \tag{6.3}$$

where q is a factor which described the influence of non-gravitational forces on the virial equilibrium, and α ranges from 0.55 to 2.4 with a typical value of 1.5 which we shall adopt here (see Bryant & Scoville (1996) for details). A possible caveat to this argument comes from the fact that if the assumption of a virialised system is not true, eq. 6.3 will tend to overestimate the true dynamical mass. Adopting a radius of the sphere corresponding to half the separation between the two components, i.e. $R \sim 15\,\mathrm{kpc}$ (corresponding to $2''$), and a FWHM width equal to the velocity offset between the line centers of the two gas resevoirs, i.e. $\Delta V_{FWHM} \sim 700\,\mathrm{km\,s^{-1}}$, leads to an enclosed dynamical mass of $M_{dyn} \lesssim 1.1 \times 10^{12}\,M_\odot$, where we have assumed that non-gravitational forces are negligible, i.e. $q << 1$. Note that since Bryant & Scoville (1996) derived eq. 6.3 by examining a large number of clouds filling up a spherical region, we have in the above assumed that the velocity and spatial separation between the two CO components is a fair approximation for ΔV_{FWHM} and R in eq. 6.3. Alternatively, we can do the more simple calculation of finding the virial mass required to keep the two clouds bound by a spherical potential. In this case the velocity dispersion becomes $\Delta V = (1/2)700\,\mathrm{km\,s^{-1}} = 350\,\mathrm{km\,s^{-1}}$, and we find $M_{virial} = G^{-1} R \Delta V^2 \simeq 4.3 \times 10^{11}\,M_\odot$, where we have assumed $R = 15\,\mathrm{kpc}$. Projection effects will only tend to make R and ΔV_{FWHM}, and therefore also the above mass estimates, larger. Thus, 4C 60.07 is a massive system with a dynamical mass comparable to that of giant elliptical galaxies seen in the present day Universe. The inferred ratio of the molecular-to-dynamic mass for the system as a whole is $M(\mathrm{H_2})/M_{dyn} \sim 0.12$, and the total gas fraction is $M_{gas}/M_{dyn} \sim 0.35$. The high gas fraction, along with the large velocity dispersion of the system suggest that 4C 60.07 is a very young system in its early stages of formation.

The fact that such a massive ($M_{dyn} \sim 10^{12}\,M_{\odot}$) system has assembled at $z = 3.8$, which corresponds to a time when the Universe was only $\sim 10\%$ of its present age, seems to favour the monolithic collapse model (e.g. Eggen, Lynden-Bell & Sandage 1962; Tinsley & Gunn 1976) of massive ellipticals over the hierarchical formation scenario (e.g. Baron & White 1987; Baugh et al. 1996; Kauffmann & Charlot 1998). Further in support of the monolithic collapse scenario is the large star-formation rate ($SFR \sim 1600\,M_{\odot}\,\mathrm{yr}^{-1}$) we infer from the far-IR luminosity. If such a large star-formation rate can be sustained it is capable of producing a giant elliptical in a time scale comparable to the dynamical time. The dynamical time-scale for a system with a mass M within a radius R is

$$t_{dyn} = 7.42 \times 10^{11} \left(\frac{R}{\mathrm{kpc}}\right)^{3/2} \left(\frac{M}{M_{\odot}}\right)^{-1/2}, \tag{6.4}$$

where t_{dyn} is measured in years (see p. 37 of Binney & Tremaine 1987). For a giant elliptical with a mass $M_{ell} = 10^{12}\,M_{\odot}$ and a radius $R = 30\,\mathrm{kpc}$, we find $t_{dyn} \simeq 1.2 \times 10^{8}\,\mathrm{yr}$. Hence, in order to form a giant elliptical within a dynamical time scale, star-formation rates of the order $M_{ell}/t_{dyn} \simeq 8000\,M_{\odot}\ \mathrm{yr}^{-1}$ are required, which is comparable to what we find in 4C 60.07. It is important to note that even if the true dynamical mass or the star-formation rate of this system are less than the above estimates, the fact that at $z = 3.8$ about $1.3 \times 10^{11}\,M_{\odot}$ in H_2 gas mass alone has assembled within 15 kpc points towards a major galaxy forming merger rather than a gradual accumulation of mass over time and redshift. This mass can only be revised upwards and typically reach $\sim 4 \times 10^{11}\,M_{\odot}$ if HI is also accounted for, thereby making the case for a monolithic collapse scenario even stronger.

4C 60.07 is not the only system with extended CO emission. Molecular gas distributed on tens of kpc scales, sometimes in separate gas components, have been observed in high redshifts quasars (e.g. Carilli et al. 2002a; Papadopoulos et al. 2001) and radio galaxies (De Breuck et al. 2003; De Breuck et al. in prep.). Thus, there is evidence to show that at least some luminous active galaxies in the early Universe, in addition to harbouring supermassive black holes in their centres, are associated with massive reservoirs of molecular gas distributed on tens of kpc scales which are in the process of merging. This observed coevality between large scale mergers of gaseous subsystems and the epoch of AGN-activity might provide clues to the origin of the tight relationship observed locally between the velocity dispersion of spheroids and the mass of their central black holes (Ferrarese & Merritt 2000).

Acknowledgements

TRG acknowledges support from the Danish Research Council and from the EU RTN Network POE. PPP acknowledges a Marie Curie Individual Fellowship HPMT-CT-2000-00875. We are grateful to Ignas Snellen and Philip Best for useful advice on $\mathcal{AIPS}$. We are also greatly indebted to Carlos De Breuck and Michiel Reuland for providing us with the IRAM PdBI CO $J = 4 - 3$ data.

References

Andreani, P., Casoli, F., & Gerin, M. 1995, A&A, 300, 43.
Archibald, E.N., Dunlop, J.S., Hughes, D.H., Rawlings, S., Eales, S. & Ivison, R.J. 2001, MNRAS, 323, 417.
Baron, E. & White, S.D.M. 1987, ApJ, 322, 585.
Baugh, C.M., Cole, S. & Frenk, C.S. 1996, MNRAS, 283, 136.

Binney, J. & Tremaine, S. 1987, "Galactic Dynamics", Princeton Series on Astrophysics, Princeton University Press.
Bryant, P.M. & Scoville, N.Z. 1996, ApJ, 457, 678.
Carilli, C.L., Röttgering, H.J.A., van Ojik, R., Miley, G.K. & van Breugel, W.J.M. 1997, ApJS, 109, 1.
Carilli, C.L., Kohno, K., Kawabe, R., Ohta, K., Henkel, C., Menten, K.M., Yun, M.S., Petric, A. & Tutui, Y. 2002a, AJ, 123, 1838.
Carilli, C.L., Cox, P., Bertoldi, F., Menten, K.M., Omont, A., Djorgovski, S.G., Petric, A., Beelen, A., Isaak, K.G. & McMahon, R.G. 2002b, ApJ, 575, 145.
Carilli, C.L., Lewis, G.F., Djorgovski, S.G., Mahabal, A., Cox, P., Bertoldi, F., & Omont, A. 2003, Science, 300, 773.
Chambers, K.C., Miley, G.K., van Breugel, W.J.M., Bremer, M.A.R., Huang, J.-S. & Trentham, N.A. 1996, ApJS, 106, 247.
Colbert, J.W., Malkan, M.A., Clegg, P.E., Cox, P., Fischer, J., Lord, S.D., Luhman, M., Satyapal, S., Smith, H.A., Spinoglio, L., Stacey, G., & Unger, S.J. 1999, ApJ, 511, 721.
Cox, P., Omont, A., Djorgovski, S.G., Bertoldi, F., Pety, J., Carilli, C.L., Isaak, K.G., Beelen, A., McMahon, R.G. & Castro, S. 2002, A&A, 387, 406.
De Breuck, C., Neri, R., Morganti, R., Omont, A., Rocca-Volmerange, B., Stern, D., Reuland, M., van Breugel, M., Röttgering, H.J.A., Stanford, S.A., Spinrad, H., Vigotti & M., Wright, M. 2003a, A&A, 401, 911.
De Breuck, Neri, R. & Omont, A. 2003b, "Radio Galaxies: Past, present and future", Leiden, 11-15 Nov 2002, eds. M. Jarvis et al.
Downes, D., Solomon, P.M. & Radford, S.J.E. 1993, ApJ, 414, L13.
Downes, D. & Solomon, P.M. 1998, ApJ, 506, 615.
Dunlop, J.S., Hughes, D.H., Rawlings, S., Eales, S. & Ward, M. 1994, Nature, 370, 347.
Eggen, O.J., Lynden-Bell, D. & Sandage, A.R. 1962, ApJ, 136, 748.
Fanaroff, B.L. & Riley, J.M. 1974, MNRAS, 167, 31.
Ferrarese, L. & Meritt, D. 2000, ApJ, 539, L9.
Fixsen, D.J., Bennett, C.L., & Mather, J.C. 1999, ApJ, 526, 207.
Gao, Y. & Solomon, P.M. 2003, in "Star formation at high angular resolution", IAU Symposium No 221, Sydney Australia, p.95.
Greve, T.R., Ivison, R.J., & Papadopoulos, P.P. 2003, ApJ, 599, 839.
Guilloteau, S., Omont, A., Cox, P., McMahon, R. & Petitjean, P. 1999, A&A, 349, 363.
Hughes, D.H., Dunlop, J.S. & Rawlings, S. 1997, MNRAS, 289, 766.
Ivison, R.J., Dunlop, J.S., Hughes, D.H., Archibald, E.N., Stevens, J.A., Holland, W.S., Robson, E.I., Eales, S.A., Rawlings, S., Dey, A., & Gear, W. K. 1998, ApJ, 494, 211.
Ivison, R.J., Dunlop, J.S., Smail, I., Dey, A., Liu, M.C., & Graham, J.R. 2000, ApJ, 542, 27.
Kauffmann, G. 1996, MNRAS, 281, 487.
Kauffmann, G. & Charlot, S. 1998, MNRAS, 294, 705.
Mao, R.Q., Henkel, C., Schulz, A., Zielinsky, M., Mauersberger, R., Störzer, H., Wilson, T.L., & Gensheimer, P. 2000, A&A, 358, 433.
McLure, R.J. & Dunlop, J.S. 2000, MNRAS, 317, 249.
Omont, A., Petitjean, P., Guilloteau, S., McMahon, R.G., Solomon, P.M., & Pecontal, E. 1996, Nature, 382, 428.
Omont, A., Cox, P., Bertoldi, F., McMahon, R.G., Carilli, C., & Isaak, K.G., 2001, A&A, 374, 371.
Papadopoulos, P. P., Röttgering, H. J. A., van der Werf, P. P., Guilloteau, S., Omont, A., van Breugel, W. J. M. & Tilanus, R. P. J. 2000, ApJ, 528, 626.

Papadopoulos, P.P. & Ivison, R.J. 2002, ApJ, 564, L9.
Papadopoulos, P.P., Ivison, R.J., Carilli, C.L., & Lewis, G. 2001, Nature, 409, 58.
Röttgering, H., van Oijk, R., Miley, G., Chambers, K., van Breugel, W. & de Koff, S. 1997 A&A, 326, 505.
Solomon, P.M., Downes, D., Radford, S.J.E. & Barrett, J.W. 1997, ApJ, 478, 144.
Stevens, J.A., Ivison, R.J., Dunlop, J.S., Smail, I., Percival, W.J., Hughes, D.H., Röttgering, H.J.A., van Breugel, W.J.M. & Reuland, M. 2003, Nature, 425, 264.
Strong, A. W., Bloemen, J. B. G. M., Dame, T. M., Grenier, I. A., Hermsen, W., Lebrun, F., Nyman, L.-A., Pollock, A. M. T. & Thaddeus, P. 1988, A&A, 201, 1.
Tinsley, B.M. & Gunn, J.E. 1976, ApJ, 203, 52.
West, M.J. 1994, MNRAS, 268, 79.

Chapter 7

An Interferometric CO Survey of Luminous Submm Galaxies

Absstract. In this paper we present results from an IRAM Plateau de Bure millimetre-wave Interferometer (PdBI) survey for CO emission towards radio-detected submillimetre galaxies (SMGs) with known optical and near-infrared spectroscopic redshifts. Five sources in the redshift range $z \sim 1$–3.5 were detected, nearly doubling the number of SMGs detected in CO. We summarise the properties of all 12 CO-detected SMGs, and use this sample to explore the bulk physical properties of the SMG population as a whole. The median CO line luminosity of the SMGs is $\langle L'_{\rm CO} \rangle = (3.8 \pm 2.0) \times 10^{10}\,{\rm K\,km\,s^{-1}\,pc^2}$. Using a CO-to-$H_2$ conversion factor appropriate for starburst galaxies, this corresponds to a molecular gas mass $\langle M({\rm H_2}) \rangle = (3.0 \pm 1.6) \times 10^{10}\,M_\odot$, about five times greater than the most luminous local ultraluminous infrared galaxies (ULIRGs) but comparable to that of the most extreme high-redshift radio galaxies and QSOs. The median CO FWHM linewidth is broad, $\langle {\rm FWHM} \rangle = 780 \pm 320$ km s^{-1} , and the SMGs often have double peaked line profiles, indicative of either a merger or a disk. From their gas reservoirs we estimate a lower limit on the typical gas-depletion time scale of $\gtrsim 30$ Myr in SMGs. This is significantly smaller than the typical ages of the starbursts in SMGs, and suggests that negative feedback processes play an important role in proloning the gas consumption time scale. We find a statistically significant correlation between the far-infrared and CO luminosities of the SMGs which extends the observed correlation for local ULIRGs to higher luminosities and higher redshifts. The non-linear nature of the correlation implies that SMGs have higher far-infrared to CO luminosity ratios, and possibly higher star-formation efficiencies, than local ULIRGs. Assuming a typical CO source diameter of $\theta \sim 0\farcs5$ ($D \sim 4$ kpc), we estimate a median dynamical mass of $\langle M_{dyn} \rangle \simeq (1.2 \pm 1.5) \times 10^{11}\,M_\odot$ for the SMG sample. Both the total gas and stellar masses imply that SMGs are very massive systems, dominated by baryons in their central regions. The baryonic and dynamical properties of these systems mirror those of local giant ellipticals and are consistent with numerical simulations of the formation of the most massive galaxies. We have been able to impose a lower limit of $\gtrsim 1.0 \times 10^{-5}\,{\rm Mpc^{-3}}$ to the co-moving number density of massive galaxies in the redshift range $z \sim 2$–3.5, which is in agreement with results from recent spectroscopic surveys and the most recent model predictions.

7.1 Introduction

The discovery of extragalactic carbon monoxide (CO) rotational line emission (Rickard et al. 1975) and, in particular, the first detections of CO at cosmologically significant redshifts in IRAS F10214+4724 at $z = 2.29$ (Brown & Vanden Bout 1991; Solomon, Downes & Radford 1992), the Cloverleaf at $z = 2.56$ (Barvainis et al. 1994) and BRI 1202−0725 at $z = 4.69$ (Omont et al. 1996) revealed the potential of CO as a tracer of molecular gas in the early Universe. Since those pioneering efforts, progress has been slow due to the severe observational obstacles: the faintness of the CO emission, except for cases were the source is gravitationally magnified; inaccurate

Greve, T.R, Bertoldi, F., Smail, I.R., Neri, R., Blain, A.W., Ivison, R.J., Chapman, S.C., Genzel, R., Omont, A., Cox, P., Tacconi, & Kneib, J.-P. 2004, MNRAS, submitted.

spectroscopic redshifts coupled with the small instantaneous bandwidth of most modern-day correlators; and in some cases, an unfortunate combination of redshift and available receiver coverage, as well as atmospheric transparency, at millimetre wavelengths. As a result only 30-or-so $z > 1$ objects have been detected to date, most of which have been extremely luminous, often gravitationally lensed, QSOs (e.g. Omont et al. 1996; Guilloteau et al. 1997, 1999; Downes et al. 1999; Cox et al. 2002; Beelen et al. 2004) and high-redshift radio galaxies (HzRGs — e.g. Papadopoulos et al. 2000; De Breuck et al. 2003a).

The slow increase in the number of CO detections contrasts with the rapid growth in samples of high-redshift galaxies selected through continuum observations at submillimetre (submm) wavelengths, which detect thermal emission from dust. The advent of large-format submm/mm cameras, SCUBA (Holland et al. 1999) and MAMBO (Kreysa et al. 1998), revealed the presence of a significant population of dust-enshrouded, and therefore hitherto undetected, galaxies at high redshifts (e.g. Smail, Ivison & Blain 1997; Barger et al. 1998; Bertoldi et al. 2000). Today such observations are routine, and several hundred submm-selected (or SCUBA) galaxies (SMGs) have been discovered (e.g. Blain et al. 2002; Scott et al. 2002; Webb et al. 2003; Borys et al. 2003).

Until recently, only two SMGs were detected in CO (Frayer et al. 1998; 1999; Downes & Solomon 2003; Genzel et al. 2003), largely owing to the extreme faintness of SMGs in the optical and the difficulties in obtaining reliably spectroscopic redshifts. However, a major step forward was made by Chapman et al. (2003b, 2004b) who used the highly-efficient, blue-sensitive LRIS-B spectrograph on the Keck Telescope to obtain spectroscopic redshifts for a large sample of SMGs. This motivated a major survey at the IRAM Plateau de Bure Interferometer (PdBI) to look for CO emission from this high-redshift sample. The observational cycle involves: identifying a robust radio counterpart to an SMG in deep VLA radio maps (see e.g. Ivison et al. 2002); placing a LRIS-B/Keck slit on this position to obtain a spectroscopic redshift (Chapman et al. 2003b, 2004b); frequently confirming the redshift in the near-infrared, usually via redshifted Hα (Swinbank et al. 2004); and, finally, searching for redshifted CO emission with PdBI. The initial results from this CO programme were described in Neri et al. (2003). Although an expensive process in terms of telescope time, this is currently the only feasible and effective route to detecting CO from SMGs.

CO observations can potentially provide unique information about the enigmatic SMG population. First and foremost, CO traces the bulk of the molecular gas in SMGs: the high-level ($J \geq 2$) transitions arise in the warm and dense gas while lowest level J lines probe the quiescent and likely cooler gas which may lurk in the outskirts of SMGs. Detecting and mapping this molecular emission enables us to precisely locate the spatial and kinematic location of the gas-rich components within an SMG. About two-thirds of SMGs are found to be large, morphologically complex systems in the optical/near-infrared and/or the radio, with typically one or more companions (e.g. Smail et al. 1999; Ivison et al. 2002; Chapman et al. 2003c, 2004a). For example, in one SMG, Neri et al. (2003) identified CO emission coincident with a second, fainter radio source $\sim 4''$ away from the radio counterpart for which the spectroscopic redshift had been found. Secondly, CO observations yield fairly accurate estimates of the amount of molecular gas available to fuel the starburst and/or the AGN responsible for the large far-infrared luminosities. While the conversion factor between the CO luminosity and molecular gas mass is uncertain, CO observations clearly provide a much better constraint on the amount of gas present in SMGs than the estimates based on submm continuum observations and an adopted spectral energy distribution (SED) and gas-to-dust ratio.

The first two CO detections of SMGs revealed the presence of copious amount of molecular gas ($\sim 10^{10}\,M_{\odot}$), suggesting that intense star formation is occcuring in these systems (Frayer et al. 1998; 1999). Furthermore, from a reliable estimate of the gas reservoir in an SMG we can say

something about the gas exhaustion time-scale, i.e. the duration of the submm-luminous phase. This, in turn, allows us to make an educated guess about the possible descendants of SMGs, and thus place them in an evolutionary context with other high- and low-redshift galaxy populations.

Observations of the shape and width of CO lines also provides important information about the kinematics in SMGs (Neri et al. 2003; Tacconi et al. 2005). In particular, if the CO emission is spatially resolved we can use that, in conjunction with the width of the line profile, to constrain the dynamical mass of the host galaxy. Estimates of the dynamical mass based on CO are likely to be 'cleaner' than estimates from optical/near-infrared spectroscopy, which are prone to extinction by dust and the effects of non-gravitational motions in the emitting gas, such as outflows. The best example of resolved CO emission in a SMG (Genzel et al. 2003) shows gas extended on scales of $\sim$ 3–5 kpc and that most of the dynamical mass ($\sim 3 \times 10^{11}\,M_{\odot}$) is baryonic. Such large, widely-distributed gas reservoirs suggest that the brightest SMGs are not merely high-redshift replicas of the local population of ULIRGs. However, a representative picture of the gas distribution in SMGs will have to await high-resolution CO observations of a large sample of SMGs.

Since CO observations provide means of 'weighing' galaxies at high redshifts, both in terms of their baryonic gas mass content and their total dynamical mass, they can be used to help piece together a picture of the mass assembly of massive galaxies in the early Universe. In the classical cold-dark matter (CDM) scenario of structure formation (White & Frenk 1991), massive spheroidal galaxies are the end products of a gradual build-up of mass via merging and, as a result, form late in the history of the Universe. However, as pointed out by Genzel et al. (2003), at least some SMGs appear to be massive, baryon-dominated galaxies already at $z \sim 2$–3. The discovery of massive, evolved early-type galaxies at $z \gtrsim 1.5$ (e.g. Cimatti et al. 2004), which could be the descendants of $z \gtrsim 2$ SMGs, suggests that massive spheroids were not all formed at $z \lesssim 1$. In fact, if the brightest 25 per cent of the SMGs are massive baryonic systems, then their abundance indicates that the build up of massive galaxies in the early Universe was much faster than previously expected, and could pose a serious challenge for current models of gas processing in galaxy formation (e.g. Cole et al. 1994; Kauffmann et al. 1999; Baugh et al. 2004).

In this paper we present the most recent results from a systematic survey of CO emission towards radio-identified SMGs with spectroscopic redshifts in the range $z \sim 1$–3.5 (corresponding to 40–10% of the age of the Universe at the respective epochs), and use these to address the issues outlined above. This is part of a major effort currently being undertaken at the PdBI with the aim of detecting and imaging CO emission towards $\sim$ 20–30 SMGs. In §7.2 and 7.3 we describe the observations and derive properties for each new source observed. In §7.4 we define a sample of 11 sources consisting of all SMGs detected in CO to date, from which the average physical properties of the bright SMG population are derived. We discuss their properties and compare with those of other galaxy populations in §7.5. Finally, §7.6 discusses the impact of our observations on models of galaxy formation and evolution. Throughout we adopt a flat cosmology, with $\Omega_m = 0.27$, $\Omega_\Lambda = 0.73$ and $H_0 = 71\,\mathrm{km\,s^{-1}\,Mpc^{-1}}$ (Spergel et al. 2003).

7.2 Observations

In total, 12 SMGs were targeted for CO observations with PdBI (see Table 7.2), drawn from five independent submm surveys: the SCUBA Lens Survey (SMM J02396−0134 — Smail, Ivison & Blain 1997); the Hubble Deep Field (SMM J12360+6210 — Chapman et al. 2003a); the Hawaii Survey Fields, SSA 13 and SSA 22 (SMM J13120+4242, SMM J13123+4239 — Chapman et al. 2004b; SMM J22174+0015 — Barger et al. 1999); The SCUBA UK 8 mJy Survey of the Lockman Hole East and ELAIS N2 (SMM J10516+5723, SMM J10523+5722, SMM J10524+5724,

SMM J16363+4055,
SMM J16363+4056, and SMM J16366+4105 — Scott et al. 2002); and a 1200-μm MAMBO survey of the same two fields (SMM J16371+4053[1] — Greve et al. 2004b).

Deep radio imaging was used to identify radio counterparts to all the targeted SMGs and accurately locate these relative to optical/near-infrared reference fields (Smail et al. 1999; Chapman et al. 2003a; Ivison et al. 2002). Subsequent spectroscopy with Keck/LRIS-B (Oke et al. 1995) and CFHT/OSIS-V in the case of SMM J02396−0134 (Soucail et al. 1999) provided UV spectroscopic redshifts for all sources (see Chapman et al. 2003b, 2004b). A subset of the sample were spectroscopically observed in the near-infrared to provide more reliable systemic redshifts from the wavelengths of redshifted Hα or [OIII] 5007 emission lines (Swinbank et al. 2004) to aid in our search for redshifted CO emission.

From our sample of 12 sources, 11 were targeted during two observing campaigns, during the winter of 2002–03 and the summer of 2003, in good to excellent weather. The observations were done in D configuration in order to maximize the sensitivity, and used five of the six available antennae, giving a total of 10 baselines. Data for the 12th source, SMM J02396−0134, was originally obtained by J.-P. Kneib and D. T. Frayer during summer/autumn of 1999, and these were retrieved from the PdBI data archive. Observations of this source were done in D and C configuration. The details of the observations of all 12 sources are summarised in Table 7.2.

While our main goal was to detect redshifted CO emission in the 3-mm waveband, we also used the 1.3-mm receivers to attempt to determine accurate continuum positions and fluxes or, in cases where a higher-J CO line would coincide with the 1.3-mm band, to search for emission from this transistion, e.g. SMM J04431+0210 (Neri et al. 2003). To achieve our goals the correlators were configured for line and continuum observations and simultaneously covered 580 MHz in the 3-mm and 1.3-mm bands: this corresponds to a typical velocity coverage of 1700 and 750 km s^{-1} at 3 and 1.3 mm, respectively.

Where a near-infrared spectroscopic redshift was unavailable we have to correct for the likely systematic blueshifts of UV line features relative to the CO emission. We therefore tuned the 3-mm receivers slightly redward of the measured spectroscopic redshift. This meant that for a typical redshift uncertainty of $\Delta z = 0.005$, any source at $z \geq 1$ would have its CO line peak fall within $0.5 \times 580\,\mathrm{MHz} = 290\,\mathrm{MHz}$ of the 3-mm band centre. In a few instances, a line was detected at the edge of the band pass. The frequency setting was then adjusted to centre the line in the bandpass, and the source was re-observed. A source was typically observed for 2–3 tracks (12–18 hrs). If no signal had been detected after this, the source was not pursued further.

All data reduction employed the IRAM GILDAS software (Guilloteau & Lucas 2000). This involved careful monitoring of the quality of the data throughout a track, and subsequent flagging of any bad and high phase-noise visibilities. For passband calibration we typically used one or more bright quasars. Phase and amplitude variations within each track were calibrated out by inter-leaving reference observations of nearby fainter quasars every 20 m. In the best conditions, the typical rms phase noise per baseline at 3 mm was $\lesssim 10°$, increasing to $\lesssim 40°$ in the worst cases. Observations of the primary calibrators, 3C454.3, 3C345, 3C273, and MWC 349, were used to determine the flux scale. Finally, naturally weighted data cubes were created using GILDAS.

No sources were detected at 1 mm and for the remainder of this paper we shall only discuss the 3 mm data. Of the 12 sources whose observations are analysed in this paper, CO emission was reliably detected in five. Including the first three (out of three) detections from our survey from Neri et al. (2003) yields a detection rate of 53% (8/15). The failure to detect CO in some of our sources can be attributed to either too large a velocity offset between the CO and optical

[1] This source was denoted MM J16371+4053 in Greve et al. (2004b)

Table 7.1: Log of the PdBI observations for the 12 SMGs analysed in this paper. The on-source time is the observing time for the equivalent six element array.

Source	Observing Dates	t_{int} (hr)	Detection
SMM J02396−0134	1999 Jun 20, 24–26, 29, Aug 24, 27, Sep 7	7.4	Y
SMM J10516+5723	2003 Apr 17, 23, May 15	13.6	N
SMM J10523+5722	2003 Apr 25, May 06	9.5	N
SMM J10524+5724	2003 Mar 27	3.9	N
SMM J12360+6210	2003 Jun 01, 03, 18, Aug 30, Sep 01	9.4	N
SMM J13120+4242	2003 May 17, 22–23, 26	9.2	Y
SMM J13123+4239	2003 Jun 23, 26, 27	4.7	N
SMM J16363+4055	2003 Mar 31, Apr 03, 21	11.2	N
SMM J16363+4056	2003 Aug 11, 22, 24	9.6	N
SMM J16366+4105	2003 Apr 13–14, 23, May 1	14.9	Y
SMM J16371+4053	2003 Jul 25–26, 29 Aug 1,2, Sep 4	17.1	Y
SMM J22174+0015	2003 May 9–13, 29–30, Jun 4, Sep 12, 14	17.3	Y

emission (putting the former outside our selected correlator coverage, see §7.4.2), a CO line with a width comparable to our correlator bandwidth, or simply that the sources are too faint in CO to be detected in the given integration time. In the latter case, the seven non-detections can provide useful upper limits on their CO luminosity and gas masses and as a result we have included them in the analysis in this paper.

7.3 The Sources

In this section we shall briefly describe the properties of the five SMGs for which new CO detections are presented in this paper.

SMM J02396−0134 The CO $J = 2 - 1$ spectrum of SMM J02396−0134 is shown in Fig. 7.1a. The blue wing of the line is missing due to the limited correlator bandwidth available in 1999, but nonetheless it is evident that the line is double peaked. The CO redshift, $z_{\rm CO} = 1.062 \pm 0.002$, was defined as the flux-weighted redshift, see section 7.4.2 for details. The widths of the two peaks were estimated by simultaneously fitting two Gaussians to the spectrum, which yielded FWHM values 180 ± 20 km s^{-1} and 430 ± 50 km s^{-1} for the blue-shifted and red-shifted peaks, respectively. The velocity offsets of the two peaks were -280 km s^{-1} and 90 km s^{-1} , respectively, measured relative to the CO redshift. From the double Gaussian fit the velocity-integrated CO $J = 2 - 1$ line flux is $I_{\rm CO} = 3.4 \pm 0.3$ Jy km s^{-1}. A single Gaussian fit to the line profile leads to a FWHM value of 780 ± 60 km s^{-1} . Due to the truncated line we can only impose a lower limit $\simeq 870$ km s^{-1} on the full width at zero intensity (FWZI).

The emission integrated over the from -460 km s^{-1} to 110 km s^{-1} is shown as contours overlaid on a K-band image in Fig. 7.2a. The emission is detected at $\geq 10\sigma$, where $\sigma = 0.40$ mJy beam^{-1}, and coincides with the optical/near-infrared counterpart to within the relative astrometrical errors. The source appears extended in the north-south direction, and an elliptical Gaussian fit to the CO emission in the image plane yields a source size of $9\farcs5 \times 5\farcs5$, which is slightly larger than the $8\farcs3 \times 5\farcs3$ synthesized beam. The two velocity components of the source have a slight spatial offset, with the blue-shifted peak (integrated from -460 to -120 km s^{-1}) $1.2''$ north of the centroid of the integrated line emission and the red-shifted peak (integrated from -120 to 110 km s^{-1}) offset $0.3''$ east and $1.6''$ south of the central position. The positional uncertainties in the maps are 0.3–0.4″, suggesting that the observed offsets are significant.

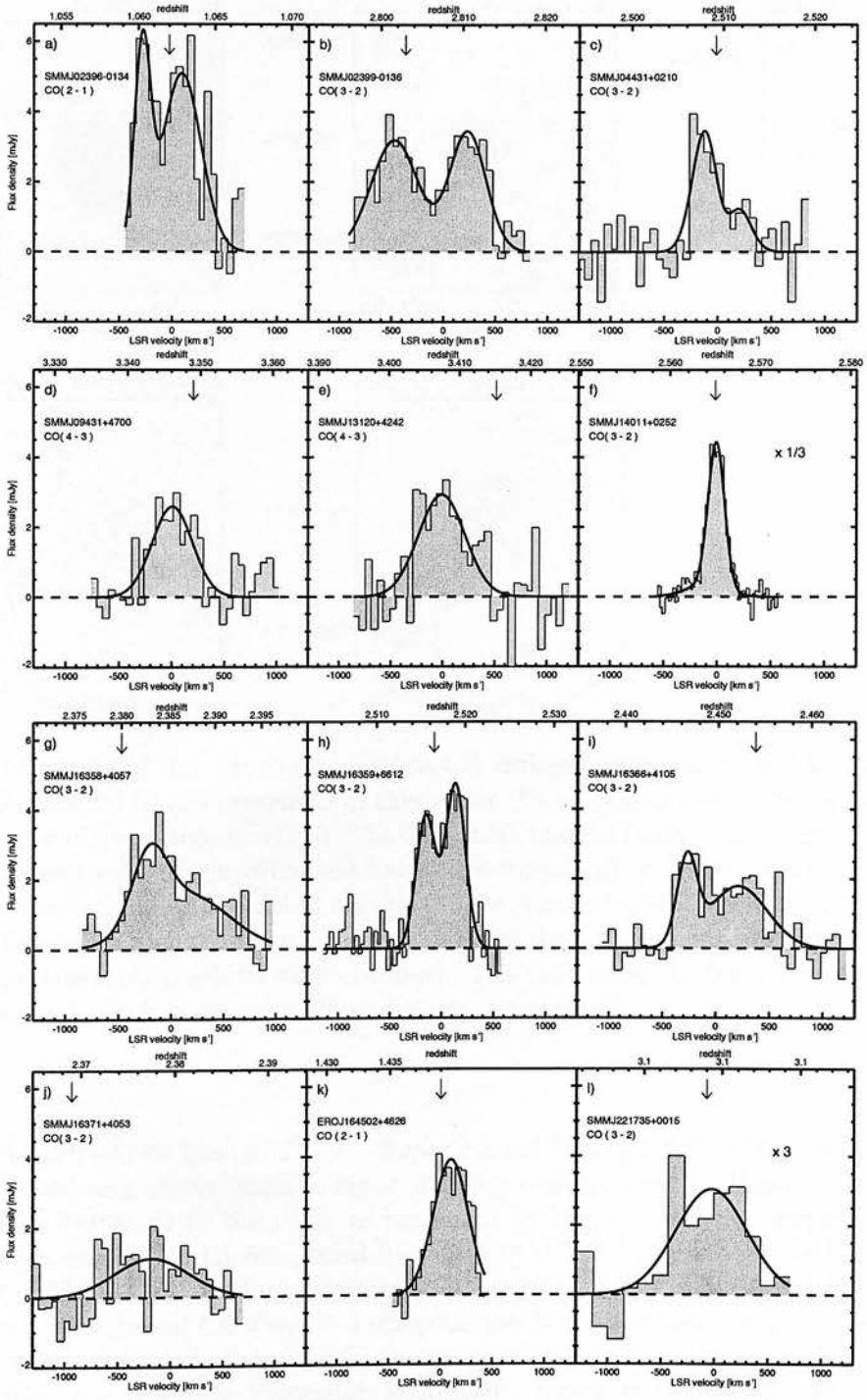

Figure 7.1: CO line profiles of the 12 SMGs detected in CO to date. The profiles have been plotted on similar flux- and velocity-scales in order to facilitate an easy comparison between individual sources, to achieve this the spectra of SMM J14011+0252 and SMM J221735+0015 have been scaled by a factor $\times 1/3$ and $\times 3$, respectively. The LSR velocity-scale is relative to the CO redshift. Optical redshifts are denoted by arrows while the redshifts derived from the CO lines are given in Table 7.3. The solid curves represent the best-fits to the spectra using either single or double Gaussian profiles. The spectra shown in c), d) and g) are taken from Neri et al. (2003), while b), f) and k) are from Genzel et al. (2003), Downes & Solomon (2003) and Andreani et al. (2000), respectively.

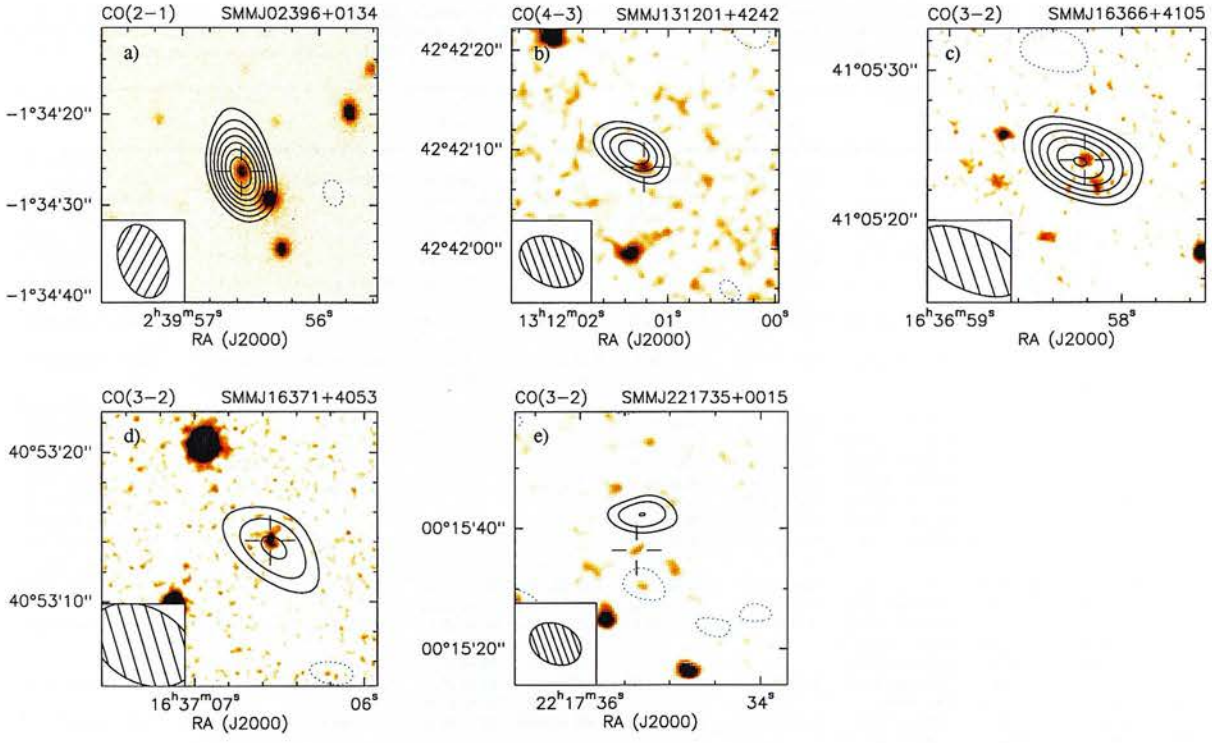

Figure 7.2: Contours of the velocity integrated CO emission overlaid on K-band images for the five new CO-detected SMGs presented in this paper. In all panels the contours start at 3σ and increase in steps of 1σ, where $\sigma = 0.40, 0.32, 0.21, 0.18$, and $0.17\,\mathrm{mJy\,beam^{-1}}$ in panels a), b), c), d), and e), respectively. The synthesized beams are (panels a) to e), shown as hatched ellipsed) $8\farcs3 \times 5\farcs3$ at position angle 15^o (east of north), $6\farcs9 \times 4\farcs8$ at 66^o, $7\farcs4 \times 3\farcs9$ at 62^o, $7\farcs4 \times 5\farcs0$ at 61^o, and $9\farcs0 \times 6\farcs6$ at 65^o. Open crosses mark the position of the optical/near-infrared counterparts for which the spectroscopic redshifts were obtained. The (1σ) uncertainties on measured positions in the optical and mm frames are $\lesssim 0\farcs1$ and $\lesssim 0\farcs3$, respectively.

SMM J13120+4242 The CO $J = 4 - 3$ spectrum of SMM J13120+4242 is shown in Fig. 7.1e. The line is broad and shows possible signs of being double peaked. However, a single Gaussian provides a better fit to the data, as measured by the χ^2 statistic. From a single Gaussian fit we estimate a velocity-integrated flux density, $1.7 \pm 0.3\,\mathrm{Jy\,km\,s^{-1}}$ and a line width of $\mathrm{FWHM} \simeq 530 \pm 50\ \mathrm{km\,s^{-1}}$. We find a systemic CO redshift of $z_{\mathrm{CO}} = 3.408 \pm 0.003$.

The velocity-integrated CO $J = 4 - 3$ emission yields a $\gtrsim 6$-σ detection at position which is offset $2.3''$ to the north-east of the optical counterpart (Fig. 7.2b). The positional error is $\sim 1''$, and so the offset appears to be marginally significant. Again, it could be a case similar to that of SMM 09431+4700, although no radio or optical/near-infrared emission coincides with the CO peak. The CO emission is unresolved.

SMM J16366+4105 The CO $J = 3 - 2$ spectrum of SMM J16366+4105 (Fig. 7.1h) is very broad with the blue edge of the line ending abruptly. The spectrum exhibits a double-peaked line similar to SMM 02396−0134, although less distinct. The CO redshift is $z = 2.450 \pm 0.002$. A simultaneous fit of two Gaussians provides a superior fit to the spectrum than a single Gaussian, and places the blue-shifted and red-shifted peaks at velocity offsets of $-270\,\mathrm{km\,s^{-1}}$ and

Table 7.2: SMGs observed in CO to date, including the submm-bright ERO J16450+4626 which although not selected in the submm is thought to be similar to the SMG population. The top section of the table lists the five new CO detections presented here and the threepreviously published detections from our survey (Neri et al. 2003); the six non-detected SMGs are listed in the middle section, while the sources from the literature are given in the bottom section of the table.

Source name	Transition	$z_{\rm spec}$	CO position		Optical/NIR position		$z_{\rm CO}$	ΔV_{FWHM}	$I_{\rm CO}$	Ref.
			α_{J2000} (h m s)	δ_{J2000} ($^\circ$ ′ ″)	α_{J2000} (h m s)	δ_{J2000} ($^\circ$ ′ ″)		(km s^{-1})	(Jy km s^{-1})	
Detections										
SMM J02396−0134[a,b]	(2−1)	1.062 ± 0.001[c]	02 39 56.59	-01 34 26.6	02 39 56.51	−01 34 25.66	1.062 ± 0.002	780 ± 60	3.4 ± 0.3	[1]
SMM J13120+4242	(4−3)	3.405[d]	13 12 01.20	+42 42 08.8	13 12 01.23	+42 42 08.2	3.408 ± 0.002	530 ± 50	1.7 ± 0.3	[1]
SMM J16366+4105	(3−2)	2.454[d]	16 36 58.23	+41 05 23.7	16 36 58.21	+41 05 23.9	2.450 ± 0.002	870 ± 80	1.8 ± 0.3	[1]
SMM J16371+4053	(3−2)	2.374[d]	16 37 06.50	+40 53 13.8	16 37 06.54	+40 53 14.1	2.380 ± 0.004	830 ± 130	1.0 ± 0.2	[1]
SMM J22174+0015	(3−2)	3.098[d]	22 17 35.20	+00 15 37.6	22 17 34.95	+00 15 33.2	3.099 ± 0.004	780 ± 100	0.8 ± 0.2	[1]
SMM J04431+0210[a,b]	(3−2)	2.5092 ± 0.0008[c]	04 43 07.25	+02 10 23.3	04 43 07.25	+02 10 24.4	2.5094 ± 0.0002	350 ± 60	1.4 ± 0.2	[2]
	(7−6)	...	...	...	...	...	...	...	≤ 0.8	[2]
SMM J09431+4700[a]	(4−3)	3.349[d]	09 43 03.74	+47 00 15.3	09 43 03.70[f]	+47 00 15.1[f]	3.3460 ± 0.0001	420 ± 50	1.1 ± 0.1	[2]
	(9−8)	...	...	...	...	...	...	...	≤ 1	[2]
SMM J16358+4057	(3−2)	2.380 ± 0.002[d]	16 36 50.43	+40 57 34.7	16 36 50.40	+40 57 34.2	2.3853 ± 0.0014	840 ± 110	2.3 ± 0.2	[2]
	(7−6)	...	16 36 50.41	+40 57 34.3	...	...	2.383	...	1.1 ± 0.2	[2]
Non-detections										
SMM J10516+5723	(4−3)	3.7[d]	...	...	10 51 55.47	+57 23 12.7	3.6851 − 3.7129	...	≤ 0.4	[1]
SMM J10523+5722	(3−2)	2.611[d]	...	...	10 52 30.73	+57 22 09.5	2.5901 − 2.6119	...	≤ 0.5	[1]
SMM J10524+5724	(3−2)	3.036[d]	...	...	10 52 38.30	+57 24 35.8	3.0593 − 3.0318	...	≤ 0.8	[1]
SMM J12360+6210	(3−2)	1.994[d]	...	...	12 36 00.20	+62 10 47.0	1.9865 − 2.0015	...	≤ 0.9	[1]
SMM J13123+4239	(3−2)	2.320[d]	...	...	13 12 32.30	+42 39 50.0	2.3115 − 2.3300	...	≤ 1.0	[1]
SMM J16363+4055	(3−2)	2.283[d]	...	...	16 36 31.47	+40 55 46.9	2.2676 − 2.2919	...	≤ 0.4	[1]
SMM J16363+4056	(2−1)	1.495[d]	...	...	16 36 39.01	+40 56 35.9	1.4802 − 1.5001	...	≤ 0.8	[1]
Literature sources										
SMM J02399−0136[a,b]	(3−2)	2.803 ± 0.003[d]	02 39 51.89	−01 35 58.9	02 39 51.88	−01 35 58.0	2.808 ± 0.002	710 ± 80	3.0 ± 0.4	[3]
	(3−2)	...	02 39 51.87	−01 35 58.8	02 39 51.85	−01 35 58.2	2.8076 ± 0.0002	≥ 1100	3.1 ± 0.4	[4]
SMM J14011+0252[a,b]	(3−2)	2.562 ± 0.002[d]	14 01 04.92	+02 52 25.6	14 01 04.95	+02 52 24.0	2.5653 ± 0.0003	200 ± 40	2.4 ± 0.3	[5]
	(3−2)	...	14 01 04.93	+02 52 24.1	...	...	2.5652 ± 0.0001	190 ± 11	2.8 ± 0.3	[6]
	(7−6)	...	14 01 04.92	+02 52 23.8	...	...	2.5651 ± 0.0002	170 ± 30	3.2 ± 0.5	[6]
SMM J16359+6612[a,b]	(3−2)	2.5165 ± 0.0015[c]	16 35 54.15	+66 12 24	16 35 54.19	+66 12 24.9	2.5168 ± 0.0003	500 ± 100	3.5 ± 0.1	[7]
	(3−2)	...	16 35 54.10	+66 12 23.8	...	...	2.5174 ± 0.0002	500 ± 100	2.50 ± 0.12	[8]
ERO J16450+4626[b]	(2−1)	1.439[c]	16 45 02.26	+46 26 26.5	16 45 02.36	+46 26 25.5	1.439 ± 0.001	400	1.4 ± 0.1	[8]
	(5−4)	...	...	...	...	...	1.440 ± 0.001	380	1.35	[9]
	(1−0)	...	...	...	...	...	...	...	0.6 ± 0.1	[10]

[a] The source is lensed, see Table 3 for magnifications $\mu_{\rm L}$.
[b] The CO emission is extended.
[c] The redshift is derived from Hα.
[d] The redshift is derived from Lyα.
[f] Position of H7, see Neri et al. (2003) for details.
[1] This work; [2] Neri et al. (2003); [3] Frayer et al. (1998); [4] Genzel et al. (2003); [5] Frayer et al. (1999); [6] Downes & Solomon (2003); [7] Sheth et al. (2004); [8] Kneib et al. (2004); [9] Andreani et al. (2000); [10] Greve et al. (2003).

+210 km s^{-1}, respectively. The velocity-integrated line flux is $I_{\rm CO} = 1.8 \pm 0.3$ Jy km s^{-1} . A single Gaussian fitted to the spectrum yields a line width FWHM=870 ± 80 km s^{-1} – the second largest line width of the sample.

The integrated CO emission, shown in Fig. 7.2c, is detected at the $\gtrsim 8$-σ level, and coincides with the radio and faint optical/near-infrared counterpart. We imaged the blue-shifted and red-shifted peaks separately, using different velocity cut-offs, in order to look for positional offsets between the two, but found no evidence for a velocity gradient across the source. It is possible that part of the CO emission is related to the faint near-infrared source $\sim 2''$ south-west of the CO centroid, the compact radio counterpart displays a similar faint tail of emission in this direction. SMM J16366+4105 is a prime target for further, higher-resolution CO observations.

SMM J16371+4053 The detection of CO $J = 3 - 2$ towards SMM J16371+4053 is the first for a MAMBO-selected source. The CO $J = 3 - 2$ line profile is shown in Fig. 7.1i. The flux-weighted, systemic CO redshift is $z_{\rm CO} = 2.380 \pm 0.004$. While clearly detected, the poor signal-to-noise ratio prevents us from defining the line profile, except to say that the line appears broad with FWZI $\gtrsim 900$ km s^{-1}. A Gaussian fit yields a formal line width of FWHM~ 830 km s^{-1} and a velocity-integrated line flux $I_{\rm CO} = 1.0 \pm 0.2$ Jy km s^{-1} .

The integrated emission is shown in Fig. 7.1d. The source is detected at $\gtrsim 5\sigma$ and coincides with the optical/near-infrared counterpart to within the positional errors.

SMM J22174+0015 The CO $J = 3 - 2$ spectrum of this source shown in Fig. 7.1k is the weakest of our detections. After heavily binning the spectrum, we estimate the line to be sig-

nificant at the $\gtrsim$ 4-σ level. We measure the flux-weighted, systemic CO redshift as $z_{\rm CO} = 3.099 \pm 0.004$. A Gaussian fit to the spectrum yields a line width of FWHM $= 780 \pm 100$ km s^{-1} and a line flux density of $I_{\rm CO} = 0.8 \pm 0.2$ Jy km s^{-1} .

Contours of the velocity-integrated CO emission are shown on a K-band image in Fig. 7.2e. The CO emission is detected at the $\sim$ 4.7-σ level ($\sigma = 0.17$ mJy beam^{-1}), at a position offset by 4.6″,1.5″ north and west from the phase centre (and the position of the spectroscopic counterpart). This is a large, but not unprecedented offset, and suggests the system may be similar to SMM 09431+4700 (Neri et al. 2003) where the CO emission is centred on a second, fainter radio/near-infrared source, $\sim 4''$ from the radio position at which the spectroscopic redshift was determined.

Non-detections In Table 7.3 we list the 3σ upper limits on the CO line flux as well as the redshift range searched for each of the 7 non-detections. In two cases, SMM J10516+5723 and SMM J10523+5722, we find tentative ($\sim 4.3\sigma$) detections of CO emission. In the latter case the line emission is seen $\sim 25''$ north-east of the expected position. The integrated CO (3–2) map of SMM J12360+6210 shows a $\sim 4\sigma$ peak slightly eastwards of the phase-center, and is thus possibly another tentative detection, albeit marginal. In the remaining cases no line emission is observed at a significance $\geq 3\sigma$.

7.4 Sample Properties

7.4.1 The sample

The main goal of this paper is to assemble a large sample of SMGs observed in CO. In order to achieve this, we add to the 12 new sources in TableZ7.2 from our survey (detections as well as non-detections) and the three earlier CO detections from this survey described in Neri et al. (2003), the two SMGs detected in CO prior to our survey: SMM J02399−0136 (Frayer et al. 1998; Genzel et al. 2003) and SMM J14011+0252 (Frayer et al. 1999; Downes & Solomon 2003). We also include the extremely red object, HR10, at $z = 1.439$ (ERO J164502+4626.4; Hu & Ridgway 1994). Initially studied because its extremely red optical–near-infrared colours, subsequent observations with SCUBA and *Hubble Space Telescope* revealed that HR10 is a powerful SMG with a distorted rest-frame UV morphology in (e.g. Cimatti et al. 1998; Dey et al. 1999). Hence, HR10 bears all the characteristics of a SMG and would have been detected in any of the SCUBA surveys to date. The CO $J = 5 - 4$, CO $J = 2 - 1$ and CO $J = 1 - 0$ lines have all been detected towards this source (Andreani et al. 2000; Greve et al. 2003).

Finally, we note that Hainline et al. (2004) detected CO $J = 3 - 2$ towards the submm source SMM J04135+10277, the first type-1 QSO to be selected at submm wavelengths (Knudsen, van der Werf & Jaffe 2003), as part of an Owens Valley Millimeter Array survey of CO emission towards high-redshift QSOs. SMM J04135+10277 is not only one of the brightest submm sources known but also an extremely luminous CO source. While SMM J04135+10277 was discovered in a blank-field (albeit lensing-assisted) submm survey and thus meets the selection criteria for our sample, only about 3 per cent of radio-identified SMGs are broad-line QSOs (Chapman et al. 2004b), suggesting that this source is not representative of the SMG population as a whole. SMM J04135+10277 is therefore not included in our sample of CO-detected SMGs.

The final SMG sample consists of 11 CO detections and 7 non-detections, their observational properties are listed in TableZ7.3. The CO line profiles of the 11 detected sources are shown in Fig. 7.1.

In the following sections we shall use the CO observations to investigate the physical properties of the SMG population, see TableZ7.4.3. In the case where a SMG is known to be gravitationally-

lensed, we have corrected the luminosities, gas masses, and linear sizes, etc., using the gravitational lensing magnification factors listed in Table 7.4.3.

7.4.2 Comparison of optical and CO redshifts

In general, CO lines provide excellent systemic redshifts for galaxies, by tracing the extended molecular gas distribution rather than the ionised gas produced by shocked outflows or accretion onto an AGN. The latter is typically traced by high-ionisation, e.g. broad C IVλ1549 lines, which have been shown to be systematically blue-shifted with respect to the systemic redshift in quasars (e.g. Richards et al. 2002), and by the Lyα line, which in the majority of high-redshift CO detections is blue-shifted with respect to the CO redshift due to outflows and dust obscuration (e.g. Richards et al. 2002; Hainline et al. 2004). The purpose of this section is to determine if similar systematic offsets between the CO and Lyα redshifts exist within the SMG population. We have measurements of the Lyα redshifts for eight of the CO-detected SMGs, see Table 7.3.

A large fraction of CO line profiles shown in Fig. 7.1 are double peaked or asymmetric, making it difficult to accurately determine the CO redshift by fitting Gaussian profiles to the spectra. Instead, the CO redshift of a source was determined by computing its flux-weighted redshift, i.e. $z_{\rm CO} = \sum I(z)z / \sum I(z)$. The error on the redshift is given by $\Delta z^2_{\rm CO} = \sum I(z)(z - z_{\rm CO})^2 / \sum I(z)$. The CO redshifts computed in this way are listed in Table 7.3.

In Fig. 7.3 we have plotted the distribution of velocity offsets corresponding to the differences between the CO and Lyα redshifts for the SMG sample (grey-shaded region) and for the 15 QSOs (dashed curve) detected in CO to date (see Table 7.5). Negative velocity-offsets correspond to blue-shifted UV emission with respect to the systemic CO redshift.

The velocity offsets between the Lyα and CO redshifts of SMGs show a slight tendency for blue-shifted offsets (five and two SMGs have blue- and red-shifted offsets, respectively, with one source consistent with no velocity offset within the errors, $\sim 150\,{\rm km\,s^{-1}}$). For the QSOs the number of blue- and red-shifted offsets are nine and two, respectively, with four sources having offsets consistent with zero. Thus SMGs, similar to QSOs, show a slight excess of sources at negative velocity offsets, although, this conclusion needs to be confirmed once a larger sample of SMGs is studied. It is clear, however, that in the majority of the SMGs, significant velocity offsets exist between the Lyα and CO emission. Such large offsets illustrate how easy it would be to miss a CO line based on blind tuning to the restframe-UV redshift, and highlight the need for future submm/mm correlators with large instantaneous bandwidths.

Realising the potential danger of not detecting some of the SMGs because of large offsets between the CO and restframe-UV redshifts, we have begun a programme to target SMGs using the near-infrared spectrographs NIRSPEC on Keck-II, OHS on Subaru and ISAAC on the VLT, to allow us to measure redshifts from restframe optical emission lines, which should provide more reliable estimates of the systemic redshifts (e.g. Swinbank et al. 2004; Simpson et al. 2004). The usefulness of this approach is demonstrated by the hashed histogram in Fig. 7.3 which shows that for the four SMGs with redshifts derived from Hα, the velocity offsets amount to no more than $\pm 75\,{\rm km\,s^{-1}}$.

7.4.3 CO Luminosities and gas masses

The CO line luminosities, $L'_{\rm CO}$, of the individual SMGs were derived from their velocity-integrated line flux densities following Solomon et al. (1997), and corrected for gravitational lensing if necessary (see Table 7.4.3). For the eight sources detected in CO $J = 3 - 2$ we find a median luminosity of $\langle L'_{\rm CO(3-2)} \rangle = (3.8 \pm 2.3) \times 10^{10}\,{\rm K\,km\,s^{-1}\,pc^2}$. Two sources were detected in CO $J = 4 - 3$ (SMM J09431+4700 and SMM J13120+4242) and two in CO $J = 2 - 1$

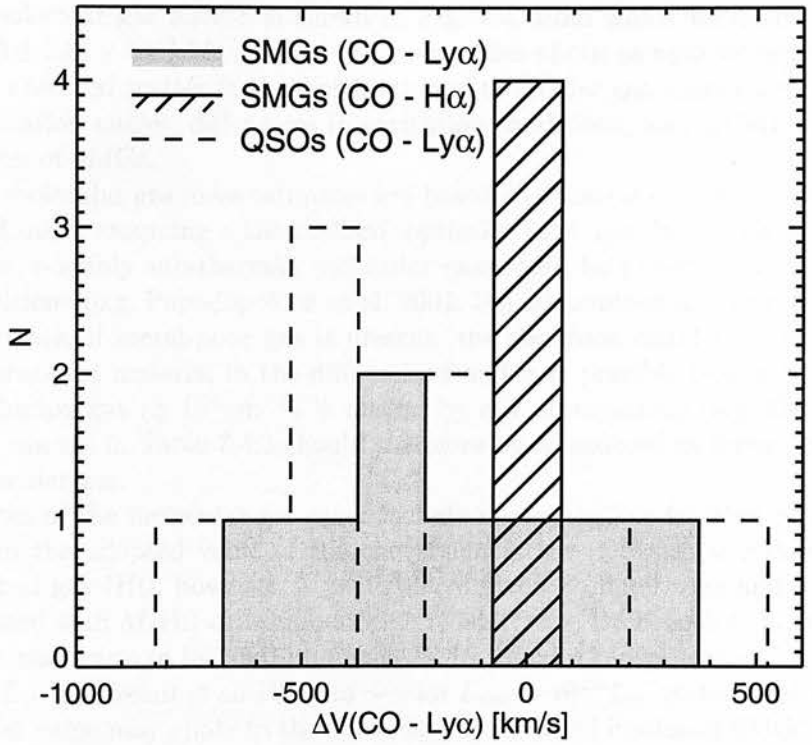

Figure 7.3: The histograms show the distribution of velocity differences derived from the redshifts from CO line observations and restframe-UV spectroscopy. We show the distribution for the eight SMGs for which spectroscopic redshifts have been derived from the Lyα line and for the QSOs in Table 7.5. The final histogram compares the redshifts between the CO and Hα emission line for the three SMGs with Hα-derived redshifts. The bin size is $150\,\mathrm{km\,s^{-1}}$ which also reflects the typical error in the velocity offsets.

(SMM J02399−0134 and
ERO J164502+4626.4). Note that for HR10/ERO J164502+4626.4 we have used the CO $J = 2 - 1$ spectrum (Andreani et al. 2000) rather than the CO $J = 1 - 0$ measurement by Greve et al. (2003) which lacks velocity information.

Assuming intrinsic velocity/area-averaged brightness temperature line ratios corresponding to an optically thick, thermalised gas, i.e. $r_{32} = T_b(3{-}2)/T_b(1{-}0) = L'(3{-}2)/L'(1{-}0) = 1$, and similarly $r_{43} = 1$ and $r_{21} = 1$, we derive a median CO $J = 1 - 0$ luminosity for the whole sample of $\langle L'_{\mathrm{CO}(1-0)} \rangle = (3.8 \pm 2.0) \times 10^{10}\,\mathrm{K\,km\,s^{-1}\,pc^2}$. If we assume more realistic values of $r_{32} = 0.64$ (Devereux et al. 1994), $r_{43} = 0.45$ (Papadopoulos et al. 2000), and $r_{21} = 0.9$ (e.g. Braine & Combes 1992; Aalto et al. 1995) as derived from ISM studies in local starburst galaxies, we instead find a median CO $J = 1 - 0$ luminosity of $\langle L'_{\mathrm{CO}(1-0)} \rangle = (5.9 \pm 3.6) \times 10^{10}\,\mathrm{K\,km\,s^{-1}\,pc^2}$.

The observed CO luminosities are converted into molecular gas masses using $M(\mathrm{H_2}) = X_{\mathrm{CO}} L'_{\mathrm{CO}(1-0)}$, where $X_{\mathrm{CO}} = 0.8\,(\mathrm{K\,km\,s^{-1}\,pc^2})^{-1} M_\odot$ is the conversion factor appropriate for UV-intense environments, as derived from observations of local ULIRGs (Downes & Solomon 1998). The molecular gas masses derived for each source are given in Table 7.4.3 for assumed (2−1)/(1−0), (3−2)/(1−0) and (4−3)/(1−0) line ratios of unity. The distribu-

tion of SMG molecular gas masses is shown in Fig. 7.4, from which we derive a median value $\langle M(\mathrm{H_2})\rangle = (3.0 \pm 1.6) \times 10^{10}\,M_\odot$. Given the modest size of our sample we are not in a position to separate the observed scatter in the distribution of molecular gas masses into components due to varying inclination angles, differences in excitation conditions, and underlying scatter in the mass distribution of SMGs.

Since these molecular gas mass estimates are based on observations of high-J CO transitions with $J \geq 2$ and made assuming a thermalised, optically thick gas, it is possible that significant amounts of cold, possibly sub-thermal, molecular gas, could be present, but only detectable in lower CO transitions (e.g. Papadopolous et al. 2001; Papadopoulous & Ivison 2002; Greve et al. 2003). Furthermore, if metal-poor gas is present, the gas mass could be higher. Finally, CO is primarily a tracer of material in the diffuse ISM and it is possible that a significant amount of dense and clumpy gas ($\gtrsim 10^4\,\mathrm{cm^{-3}}$) is missed by our observations (e.g. Carilli et al. 2004). The quoted $\mathrm{H_2}$ masses in Table 7.4.3 should therefore be considered as lower limits to the total amount of molecular gas.

Our estimates of the molecular gas mass include a non-neglible fraction of Helium which is accounted for in the adopted value of the conversion factor (Downes & Solomon 1998). The amount of neutral gas (HI), however, is particular difficult to determine and significant uncertainty is associated with M(HI)-estimates at high redshift (e.g. De Breuck et al. 2003). Estimates of the $\mathrm{H_2}$-to-HI mass ratio in infrared-luminous *IRAS* galaxies range from ~ 0.5 in systems with $L_{\rm FIR} \sim 10^{10-11}\,L_\odot$ (Andreani et al. 1995) to ~ 4 for $L_{\rm FIR} \sim 10^{12}\,L_\odot$ systems (Mirabel & Sanders 1989). The latter value may apply to the extremely far-infrared luminous SMGs. However, most of the neutral gas in local galaxies is on very large scales ($\gtrsim 10\,\mathrm{kpc}$) and thus is not relevant for our estimates.

Finally, we have looked for evidence of a correlation between molecular gas content and redshift. Such a trend would be indicative of evolution within the redshift range spanned by the SMG population. If we only consider the 14 sources observed in CO as part of our survey (Table 7.3) and split the sample into low- and high-redshift halves at the median redshift of the sample, $<z>= 2.4$, we find that the CO detection rate in the high-redshift ($z > 2.4$) subset is 5/8 (63 per cent) compared to just 2/6 (33 per cent) for sources at $z < 2.4$. The higher detection rate at $z > 2.4$ could be indicative of evolution over the redshift range $z \sim 1$–3 in the gas masses associated with the most luminous starbursts. Using a Cox/Hazard survival analysis, we find that the likelihood of a variation in detection rate with redshift in the 14 sources observed by our survey is $P = 0.9946$. If we instead include all the sources listed in Table 7.3 the detection rates become 5/8 and 8/11 for the low- and high-redshift bins, respectively, and the likelihood of a trend becomes $P = 0.7899$. However, we caution that the bias against publishing non-detections in the literature means that this comparison is less reliable than that for our statistically-complete sample. The modest size of our unbiased sample is insufficient for a robust determination of whether the gas mass in luminous SMGs evolves with redshift or not.

7.4.4 Line widths and dynamical masses

A striking feature of the SMG population, with the exception SMM J14011+0252 which has FWHM = 190 $\mathrm{km\,s^{-1}}$, is their extremely broad CO line profiles, see Table 7.4.3. The median observed FWHM of the sample is $780 \pm 320\ \mathrm{km\,s^{-1}}$ and the median FWZI is $850\ \mathrm{km\,s^{-1}}$. These values do not take into account any geometrical effects, such as inclination angle, which could effect the individual estimated line widths by more than a factor of two. For example, in the case of SMM J14011+0252 it is plausible that the relatively small line width is due to the fact that the angular momentum vector of the system is closely aligned to our line-of-sight (Tecza et al. 2004).

Table 7.3: Physical properties derived from the CO observations.

Source	$\mu_{\rm L}^a$	$D(1'')^b$ (kpc)	Transition	$L'_{\rm CO}{}^b$ ($\times 10^{10}\,{\rm K\,km\,s^{-1}pc^2}$)	$M({\rm H_2})^{b,c}$ ($\times 10^{10}\,M_\odot$)	$\Delta V_{\rm FWHM}$ (${\rm km\,s^{-1}}$)	$M^d_{\rm dyn}$ ($\times 10^{11} M_\odot$)
SMM J02396−0134	2.5	3.3	(2−1)	2.1 ± 0.2	1.7 ± 0.2	780 ± 60	1.2
SMM J02399−0136	2.5	3.2	(3−2)	4.8 ± 0.8	3.8 ± 0.6	1360 ± 50	3.5
SMM J04431+0210	4.4	1.9	(3−2)	1.1 ± 0.2	0.9 ± 0.2	350 ± 60	0.1
SMM J09431+4700	1.2	6.3	(4−3)	2.7 ± 0.3	2.2 ± 0.2	420 ± 50	0.7
SMM J10516+5723	1.0	7.3	(4−3)	≤ 1.4	≤ 1.1	...	...
SMM J10523+5722	1.0	8.1	(3−2)	≤ 1.8	≤ 1.4	...	...
SMM J10524+5724	1.0	7.8	(3−2)	≤ 3.8	≤ 3.0	...	...
SMM J12360+6210	1.0	8.5	(3−2)	≤ 2.0	≤ 1.6	...	...
SMM J13120+4242	1.0	7.5	(4−3)	5.3 ± 0.9	4.2 ± 0.7	530 ± 50	1.2
SMM J13123+4239	1.0	8.3	(3−2)	≤ 3.0	≤ 2.4	...	...
SMM J14011+0252[e]	5.0	1.6	(3−2)	1.9 ± 0.2	1.5 ± 0.2	190 ± 11	0.03
SMM J16358+4057	1.0	8.3	(3−2)	7.0 ± 0.6	5.6 ± 0.5	840 ± 110	3.5
SMM J16359+6612	22	0.4	(3−2)	0.4 ± 0.2	0.3 ± 0.2	500 ± 100	0.06
SMM J16363+4055	1.0	8.3	(3−2)	≤ 1.1	≤ 0.9	...	...
SMM J16363+4056	1.0	8.5	(2−1)	≤ 2.3	≤ 1.8	...	...
SMM J16366+4105	1.0	8.2	(3−2)	5.7 ± 1.0	4.6 ± 0.7	870 ± 80	3.7
SMM J16371+4053	1.0	8.3	(3−2)	3.0 ± 0.9	2.4 ± 0.7	830 ± 130	3.4
ERO J16450+4626	1.0	8.5	(2−1)	3.8 ± 0.3	3.0 ± 0.2	400 ± 20	0.8
SMM J22174+0015	1.0	7.8	(3−2)	3.8 ± 1.0	3.0 ± 0.7	780 ± 100	2.8
Median		7.5 ± 3.1		3.8 ± 2.0	3.0 ± 1.6	780 ± 320	1.2 ± 1.5

[a] Assuming equal flux amplification and linear amplification.
[b] Corrected for the lensing amplification $\mu_{\rm L}$.
[c] Derived assuming $X_{\rm CO}$=0.8 $({\rm K\,km\,s^{-1}\,pc^2})^{-1} M_\odot$.
[d] Adopting a source diameter of 0.″5.
[e] The amplification factor for this source was recently revised from ~ 2.5 to 5 (see discussion in Swinbank et al. 2004).

Hence the observed FWHM are firm lower-limits to the true orbital velocities and assuming our sample has random orbital inclinations, then the average correction should be $\sec \pi/4 = 1.4\times$.

In order to use our observed CO line widths to derive the dynamical mass of the SMGs we must know the spatial extent of the CO. However, so far CO emission has been reliably resolved in only one SMG: SMM J02399−0136 (Genzel et al. 2003). While a number of SMGs show tentative evidence of extended CO emission (Ivison et al. 2001; Neri et al. 2003; Greve et al. 2003), their low signal-to-noise ratios prevent a robust determinations of the source size. Instead, we have assumed a conservative source diameter of $\sim 0.5''$, which corresponds to a median linear diameter of 3.7 kpc (correcting for gravitational lensing where relevant), see Table 7.4.3. This is a factor of two smaller than the source sizes estimated by Neri et al. (2003), but consistent with characteristic size estimates from recent high-resolution radio observations of SMGs with MERLIN by Chapman et al. (2004a), and with results from high-resolution PdBI CO observations (Tacconi et al. 2005) of the three SMGs detected in CO by Neri et al. (2003).

Another notable feature of our sample is the high fraction of SMGs which show evidence of double-peaked CO line profiles. Four sources (SMM J02396−0134, SMM J02399−0136, SMM J16359+6612 and SMM J16366+4105) show unambigous double-peaked profiles, and a further two sources (SMM J04431+0210 and SMM J16358+4057) are better fit by a double Gaussian than a single Gaussian, as measured by the reduced χ^2 of the fit. Thus, at least 4/12 (33 per cent), and possibly as many as 6/12 (50 per cent), of the detected sample show evidence of having more than one CO-emitting component in their spectra. Comparing the occurence of double-peaked line profiles in sources as a function of redshift within our sample, we see that the double-peaked sources appear to lie at the lower-redshift end of our sample, 5/7 at $z \lesssim 2.5$, compared to 1/5 for the SMGs at $z \gtrsim 2.5$. A possible explanation for this tentative trend is

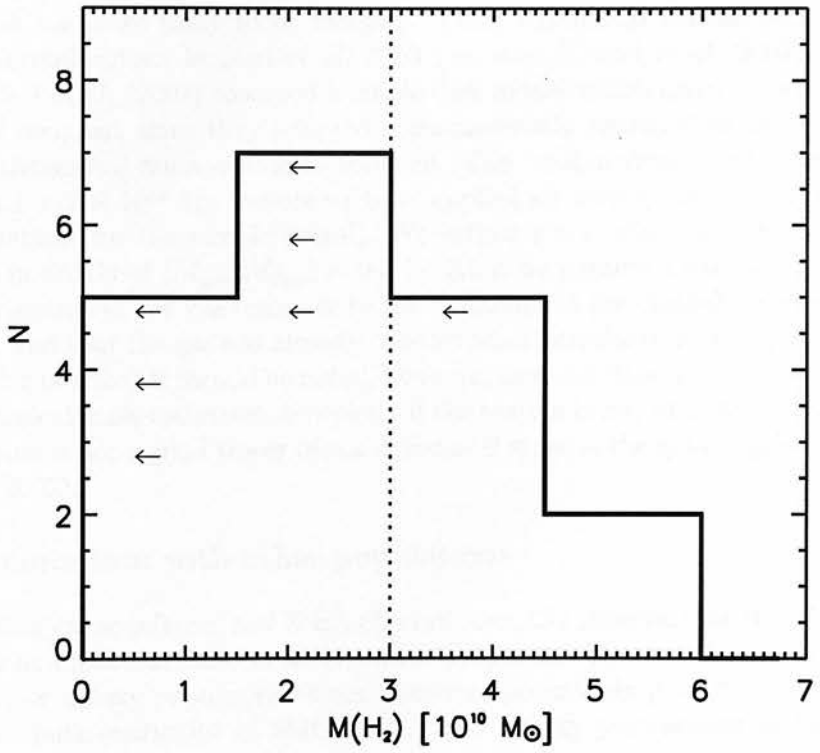

Figure 7.4: The distributions of molecular gas masses of the SMG sample assuming a conversion factor of $X_{\rm CO}$=0.8 (K km s^{-1} pc^2)$^{-1}$ $M_\odot$ and line ratios $r_{32} = r_{43} = 1$. Non-detections are included as upper limits (arrows). The median gas mass is $\langle M({\rm H_2})\rangle = (3.0\pm1.6)\times10^{10}\,M_\odot$ (dotted vertical line).

discussed later.

Such multi-peaked line profiles are a tell-tale sign of orbital motion under the influence of gravity, and can usually be attributed to either a disk or a merger. To determine the likely structure of the gas reservoir, we use our median gas mass ($3 \times 10^{10}\,M_\odot$) and adopt a typical diameter of ~ 4 kpc for the gas reservoir, to derive a mass surface density of ($\Sigma \sim 3\times10^3\,M_\odot$ pc^{-2}) for this structure. This is extremely high and implies that if the gas is present in a disk then this will have a Toomre parameter $Q < 1$[2] , indicating it will be unstable to bar formation. The disk would then collapse on a timescale comparable to the sound crossing time, which is much shorter than the expected $\sim$ 10–100 Myr duration of the SMG phase, see §7.6. We conclude that the kinematics responsible for the double-peaked CO lines are unlikely to arise from gas distributed in a stable disk, instead a more likely scenario is that they reflect a merger of two gas-rich components or from a disk collapsing under gravitational instability.

With almost all of the SMGs being spatially unresolved in CO we are unable to determine whether SMGs typically contain gaseous disks in their centres or if they are mergers. However, given their large gas mass densities, as well as the high fraction of double-peaked profiles we

[2] Toomre's stability criterion says that $Q = \frac{2v_s\Omega}{\pi G\Sigma} \geq 1$ in order for a gaseous disk to be stable: see e.g. Binney & Tremaine (1987). For a surface density $\Sigma = 3 \times 10^3\,M_\odot$ pc^{-2}, Q will always be *less* than one for any realistic values of the sound speed v_s and circular frequency Ω.

feel that SMGs are more likely to be mergers. Thus, dynamical masses were calculated using the 'merger' formula given in Neri et al. 2003 (see also Genzel et al. 2003), and reported in Table 7.4.3. Neri et al. (2003) assumed a stable disk model which gives dynamical masses lower by a factor of two; but since they adopted a characteristic source sizes twice as large as ours, the resulting dynamical mass estimates coincide. The median dynamical mass of the SMGs is $\langle M_{dyn} \rangle \simeq (1.2 \pm 1.5) \times 10^{11}\, M_{\odot}$, where we have applied an average correction of 1.4×, assuming random inclinations for the sample overall. We estimate a median molecular gas-to-dynamical mass fraction in SMGs of $\langle M_{\rm gas}/M_{\rm dyn} \rangle \sim 0.3$ (~ 0.5 if we assume a disk model). This indicates that the contribution of the gas reservoir to the dynamics of the central regions of typical SMGs is substantial, and that the gas has already concentrated into the central regions of the galaxy by some dissipative process. It should be noted, however, that significant uncertainties are associated with the dynamical mass estimates, especially if the system is not in dynamical equilibrium, or if the observed line is not a good tracer of the dynamical state of the galaxy (also see the discussion in Neri et al. 2003).

7.5 Comparison with other populations

Unlike optical/near-infrared and X-ray observations, CO observations are relatively unaffected by either dust extinction or AGN activity, and a comparison between the CO properties of SMGs and that of other galaxy populations could therefore potentially provide us with a clean way of comparing the bulk energetics of SMGs with other galaxy populations at both high and low redshifts.

We list in Table 7.5 *all* non-SMG CO sources detected at $z \geq 1$. The bulk of these are for extreme AGN such as submm-bright, high-redshift radio galaxies (HzRGs) or QSOs (e.g. Omont et al. 1996; Papadopoulos et al. 2000; Cox et al. 2002).

Due to their similar properties, in particular their large far-infrared luminosities, distorted morphologies and optical/near-infrared colours (e.g. Ivison et al. 2002; Smail et al. 2004), SMGs are commonly thought to be high-redshift analogues of local ULIRGs. To test this claim we now compare the CO properties of SMGs with ULIRGs. To this end we have used the samples of Sanders et al. (1991; SA91) and Solomon et al. (1997; SO97) which consist of 48 and 37 local ULIRGs (and less luminous LIRGs) in the redshift range $z = 0.03$–0.27 respectively, and the sample of 60 (U)LIRGs from Yao et al. (2003; Y03), selected from the SCUBA Local Universe Galaxy Survey (SLUGS, Dunne et al. 2000).

7.5.1 CO luminosities and gas masses

In Fig. 7.5 we plot the CO luminosities of the SMG sample as a function of redshift along with the CO $J = 1 - 0$ luminosities of the (U)LIRG samples of SA91, SO97, and Y03. From Fig. 7.5 it is clear that while the most luminous ULIRGs have CO luminosities comparable to those of the faintest detected SMGs, SMGs are generally more CO luminous than the local (U)LIRGs. In §7.4.3 we found the median CO line luminosity of the SMG sample to be $\langle L'_{\rm CO} \rangle = (3.8 \pm 2.0) \times 10^{10} {\rm K\,km\,s^{-1}\,pc^2}$, which is almost a factor of four greater than the average CO luminosity of the ULIRGs from SO97. Furthermore, while the CO luminosities of the (U)LIRGs are all based on the lowest and least excitation-biased CO $J = 1 - 0$ rotational line, all of the SMGs are detected in higher transitions. Hence, the CO luminosities based on the high-J lines for SMGs should be regarded as lower limits on the CO $J = 1 - 0$ luminosities, unless the lines are fully thermalised at high temperatures and optically thick.

Table 7.4: List of published high-redshift CO detections of LBGs, QSOs and HzRGs. The sources are sorted according to their redshifts. This table, together with Table ?? summarises the complete list of CO detections of sources at $z \geq 1$ to date. The velocity-integrated line fluxes, $I_{\rm CO}$, have not been corrected for gravitational amplification.

Source	Type	Transition	$z_{\rm spec}$	$z_{\rm CO}$	$\Delta V_{\rm FWHM}$ ($\rm km\,s^{-1}$)	$I_{\rm CO}$ ($\rm Jy\,km\,s^{-1}$)	Ref.
MS 1512−cB 58[a]	LBG	(3−2)	2.727	2.7265 ± 0.0004	174 ± 43	0.37 ± 0.08	[1]
Q 0957+561[a]	QSO	(2−1)	1.413	1.414	440	1.2	[2],[3]
IRAS F10214+4724[a]	QSO	(3−2)	2.286	2.2867 ± 0.0003	250	21	[4],[5]
		(3−2)	...	2.2855 ± 0.0003	230 ± 30	4.1 ± 0.9	[6]
		(3−2)	...	2.2854 ± 0.0001	220 ± 30	4.2 ± 0.8	[7]
		(6−5)	...	2.2857 ± 0.0003	240 ± 30	9.4 ± 2.0	[6]
H 1413+117[a]	QSO	(3−2)	2.5582 ± 0.0003	2.558	326	8.1	[8]
		(3−2)	...	...	352 ± 81	14.4 ± 4.4	[9]
		(3−2)	...	2.5579	362 ± 23	9.9 ± 0.6	[10]
		(3−2)	...	2.55784 ± 0.00003	416 ± 6	13.2 ± 0.2	[11]
		(4−3)	...	2.5579	375 ± 16	21.1 ± 0.8	[10]
		(5−4)	...	2.5579	398 ± 25	24.0 ± 1.4	[10]
		(7−6)	...	2.5579	376	47.3 ± 2.2	[10]
VCV J1409+5628	QSO	(3−2)	2.562	2.585 ± 0.001	370 ± 60	2.4 ± 0.7	[12]
		(3−2)	...	2.5832 ± 0.0001	311 ± 28	2.3 ± 0.2	[13]
		(7−6)	...	...	...	4.1 ± 1.0	[13]
MG 0414+0534[a]	QSO	(3−2)	2.639 ± 0.002	2.639	580	2.6	[14]
LBQS 1230+1627B	QSO	(3−2)	2.735 ± 0.005	2.741 ± 0.002	...	0.80 ± 0.26	[15]
RX J0911+0551[a]	QSO	(3−2)	2.800	2.796 ± 0.001	350 ± 60	2.9 ± 1.1	[12]
SMM J04135+1027[a]	QSO	(3−2)	2.837 ± 0.003	2.846 ± 0.002	340 ± 120	5.4 ± 1.3	[12]
MG 0751+2716[a]	QSO	(4−3)	3.200 ± 0.001	3.200	390 ± 38	5.96 ± 0.45	[16]
APM 08279+5255[a,b]	QSO	(1−0)	3.87	3.9	...	0.150 ± 0.045	[17]
		(1−0)	...	...	...	0.22 ± 0.05	[18]
		(2−1)	...	...	...	1.15 ± 0.54	[17]
		(4−3)	...	3.9114 ± 0.0003	480 ± 35	3.7 ± 0.5	[19]
		(9−8)	...	3.9109 ± 0.0002	...	9.1 ± 0.8	[19]
PSS J2322+1944[a]	QSO	(1−0)	4.1108 ± 0.0005	4.1192 ± 0.0004	200 ± 70	0.19 ± 0.08	[20]
		(2−1)	...	...	...	0.92 ± 0.03	[20]
		(4−3)	...	4.1199 ± 0.0008	375 ± 41	4.21 ± 0.40	[21]
		(5−4)	...	4.1199 ± 0.0008	273 ± 50	3.74 ± 0.56	[21]
BRI 0952−0115[a]	QSO	(5−4)	4.426 ± 0.020	4.4337 ± 0.0006	230 ± 30	0.91 ± 0.11	[15]
BRI 1335−0417[b]	QSO	(5−4)	4.398 ± 0.028	4.4074 ± 0.0015	420 ± 60	2.8 ± 0.3	[22]
BRI 1202−0725[b]	QSO	(2−1)	4.69	...	...	0.49 ± 0.09	[23]
		(4−3)	...	...	280 ± 30	1.5 ± 0.3	[24]
		(5−4)	...	4.6932 ± 0.002	320 ± 35	2.40 ± 0.30	[25]
		(5−4)	...		220 ± 74	2.7 ± 0.41	[25]
		(7−6)	...	4.6915 ± 0.001	$250 - 300$	3.1 ± 0.86	[24]
SDSS J1148+5251	QSO	(3−2)	6.43 ± 0.05	6.418 ± 0.004	320	0.18 ± 0.04	[26]
		(6−5)	...	6.4187 ± 0.0006	279	0.73 ± 0.076	[27]
		(7−6)	...	6.4192 ± 0.0009	279	0.64 ± 0.088	[27]
53 W002	HzRG	(3−2)	2.390 ± 0.004	2.394 ± 0.001	540 ± 100	1.5 ± 0.2	[28]
		(3−2)	...	2.3927 ± 0.0003	420 ± 40	1.20 ± 0.15	[29]
B3 J2330+3927[b]	HzRG	(4−3)	3.087 ± 0.004	3.094	500	1.3 ± 0.3	[30]
TN J0121+1320	HzRG	(4−3)	3.516	3.520	700	1.2 ± 0.4	[31]
4C 41.17	HzRG	(4−3)	3.798	3.7943	750	1.5	[31]
6C 1909+722	HzRG	(4−3)	3.5356	3.532	530 ± 70	1.62 ± 0.30	[32]
4C 60.07[b]	HzRG	(1−0)	3.788	3.791	≥ 1000	0.24 ± 0.03	[33]
		(4−3)	...	3.791	...	2.50 ± 0.43	[32]

[a] The source is gravitationally lensed.
[b] The CO emission is resolved.
[1] Baker et al. (2004); [2] Planesas et al. (1999); [3] Krips et al. (2003); [4] Brown & Vanden Bout (1991); [5] Solomon et al. (1992a); [6] Solomon et al. (1992b); [7] Downes et al. (1995); [8] Barvainis et al. (1994); [9] Wilner et al. (1995); [10] Barvainis et al. (1997); [11] Weiss et al. (2003); [12] Hainline et al. (2004); [13] Beelen et al. (2004); [14] Barvainis et al. (1998); [15] Guilloteau et al. (1999); [16] Barvainis et al. (2002); [17] Papadopoulos et al. (2001); [18] Lewis et al. (2004); [19] Downes et al. (1999); [20] Carilli et al. (2002b); [21] Cox et al. (2002); [22] Guilloteau et al. (1997); [23] Carilli et al. (2002a) [24] Omont et al. (1996); [25] Ohta et al. (1996); [26] Walter et al. (2003); [27] Bertoldi et al. (2003); [28] Scoville et al. (1997); [29] Alloin et al. (2000); [30] De Breuck et al. (2003a); [31] De Breuck et al. (2003b); [32] Papadopoulos et al. (2000); [33] Greve et al. (2004a).

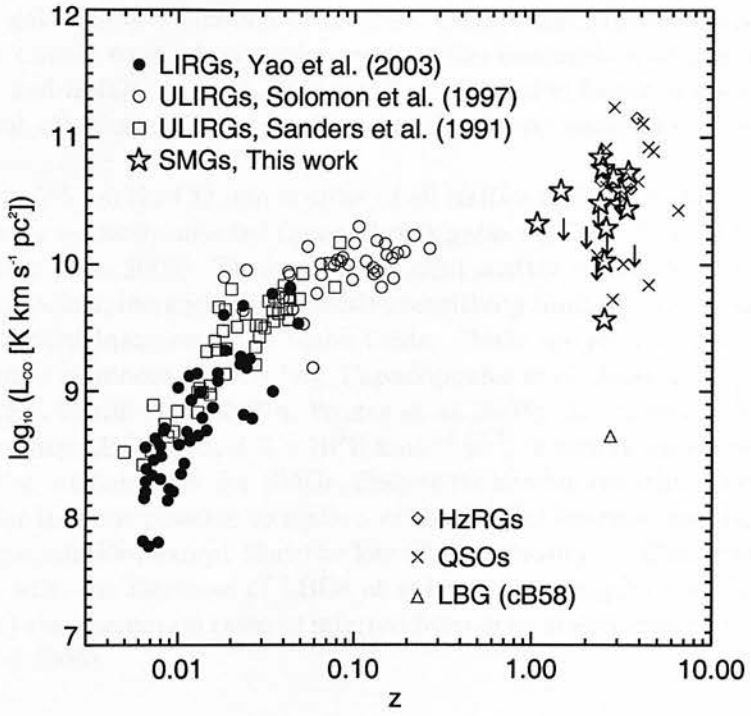

Figure 7.5: The relationship of $\log_{10}(L'_{\rm CO})$ with redshift for the (U)LIRGs samples of Sanders et al. (1991), Solomon et al. (1997), and Yao et al. (2003), and for the sample of high-redshift (sub)mm-selected sources presented in this paper. The CO luminosities have been corrected for gravitational amplification where necessary. Also shown are the (lensing-corrected) CO luminosities for HzRGs, QSOs and LBGs listed in Table 7.5, with the exception of Q 0957+561 and MG 0414+0534 which have unknown gravitational magnification factors. The CO luminosities for the (U)LIRGs are all based on the CO $J = 1 - 0$ line, whereas the luminosities of the high-redshift sources are entirely derived from CO $J = J + 1 \rightarrow J$ transitions with $J + 1 \geq 2$ (Table 7.5). Upper limits on the CO luminosities for the 7 SMGs not detected in CO are represented by downward pointing arrows.

The (U)LIRGs lie on a well-defined locus in the Fig. 7.5, which is extended to the highest redshifts and CO luminosities by the SMG sample. The lower boundary of this trend is determined by the sensitivity limits of the CO observations, while the upper bound is a real astrophysical limit. This suggests that the CO luminosity, and presumably therefore also the molecular gas content, of infrared-luminous galaxies increases with redshift. It is likely that this behaviour is due to the combined effects of a flux-limited sample and evolution of the gas content in ULIRGs/SMGs. While the lack of less luminous objects at higher redshifts can easily be explained by the limited sensitivity of the surveys, the lack of very luminous objects at $z \lesssim 0.02$ is unlikely to be purely because of the smaller volumes probed at low redshifts. The (U)LIRGs were selected from the Revised Bright Galaxy Sample of *IRAS* galaxies (Soifer et al. 1987) which covered a substantial part of the sky, and would have detected the most extreme luminous ULIRGs no matter how low their surface density. The steady decline in the CO luminosity of SMGs to ULIRGs and LIRGs

seen in Fig. 7.5 is therefore likely to reflect the evolution in the molecular gas-content of the most luminous starburst galaxies as a function of redshift, despite the expected increasing mass of a typical galaxy with cosmic time. A possible caveat is the assumption of a constant conversion factor in (U)LIRGs and SMGs. In (U)LIRGs the $X_{\rm CO}$ conversion factor is about 4.5 times lower than in normal spiral galaxies, and it is possible that for the yet more luminous SMGs it is even lower.

Also shown in Fig. 7.5 are the CO luminosities of all HzRGs and QSOs detected to date (Table 7.5), as well as the only optically-selected Lyman break galaxy (LBG), MS 1512–cB58 ($z = 2.73$), detected in CO (Baker et al. 2003). Their large apparent scatter is due to many of these objects being gravitationally-lensed, increasing the effective sensitivity limits of their observations beyond the capabilities of current instruments in blank fields. SMGs are seen to have CO luminosities comparable to the most luminous HzRGs (e.g. Papadopoulos et al. 2000; De Breuck et al. 2003a, 2003b) and QSOs (e.g. Carilli et al. 2002a; Walter et al. 2003). In contrast, the CO luminosity of the typical-luminosity LBG cB58, $4.2 \times 10^9 {\rm K\,km\,s^{-1}\,pc^2}$, is nearly two orders of magnitude ($\sim 90\times$) less than the median value for SMGs, despite its similar redshift. With only one LBG detected in CO so far it is not possible to make any meaningful conclusions about the molecular gas content of this population, except that the low CO luminosity of cB58 compared to that of SMGs is consistent with the faintness of LBGs at submm wavelengths and their relatively low (compared to SMGs) star-formation rates as inferred from optical spectroscopy (Blain et al. 1999; Adelberger & Steidel 2000).

7.5.2 CO line widths and dynamical masses

In §7.4.4 we found that $\gtrsim 33$ per cent of the observed SMGs have double-peaked CO profiles. This is comparable to the fraction of double-peaked CO spectra in local ULIRGs (SO97). The median FWHM CO linewidth for the SMG sample is $780 \pm 320\,{\rm km\,s^{-1}}$, about 3 and 4 times larger than the averages for the SA91 and SO97 ULIRG samples, respectively. Since the dynamical mass depends on the square of the velocity dispersion ($M_{dyn} \sim R\sigma^2$), this would naively suggest that the dynamical masses of the SMGs are $\sim$ 9–16 times larger than that of ULIRGs (if the gas kinematics sample similar radii in the galaxies). From detailed interferometric studies of the circumnuclear gas in local ULIRGs Downes & Solomon (1998) find a median dynamical mass of $\sim 6 \times 10^9\,M_\odot$ within $R \lesssim 0.6\,{\rm kpc}$ – about $20\times$ smaller than the mass enclosed within $R \lesssim 2\,{\rm kpc}$ in SMGs (see Table 7.4.3). Assuming an isothermal mass distribution, the SMGs will have dynamical masses within 0.6 kpc roughly $6\times$ that of local ULIRGs.

We now turn to the comparison between SMGs and other high-redshift galaxy populations. Fig. 7.6a compares the distribution of velocity dispersions of our SMG sample with that of all high-redshift QSOs and HzRGs detected in CO to date. While there is a substantial overlap between the SMG and QSO distributions, the latter is seen to peak at somewhat lower velocity dispersions than SMGs and we note that all QSOs have $\log\sigma \leq 2.4$ (corresponding to FWHM $\leq 590\ {\rm km\,s^{-1}}$). Also, no QSO detected in CO show evidence of a double peaked line profile (although a few are spatially resolved – Papadopoulos et al. 2001; Carilli et al. 2002a). A Kolmogorov-Smirnov test suggests that the two distributions are formally different at the 95 per cent confidence level. The apparently lower CO linewidths of QSOs is not clear, although it is posssible that they are either intrinsically lower-mass systems or have smaller gas disks. In contrast, there is no discernable difference between the CO line widths of the SMGs and those HzRGs detected in CO. This suggest that the brightest SMGs have similar dynamical masses, and therefore possibly similar dark-matter halo masses, to HzRGs which are believed to be amongst the most massive objects in the high-redshift Universe (infered from both the presence of a supermassive black hole and the

strong clustering of HzRGs). Although, such a conclusion is uncertain due to the small number of objects involved and will have to wait until a larger sample of HzRGs has been observed in CO.

In Fig. 7.6b we compare the CO line widths from our SMG sample with measurements of the width of the Hα line from a recent near-infrared spectroscopic survey of 29 SMGs and high redshift, optically-faint μJy radio galaxies (OFRGs — see e.g. Chapman et al. 2004b) by Swinbank et al. (2004). The two distributions span a similar range of velocity dispersions, but the CO sample is skewed towards higher values, resulting in a higher median value. We find that the average ratio between the CO and Hα line widths for SMGs is $\langle \mathrm{FWHM_{CO}} \rangle / \langle \mathrm{FWHM_{H_\alpha}} \rangle \sim 2$. The main reason for this is likely to be due to the CO tracing multiple components in the SMG whereas the long-slit Hα spectroscopy is identifying only a single component due to the slit orientation or due to extreme obscuration in the second component. Part of the discrepancy may also reflect dust-obscuration within the galaxy providing only a partial view of the kinematics of the system, in contrast to the obscuration-independent measurement provided by CO. If this is the case, it could mean that the dynamical masses of SMGs are larger than suggested from their rest-frame optical spectra.

7.5.3 Star-formation efficiency and the L_{CO}-L_{FIR} relation

While the luminosity of the CO lines tells us how much molecular gas a galaxy contains, it does not necessarily measure how efficiently this gas is being turned into stars. The star-formation efficiency (SFE) can be estimated from the ratio of the far-infrared luminosity of the system to the amount of molecular gas available to form stars, i.e. SFE$= L_{\mathrm{FIR}}/M(\mathrm{H_2})$.

The far-infrared luminosities of the SMGs were calculated following Neri et al. (2003), $L_{\mathrm{FIR}} = 1.9\times10^{12} S_{850}$, where L_{FIR} is in $L_\odot$ and S_{850} in mJy. This assumes a modified grey-body model for the far-infrared emission with a dust temperature of $T_d = 40$ K and emissivity $\propto \nu^{1.5}$. The median far-infrared luminosity of the SMG sample is $\langle L_{\mathrm{FIR}} \rangle = (1.5\pm0.7)\times10^{13}\, L_\odot$ which is nearly an order of magnitude larger than the most luminous local ULIRGs (Solomon et al. 1997) . Assuming that the bulk of the far-infrared luminosity is powered by star-formation (Frayer et al. 1998; Alexander et al. 2004), we find a median star-formation efficiency of $\langle SFE \rangle = 450 \pm 170\, L_\odot\ {M_\odot}^{-1}$ for the SMG sample, in agreement with the initial findings of Neri et al. (2003).

Perhaps a more straightforward measure of the star-formation efficiency is the continuum-to-line luminosity ratio, $L_{\mathrm{FIR}}/L'_{\mathrm{CO}}$, since it does not depend on X_{CO}. Locally, (U)LIRGs are observed to follow a scaling relation between L'_{CO} and L_{FIR} with the more far-infrared luminous galaxies having proportionally higher CO luminosities (Rickard & Harvey 1984; Young et al. 1984, 1986; Sanders & Mirabel 1985). In Fig. 7.7 we have plotted the SMGs onto the L'_{CO}–L_{FIR} diagram along with the (U)LIRGs from our three low-redshift comparison samples. The SMGs extend the general trend seen for the local (U)LIRGs out to far-infared luminosities $\gtrsim 10^{13}\, L_\odot$. A power-law fit to all three (U)LIRG samples yields $\log L'_{\mathrm{CO}} = (0.62\pm0.09) \log L_{\mathrm{FIR}} + (2.41\pm1.06)$, Fig. 7.7. Including the SMGs in the fit yields $\log L'_{\mathrm{CO}} = (0.62 \pm 0.08) \log L_{\mathrm{FIR}} + (2.33 \pm 0.93)$, i.e. virtually no change in the fit at all. The combined SMG and local ULIRG sample has a statistically-significant correlation, as shown by Pearson's rank coefficient, Spearman's rank-order correlation coefficient and Kendall's τ: $r = 0.92$, $r_S = 0.93$ and $\tau = 0.77$. From Fig. 7.7 there is even some evidence of a L'_{CO}–L_{FIR} correlation within the SMG population itself (Pearson's rank coefficient of $r = 0.92$). Moreover, the slope of the $L'_{\mathrm{CO}} - L_{\mathrm{FIR}}$ correlation inferred from the fit is significantly less than unity. This is clearly illustrated in Fig. 7.7 where the locus defined by the data points is seen to have a shallower slope than the line of equality.

The observed slope of the correlation in Fig. 7.7 implies that the $L_{\mathrm{FIR}}/L'_{\mathrm{CO}}$ ratio increases with

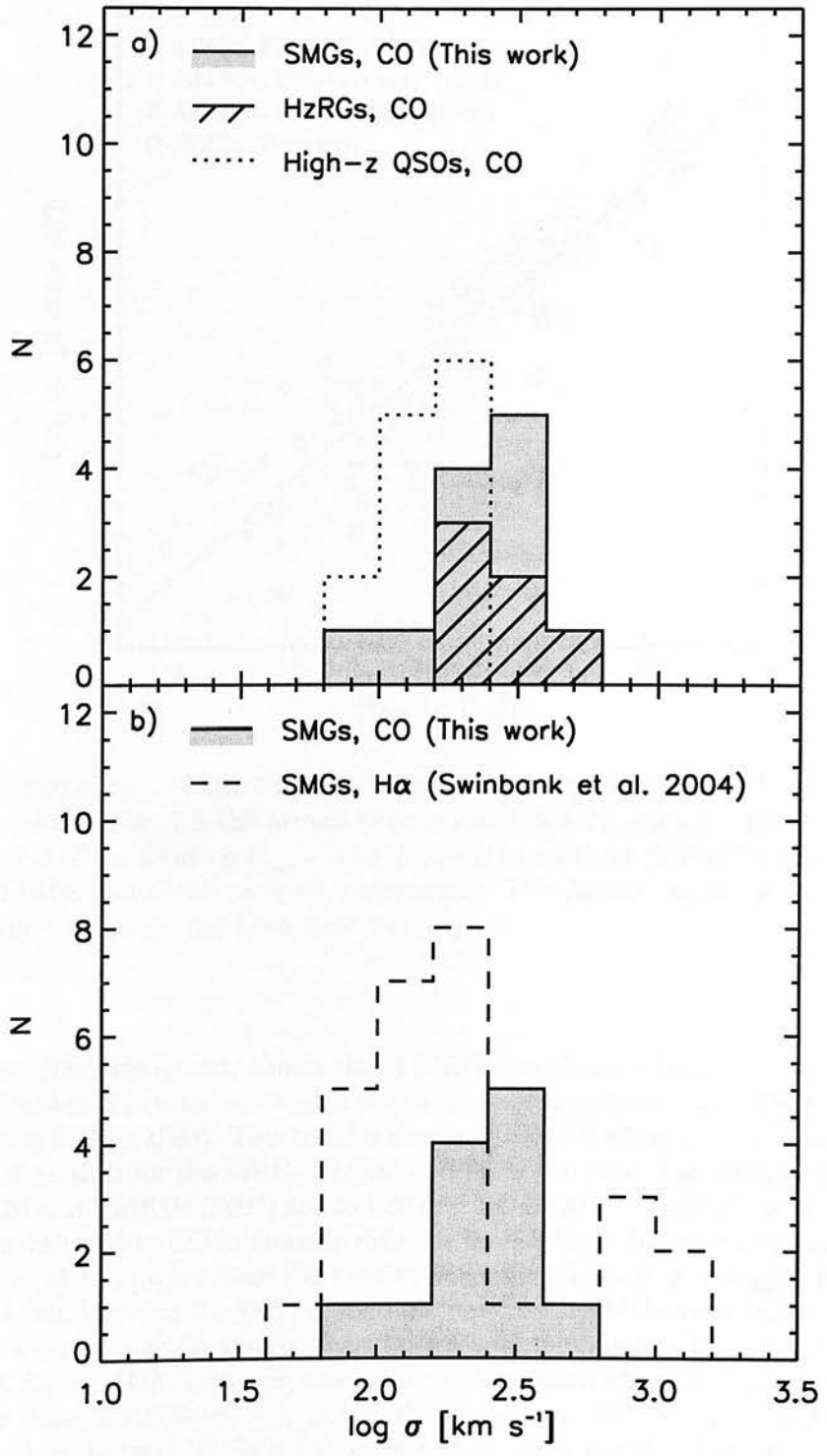

Figure 7.6: **a)** Distribution of CO velocity dispersions for high-redshift QSOs and HzRGs from Table 7.3 and our sample of CO-detected SMGs. In **b)**, we compare with the measurements of the line widths of the Hα line from near-infrared spectroscopy of a large sample of SMGs (Swinbank et al. 2004).

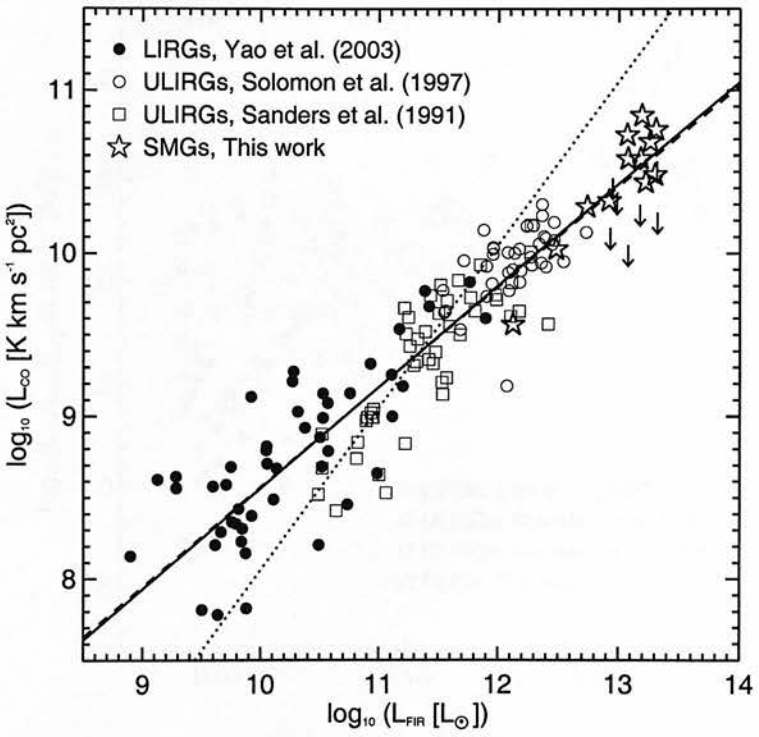

Figure 7.7: A comparison of the CO and far-infrared luminosities ($L'_{\rm CO}$, $L_{\rm FIR}$) for SMGs and local ULIRGs. As in Fig. 7.5 the arrows denote the 7 non-detections. The solid and dashed lines represent fits of the form $\log L'_{\rm CO} = \alpha \log L_{\rm FIR} + \beta$ to all three (U)LIRGs samples and to the combined (U)LIRGs and SMGs samples, respectively. The dotted line is the best fit to all four samples but where the slope has been fixed to unity.

$L_{\rm FIR}$. Several studies have already shown that ULIRGs have higher $L_{\rm FIR}/L'_{\rm CO}$ ratios than the less luminous LIRGs, which in turn have higher ratios than spiral galaxies and GMCs (e.g. Sanders et al. 1986; Solomon & Sage 1988). This trend is shown in Fig. 7.8 where $L_{\rm FIR}/L'_{\rm CO}$ has been plotted as a function of redshift for the LIRG, ULIRG and SMG samples. The median $L_{\rm FIR}/L'_{\rm CO}$ ratios for LIRGs (Y03) and ULIRGs (S097) are 50 ± 30 and $180 \pm 130\, L_\odot$ $({\rm K\,km\,s^{-1}pc^2})^{-1}$, respectively. The median far-infrared to CO luminosity ratio for the SMGs is $360 \pm 140\, L_\odot$ $({\rm K\,km\,s^{-1}pc^2})^{-1}$, which is a factor of two higher than the median value for ULIRGs, and suggests that although some overlap exists between the two populations, in general SMGs have higher star-formation efficiencies, or a larger contribution to their far-infrared luminosities from a source other than star formation, e.g. an AGN. However, the latter seems unlikely since only around 20-30 per cent of SMGs show signs of AGN-activity, and in those cases the AGNs appear to be energetically comparable to those in local ULIRGs (Alexander et al. 2003; see also discussion in Chapman et al. 2004).

As a final check we repeated the above analysis using SMG far-infrared luminosities derived from their radio fluxes and using the radio-FIR correlation (Condon 1992; Yun, Reddy & Condon 2001). There is tentative evidence that this correlation applies out to high redshifts (Garrett 2002; Appleton et al. 2004), and arguably provides a more reliable estimate of the far-infrared

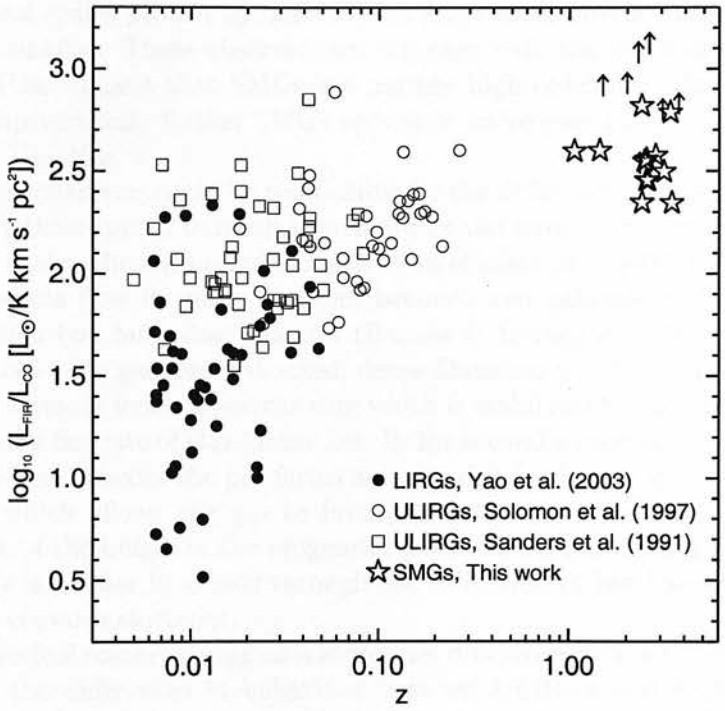

Figure 7.8: The star-formation efficiency as indicated the observed ratio $L_{\rm FIR}/L'_{\rm CO}$ as a function of redshifts. Upward pointing arrows represent the 7 SMGs not detected in CO.

luminosity than that based on the submm flux which has significant uncertainty associated with it due to the unknown dust properties of SMGs. The far-infrared luminosities derived using the radio information are generally larger, and the $L'_{\rm CO} - L_{\rm FIR}$ correlation therefore shallower ($\alpha = 0.59 \pm 0.08$). In this case, the SMG sample also exhibits a highly significant correlation (Pearson $r = 0.84$), although this can partly be explained by the luminosity distance-squared stretching of the data points.

7.5.4 Discussion

In the previous three sections it was found that SMGs have on average four times larger CO luminosities, 3–4 times larger line widths and a median $L_{\rm FIR}/L'_{\rm CO}$ ratio twice that of local ULIRGs. As argued in §7.4.4, the large line widths and molecular gas masses seen in SMGs are difficult to reconcile with a scenario in which the gas resides in a circumnuclear disk. This is in contrast to what is observed in local ULIRGs where the bulk of the gas is found in a $r \sim 0.5$ kpc disk or ring. In SMGs the gas is more likely to be distributed on scales of 2–3 kpc, as suggested by their radio morphologies (Chapman et al. 2004a) as well as by high-resolution CO observations of SMGs (Genzel et al. 2003; Tacconi et al. 2005). The typical gas-to-dynamical mass fraction in SMGs was estimated in §7.4.4 to be ~ 0.3 – almost two times higher than the median gas mass fraction in ULIRGs (~ 0.16, Downes & Solomon 1998), assuming that the CO–H_2 conversion factor is the same for ULIRGs and SMGs. The local gas mass fraction in ULIRGs

is measured within the molecular disk ($R \lesssim 0.5\,\mathrm{kpc}$) – but when averaged over scales of 2-3 kpc, which are the typical scales probed by our CO observations of SMGs, the gas fraction is likely to be significantly smaller. These observations, together with the generally higher far-infrared luminosities of SMGs, suggest that SMGs are neither high-redshift replicas of local ULIRGs, nor simply scaled-up versions. Rather SMGs appear to more gas-rich and more efficiently star-forming than local ULIRGs.

What physical mechanisms could be responsible for the differences between local ULIRGs and SMGs? Both populations appear to result from mergers and strong interactions (e.g. Chapman et al. 2003c), so what makes the starbursts so much more efficient in SMGs? Numerical simulations have compared the gas flow in major mergers between two galaxies with strong bulges, and between two, gas-rich but bulge-less galaxies (Barnes & Hernquist 1996; Iono, Yun & Mihos 2004). In the first case, the gas forms shocked, dense filaments which dissipate energy and flows towards the centre where it forms a nuclear ring which is stabilised by the gravitational potential of the bulges – slowing the rate of star formation. In the second scenario, the merger between two gas-rich, but bulge-less, galaxies the gas forms an extended ($\sim 6\,\mathrm{kpc}$), gravitationally-significant bar-like structure which allows the gas to funnel towards the centre. However, without the stabilising influence of the bulges in the progenitor galaxies, the gas cannot form a stable ring or disk and its density is further increased through the formation of bar-like structures, leading to a wide-spread and vigorous starburst.

These two theoretical scenarios suggest a structural difference between the progenitor galaxies is at the heart of the differences in behaviour between ULIRGs and SMGs. The suggested structural differences are consistent with the expectations for the typical galaxies involved in mergers at low- and high-redshifts, with the former involving disk-galaxies with significant bulge components (e.g. Lilly et al. 1998), while the progenitor galaxies of SMGs at high redshift are much more likely to be gas-rich, disk-dominanted systems with little or no bulge component (Wyse, Gilmore & Franx 1997; Ravindranath et al. 2004). If such structural differences between local and distant starbursts are real, the next question is: at what redshift does the transition occur? In §7.4.3 we found that SMGs at $z \sim 3$ have a higher CO detection rate than SMGs at $z \sim 2$ – consistent with the former beeing more gas-rich. Secondly, the preponderance of double-peaked CO line profiles at $z \sim 2$ is consistent with that of local ULIRGs and in contrast to SMGs at $z \sim 3$ (see §7.4.3 and §7.4.4). Together these trends may indicate a profound difference in the physical processes responsible for triggering intense star formation in massive galaxies at $z \sim 2$ compared to $z \sim 3$, with major mergers being responsible for much of this acitivity at lower redshifts (as is the case for local ULIRGs), but a separate mode (requiring less intense pertubations) capable of triggering similar bursts in the more gas-rich systems present at even higher redshifts.

In this respect it is important to draw attention to observational studies of the depletion of molecular gas with starbursts in ULIRGs. In a sample of more than 50 (U)LIRGs, Gao et al. (1999) found a correlation between the CO $J = 1 - 0$ luminosity and the projected separation of the merging nuclei, which they took as evidence for molecular gas being rapidly depleted due to intense star formation as the merger progresses. If a similar picture applies at high redshift, the large CO luminosities and gas masses we find for SMGs would imply that these systems are extended, and caught in the early stages of merging. However, this might be a premature conclusion since Rigopoulou et al. (1999) did not find any evidence for a correlation between the gas mass and merger phase for local ULIRGs.

In §7.5.3 we showed that SMGs extend the $L_{\mathrm{CO}} - L'_{\mathrm{FIR}}$ relation of local ULIRGs to higher redshifts and luminosities, and accordingly have higher star-formation efficiencies than ULIRGs.

Although, the star-formation efficiencies found for the SMGs could be severely overestimated if an AGN contributes significantly to the far-infrared luminosity, the detection of large amounts of molecular gas in SMGs along with recent X-ray (Alexander et al. 2003, 2004) and radio studies (Chapman et al. 2004a) strongly suggest that the bulk of the far-infrared emission from SMGs is powered by a large-scale starburst and not from an AGN. While CO $J = 1 - 0$ is a good indicator of the total metal-rich H_2 gas reservoir, it may be a worse indicator of the amount of dense gas present ($n \geq 10^5\,\mathrm{cm}^{-3}$), that actually fuels star formation (Carilli et al. 2004). The latter could be particular true in the tidally disrupted giant molecular clouds (GMCs) expected in ULIRGs, where a diffuse phase may dominate the CO $J = 1 - 0$ emission but has little to do with star formation (Downes & Solomon 1998; Sakamoto et al. 1999). Such a diffuse phase could be even more pronounced in SMGs with their more extended distributions (Chapman et al. 2003c; Conselice et al. 2003). This would explain why the $L_{\mathrm{FIR}}/L'_{\mathrm{CO}}$ ratio is found to be such a strong function of L_{FIR}, increasing for merging systems usually associated with the highest far-infrared luminosities. Interestingly, recent work shows that the SFE of dense gas, parametrised by the $L_{\mathrm{FIR}}/L_{\mathrm{HCN(1\text{-}0)}}$ ratio (the HCN $J = 1 - 0$ critical density is $2 \times 10^5\,\mathrm{cm}^{-3}$), remains constant from GMCs all the way to ULIRG system (Gao & Solomon 2003; Solomon et al. 2003; Carilli et al. 2004).

Our findings in §7.5.1 and §7.5.2 have shown that SMGs are massive gas-rich galaxies with molecular gas masses large enough to sustain a star-formation rate of $\sim 10^3\,M_\odot\ \mathrm{yr}^{-1}$ for $\tau_{SMG} \sim M(\mathrm{H_2})/SFR \sim 3 \times 10^{10}\,M_\odot/10^3\,M_\odot\ \mathrm{yr}^{-1} \sim 30\,\mathrm{Myr}$. By the end of such a burst most of the stellar mass corresponding to that of a massive spheroid would be in place. A gas depletion timescale of $\tau_{SMG} \sim 30\,\mathrm{Myr}$ is somewhat smaller than the typical starburst ages ($\sim$ 100–200 Myr) derived from photometric modeling of the broad band optical/near-infrared colours of SMGs (Smail et al. 2004), although we note that large uncertainties are associated with both methods. Furthermore, the above gas consumption time scale assumes a continuous starburst untill all the gas is used – an unlikely scenario since it ignores the negative feedback effects from newborn massive stars and supernovae. For example, one could imagine the starburst terminating prematurely if the gas is removed by starburst- and/or AGN-driven winds only to fall back onto the galaxy at a later stage to fuel a second starburst, thus making the true gas exhaustion time scale longer. The 30 Myr should therefore be considered a strict lower limit on the starburst phase of SMGs.

An alternative estimate of the duration of the SMG phase can be made from the recent findings by Page et al. (2004) that the 15 per cent of QSOs at $z \sim 2$ which show absorption in their X-ray spectrum are detectable in the submm. Since only 3 per cent of radio-identified SMGs are QSOs (Chapman et al. 2004b) this means that SMGs would have a typical lifetime which is $\sim 0.15/0.03 = 5$ times longer than that of QSOs. Adopting a QSO lifetime of 40 Myr (Martini & Weinberg 2001) yields a SMG life expectancy of $\tau_{SMG} \sim 200\,\mathrm{Myr}$ — again larger than the gas consumption time scale.

If we assume that a large fraction of the gas mass of SMGs is eventually converted into stars (perhaps through repeated cycles of expulsion, infall and star formation), what are the resulting stellar masses of the descendents? Clearly SMGs already contain (perhaps substantial) stellar populations, however the stellar masses for SMGs are difficult to estimate due to significant dust extinction and the resulting uncertainties from the degeneracies between dust reddening and age in evolutionary spectral synthesis models. The best estimates to date, based on IJK photometry of 96 SMG and optically-faint μJy radio galaxies (Smail et al. 2004), suggest typical stellar masses of $M_{stars} \simeq 3 \times 10^{10}\,M_\odot$. Thus, combining the gas and stellar mass estimates we find that on average SMGs have baryonic masses of $\gtrsim 6 \times 10^{10}\,M_\odot$, which is comparable to the masses of

local early type L^* galaxies.

The above strongly suggests that SMGs are in fact the progenitors of massive spheroids in the present-day Universe and that the build-up of the stellar population occurs rapidly ($30 \lesssim \tau_{SMG} \lesssim 100$ Myr), consistent with the old stellar populations of local ellipticals. Further in support of this is a) the strong clustering properties of SMGs (Blain et al. 2004b), and b) the fact that the rest-frame optical properties of SMGs match the bright end of the luminosity function of spheroidal galaxies in nearby clusters (Smail et al. 2004).

7.6 Implications for structure-formation models

Semi-analytical models of galaxy formation and evolution (Cole et al. 1994; Kauffmann et al. 1999; Cole et al. 2000; Somerville et al. 2001) have enjoyed a fair amount of success in that they have been able to reproduce the properties of galaxies in the local Universe reasonably well, e.g. the luminosity function, the distribution of colours and disk scale lengths of galaxies, the observed mix of morphologies and the Tully-Fisher relation (e.g. Kauffmann et al. 1999; Cole et al. 2000). However, the key observable with which to benchmark models of galaxy formation and evolution is the mass assembly of galaxies, and in particular the assembly of baryonic mass, as a function of redshift.

Genzel et al. (2003) pointed out that if the extremely large baryonic mass ($\gtrsim 10^{11}\,M_{\odot}$) of SMM J02399−0136 was representative of the bright SMG population, then the high surface density of such sources would imply that the abundance of very massive baryonic systems at high redshift was about an order of magnitude larger than predicted by semi-analytical models (see also Tecza et al. 2004).

Here we shall use the 10 SMGs in our sample which lie in the redshift range $z = 2$–3.5 and have reliable gas mass estimates, to put lower limits on the co-moving number density of massive galaxies at high redshifts. The redshift interval considered translates into ~ 1.5 Gyr in terms of elapsed cosmic time, and corresponds to a co-moving volume of 1.8×10^7 Mpc^3 per square degree. The average submm flux of the 10 SMGs is $\langle S_{850\mu m} \rangle = 8 \pm 4$ mJy. The surface density on the sky of SMGs with fluxes $\gtrsim 8$ mJy is $\sim 285\,\mathrm{deg}^{-2}$ (Borys et al. 2003). Taking into account that a) about 60 per cent of the bright SMG population lie within $z = 2$–3.5 (Chapman et al. 2003; Chapman et al. 2004b), and b) the CO detection fraction of our sample is 10/14 (~ 71 per cent), we estimate that the co-moving number density of galaxies with baryonic masses $\gtrsim 6 \times 10^{10}\,M_{\odot}$ in the redshift interval $z = 2$–3.5 is $\sim 6.7^{+10.0}_{-4.5} \times 10^{-6}\,\mathrm{Mpc}^{-3}$. The errors are estimated by propagating the 1-σ limits on the submm flux through the same calculation.

Since we only observe SMGs during their submm-luminous phase, we have to correct the derived space density by a factor corresponding to the ratio between the 1.5 Gyr which has elapsed over the redshift range $z = 2.0$–3.5 and the typical duration of the 'SMG phase'. The latter is uncertain, but as we saw in §7.5.4 it is likely to lie in the range 30–200 Myr. Adopting 200 Myr as as a conservative upper value for the submm luminous phase, we estimate a correction factor of ~ 8.

In Fig. 7.9 we have plotted our estimate of the co-moving number density of $\gtrsim 6 \times 10^{10}\,M_{\odot}$ systems at $z \sim 2.8$ and the (conservative) correction factor which must be applied. Our estimate of the abundances of massive galaxies at $z \sim 2.8$ is in good agreement with independent measurements at similar redshifts (Daddi et al. 2004; Saracco et al. 2004), and confirms the slow decline in the space density of massive galaxies as a function of redshift (Genzel et al. 2003; Glazebrook et al. 2004).

The abundance tracks of $\geq 5 \times 10^{10}$ and $\geq 7 \times 10^{10}\,M_{\odot}$ systems as predicted by the most recent GALFORM models (Cole et al. 2001; Baugh et al. 2004) are seen to envelope our estimated

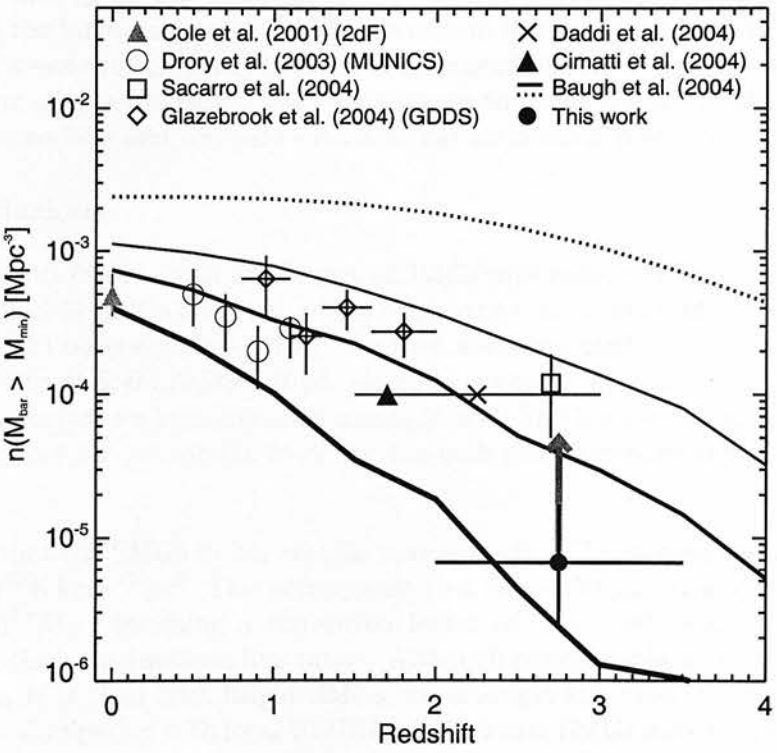

Figure 7.9: The co-moving number density of galaxies with baryonic masses $\sim 6 \times 10^{10}\,M_{\odot}$ as derived from CO observations of SMGs. The GALFORM model (Cole et al. 2001; Baugh et al. 2004) predictions of the abundances of galaxies with baryonic massses $\geq 5\times$, $7\times$, and $10\times10^{10}\,M_{\odot}$ as a function of redshift are shown as thin, medium and thick solid lines, respectively. The dotted curve represents the total baryonic matter content available in $\geq 10^{11}\,M_{\odot}$ dark matter halos, and is obtained by scaling the abundance of halos with the cosmological baryon-to-dark matter density ($\Omega_b/\Omega_{DM} = 0.13$). This provides a strict upper limit on the number density of massive baryonic galaxies at a given redshift. The observations can be reconciled within the CDM framework, provided that ~ 10 per cent of all baryons within dark matter halos are rapidly assembled into galaxies.

volume density. There are two reasons for the closer agreement between the observations and models: a) the typical baryonic mass of bright SMGs is not 2–3 m^* but rather $\sim 0.6\,m^*$ and b) the new GALFORM model, which employs a top-heavy initial mass function (IMF) in order to acccount for the 850 μm number counts (Baugh et al. 2004), also predicts higher abundances of massive galaxies at high redshifts than previous models. Other semi-analytical models (Fontana et al. 2004; Granato et al. 2004) have also modified their recipes so that their models fit the data.

We stress, however, that by using a SMG timescale of 200 Myr, and not 30 Myr as suggested by the CO observations, our estimate of the correction factor is a conservative one. Furthermore, if the population of OFRGs, whose faint levels of submm flux is believed to be due their higher dust temperatures (Blain et al. 2004a; Chapman et al. 2004b), have similar gas masses as classical SMGs (Swinbank et al. 2004; Smail et al. 2004), this would double our current estimate of the abundance of massive baryonic galaxies at high redshifts.

We conclude that given the small number of sources and crude redshift bins used in our calculations, and the large uncertainty on the correction factors which have to be applied, there is no evidence for a severe discrepancy between observations and the latest theoretical predictions. An increase in our sample size would not only allow us to confirm this but also allow us to split the sample into mass bins and compare with different mass track predictions.

7.7 Conclusions

We present results from a PdBI CO Survey of SMGs with radio counterparts. We successfully detect CO in 4 out of 11 SMGs observed, which brings the total number of SMGs detected by our survey to 7 out of 14 observed. In addition, we have also presented a detection of CO based on archival observations of SMM J02396−0134. Combining these 15 sources with four CO-detected SMGs from the literature we have compiled a sample of 19 SMGs observed in CO of which 12 are detected. We use this unique sample to derive the bulk gas properties and masses of the most luminous SMGs.

- We find that the SMGs in our sample have a median CO luminosity of $\langle L'_{\rm CO}\rangle = (3.8 \pm 2.0) \times 10^{10}\,{\rm K\,km\,s^{-1}\,pc^2}$. This corresponds to a molecular gas mass of $\langle M({\rm H_2})\rangle = (3.0 \pm 1.6) \times 10^{10}\,M_\odot$, assuming a conversion factor of $X_{\rm CO}$= $0.8\,({\rm K\,km\,s^{-1}\,pc^2})^{-1} M_\odot$ and optically thick, thermalised line ratios. Although considerable uncertainty is associated with $X_{\rm CO}$ it is clear that bright SMGs are amongst the most gas-rich systems in the Universe. Comparing with local ULIRGs, we find that SMGs have molecular gas resevoirs on average about four times greater than even the most CO-luminous ULIRGs. We argue that this is largely due to the evolution in the molecular gas content of the most far-infrared luminous galaxies with redshift.

- In general, the SMGs in our sample have extremely broad line profiles. The median FWHM is $780 \pm 320\ {\rm km\,s^{-1}}$, which is $\gtrsim 3$ times larger than the average CO $J = 1 - 0$ line width of local ULIRGs. The large line widths, and in some cases multiple-peaked CO spectra and extended CO emission, together with the vast amounts of molecular gas, suggests that the brightest SMGs are merger events. We argue that the observed gas properties are difficult to reconcile with the scenario witnessed in local ULIRGs where the bulk of the molecular gas resides in a compact circumnuclear disk.

  We find that the median dynamical mass of the SMG sample is $\langle M_{dyn}\rangle = (1.2 \pm 1.5) \times 10^{11}\,M_\odot$ within the central $\sim$2 kpc. This suggests that at least the brightest SMGs, are amongst the most massive objects in the Universe, comparable in mass to the most extreme HzRGs and QSOs, rather than being high-z replicas of local ULIRGs. Taking into account the stellar mass component we estimate that the total baryonic mass content of SMGs is $\gtrsim 6 \times 10^{10}\,M_\odot$. Thus we conclude that not only are SMGs very massive baryonic systems, but the baryons can account for a substantial fraction of the total mass in the central regions.

- From the inferred molecular gas masses we estimate a typical gas consumption timescale of $\gtrsim 30$ Myr. This is sufficient time to build up a $\gtrsim L^*$ elliptical, and argues in favour of SMGs being the progenitors of giant ellipticals. A SMG phase of ~ 30 Myr is on the low side of the best age estimates of the starbursts in SMGs (Tecza et al. 2004; Smail et al. 2004), which in turn agree favourably with independent estimates of the duration of the SMG phase obtained by requiring a scenario in which SMGs go through a $\sim$ 10-Myr QSO phase at $z \sim 2$, becoming massive evolved galaxies at $z \sim 1$, followed by a period

of passive evolution which sees them ending up as old $\gtrsim L^*$ ellipticals in the present day. However, the short gas consumption time scales can easily be prolonged by invoking negative feedback processes, and may be taken as evidence that such processes play an important role in the build-up of massive galaxies.

- We have shown that the SMGs exhibit a non-linear correlation between far-infrared and CO luminosity, similar to that observed for local ULIRGs. This not only extends the $L_{\rm CO}$–$L'_{\rm FIR}$ relation to higher luminosities ($L_{\rm FIR} \sim 10^{12-14}\,L_{\odot}$) but also shows that it holds at the highest redshifts. The main implication of this is that SMGs have higher $L_{\rm FIR}/L'_{\rm CO}$ ratios than ULIRGs, and therefore possibly higher star-formation efficiencies. However, a clearer picture of the star-formation efficiency of SMGs has to await a future systematic survey for high-redshift HCN, which will trace the dense star-forming gas.

- From our observations, we place a lower limit on the co-moving number density of massive baryonic systems in the redshift range $z = 2$–3.5 of $n(M_{bar} \geq 0.6 \times 10^{11}\,M_{\odot}) \gtrsim 6.7{\times}10^{-6}\,{\rm Mpc}^{-3}$ in agreement with recent results from recent near-infrared/spectroscopic surveys (e.g. Saracco et al. 2004; Glazebrook et al. 2004). Given the substantial uncertainties involved, we find no significant discrepancy between the data and the predicted abundances of massive galaxies at high redshifts.

Acknowledgements

TRG acknowledges support from the Danish Research Council and from the European Union RTN network, POE. IRS acknowledges support from the Royal Society. AWB acknowledges support from NSF grant AST-0205937, from the Research Corporation and the Alfred P. Sloan Foundation. We are grateful to Dave Frayer for letting us use the PdBI CO data on SMM J02396−0134.

References

Aalto S., Booth R. S., Black J. H., Johansson L. E. B., 1995, A&A, 300, 369.
Adelberger K. L., Steidel C. C., 2000, ApJ, 544, 218.
Alloin D., Barvainis R., Guilloteau S., 2000, ApJ, 528, L81.
Appleton P. N., Fadda S. T., Marleau F. R., 2004, ApJS Spitzer Special Issue, 154, 147.
Alexander D. M. et al., 2003, AJ, 126, 539.
Andreani P., Casoli F., Gerin M., 1995, A&A, 300, 43.
Andreani P., Cimatti A., Loinard L., Röttgering H., 2000, A&A, 354, L1.
Baker A. J., Tacconi L. J., Genzel R., Lehnert M. D., Lutz D., 2004, ApJ, 604, 125.
Barger A. J., Cowie L. L., Sanders D. B., Fulton E., Taniguchi Y., Sato Y., Kawara K., Okuda, H., 1998, Nature, 394, 248.
Barger A. J., Cowie L. L., Sanders D. B., 1999, ApJ, 518, L5.
Barnes J. E., Hernquist L., 1996, ApJ, 471, 115.
Barvainis R., Tacconi L., Antonucci R., Alloin D., Coleman P., 1994, Nature, 371, 586.
Barvainis R., Maloney P., Antonucci R., Alloin D., 1997, ApJ, 484, 695.
Barvainis R., Alloin D., Guilloteau S., Antonucci R., 1998, ApJ, 492, L13.
Barvainis R., Alloin D., Bremer M., 2002, A&A, 385, 399.
Baugh C. M, Lacey C. G., Frenk C. S., Granato G. L., Silva L., Bressan A., Benson A. J., Cole S., 2004, MNRAS, in press, (astro-ph/0406069).
Beelen A. et al., 2004, A&A,423, 441.

Bertoldi F., Menten K. M., Kreysa E., Carilli C. L., Owen F., 2000, 24th meeting of the IAU, Joint Discussion 9, Manchester, England.
Bertoldi, F. et al., 2003, A&A, 409, L47.
Binney J., Tremain S., 1987, "Galactic Dynamics", Princeton Series on Astrophysics, Princeton University Press.
Blain A. W., Jameson A., Smail I., Longair M. S., Kneib J.-P., Ivison R. J., 1999, MNRAS, 309, 715.
Blain A. W., Smail I., Ivison R. J., Kneib J.-P., Frayer D. T., 2002, PhR, 369, 111.
Blain A. W., Chapman S. C., Smail I., Ivison R. J., 2004, ApJ, 611, 52.
Blain A. W., Chapman S. C., Smail I., Ivison R. J., 2004b, ApJ, 611, 725.
Borys C., Chapman S. C., Halpern M., Scott D., 2003, MNRAS, 344, 385.
Braine J., Combes, F., 1992, A&A, 264, 433.
Brown R. L., Vanden Bout P. A., 1991, AJ, 102, 1956.
Carilli C. L. et al., 2002a, AJ, 123, 1838.
Carilli C. L. et al., 2002b, ApJ, 575, 145.
Carilli C. L. et al., 2004, ApJ, in press. (astro-ph/0409054).
Chapman S. C. et al. 2003a, ApJ, 585, 57.
Chapman S. C., Blain A. W., Ivison R. J., Smail I., 2003b, Nature, 422, 695.
Chapman S. C., Windhorst R., Odewahn S., Yan H., Conselice C.J., 2003c, ApJ, 599, 92.
Chapman S. C., Smail I., Windhorst R., Muxlow T., Ivison R. J., 2004a, ApJ, 611, 732.
Chapman S. C., Blain A. W., Ivison R. J., Smail I., 2004b, ApJ, in press.
Cimatti A., Andreani P., Röttgering H., Tilanus R., 1998, Nature, 392, 895.
Cimatti A. et al., 2004, Nature, 430, 184.
Cole S., Aragon-Salamanca A., Frenk C. S., Navarro J. F., Zepf S. E., 1994, MNRAS, 271, 781.
Cole S., Lacey C. G., Baugh C. M., Frenk C. S., 2000, MNRAS, 319, 168.
Cole S. et al., 2001, MNRAS, 326, 255.
Condon J. J., 1992, ARA&A, 30, 575.
Conselice C. J., Chapman S. C., Windhorst R. A., 2003, ApJ, 596, 5L.
Cox P., Omont A., Djorgovski S. G., et al. 2002, A&A, 387, 406.
Daddi E., Cimatti A., Renzini A., 2004, ApJ, 600, L127.
De Breuck, C. et al., 2003a, A&A, 401, 911.
De Breuck C., Neri R., Omont A., 2003b, NewAR, 47, 285.
Devereux N., Taniguchi Y., Sanders D. B., Nakai N., Young J. S., 1994, AJ, 107, 2006.
Dey A., Graham J. R., Ivison R. J., Smail I., Wright G. S., Liu M. C., 1999, ApJ, 519, 610.
Downes D., Solomon P. M., Radford S. J. E., 1995, ApJ, 453, L65.
Downes D., Solomon P. M., 1998, ApJ, 507, 615.
Downes D., Neri R., Wiklind T., Wilner D. J., Shaver, P. A., 1999, ApJ, 513, L1.
Downes D., Solomon P. M., 2003, ApJ, 582, 37.
Drory N., Bender R., Snigula J., Feulner G., Hopp U., Maraston C., 2001, ApJ, 562, L111.
Drory N., Bender R., Snigula J., Feulner, G., Hopp, U., Maraston C., Hill G. J., Mendes de Oliveira C., 2003, in The Masses of Galaxies at Low and High Redshift, ed. R. Bender & A. Renzini (Berlin: Springer) (astro-ph/0201207).
Dunne L., Eales S., Edmunds M., Ivison R. J., Alexander P., Clements D. L., 2000, MNRAS, 315, 115.
Fontana A., Pozzetti L., Donnarumma I., 2004, A&A, 424, 23.
Frayer D. T., Ivison R. J., Scoville N. Z., Yun M., Evans A. S., Smail I., Blain A. W., Kneib J.-P., 1998, ApJ, 506, L7.
Frayer D. T. et al., 1999, ApJ, 514, 13L.

Gao Y., Solomon P. M., 1999, ApJ, 512, L99.
Gao Y., Solomon P. M., 2003, ApJ, 606, 271.
Garrett M. A., 2002, A&A, 384, L19.
Genzel R., Baker A. J., Tacconi L. J., Lutz D., Cox P., Guilloteau S., Omont A., 2003. ApJ, 584, 633.
Glazebrook K., Abraham R., McCarthy P., 2004, Nature, 430, 181.
Granato G. L., DeZotti G., Silva L., Bressan A., Danese, L., 2004, ApJ, 600, 580.
Greve T. R., Ivison R. J., Papadopoulos P. P., 2003, ApJ, 599, 839.
Greve T. R., Ivison R. J., Papadopoulos P. P., 2004a, A&A, 419, 99.
Greve T. R., Ivison R. J., Bertoldi F., Stevens J. A., Dunlop J. S., Lutz D., Carilli C. L., 2004b, MNRAS, in press. (astro-ph/0405361).
Guilloteau S., Omont A., McMahon R. G., Cox P., Petitjean P., 1997, A&A, 328, L1.
Guilloteau S., Omont A., Cox P., McMahon R. G., Petitjean P., 1999, A&A, 349, 363.
Guilloteau S., Lucas R., 2000, in "Imaging at Radio through Submillimeter Wavelengths", ed. J.G. Magnum & S.J.E. Radford (San Francisco: ASP), 299.
Hainline L. J., Scoville N. Z., Yun M. S., Hawkins D. W., Frayer D. T., Isaak K. G., 2004, ApJ, 609, 61.
Holland W. S. et al. 1999, MNRAS, 303, 659.
Hu E. M., Ridgway S. E., 1994, AJ, 107, 1303.
Iono D., Yun M. S., Mihos J. C., 2004, ApJ, in press. (astro-ph/0407609).
Ivison R. J., Dunlop J. S., Smail I., Dey A., Liu M. C., Graham J. R., 2000, ApJ, 542, 27.
Ivison R. J., Smail I., Frayer D. T., Kneib J.-P., Blain A. W., 2001, ApJ, 561, L45.
Ivison R. J. et al., 2002, MNRAS, 337, 1.
Kauffmann G., Colberg J. M., Diaferio A., White S. D. M., 1999, MNRAS, 303, 188.
Knudsen K. K., van der Werf P. P., Jaffe W., 2003, A&A, 411, 343.
Kreysa E. et al., 1998, SPIE, 3357, 319.
Krips M., Neri R., Eckart A., Martin-Pintado J., Planesas P., Colina L., 2003, "Proceedings of the 4th Cologne-Bonn-Zermatt-Symposium", ed. S. Pfalzner, C. Kramer, C. Straubmeier, and A. Heithausen (Springer Verlag).
Lewis G. F., Carilli C. L., Papadopoulo P. P., Ivison R. J., 2002, MNRAS, 330, L15.
Lilly S. et al., 1998, ApJ, 500, L75.
Martini P., Weinberg D. H., 2001, ApJ, 547, 12.
Mirabel I. F., Sanders D. B., 1989, 340, L53.
Neri R. et al., 2003, ApJ, 597, L113.
Ohta K., Yamada T., Nakanishi K., Kohno K., Akiyama M., Kawabe R., 1996, Nature, 382, 426.
Oke J. B. et al., 1995, PASP, 107, 375.
Omont A., Petitjean P., Guilloteau S., McMahon R.G., Solomon P. M., Pecontal E., 1996, Nature, 382, 428.
Page M., Stevens J. A., Ivison R. J., Carrera F. J., 2004, ApJ, 611, L85.
Papadopoulos P. P., Röttgering H. J. A., van der Werf P. P., Guilloteau S., Omont A., Breguel W. J. M., Tilanus R. P. J., 2000, ApJ, 528, 626.
Papadopoulos P. P., Ivison R. J., Carilli C. L., Geraint L., 2001, Nature, 409, 58.
Papadopoulos P. P., Ivison R. J., 2002, ApJ, 564, L9.
Ravindranath S. et al., 2004, ApJ, 604, L9.
Richards G. T., Vanden Berk D. E., Reichard T. A., Hall P. B., Schneider D. P., SubbaRao M., Thakar A. R., York D. G., 2002, AJ, 124, 1.
Rickard L. J., Palmer P., Morris M., Turner B. E., Zuckerman B., 1975, ApJ, 199, L75.
Rickard L. J., Harvey P. M., 1984, AJ, 89, 1520.

Rigopoulou D., Spoon H. W. W., Genzel R., Lutz D., Moorwood A. F. M., Tran Q. D., 1999, AJ, 118, 2625.
Saracco P. et al., 2004, A&A, 420, 125.
Sakamoto K., Scoville N. Z., Yun M. S., Crosas M., Genzel R., Tacconi L. J., 1999, ApJ, 514, 68.
Sanders D. B., Mirabel I. F., 1985, ApJ, 298, 31L.
Sanders D. B., Scoville N. Z., Young J. S., Soifer B. T., Schloerb F. P., Rice W. L., Danielson G. E., 1986, ApJ, 305, L49.
Sanders D. B., Scovillle N. Z., Soifer B. T., 1991, ApJ, 370, 158.
Scott S. E. et al., 2002, MNRAS, 331, 817.
Scoville N. Z., Yun M. S., Windhorst R. A., Keel W. C., Armus L., 1997, ApJ, 485, L21.
Smail I., Ivison R. J., Blain A. W., 1997, ApJ, 490, L5.
Smail I., Ivison R. J., Kneib J.-P., Cowie L. L., Blain A. W., Barger A. J., Owen F. N., Morrison, G., 1999, MNRAS, 308, 1061.
Smail I., Chapman S. C., Ivison R. J., Blain A. W., Takata T., Heckman T. M., Dunlop J. S., Sekiguchi K., 2003, MNRAS, 342, 1185.
Smail I., Chapman S. C., Blain A. W., Ivison R. J., 2004, ApJ, in press.
Soifer B. T., Sanders D. B., Madore B. F., Neugebauer G., Danielson G. E., Elias J. H., Lonsdale C. J., Rice W. L., 1987, ApJ, 320, 238.
Solomon P. M., Sage L. J., 1988, ApJ, 334, 613.
Solomon P. M., Downes D., Radford S. J. E., 1992a, Nature, 356, 318.
Solomon P. M., Downes D., Radford S. J. E., 1992b, ApJ, 398, L29.
Solomon P. M., Downes D., Radford S. J. E., Barrett J. W., 1997, 478, 144.
Solomon P. M., Vanden Bout P., Carilli C. L., Guelin M., 2003, Nature, 426, 636.
Somerville R. S., Primack J. R., Faber S. M., 2001, MNRAS, 320, 504.
Soucail G., Kneib J.-P., Bezecourt J., Metcalfe L., Altieri B., Le Borgne J. F., 1999, A&A, 343, L70.
Spergel D. N. et al., 2003, ApJS, 148, 175.
Swinbank A. M., Smail I., Chapman S. C., Blain A. W., Ivison R. J., Keel W. C., 2004, ApJ, in press.
Tacconi, L. et al., 2005, ApJ, submitted.
Tecza M. et al., 2004, ApJ, 604, L109.
Walter F., Bertoldi F., Carilli C. L., Cox P., Lo K. Y., Neri R., Fan X., Omont A., Strauss M. A., Menten K. M., 2003, Nature, 424, 406.
Webb T. M. et al., 2003, ApJ, 587, 41.
Weiss A., Henkel C., Downes D., Walter F., 2003, A&A, 409, L41.
White S D M., Frenk C. S., 1991, ApJ, 379, 52.
Wilner D. J., Zhao, J.-H., Ho P. T. P., 1995, ApJ, 453, L91.
Wyse R. F. G., Gilmore G., Franx M., 1997, ARA& A, 35, 637.
Yao L., Seaquist E. R., Kuno N., Dunne L.,, 2003, ApJ, 588, 771.
Young J. S., Kenney J., Lord S. D., Schloerb F. P., 1984, ApJ, 287, L65.
Young J. S., Schloerb F. P., Kenney J. D., Lord S. D., 1986, ApJ, 304, 443.
Yun M. S., Reddy N. A., Condon J. J., 2001, ApJ, 554, 803.

Chapter 8

Summary

In this chapter I will summarise the main scientific results obtained in the previous chapters.

- Deep 1200μm maps of the two survey regions ELAIS N2 and Lockman Hole East have been obtained using the Max Planck Millimetre Bolometer Array (MAMBO) on the IRAM 30 m telescope in Granada. This work is amongst the very first MAMBO maps to have been published. A source extraction technique has been developed and extensive monte carlo simulations have been performed in order to assess the reliability of the sources, their fluxes and positions.

  This has resulted in the most accurate 1200μm number counts at bright flux levels to date. The counts can account for about 10 per cent of the extragalactic background at 1200μm. In order to account for the high surface density of MAMBO sources, substantial evolution must have taken place between the likely redshift of these sources ($z \sim 2$) and the present day. Using simple parametric models of galaxy evolution we have been able to reproduce the observed number counts at 1200 as well as 850μm, suggesting that there could be a substantial overlap between the two populations.

  We have performed the first unbiased comparison between MAMBO and SCUBA maps of the same regions, confirming about half of the most significant SCUBA sources. We have defined an extremely robust sub-sample of 13 SMGs detected by both MAMBO and SCUBA, of which only one has no radio counterpart. We have searched for extremely high redshift ($z >> 3$) SCUBA drop-outs from an analysis of the 850-to-1200μm flux ratios of the 18 MAMBO sources not detected by SCUBA but find no conclusive evidence for such sources.

- Using the IRAM Plateu de Bure Inteferometer we have obtained interferometric maps and spectra of the CO emission towards five sub-mm selected galaxies. This has almost doubled the number of SMGs detected in CO to date and represents an important step forward in our understanding of sub-mm selected galaxies in the sense that it has allowed us for the first time to study the gas properties in a statistically significant sample of SMGs.

  An important finding from this study is that SMGs appear to be scaled-up versions of the local ULIRG population in that they are not only more CO luminous and gas-rich, but they have also much broader line widths and dynamical masses. In fact, SMGs are as gas-rich and have dynamical masses comparable to that of high-z QSOs and HzRGs - the most extreme objects in the Universe.

  A feature which SMGs appear to have in common with far-infrared luminous starburst galaxies at the present epoch is the fact that they both seem to exhibit a non-linear

correlation between CO and far-infrared luminosity. Well established for local starburst galaxies, our study has shown that this correlation also holds for SMGs which not only have higher far-infrared luminosities but also lie at much higher redshifts.

While it has long been postulated that SMGs could be the long sought for progenitors of local ellipticals, the only piece of evidence in support of this idea was their extremely large starformation rates. Here we have demonstrated that SMGs in general, and not just in a few cases, habour enough molecular gas to fuel the intense starformation for long enough time to form a massive spheroid. We have put a firm lower limit on the typical gas exhaustion time-scale in SMGs of $\gtrsim 30\,\mathrm{Myr}$. This is a significant result since it implies that over the redshift range in which SMGs are typically found, the luminous sub-mm phase is a transitory phenomenon - suggesting that the true space density of SMGs could be as much as an order of magnitude higher than that observed. This would bring the space density of SMGs in line with that of X-ray absorbed, sub-mm bright QSOs at $z \sim 2$, massive evolved spheroids at $z \sim 1$, and finally old giant ellipticals at the present epoch - thus strongly implying an evolutionary sequence between these four populations.

Secondly, we have established that SMGs have dynamical masses comparable to that of giant ellipticals at the present epoch, and that a significant fraction of the mass is baryonic. Lower limits have been imposed on the co-moving number density of massive ($\gtrsim 0.6 \times 10^{11}\,M_{\odot}$) baryonic systems in the redshift range $2 \lesssim z \lesssim 3.5$. Our study adds to the growing observational evidence that the assembly of massive galaxies occurs much more rapidly than previously thought, and highlights our poor understanding of the dissipative physics and feed-back processes involved in massive galaxy formation in the early Universe.

- Perhaps a less obvious outcome of my thesis has been to underline the power of sensitive interferometric observations of molecular gas in the high redshift Universe. Such observations provide crucial information on the (gas) masses of galaxies in the process of being formed, and hence with most of their baryonic mass in the form of gas. This was exemplified in chapters 4 and 5 where high-resolution VLA observations of the molecular gas in the Extremely Red Object ERO J16540+4626 and the high-redshift radio galaxy 4C 60.07 were used to map the molecular gas in these systems, which in turn provided valuable insight into their dynamical masses and evolutionary stage. Even crude attempts at assessing the excitation conditions of the ISM in these two objects were made.

  With less than 35 high-redshift sources detected in CO to date, each requiring substantial amounts of integration time, observations of molecular lines at high redshifts are still far from being routine. However, our on-going systematic CO survey of SMGs, which in many ways acts as a spearhead project for the Atacama Large Millimeter Array (ALMA), has opened up the door for follow-up observations of other molecular lines and species (e.g. HCN and CI), and could provided us with a first taste of the 'golden age' we can expect once ALMA comes online.